AD_____

Award Number: W81XWH-05-2-0027

TITLE: IMPACT (Imaging and Molecular Markers for Patients with Lung Cancer: Approaches with Molecular Targets and Complementary, Innovative and Therapeutic Modalities)

PRINCIPAL INVESTIGATOR: Waun Ki Hong, M.D.
                                              Roy Herbst, M.D., Ph.D. (Co-Principal Investigator)

CONTRACTING ORGANIZATION: M.D. Anderson Cancer Center
                                                     Houston, TX 77030

REPORT DATE: March 2009

TYPE OF REPORT: Annual

PREPARED FOR: U.S. Army Medical Research and Materiel Command
                          Fort Detrick, Maryland 21702-5012

DISTRIBUTION STATEMENT: Approved for Public Release;
                                          Distribution Unlimited

The views, opinions and/or findings contained in this report are those of the author(s) and should not be construed as an official Department of the Army position, policy or decision unless so designated by other documentation.

REPORT DOCUMENTATION PAGE

Form Approved
OMB No. 0704-0188

Public reporting burden for this collection of information is estimated to average 1 hour per response, including the time for reviewing instructions, searching existing data sources, gathering and maintaining the data needed, and completing and reviewing this collection of information. Send comments regarding this burden estimate or any other aspect of this collection of information, including suggestions for reducing this burden to Department of Defense, Washington Headquarters Services, Directorate for Information Operations and Reports (0704-0188), 1215 Jefferson Davis Highway, Suite 1204, Arlington, VA 22202-4302. Respondents should be aware that notwithstanding any other provision of law, no person shall be subject to any penalty for failing to comply with a collection of information if it does not display a currently valid OMB control number. **PLEASE DO NOT RETURN YOUR FORM TO THE ABOVE ADDRESS.**

1. REPORT DATE 1 March 2009	2. REPORT TYPE Annual	3. DATES COVERED 1 Feb 2008 – 31 Jan 2009

4. TITLE AND SUBTITLE	5a. CONTRACT NUMBER
IMPACT (Imaging and Molecular Markers for Patients with Lung Cancer: Approaches with Molecular Targets and Complementary, Innovative and Therapeutic Modalities)	**5b. GRANT NUMBER** W81XWH-05-2-0027
	5c. PROGRAM ELEMENT NUMBER
6. AUTHOR(S)	**5d. PROJECT NUMBER**
Waun Ki Hong, M.D., Principal Investigator Roy Herbst, M.D.,Ph.D., Co-Principal Investigator E-Mail: whong@mdanderson.org	**5e. TASK NUMBER**
	5f. WORK UNIT NUMBER

7. PERFORMING ORGANIZATION NAME(S) AND ADDRESS(ES) M.D. Anderson Cancer Center Houston, TX 77030	8. PERFORMING ORGANIZATION REPORT NUMBER

9. SPONSORING / MONITORING AGENCY NAME(S) AND ADDRESS(ES) U.S. Army Medical Research and Materiel Command Fort Detrick, Maryland 21702-5012	10. SPONSOR/MONITOR'S ACRONYM(S)
	11. SPONSOR/MONITOR'S REPORT NUMBER(S)

12. DISTRIBUTION / AVAILABILITY STATEMENT
Approved for Public Release; Distribution Unlimited

13. SUPPLEMENTARY NOTES

14. ABSTRACT

The projects in this proposal specifically target several signal transduction pathways known to be critical for NSCLC pathogenesis including the EGFR pathway and the more downstreamras/raf/Mek/ERK pathway. These projects combine targeted approaches using molecular and imaging techniques to validate activity against a target and monitor response using imaging modalities specific to the receptor using either small molecules or targeted peptide approaches.

15. SUBJECT TERMS
 Lung cancer, molecular markers, molecular imaging, targeted therapy

16. SECURITY CLASSIFICATION OF:			17. LIMITATION OF ABSTRACT	18. NUMBER OF PAGES	19a. NAME OF RESPONSIBLE PERSON USAMRMC
a. REPORT U	**b. ABSTRACT** U	**c. THIS PAGE** U	UU	238	**19b. TELEPHONE NUMBER** *(include area code)*

Standard Form 298 (Rev. 8-98)
Prescribed by ANSI Std. Z39.18

Table of Contents

IMPACT: Imaging and **M**olecular Markers for **P**atients with **L**ung **C**ancer: **A**pproaches with Molecular Targets, **C**omplementary, Innovative and **T**herapeutic Modalities

INTRODUCTION

Lung cancer is the most prevalent cancer worldwide and the leading cause of cancer-related mortality in both men and women in the United States. Conventional multimodality therapies (surgery, radiation and chemotherapy) have reached a therapeutic ceiling in improving the five-year overall survival rate of non-small cell lung cancer (NSCLC) patients, clinically in large part due to chemo- and radiation-resistant locoregional and metastatic spread but ultimately due to poor understanding of the disease and its resistance to the therapy.

Lung cancer is a heterogeneous disease, resulting from accumulated genetic abnormalities over years, which thus requires a coordinated attack in a truly integrated fashion on multiple altered signal pathways. Emerging targeted therapy aims to target key molecular abnormalities in cancer and has succeeded in some tumor types such as chronic myeloid leukemia (CML) (Druker et al., 2004; Druker and Sawyers et al., 2001; Druker and Talpaz et al., 2001), gastrointestinal stromal tumor (Demetri et al., 2002), colon cancer (Hurwitz et al., 2003), and breast cancer (Howell et al., 2005). Thus, the incorporation of targeted therapy into conventional treatments appears to be a new promising approach to treatment of lung cancer.

The program project IMPACT has proposed to integrate targeted therapy in the lung cancer research program when initial clinical results showed disappointing response rates and survival benefit of epidermal growth factor receptor (EGFR) inhibitor Gefitinib (Iressa) for non-selected lung cancer patients (Herbst et al., 2002, 2003,2004; Herbst, 2004; Kris et al., 2003; Giaccone et al., 2004). It aims to validate molecular mechanisms of targeted agents alone and in combination with chemo and/or radiation therapies in preclinical and clinical settings. It also aims to develop effective molecular imaging and cancer cell-targeted peptide-based delivery tools to help improve efficacy of the targeted agents. Specifically, our objectives are:

- To validate preclinically and clinically several key signaling pathways and their agents for therapeutic potentials alone or in combination with each other or with chemo and /or radiotherapy
- To explore applications of molecular imaging for targeted therapy and identify cancer cell-targeted peptides for systemic delivery of therapeutic and imaging agents
- To discover and evaluate new molecular abnormalities and therapeutic predictors in lung cancer
- To develop an educational program for teens and young adults for smoking risk and resultant lung cancer occurrence.

IMPACT is composed of 6 research projects, 1 Biostatistics Core, 1 Molecular Pathology Core, 1 Molecular Imaging Core, 2 career development projects, and 2 developmental research projects. Here we present their scientific progresses in the fourth grant year as follows.

Project 1: Targeting epidermal growth factor receptor signaling to enhance response of lung cancer to therapeutic radiation.

(PI and co-PI: Raymond E. Meyn, Ph.D., Ritsuko Komaki, M.D.)

In spite of significant technical advances including intensity-modulated radiation therapy (IMRT) and chemoradiation, locally advanced lung cancer continues to have a dismal prognosis as many patients' tumors appear to be resistant to radiation therapy. The molecular basis for radiation resistance is not fully understood, but tumor cells have an enhanced survival response that involves increased capacity for DNA repair and suppressed apoptosis. Both apoptosis propensity and DNA repair capacity are thought to be partly controlled by the upstream signal transduction pathways triggered by EGFR activation, which is constitutively activated in many NSCLCs, and its activation leads to a radiation-resistant phenotype. We hypothesize that the response of NSCLC to radiation can be improved through the use of inhibitors of EGFR signaling.

Aim 1   To test the combination of external beam radiation and the selective EGFR-tyrosine kinase inhibitor erlotinib (Tarceva) in locally advanced NSCLC.

<u>Summary of Research Findings</u>

2005-1023, A Phase II Study of Tarceva (erlotinib) in Combination with Chemoradiation in Patients with Stage IIIA/B Non-Small Cell Lung Cancer (NSCLC), completed a comprehensive review by our Institutional Review Board (IRB), the US Department of Defense (DoD), Genentech, and Food and Drug Administration (FDA), and was finally approved in November 2007. The trial was subsequently activated (11/20/07) and patient accrual has begun. An amendment is pending to reduce total accrual from 72 patients to 48 patients by using progression-free survival rather than time to progression as the endpoint.

This trial uses chemoradiotherapy followed by a molecularly targeted treatment (erlotinib, targeting the EGFR tyrosine kinase) with/without radiotherapy for stage III NSCLC to improve the therapeutic ratio (i.e., increase malignant cell cytotoxicity without increasing normal cell cytotoxicity). The primary objective is to determine the efficacy of concurrent chemoradiotherapy followed by erlotinib/radiation and erlotinib alone, which will be repeated for 7 weeks, then two cycles of consolidation chemotherapy as measured by progression-free survival. Secondary objectives include determining: 1) safety, as measured by the rate of grade 3 or worse non-hematological toxicity (dose-limiting toxicity, DLT) occurring prior to the beginning of consolidation therapy (including all toxicities attributed to chemoradiation occurring within 90 days of the start of radiation therapy); 2) compliance, which is defined to be completion of concurrent chemoradiation and erlotinib/radiotherapy with no more than minor variations; 3) response rate (complete and partial response rates); 4) overall survival rates (one- and two-year rates, median survival); 5) disease (local) control rate; 6) association between EFGR expression and toxicity, response, overall survival, and progression (exploratory analysis); and 7) association between EGFR expression and response correlated with imaging study. A total of 48 patients will be treated with concurrent chemoradiation [RT: 63 Gy/35 fractions/7weeks (+/- 5 days), 1.8 Gy/ fraction, a total dose of 63.0 Gy in 35 fractions over 7 weeks plus Paclitaxel, 45mg/m², and carboplatin, AUC=2, weekly on day 1 for 7 weeks] and erlotinib (erlotinib, 150 mg p.o. daily for 7 weeks, starting with radiotherapy on day 2-5 followed by erlotinib 150 mg p.o. alone on day 6 -7 for 7 weeks). Patients will get one month off treatment, followed by consolidation therapy of chemotherapy alone (weeks 11-17: paclitaxel, 200 mg/m², and carboplatin, AUC=6, every 3 weeks for two cycles).

Currently, a total of 22 patients were enrolled on this protocol between November 2007 and February 8, 2009, with an average accrual rate of 1.6 patients/ month. Accrual rate for the first several months after activation was lower than predicted, but has increased to 2-4 patients/month since August 2008. We anticipate completion of the study within the next 12 months; thus, a request for a no-cost extension to continue to support this work has been submitted.

Response
Fourteen patients have completed the treatment regimen per protocol. Twelve of these patients had a measurable response (RECIST) to the treatment; seven patients had a complete response (CR) and five patients achieved partial response (PR). One of the patients exhibited disease progression during the treatment schedule and treatment was discontinued. Another patient's tumor response was not able to be assessed due to the tumor being obscured by radiation pneumonitis. During the follow-up time period, one patient developed a brain metastasis two months after completion of treatment, with CR in the primary disease site of the left lingular lobe of the lung. A second patient developed a malignant pleural effusion two months after completion of his treatment with PR in the primary disease site. A third patient failed in the primary site where he received radiotherapy, eight months after completion of his treatment, without any distant metastasis. The rest (10/14) of patients are in the follow-up process with visits and scans for tumor assessment every three months. Eight of these patients have not yet returned for their first follow–up visit, so it is too early to summarize these results.

Toxicity
Toxicity data is available for 22 patients either having completed therapy, or who are presently receiving treatment. Severe acute toxicities (grade 3 or higher according to CTC.3) related to treatments were recorded as the following events:
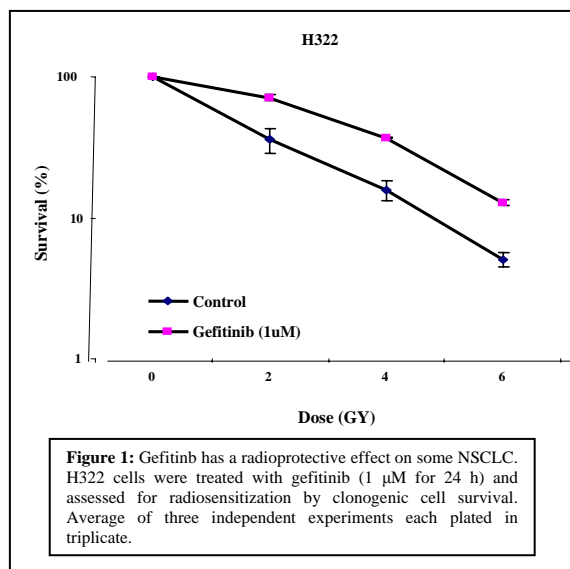- Rash, Grade 3 in 3 patients
- Acne, Grade 3 in 2 patients
- Diarrhea, Grade 3 in 1 patient
- Pneumonitis, Grade 3 in 3 patients
- Leukopenia, Grade 3 in 3 patients, Grade 4 in 1 patient
- Neutropenia Grade 3 in 1 patient, Grade 4 in 2 patients
- Thrombocytopenia, Grade 3 in 1 patient
- Hypomagnesemia, Grade 3 in 1 patient
- Hypokalemia, Grade 3 in 1 patient
- Pneumonia, Grade 3 in 4 patients
- Dehydration, Grade 3 in 1 patient.

Protocol 2005-1023 appears to have a toxicity profile that is comparable to other chemoradiotherapy regimens reported in this patient population. Preliminary response data seems favorable, although it is too early in the study to be certain of whether this result is significant. Continuation of the study is warranted.

Correlation of biomarkers from the biopsy specimen from the primary site with response is underway. We are going to analyze correlation between biomarkers and responses as well as toxicity when 20 patients will complete treatment. The results will be submitted to a major international scientific meeting such as AACR or others. If the rate of accrual of 3-4 patients/month continues, we will complete this trial by the end of this year.

Aim 2   To test the hypothesis that activation of the EGFR pathway leads to radiation resistance in NSCLC cells due to an enhanced capacity for repairing DNA lesions.

Summary of Research Findings

Figure 1: Gefitinib has a radioprotective effect on some NSCLC. H322 cells were treated with gefitinib (1 μM for 24 h) and assessed for radiosensitization by clonogenic cell survival. Average of three independent experiments each plated in triplicate.

As reported previously, 2 NSCLC cell lines, A549 and H1299, displayed a significant radiosensitization by gefitinib correlating with a gefitinib-mediated inhibition of radiation-induced DNA double-strand breaks (DSBs). Since then, we have extended this analysis to other cell lines including additional NSCLC lines and normal cells as well. Although some other NSCLC cell lines are radiosensitized by gefitinib, we also discovered that some lines are rendered radioresistant by gefitinib treatment. For example, survival curves for H322 cells have shown that gefitinib induces a rather profound degree of radioresistance (Fig. 1). A similar effect is seen in several normal cell lines including normal human bronchial epithelial cells (HBECs) (Fig. 2).

Although we haven't analyzed all of these different cell lines for the effects of gefitinib on DSB repair, we have examined the results on the H322 line, and gefitinib appears to accelerate the repair of DSBs compared to the radiation alone case (Fig. 3). During this past year, we have begun an extensive investigation to uncover the basis for these differences in the ability of NSCLC cell lines to be radiosensitized by EGFR inhibitors. As will be presented in the next section, we hypothesize that this difference is related to whether the cell line is epithelial-like or mesenchymal-like.
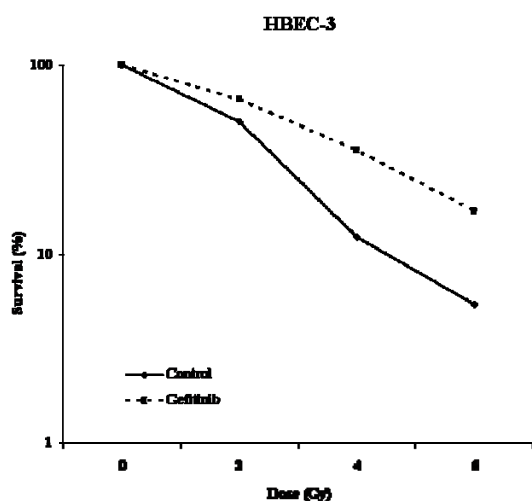
Figure 2. Effect of Gefitinib on radiosensitivity of normal cells. HBEC-3 cells were treated with gefitinib (1μM for 24 h) and assessed for radiosensitization by clonogenic cell survival immediately. Each data point represents the average of three independent experiments each plated in triplicate.
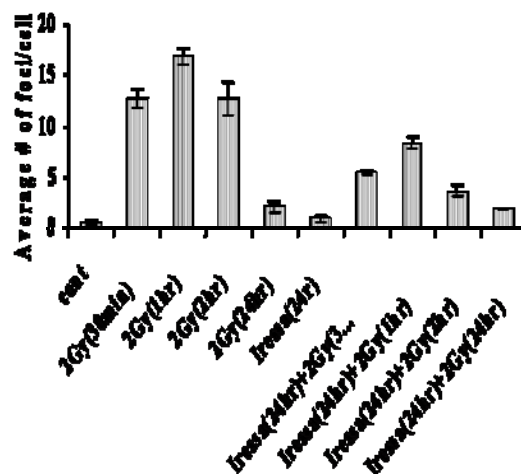

Figure 3. Gefitinib enhances the repair of radiation-induced DSBs detected on the basis of γ-H2AX foci. H322 cells growing on cover slips in 35 mm dishes were exposed to gefitinib (1μM) for 24 h, irradiated (2 Gy), and fixed at the specified time for analysis of nuclear γ-H2AX foci using immunofluorescence microscopy. Quantitative analysis of foci present in the cells following various treatments is presented. Columns, mean of three independent experiments. Bar: SE.

Aim 3   **To test the hypothesis that clinically useful inhibitors of EGFR signaling abrogate DNA repair capacity, restore apoptotic response and radiosensitize NSCLC cells.**

Summary of Research Findings

Several recently published papers have reported that the sensitivity of NSCLC cells to antagonists of the EGFR correlates with whether they have undergone the epithelial-to-mesenchymal transition (EMT). Specifically, cells that have undergone EMT proved resistant to gefitinib or erlotinib as a single agent. We have now observed an EMT-related relationship amongst our NSCLC lines, some of which were the same lines as in these published reports. Cell lines that were reported to be epithelial-like (sensitive to gefitinib) were rendered radioresistant by the drug in our studies and cell lines reported to be mesenchymal-like (resistant to gefitinib) were radiosensitized by the drug in our experiments. This suggests that the activities of gefitinib for drug-induced cytotoxicity and drug-modulation of radiosensitivity are different. Based on the correlation between our observed results and reported results in the literature regarding the same cell lines, we decided to expand our panel of cell lines to include additional lines identified in those reports. Thus, we have now analyzed a total of 8 NSCLC cell lines for their response to a pre-irradiation treatment with 1 μM of gefitinib. Although complete clonogenic survival curves were generated for all 8 lines with and without gefitinib, we have summarized the results in Figure 4 where we present the SF_2 values for all of these survival curves (error bars omitted from Fig. 4). However, each value is the average of 3 independent experiments, each plated in triplicate. Statistical analysis indicated that the gefitinib treated vs. non-gefitinib treated value was significant at the p<.05 level for each cell line.
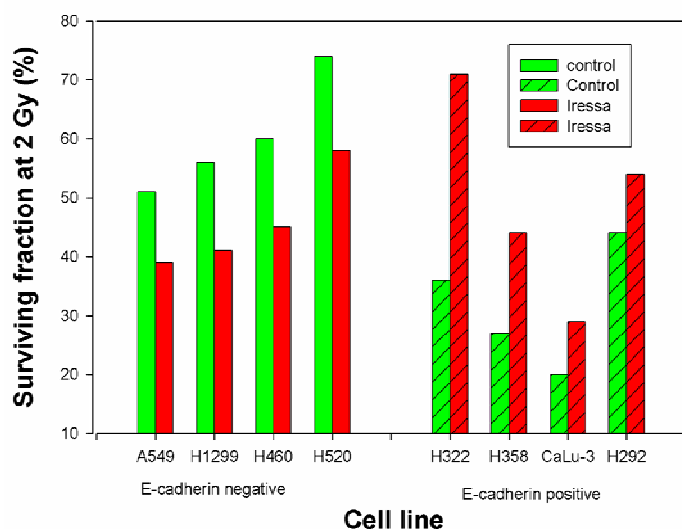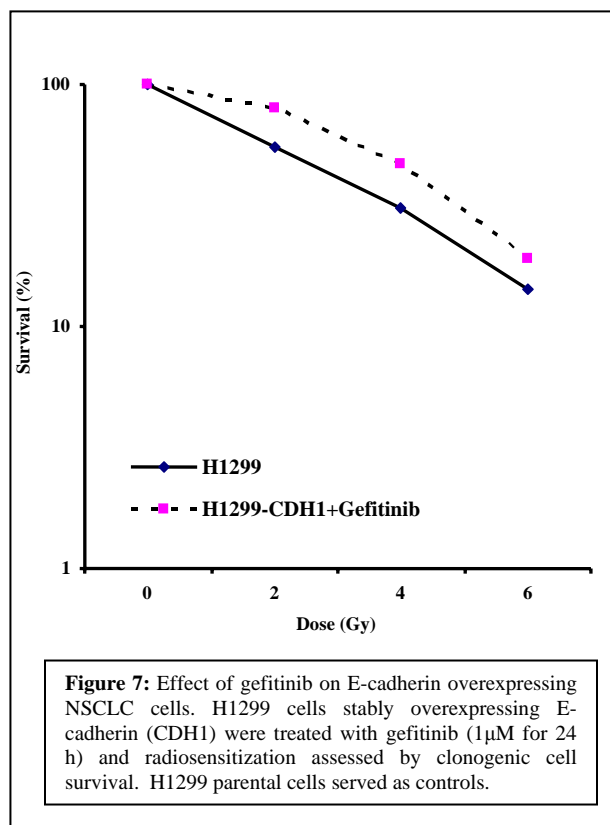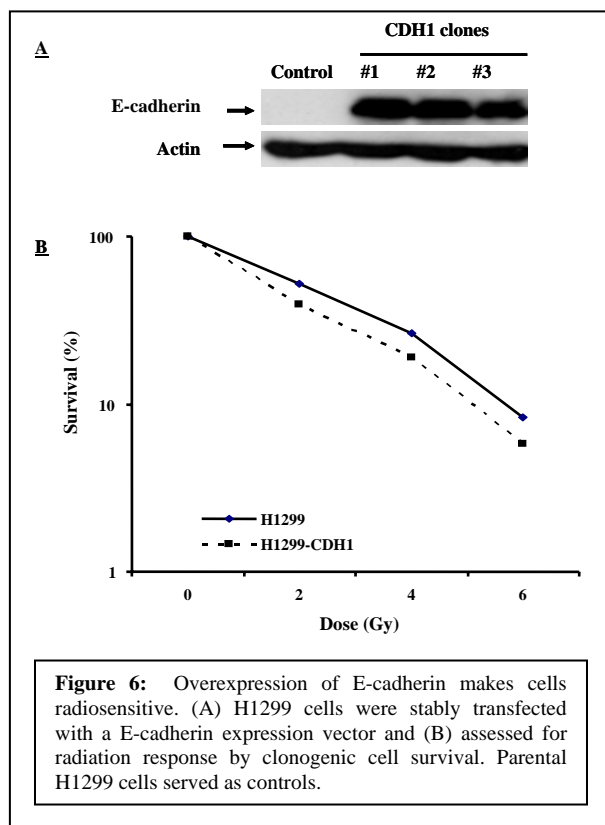

Figure 4. Comparison of SF2 values in E-cadherin positive versus E-cadherin negative cell lines following exposure to Gefitinib. Cells were exposed to Gefitinib (1µM) for 24 h following which they were assessed for radiosensitization by clonogenic cell survival.

The EMT is primarily indicated and, in at least some cases, dictated by the presence or loss of E-cadherin expression. To validate that the cell lines in our NSCLC panel had or had not undergone EMT, we performed immunoblot analysis of E-cadherin expression for all lines under study. The results indicated that, as reported for these same lines in the literature, the H322, H358, H292 and Calu3 lines express E-cadherin and the A549, H1299, H460, Calu6 and H520 lines do not (Fig. 5). The HBECs, as expected, express E-cadherin (not shown). Cells that have undergone EMT and have lost E-cadherin sometimes express mesenchymal markers such as vimentin, although this is not an absolute marker for EMT. We assessed vimentin in our panel of cell lines; all of the lines with the mesenchymal phenotype express vimentin except A549 cells, which express N-cadherin and fibronectin (2 other mesenchymal markers) instead. One cell line with epithelial phenotype also expresses vimentin, illustrating that this marker is not 100% specific compared to E-cadherin for EMT status.

8

Figure 5. Immunoblot analysis for EMT markers in a panel of NSCLC cell lines
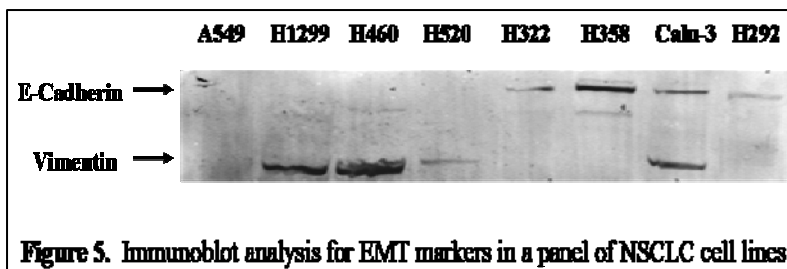
Although we have established the relationships of EMT status to tumor cell radiosensitivity in our panel of 8 NSCLC lines (the epithelial lines, H358, H322, CaLu-3 and H292, have SF_2 values of <0.45 and the mesenchymal lines, A549, H1299, H460 and H520, have SF_2 values of >0.50), this is an observed correlation and does not prove an absolute relationship between E-cadherin expression and cell sensitization. Therefore, we have begun a series of experiments to test whether restoring E-cadherin expression in the mesenchymal-like lines sensitizes them to radiation. We have transfected H1299 cells with a *CDH1*-expression vector and isolated clones based on drug-selection markers in the vector. Several clones were selected and analyzed for E-cadherin expression. One such clone, H1299-CDH1 (clone #1), has subsequently been tested for radiosensitivity compared to the parental line and the results are presented in Fig. 6. Although this experiment will have to be repeated and additional clones tested, this result suggests that restoration of E-cadherin expression in mesenchymal-like NSCLC cells produces a radiosensitizing effect.

Figure 6: Overexpression of E-cadherin makes cells radiosensitive. (A) H1299 cells were stably transfected with a E-cadherin expression vector and (B) assessed for radiation response by clonogenic cell survival. Parental H1299 cells served as controls.

Figure 7: Effect of gefitinib on E-cadherin overexpressing NSCLC cells. H1299 cells stably overexpressing E-cadherin (CDH1) were treated with gefitinib (1μM for 24 h) and radiosensitization assessed by clonogenic cell survival. H1299 parental cells served as controls.

Using the same clone of H1299 cells with restored E-cadherin expression, described above, we tested the effects of a gefitinib pretreatment compared to parental cells. The results of this
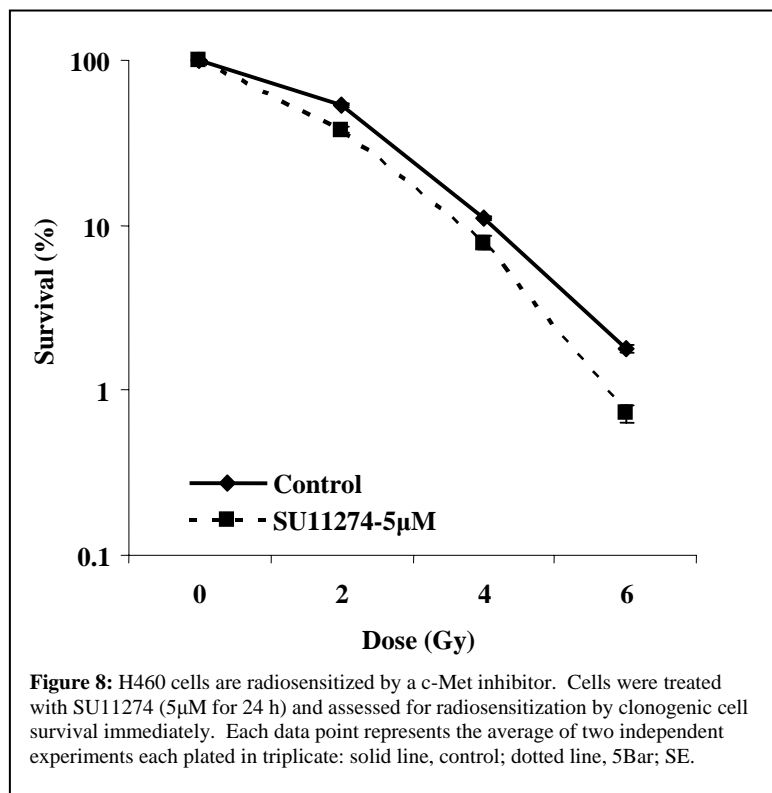
experiment indicate that instead of being sensitized to radiation, as shown for the parental cells in Figure 1, the same pretreatment with gefitinib exerts a radioprotective effect on these H1299-CDH1 cells (Fig. 7). Again, these experiments will have to be repeated and additional clones produced and analyzed. Moreover, this H1299-CDH1 clone was compared to parental cells in these experiments and we are in the process of making empty-vector control cell lines to use in further studies related to these questions. E-cadherin expressing clones of A549 cells have been produced and initial testing of one clone suggests that while gefitinib pretreatment does not render the A549-CDH1 cells radioresistant, it no longer induces a radiosensitizing effect compared to results in parental cells as shown in Figure 1 (data not shown).

Aim 4   To test the hypothesis that targeting both EGFR and its downstream signaling pathways will have at least an additive radiosensitizing effect on NSCLC.
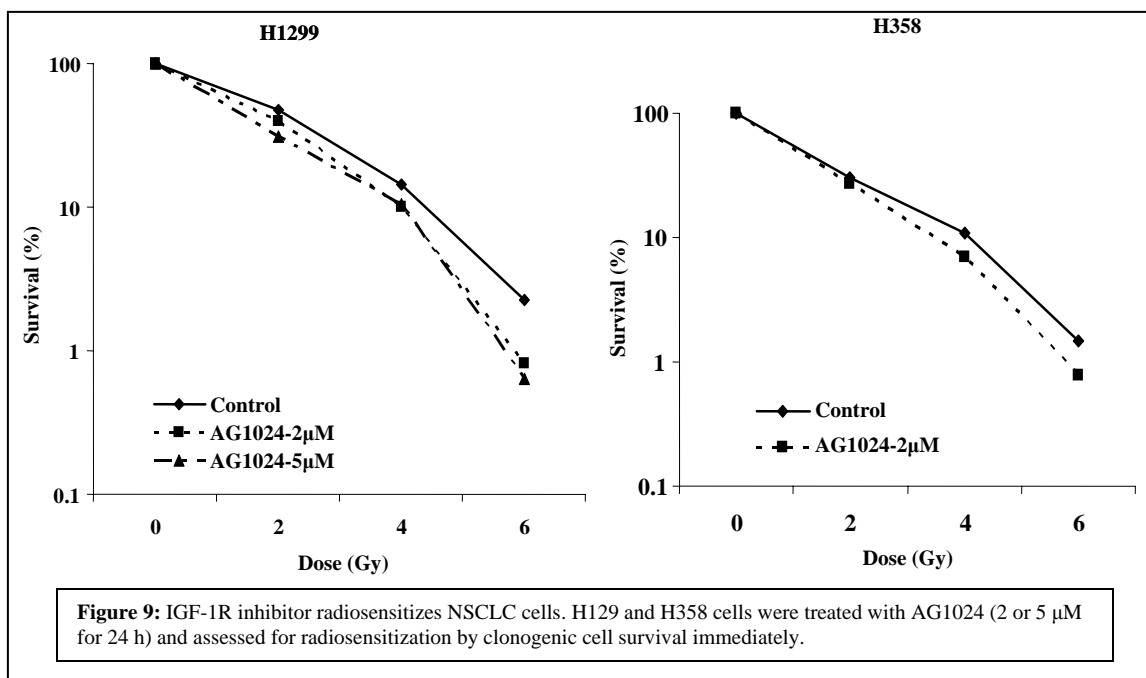
<u>Summary of Research Findings</u>

It is now understood that resistance to EGFR inhibitors such as gefitinib and erlotinib may be due to compensatory signaling pathways. Two such pathways are now known: the c-Met and IGF1R mediated pathways. During this past funding period, we have continued to examine both of these pathways in order to understand why some cell lines are resistant to radiosensitization by inhibition of EGFR. For these experiments, we have used commercially available inhibitors of c-Met (e.g., SU11274) and of IGF1R (e.g., AG1024).

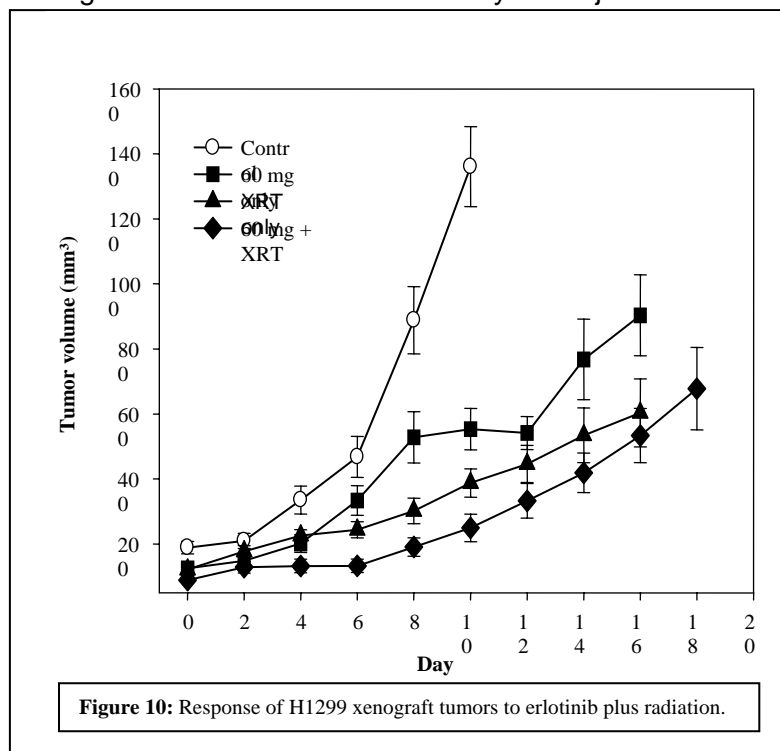We examined the ability of both of these inhibitors to radiosensitize NSCLC cell lines. Last year, we reported that the c-Met inhibitor SU11274 has a significant radiosensitizing effect on H1299 cells, and we have extended this finding to H460 cells (Fig. 8). This finding is consistent with the emerging hypothesis that resistance to radiosensitization with EGFR inhibition may be due to compensatory signaling by the c-Met receptor, and that inhibition of c-Met signaling may be a useful strategy for radiosensitizing NSCLC cells either with or without combining with EGFR inhibitors. Similarly, we have shown that the H1299 and H358 cells are potentially radiosensitized by the IGF1R inhibitor, AG1024 (Fig. 9). Thus, inhibition of the IGF1R pathway may also be a viable strategy for enhancing the radiation response of NSCLC cells.

Figure 8: H460 cells are radiosensitized by a c-Met inhibitor. Cells were treated with SU11274 (5μM for 24 h) and assessed for radiosensitization by clonogenic cell survival immediately. Each data point represents the average of two independent experiments each plated in triplicate: solid line, control; dotted line, 5Bar; SE.

Figure 9: IGF-1R inhibitor radiosensitizes NSCLC cells. H129 and H358 cells were treated with AG1024 (2 or 5 μM for 24 h) and assessed for radiosensitization by clonogenic cell survival immediately.

Aim 5   To test whether the strategies developed in Specific Aims 2-4 have efficacy in a xenograft tumor model.

Summary of Research Findings

We also investigated the ability of erlotinib to mediate its radiosensitizing effect *in vivo*. Xenograft tumors were established by s.c. injection of 5×10^6 viable H1299 cells, suspended in PBS, into the hind legs of 6-8 week-old athymic nude mice (nu/nu; Charles River). Treatment was initiated when the tumors reached 100mm^3 with either erlotinib alone (60mg/kg daily for a total of nine doses), radiation alone (5 Gy), or erlotinib (60mg/kg daily) plus radiation. For *in vivo* radiation treatments, animals bearing xenograft tumors were irradiated while anesthetized using a ^{60}Co teletherapy unit. Radiation was given 24 h after the last injection of erlotinib. Tumor growth delay was assessed following treatment. Tumors were measured every other day in two orthogonal dimensions, and the tumor volume was estimated assuming an ellipsoid shape. Animals were sacrificed when the tumor volume reached 1000mm^3.

Figure 10: Response of H1299 xenograft tumors to erlotinib plus radiation.

A modest tumor growth delay was observed in the group that received erlotinib plus radiation treatment when compared with radiation or erlotinib treatments alone (Fig. 10).

Key Research Accomplishments

- Entered 22 patients onto the erlotinib (Tarceva) plus radiotherapy for locally advanced NSCLC trial and completed evaluation of 12 of these patients.
- Discovered relationship between the epithelial-to-mesenchymal transition and radiosensitivity of NSCLC cells.
- Demonstrated that pretreatment with gefitinib exerts a radioprotection of H1299-CDH1 cells.
- Demonstrated that small molecule inhibitors of both c-Met and IGF-1R produce a significant radiosensitizing effect on NSCLC cells.
- Completed an assessment of the combination of erlotinib (Tarceva) and radiation in a NSCLC xenograft tumor model.

Conclusions

We conclude that the epithelial-to-mesenchymal transition (EMT) plays a significant role in governing not just the intrinsic radiosensitivity of NSCLC cells, but also their sensitivity to inhibitors of the epidermal growth factor receptor (EGFR) and the ability of such inhibitors to radiosensitize these cells. It would be useful to assess the EMT status of patients treated with these combinations. In spite of this finding, results suggest that such combinations might be useful in the clinic. In addition, we conclude that targeting other growth factor receptors such as the c-Met and IG-F1R receptors may be an alternative strategy to using EGFR inhibitors.

Project 2: Molecular Imaging of EGFR Expression and Activity in Targeting Therapy of Lung Cancer

(PI and co-PI: Juri Gelovani, M.D., Ph.D.; Roy Herbst, M.D., Ph.D.)

Aim 1   To synthesize novel pharmacokinetically optimized ^{124}I and ^{18}F-labeled IPQA derivatives for PET imaging of EGFR kinase activity and conduct *in vitro* radiotracer accumulation studies in tumor cells expressing different levels of EGFR activity.

During the third year of funding of Project 2, our research continued to be focused on Aims 2 and 3 of this Project. This Aim was completed during the previous project year.

Aim 2   To assess the biodistribution (PK/PD) and tumor targeting by novel ^{124}I and ^{18}F-labeled EGFR kinase-specific IPQA derivatives using PET imaging in orthotopic mouse models of lung cancer and compare *in vivo* radiotracer uptake/retention with phospho-EGFR levels *in situ*.

Summary of Research Findings

As part of Aim 2, we've developed the fifth-generation of more water-soluble polyethylene glycol (PEG)-ylated 3-iodo-4-(phenylamino)quinazoline-6-acrylamide (IPQA) derivatives labeled with ^{18}F, which will simplify the translation of EGFR kinase imaging agents into the clinic in comparison with ^{124}I-JGAP5. These novel fifth generation ^{18}F-labeled compounds

were synthesized by the Imaging Core D. The compound [18F]fluoro-hexa-PEG-IPQA was developed based on our previous studies to improve tracer's solubility, resulting in less hepato-biliary clearance and a longer plasma circulation half-time.
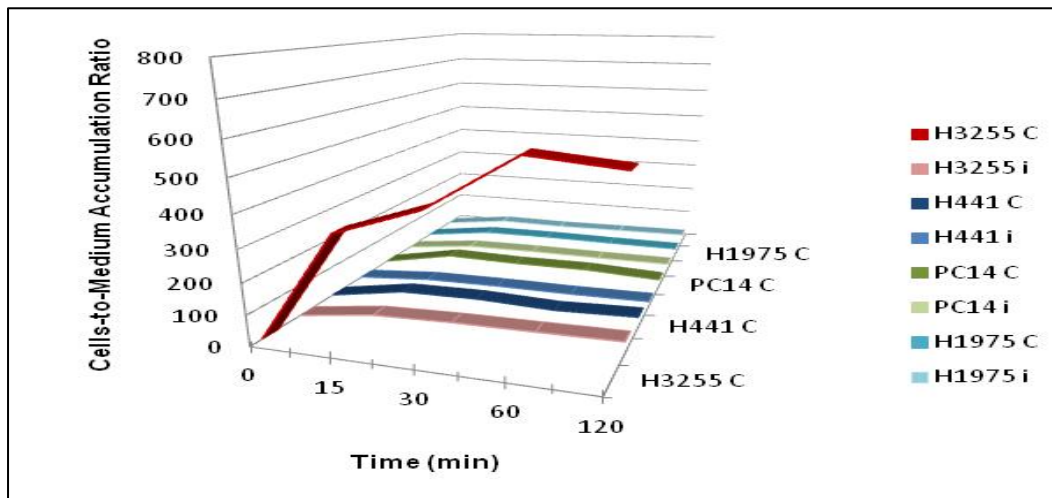
Figure 1. Time-dependent accumulation and washout of [18F]fluoro-hexa-PEG-IPQA in different NSCLC cell lines. Similar studies were preformed after treatment with Iressa.

[18F]fluoro-hexa-PEG-IPQA was first assessed *in vitro* for its accumulation and washout kinetics in human NSCLC cells (PC14, H441, H3255, H1975) with different EGFR signaling profiles (Fig. 1). The highest cell-to-medium ratios of the four cell lines were observed at approximately 20 minutes when a steady state of post-treated radiotracer exposure was reached.
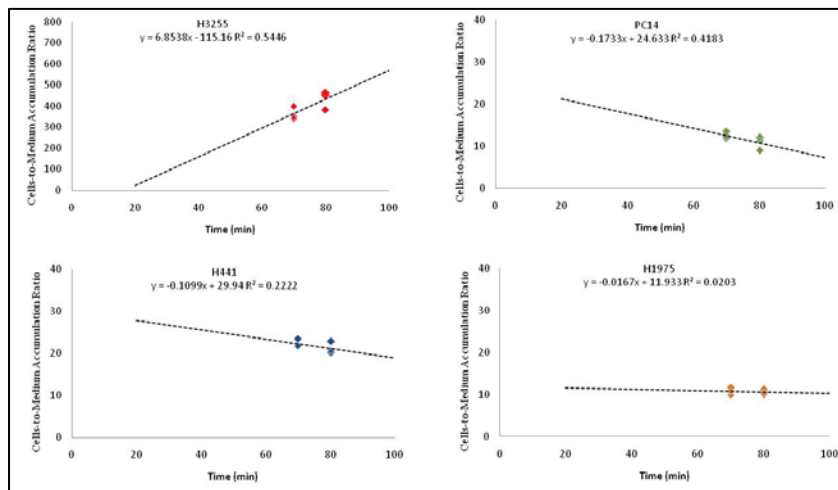
Figure 2. Washout phases of [18F]fluoro-hexa-PEG-IPQA in different NSCLC cell lines.

The amount of accumulation of [18F]fluoro-hexa-PEG-IPQA is indicative of the levels of EGFR expression and activity in corresponding cell lines. As predicted for the chosen cell lines, H3255 had a highest uptake (10 folds) among all cell lines (580 ± 109 cell/medium ratios) tested. Among the 4 cell lines, H3255 was the only one with increased levels of retained [18F]fluoro-hexa-PEG-IPQA after washout phases and increased incubation time of the tracer (Fig. 2). The H3255 washout phase can be described as a very rapid initial loss (50%) of the tracer, followed by a plateau with no further washout. Results indicated that

binding of tracer to H3255 cells is continual and strong. This washout characteristic was not, however, observed in other 3 cell lines. Instead, they had shown rapid initial losses of [^{18}F]fluoro-hexa-PEG-IPQA, followed by slow decreases with increased incubation time of the tracer. The regression lines of washout profiles of these 3 cell lines were relatively flat (with negative slopes), indicating that significant uptake of [^{18}F]-fluoro-hexa-PEG-IPQA took place at the initial incubation stage with limited capacity.

In PC14 and H1975, the profiles of accumulation and washout of [^{18}F]fluoro-hexa-PEG-IPQA were similar (PC14 11.0 ± 0.9; H1975 9.1 ± 0.4) and the retention of [^{18}F]fluoro-hexa-PEG-IPQA after washout were under 10 cell/medium ratio. In the EGFR^{WT}, H441 which has similar EGFR expression as that of H3255, the cell-to-medium ratio was more than 10 times lower than H3255. The residual level of [^{18}F]-fluoro-hexa-PEG-IPQA didn't increase over time after washout.

Aim 3   Using selected ^{124}I or ^{18}F-labeled IPQA derivative, to conduct pre-clinical studies in animals with orthotopic models of lung cancer xenografts with different levels of EGFR expression/activity, and to assess the value of PET imaging as the inclusion criterion for therapy by EGFR inhibitors, as well as for monitoring the efficacy of treatment with EGFR-targeted drugs.

In vivo [^{18}F]fluoro-hexa-PEG-IPQA PET imaging of the H3255 subcutaneous tumor xenograft demonstrated superior binding of the tracer (Figs. 3 and 5). MicroPET images in mice provided the heterogeneous accumulation of [^{18}F]fluoro-hexa-PEG-IPQA in H3255 s.c. tumor xenografts. Hot spots and uptake layers could be identified in the central and peripheral regions of the tumor (Fig. 3, left middle panel, axial image at 60 min post-administration). The accumulation of [^{18}F]fluoro-hexa-PEG-IPQA displayed a one-phase exponential association kinetics in the first 10-15 minutes. The accumulation reached equilibrium at ~ 20 minutes (2.24 ± 0.11 %ID/g) after administration of radiotracer. Thereafter, the accumulation slowly increased till the last imaging time point (55-65 min). This seemed to indicate that the binding between [^{18}F]fluoro-hexa-PEG-IPQA and EGFR^{L858R} was on going during the entire imaging period. The optimal tumor-to-muscle concentration ratio was 2.07 ± 0.15 and tumor-to-blood ratio was 1.10 ± 0.21. We recorded a measurable difference between these results and the [^{18}F]fluoro-hexa-PEG-IPQA PET imaging of H441 tumor xenograft. Although H441 has the same magnitude of EGFR expression, it has lower EGFR activity as compared with H3255. H441 reached equilibrium in the first 3-6 minutes post injection at a level of 70 – 75% accumulation of that in H3255, and maintained a similar slow uptake over the subsequent period.   PC14 and H1975, the negative controls in this study, showed much lower uptake ratio which is consistent with the results observed in cellular studies. In summary, the accumulation of H3255 was 1.4, 6.3 and 7.6 folds more than that of H441, PC14 and H1975 ($p < 0.001$; paired student t-test), respectively.

After treatment with Iressa, H3255, the most sensitive cell line, was significantly inhibited. The uptake ratio decreased from 2.27 before treatment to 0.65% ID/g (at 15 min post-administration) after treatment. Compared to H441 control group (1.89 %ID/g), there was only 15% uptake ratio left in H441-Iressa group (0.49 %ID/g). No significant difference was observed in the PC14 and H1975 before and after Iressa treatment.

The rate of [^{18}F]fluoro-hexa-PEG-IPQA accumulation by tumor xenografts in mice, *ki*, can be obtained from Patlak plot shown in Figure 4. The *ki* values were determined between 5-20

minutes (enzymatic phase) after radiotracer administration and they corresponded to the EGFR expression and activity.

Quantitative autoradiography (QAR)

QAR distribution was validated by whole-body quantitative autoradiography (Fig. 3, transverse section); high resolution QAR images demonstrated an impressive difference in the accumulation among the four s.c. tumor xenograft models (Fig. 3, left middle panel). H3255 (3.01± 0.84) had the highest tracer accumulation and it was followed by H441 (2.53 ± 0.15), H1975 (1.97 ± 0.80) and PC14 (1.59 ± 0.58). High levels of radioactivity were also observed in brown fat, skin, liver, bone marrow, but considered relatively lower in heart, skeletal muscle and spinal cord. In contrast, the Iressa-treated group presented approximately 4 times lower uptake in H3255 (from 3.01 to 0.78 %ID/g) and approximately 3 times lower in H441 (from 2.53 to 0.92 %ID/g). Similar accumulation was observed in PC14 and H1975 before and after treatment with Iressa (Fig. 3, lower middle panel).
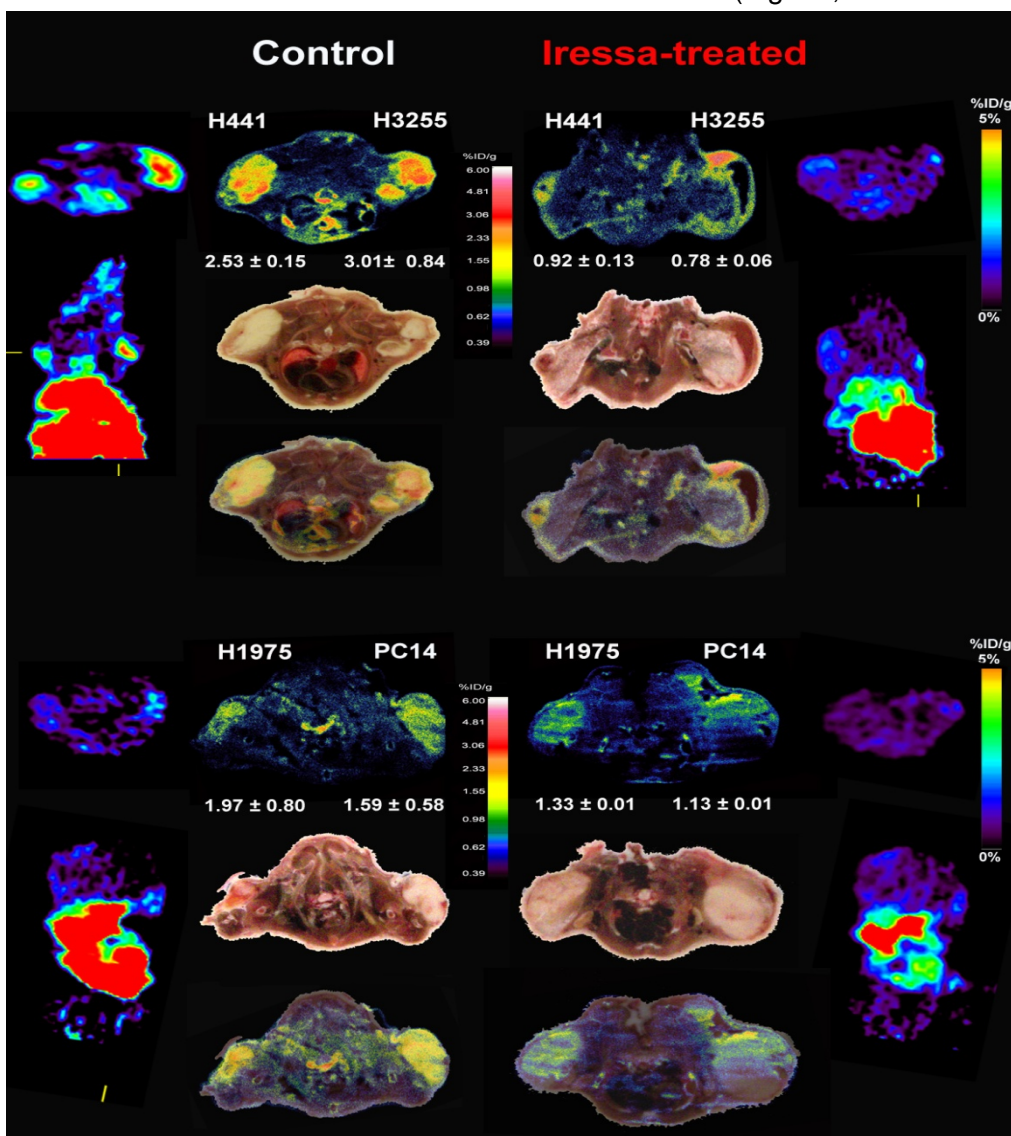
Figure 3: Representative PET and QAR images of [^{18}F]fluoro-hexa-PEG-IPQA in mice bearing different NSCLC cell lines.
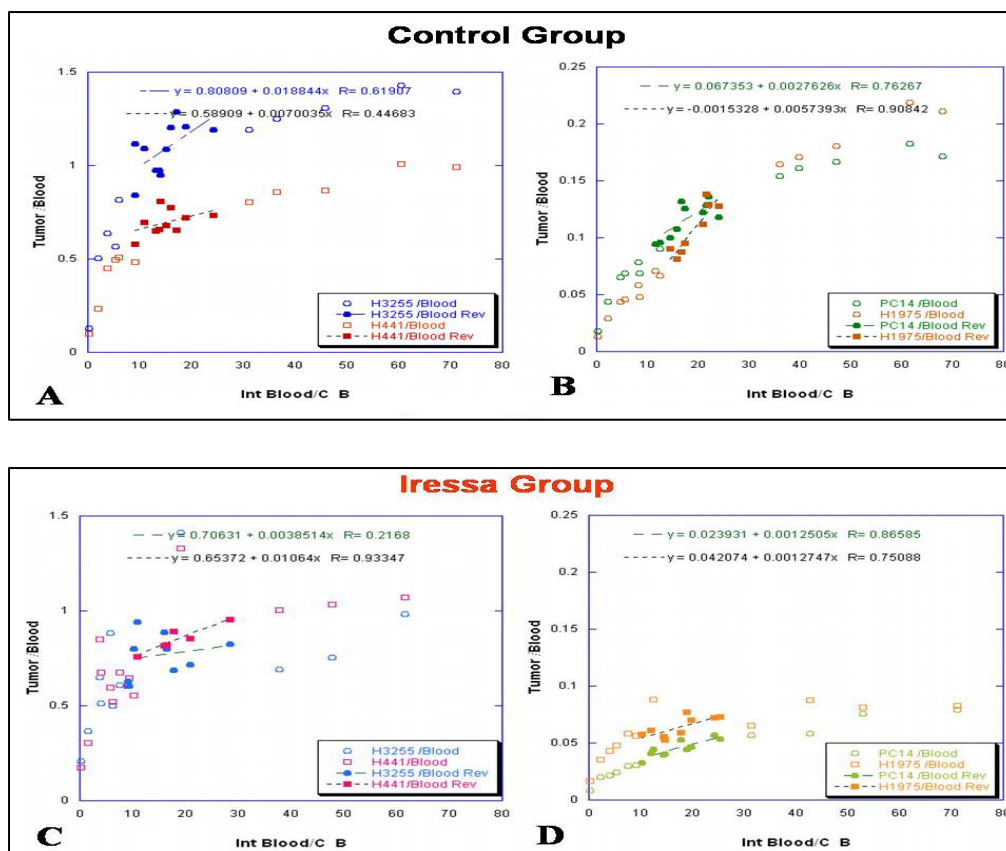
Figure 4. Patlak plots of [^{18}F]-PEG6-IPQA in mice bearing different NSCLC cell lines. The accumulation rate, *ki,* was calculated based on the input function obtained from blood.
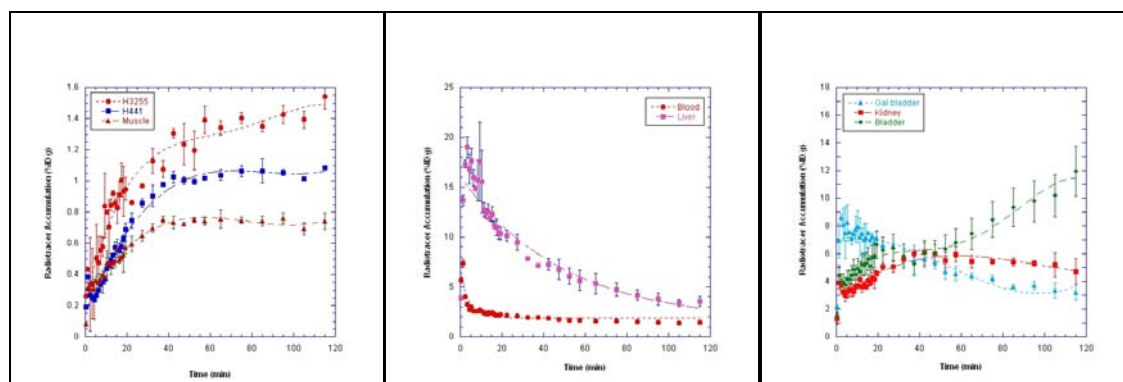
Figure 5. The dynamics of accumulation and clearance of [^{18}F]fluoro-hexa-PEG-IPQA derived radioactivity (%ID/g) in tumors, individual organs, and tissues.

After 2 hours administration of [^{18}F]fluoro-hexa-PEG-IPQA, radioactivity was well distributed into organs (Table 1). The highest uptake was observed in small intestine (8.12 ± 0.13 %ID/g) and it was followed by kidneys (4.58 ± 0.82 %ID/g), liver (3.30 ± 0.28 %ID/g), and the lungs (3.25 ± 0.29 %ID/g). The distribution of tracer in different tumors also corresponded to the level and magnitude of EGFR expression and activity (H3255 2.55 ± 0.58, H441 2.20 ± 0.40, PC14 1.86 ± 0.39, H1975 1.86 ± 0.24 %ID/g). In the blocking study, an excess of Iressa was administered 1 hour before injection of radiotracer. We observed higher radioactivity in the majority of examined organs (Fig. 5).

	%ID/g (Average ± SD)	
Organ	Control	Iressa
Blood	1.99 ± 0.07	2.25 ± 0.07
Liver	3.30 ± 0.28	3.56 ± 0.07
Kidney	4.58 ± 0.82	6.23 ± 1.98
Small intestine	8.12 ± 0.13	5.11 ± 2.59
Large intestine	2.03 ± 0.03	2.01 ± 0.58
Spleen	1.88 ± 0.15	2.00 ± 0.30
Pancreas	1.27 ± 0.09	1.67 ± 0.24
Lung	3.25 ± 0.29	3.52 ± 1.84
Heart	1.60 ± 0.01	1.77 ± 0.24
Stomach	1.92 ± 0.15	1.78 ± 0.12
Brain	1.44 ± 0.01	1.29 ± 0.27
Bone	1.45 ± 0.29	1.14 ± 0.33
Muscle	1.29 ± 0.01	1.42 ± 0.20
Skin	1.48 ± 0.01	1.79 ± 0.34
H3255	2.55 ± 0.58	2.34 ± 0.36
H441	2.20 ± 0.40	2.62 ± 0.48
PC14	1.86 ± 0.39	2.42 ± 0.42
H1975	1.86 ± 0.24	1.36 ± 0.16

Table 1. Radioactivity levels (%ID/g) in different tissues at the end of PET imaging.

Study of pharmacokinetics, biodistribution, radiation dosimetry, and metabolites of [^{18}F]fluoro-hexa-PEG-IPQA in nonhuman primates

One of the most important pre-clinical studies for a novel PET imaging tracer in the development process is to evaluate the tracer in nonhuman primates. During this study, the pharmacokinetics, biodistribution, excretion pathway, metabolites, and radiation dosimetry of the tracer can be assessed. Based on these results, the dosimetry for the first cohort in human phase I can be calculated to improve the overall safety of the study. We have completed this study in six rhesus macaques. Results of the study constitute an important part in the investigational new drug (IND) application to the Food and Drug Administration (FDA) for their approval of our phase I study.

Six healthy rhesus macaques were injected intravenously with [^{18}F]fluoro-hexa-PEG-IPQA (5mCi/animal). Dynamic imaging was performed on a PET/CT scanner for the first 30 minutes covering the thoracic-abdominal area, and it was followed by whole-body static imaging at 30, 60, 90, 120, and 180 minutes. The biodistribution and radiation dosimetry estimates were obtained from blood sampling and volume of interest analysis (VOI) data measured on PET/CT images.

Based on data from the first six rhesus macaques available to-date, [^{18}F]fluoro-hexa-PEG-IPQA exhibited a rapid redistribution after i.v. injection and a relatively fast blood clearance with half-

times of 1.4 minutes (mono-exponential fitting) via both hepatobiliary and renal pathways. Data indicated that [^{18}F]fluoro-hexa-PEG-IPQA degraded to radioactive metabolite with a $T_{1/2}$ ~ 4min post administration (Fig. 6). Inferior vena cava, heart, lung, liver, kidney, gall bladder, small intestine, upper large intestine, and urinary bladder were visually identified as organs with moderate to high tracer uptakes (Fig. 7). The critical organ was the gallbladder (0.470 mSv/MBq); other organs with higher radiation dose were the kidney (0.0999 mSv/MBq), small intestine (0.0694 mSv/MBq), upper large intestine wall (0.0495 mSv/MBq), and liver (0.0425 mSv/MBq). Lung tissue exhibited low uptake of 18F-PEG6-IPQA.

Figure 6: Plasma clearance curve for [^{18}F]fluoro-hexa-PEG-IPQA
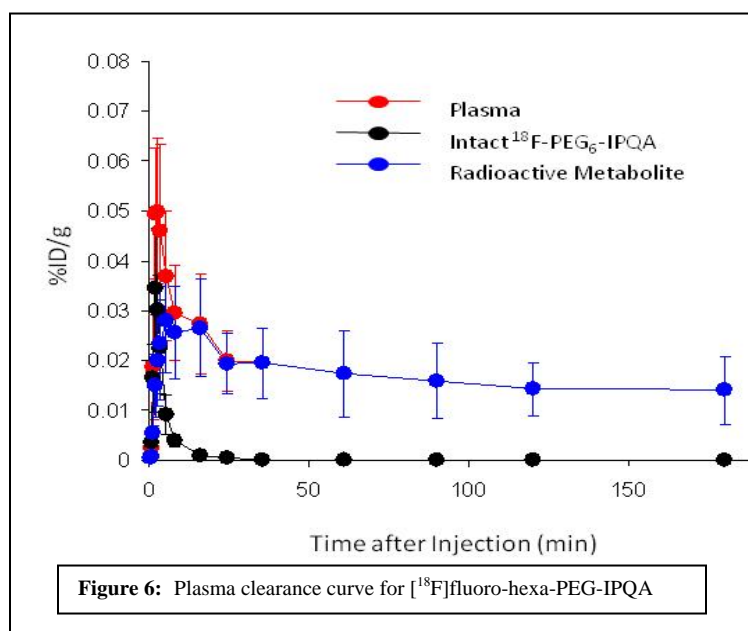
The residence time of [^{18}F]fluoro-hexa-PEG-IPQA for each source organ was calculated from whole-body PET images. The persistent radioactivity accumulation in the gall bladder, liver, small intestine, and kidneys resulted in the highest residence organ time. There was no observable evidence of acute cardiac toxicity based on EKG, and no acute or delayed systemic toxicity based on blood hematological and chemical analyses was measured. The dose for the first cohort of humans in the phase I trial will be based on the dosimetry calculation from this non-human primate study. The radiation exposure to critical organs in humans will be administered at doses lower than the regulated limits.

Figure 7: Time-activity distribution of [18F]fluoro-hexa-PEG-IPQA in a non-human primate.
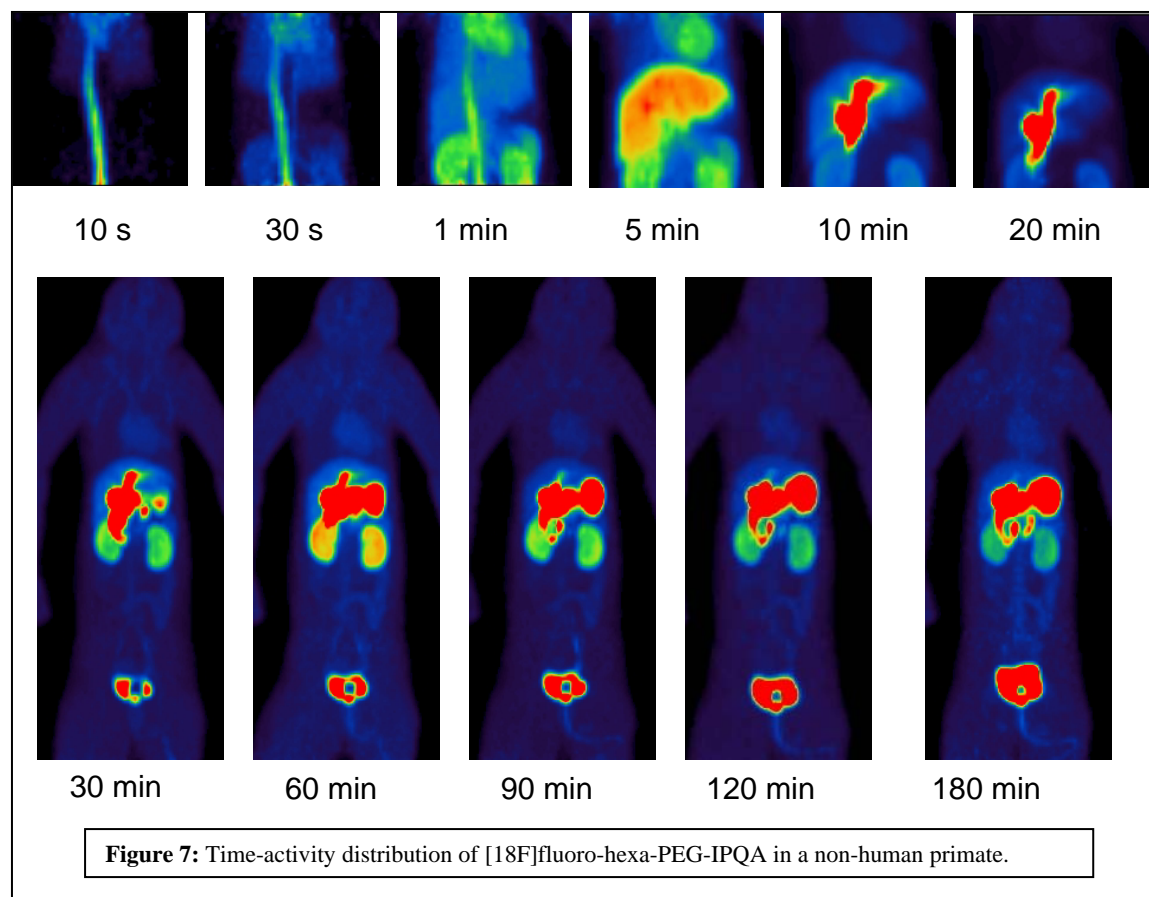
Material manufacturing

We have initiated manufacturing the non-radio labeled (cold) fluoro-hexa-PEG-IPAQ and the precursor with Advanced Biomedical Compounds (ABX). The synthesis schemes of the cold compound were developed by our chemistry team (Fig. 8), and materials will be delivered to us in late March 2009 for use. The cold fluoro-hexa-PEG-IPQA (compound 1 from schemes 1&2) will be used in the IND-directed toxicology study at Charles River Laboratory (CRL). The precursor (compound 9 from scheme 3) will be used to manufacture ^{18}F-fluoro hexa PEG-IPQA clinical dose for phase I study.

Synthesis of fluoro-hexa-PEG-IPQA

Figure 8: Synthesis schemes for cold fluoro-hexa-PEG-IPQA (1) and precursor (9).
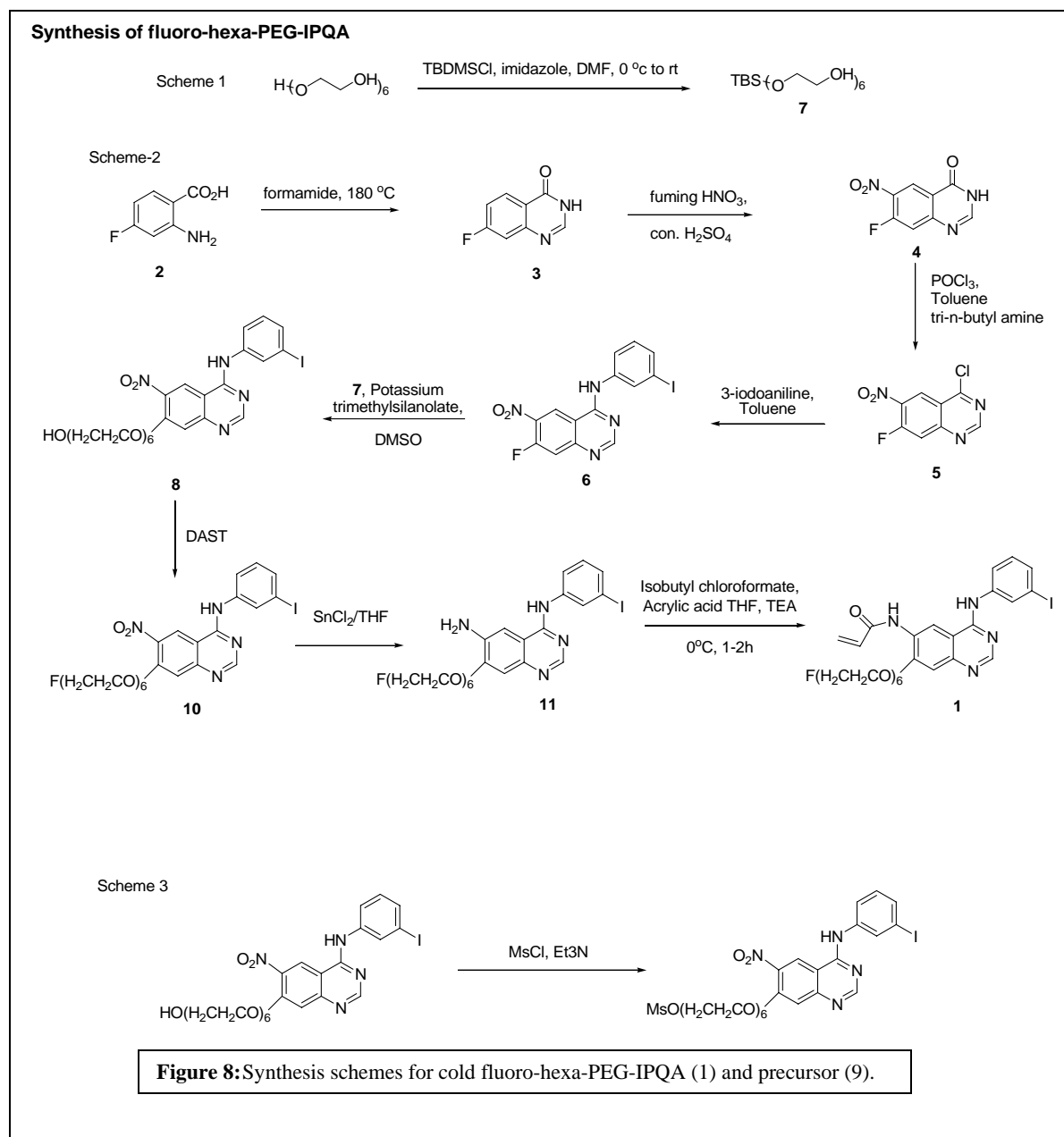
IND-directed Toxicology Study

We have finalized with CRL the toxicology protocol (Table 2) for the proposed rodent study. We incorporated the FDA's input resulting from a most current pre-IND conference we had with the FDA reviewers. To prepare the toxicology study for initiation as soon as the material is available from ABX, we have sent CRL our analytical method to begin study preparations based on the properties of our compound. Results from this study constitute part of the pharmacology and toxicology section of the IND in preparation.

Title:	A single-dose IV study of [^{18}F]flouro-hexa-PEG-IPQA in rats with a 14-day recovery period			
Study site:	Charles River facility, preclinical services Arkansas			
Compliance:	GLP			
Species/Strain:	Sprague-Dawley rats			
Dose Formulation Preparation:	Standard dose formulation prepared once. Standard sample collection for concentration verification once			
Dose Formulation Analysis:	Analysis on 1 occasion using validated HPLC methodology			
Dosing regimen:	Single dose on Study Day 1.			
Route of Administration:	Intravenous (bolus) dose administration			
Test system:	Group	Dose	Number of animals	
			Male	Female
	1	Control	10 M + 5 R	10 M + 5 R
	2	100 times	10 M + 5 R	10 M + 5 R
	M= main study animals sacrificed on Study Day 2. R= Recovery animals sacrificed on Study Day 15.			
Spares:	10 animals			
Total population:	70 animals			
Age:	Approximately 5 – 7 weeks at receipt			
Source:	Charles River			
Pretreatment period:	Approximately 10 days.			
Mortality observations:	Mortality/viability observations will be conducted twice daily on all animals.			
Detailed observations:	Daily on all animals.			
Body weight:	Daily on all animals			
Special Assessments:	General examination by veterinarian of all animals for study selection.			
Clinical Pathology parameters:	Coagulation, hematology, and clinical chemistry taken from all animals near termination.			
Toxicokinetics sample collection:	No bioanalytical samples obtained.			
Terminal procedures:	Full gross necropsy with organ weights and tissue collection on all main and recovery animals.			
Histopathology:	Standard histopathology on 65 tissue sections (including injection site) on 60 main and recovery animals.			
Audited draft report:	Audited draft report provided in approximately 12 weeks from the time of in-life completion.			

Table 2. IND-directed toxicology study protocol

cGMP manufacturing
We have continued improvements on lab-scale radiosynthesis (Fig. 9) so that it is readily scaled up and adopted by the cGMP manufacturing. We are working on an automated cGMP manufacturing process using GE Tracerlab with product specific hardware modifications. This automated process will be fully validated to meet cGMP requirements, and all QC methods for product release will also be validated. Results from this work constitute the chemistry, manufacturing, and control (CMC) section of the IND in preparation.

Figure 9 Radio labeling precursor to form [18F] fluoro-hexa-PEG-IPQA.
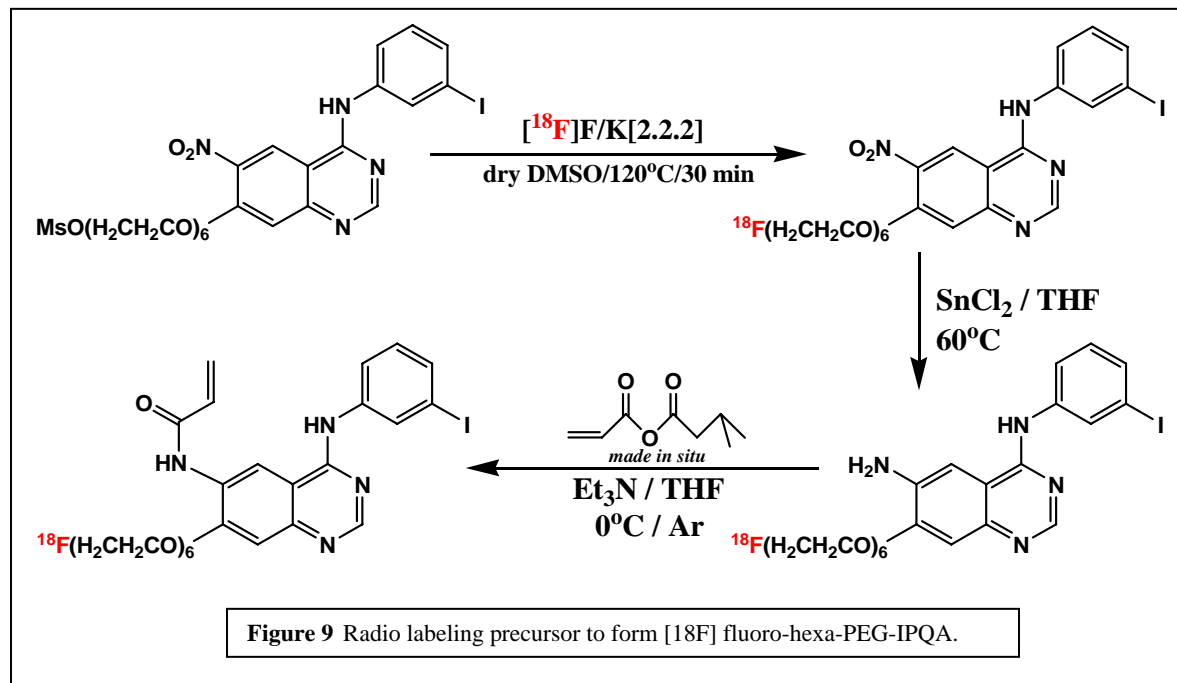
The development of a clinical trial protocol is underway, which will be led by Dr. David Stewart , M.D.(Deputy Chair, Thoracic/Head and Neck Medical Oncology). Our research team held a preliminary meeting with oncologists to discuss patient recruitment and study objectives. The primary and secondary objectives of the study are as follows:

Primary:

- To determine the optimum dosimetry of [^{18}F]fluoro-hexa-PEG-IPQA injection based on critical organ safety and detection sensitivity.
- To obtain data on [^{18}F]fluoro-hexa-PEG-IPQA distribution, pharmacokinetics, radiation dosimetry, and metabolites.
- To assess the safety of a single intravenous administration of [^{18}F]fluoro-hexa-PEG-IPQA in subjects with lung carcinoma.

Secondary:

- To obtain preliminary data on the feasibility of detection of both primary and metastatic tumor lesions in lung carcinoma using [^{18}F]fluoro-hexa-PEG-IPQA as compared to standard of care modalities.
- To correlate the magnitude of tumor [^{18}F]fluoro-hexa-PEG-IPQA uptake and retention with EGFR expression and/or treatment response.

Additional meetings will be held to discuss and refine inclusion and exclusion criteria, imaging procedures, safety monitoring, etc, to fully complete the protocol.   We anticipate activation of the protocol in late summer or early fall of 2009; thus, a request for a no-cost extension to continue to support this work has been submitted.

Key Research Accomplishments

- Developed the fifth-generation of more water-soluble polyethylene glycol (PEG)-ylated 3-iodo-4-(phenylamino)quinazoline-6-acrylamide (IPQA) derivatives labeled with ^{18}F to simplify the translation of EGFR kinase imaging agents in the clinic in comparison with ^{124}I-JGAP5.
- Discovered [^{18}F]fluoro-hexa-PEG-IPQA has less hepato-biliary clearance and a longer plasma circulation half-time.
- Completed the evaluation of [^{18}F]fluoro-hexa-PEG-IPQA as a novel PET imaging tracer in six rhesus macaques.
- Initiated manufacturing the non-radio labeled (cold) fluoro-hexa-PEG-IPAQ and the precursor with Advanced Biomedical Compounds (ABX). The precursor (compound 9 from scheme 3) will be used to manufacture ^{18}F-fluoro hexa PEG-IPQA clinical dose for phase I study.
- Finalized the toxicology protocol for the proposed rodent study with Charles River Labs.
- Improved lab-scale radiosynthesis to meet cGMP manufacturing guidelines.
- Held a preliminary meeting with oncologists to discuss patient recruitment and study objectives for a future clinical trial.
- Presented study results at the 2008 World Molecular Imaging Congress.

Conclusions

The development of [^{18}F]fluoro-hexa-PEG-IPQA into a clinical trial has been actively pursued with clearly defined milestones and timelines. Studies will focus on determining the optimum dosimetry of [^{18}F]fluoro-hexa-PEG-IPQA injection based on critical organ safety and detection sensitivity. Data will be obtained on agent distribution, pharmacokientics, radiation dosimetry, and metabolites to build upon our current knowledge base and to shape future studies. We have initiated all fronts of the IND development work to expedite the translational process.

Project 3: Targeted Peptide-based Systemic Delivery of Therapeutic and Imaging Agents to Lung Cancer

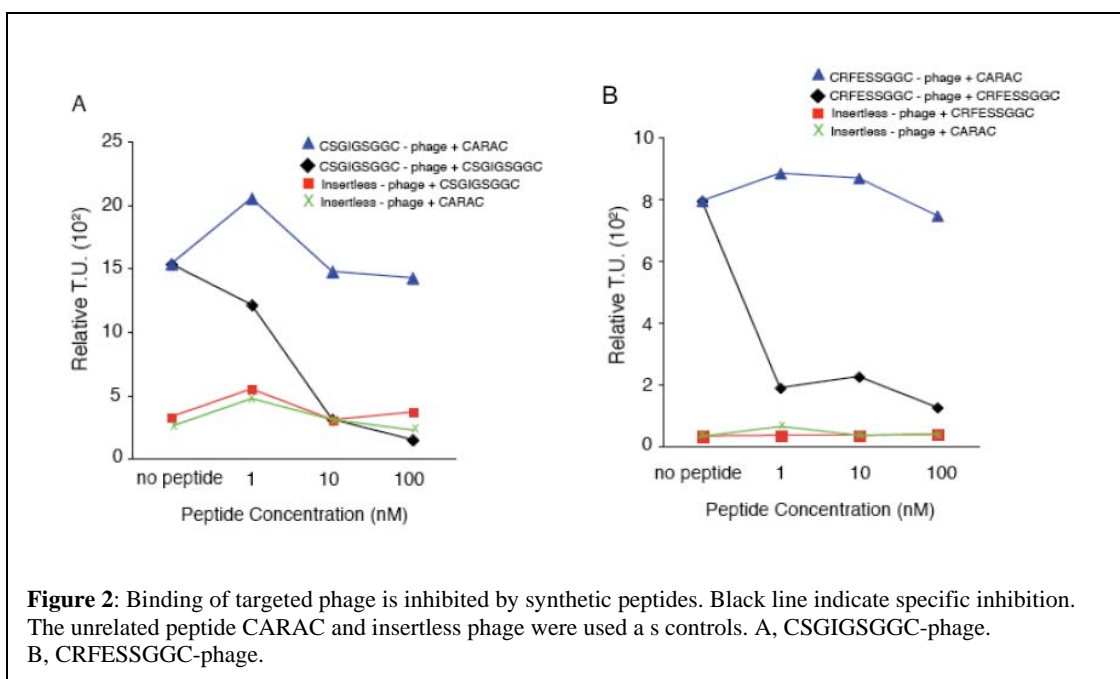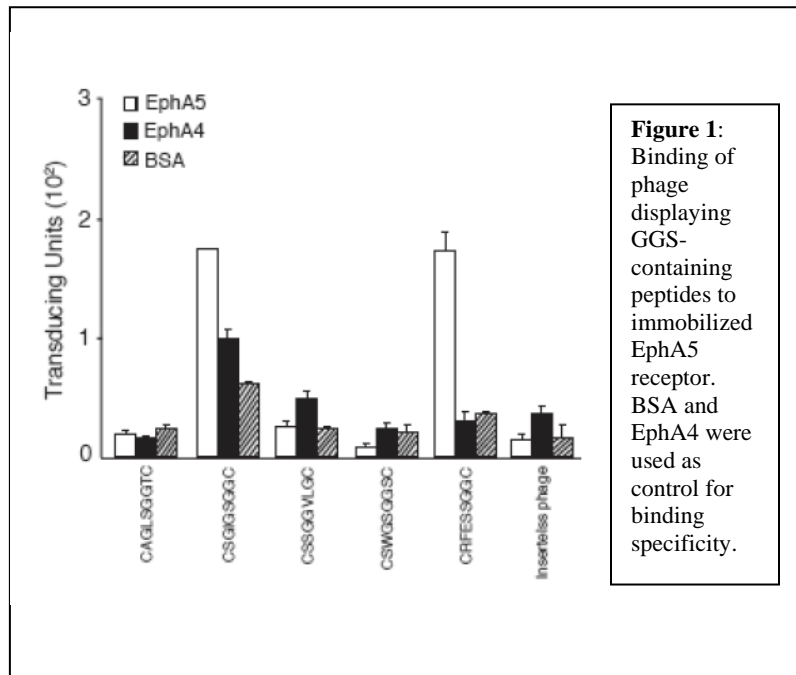(PI and co-PI: Renata Pasqualini, Ph.D., Wadih Arap, M.D., Ph.D.)

The studies outlined in this proposal focus on the use of peptide sequences with selective lung tumor-targeting properties. We will seek to validate these probes as delivery vehicles in drug and gene-targeting approaches. This approach directly selects *in vivo* for circulating probes capable of preferential homing into tumors. The strategy will be to combine homing peptides in the context of phage as gene therapy vectors. Given that many of our peptides also target angiogenic vasculature in addition to tumor cells, these studies are likely to enhance the effectiveness of therapeutic apoptosis induction and imaging technology.

Aim 1   To select peptides targeting primary and metastatic tumors in lung cancer patients.
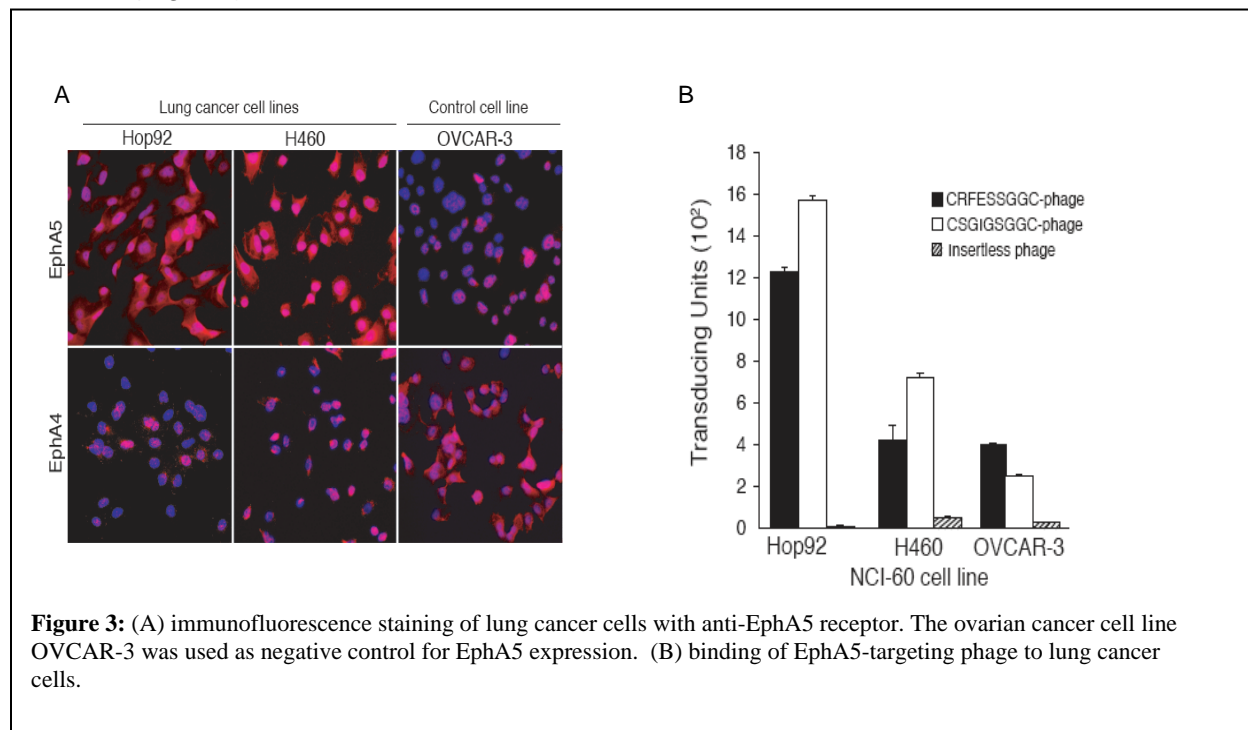
Summary of Research Findings

Phage display screening on human cancer cells from the NCI-60 panel of cell lines suggested that the tripeptide motif GGS specifically targets human lung cancer cells.

Standard BLAST homology search and detailed protein sequence alignment of peptides displaying the motif GGS indicated members of the ephrin family of proteins as the proteins potentially mimicked by GGS-containing peptides. To validate this hypothesis, we tested a series of phage displaying distinct peptides containing the GGS domain for its ability to bind to EphA5 receptor. EphA4 and BSA were used as controls (Fig.1). Phage displaying the peptide sequences CSGIG<u>SGG</u>C and CRFES<u>SGG</u>C showed specific binding to the candidate receptor and were selected for further characterization. Competition assays with synthetic peptide confirmed binding specificity (Fig. 2).

Figure 1: Binding of phage displaying GGS-containing peptides to immobilized EphA5 receptor. BSA and EphA4 were used as control for binding specificity.

Figure 2: Binding of targeted phage is inhibited by synthetic peptides. Black line indicate specific inhibition. The unrelated peptide CARAC and insertless phage were used a s controls. A, CSGIGSGGC-phage. B, CRFESSGGC-phage.

24

We also tested binding of the selected phage to the endogenous receptor expressed on the surface of lung cancer cells. Receptor expression was first confirmed by immunofluorescence of two lung cancer cell lines: H460 and Hop92. The ovarian cancer cell line OVCAR-3 and EphA4 were used as negative controls. As shown in Figure 3A, lung cancer cell lines express high levels of EphA5 on their surface. Moreover, phage binding was specific to EphA5-expressing cell lines (Fig. 3B).


Figure 3: (A) immunofluorescence staining of lung cancer cells with anti-EphA5 receptor. The ovarian cancer cell line OVCAR-3 was used as negative control for EphA5 expression. (B) binding of EphA5-targeting phage to lung cancer cells.

In vitro functional properties of EphA5-targeting peptides

We established in vitro assays to study the biological effects of EphA5 targeting peptides on human lung cancer cells. Receptor phosphorylation was induced with the mimicked ligand in presence or absence of the competing peptide. We observed inhibition of EphA5 phosphorylation in the presence of both CRFESSGGC and CSGIGSGGC synthetic peptides (Fig. 4).
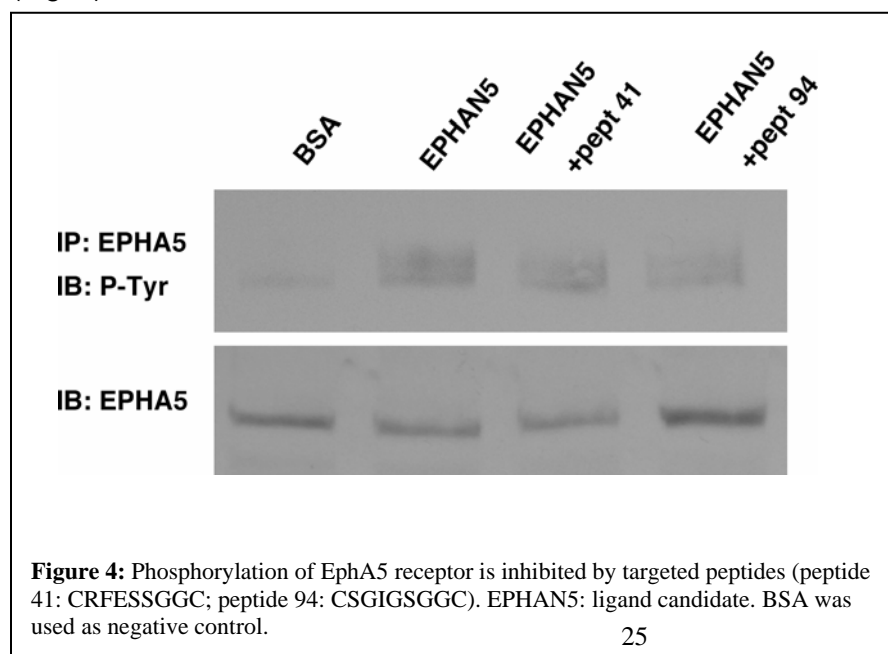
Targeted peptides were able to inhibit phosphorylation of ERK1/2 (p44/p42) (Fig. 5), indicating suppression of the MAP kinase pathway and the involvement of EphA5 in the maintenance of lung cancer cells proliferation and survival. The same effect was observed in the phosphorylation of JNK, supporting the role

Figure 4: Phosphorylation of EphA5 receptor is inhibited by targeted peptides (peptide 41: CRFESSGGC; peptide 94: CSGIGSGGC). EPHAN5: ligand candidate. BSA was used as negative control.

25

of EphA5 in tumor cell proliferation/survival. Consistently, we did not observe alterations in the phosphorylation of pathways involved in cell migration (phosphorylation of p38).
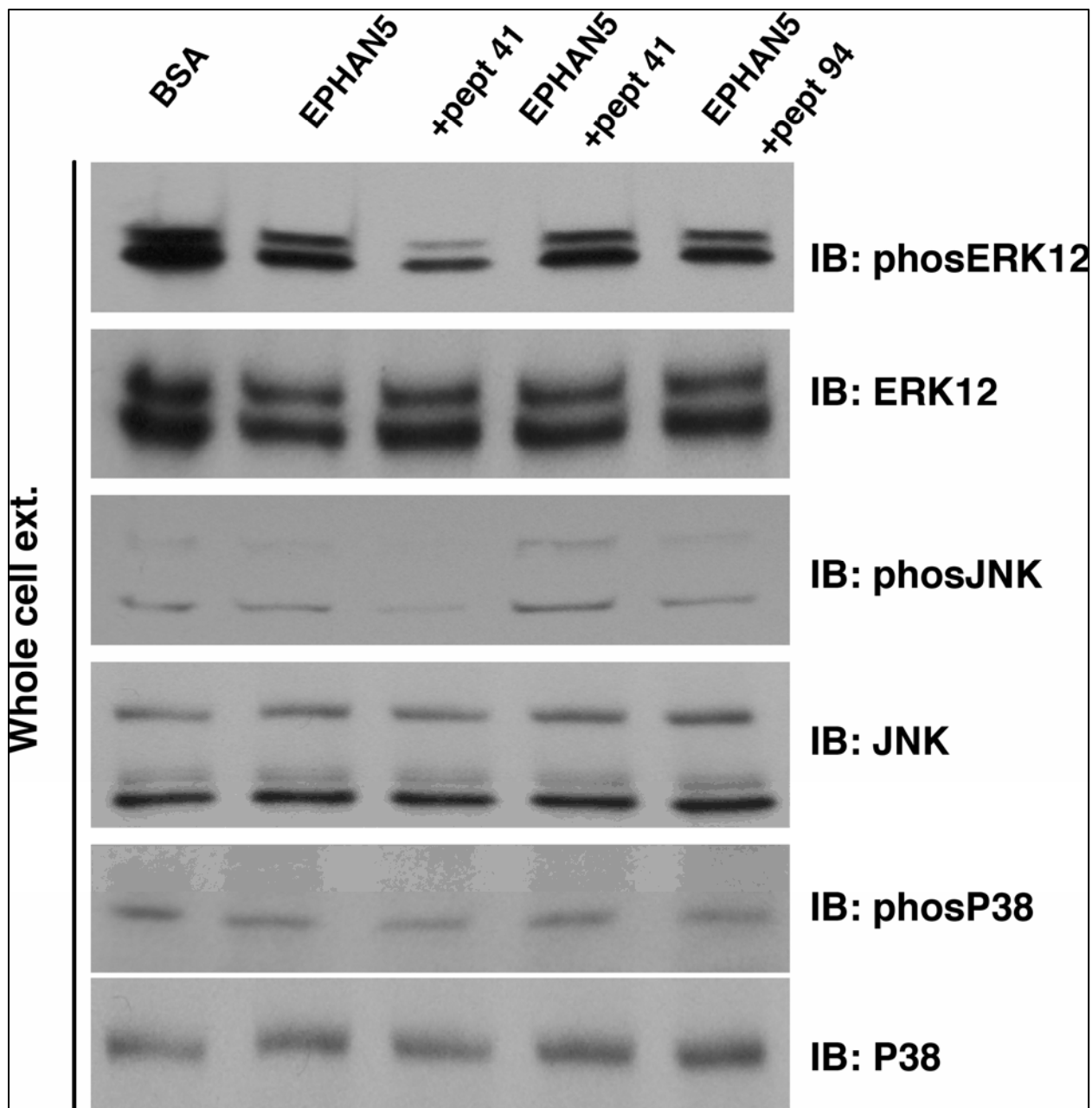
Figure 5: Activation of MAP kinase pathway was analyzed in presence or absence of targeted peptides. Arrows point to phosphorylated ERK1/2 and JNK. Inhibition of phosphorylation was observed in both cases. We did not detect alterations in the phosphorylation levels of P38.

As mentioned above, peptides selected from phage libraries have allowed the cloning of vascular receptors in non-proliferating and in angiogenic blood vessels. Although the biological basis for vascular heterogeneity is unknown, peptides selected by homing to blood vessels in mouse models have been used by several groups as carriers to guide the delivery of cytotoxic drugs, pro-apoptotic peptides, metalloprotease inhibitors, cytokines, fluorophores, and genes.

Generally, coupling of a given entity to homing peptides yields targeted compounds that are more effective and less toxic than the parental entity. Moreover, vascular receptors corresponding to the selected peptides have been identified in blood vessels of normal organs and tumors. These results show that it is possible to develop therapeutic strategies based on selective expression of vascular receptors.

Aim 2   To validate receptors for targeting human lung cancer.

Summary of Research Findings

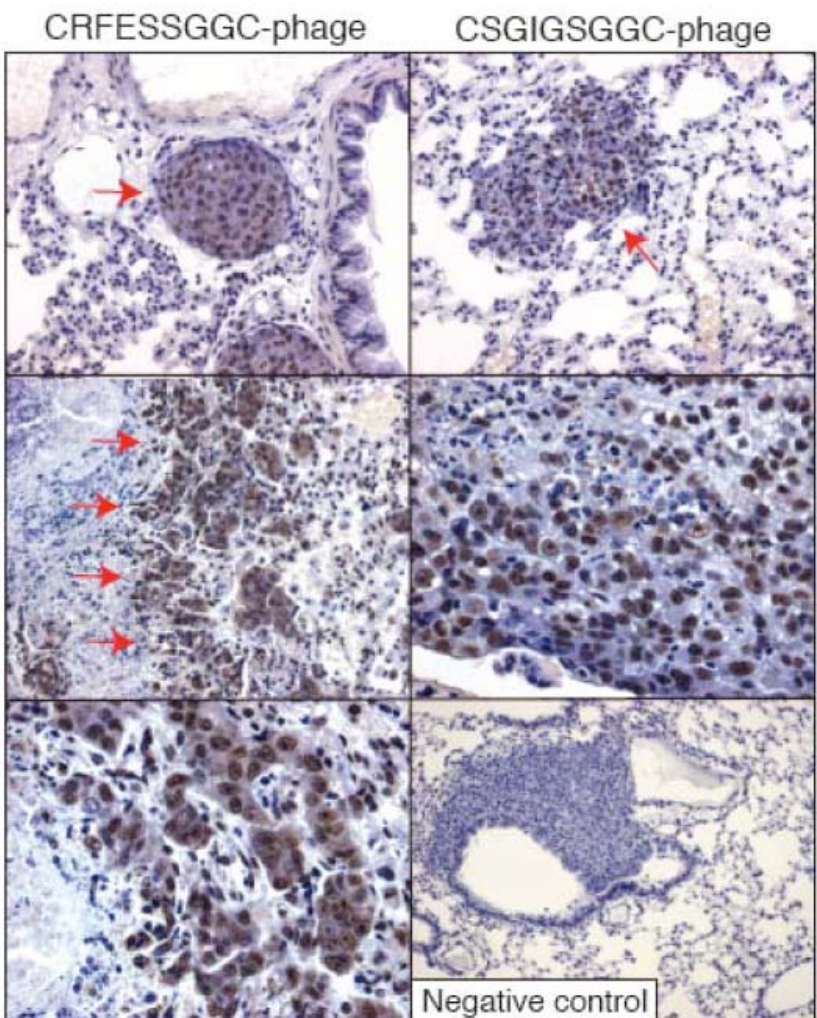Homing of targeted phage to orthotopic human lung cancer model.
We examined the expression of EphA5 in samples of human lung cancer (Fig. 6). We observed over-expression of EphA5 in non-small lung adenocarcinoma epithelium (indicated by the arrows).

Second, to evaluate the targeting properties of the selected peptides in vivo, we administered targeted phage intravenously into human lung cancer-bearing mice. Lung and control organs were harvested and examined by IHC for presence of phage particles after 1h, 6h, and 24h of systemic circulation. We observed specific homing of phage to lung cancer colonies in all
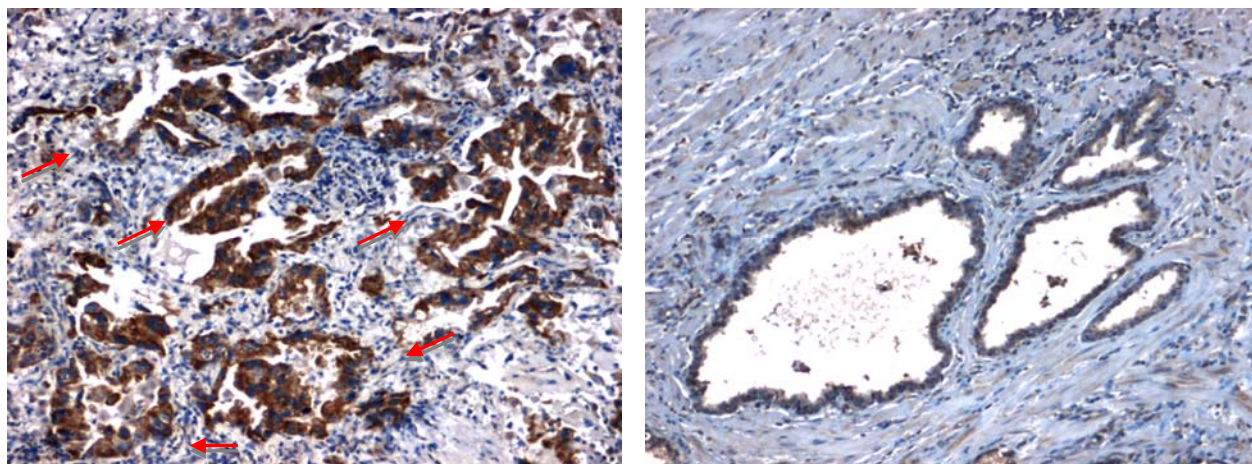
Figure 6: Human lung adenocarcinoma (pictured left) and control tissue (prostate, pictured right).

time points (Fig. 7, arrows). We did not detect phage in normal lung; uptake of phage was found to be restricted to lung cancer cells. Insertless phage was used as negative control and showed only background staining (Fig. 7).

Figure 7: Homing of targeted phage to orthotopic model of human lung cancer. Arrows point to cancer cells targeted by phage. Insertless phage was used as negative control and showed only background staining.

Treatment of orthotopic human lung cancer with BMTP-11 and BMTP-78.

Here we analyzed the effect of BMTP-11 and BMTP-78 in human lung cancer-bearing mice. Animals (15 animals/group) were treated weekly with 10mg/kg of each compound (ip) for the period of 4 weeks. Control group did not receive any type of treatment. At the end of treatment, lungs and control organs were collected for (i) tumor colony count and (ii) tissue weight. We observed significant reduction of both tissue weight and tumor growth in animals treated with BMTP-11 and BMTP-78 (Fig. 8, p<0.05). Staining of apoptotic cells demonstrated specific killing of lung cancer cells in animals treated with both BMTP-11 and BMTP-78 (Fig. 9).

Targeted anti-cancer drug development program: BMTP-11 IND and BMTP-78 pre-IND

Our first MDACC-sponsored IND, based on BMTP-11, has received a "safe to proceed" status by the FDA in January 2009. The first-in-human clinical trial has a projected activation date of March 2009. Our second cancer IND filing with the FDA will focus on BMTP78. These peptidomimetics are targeted to the IL-11R and to GRP 78. Extensive studies have been performed and clearly established the relevance of these targets in human cancer tissue samples from nearly every type of tumor evaluated (including lung cancer). These studies indicate that these targets are suitable for delivery of therapies and imaging agents. Extensive toxicology work has been completed in mice and cynomolgus monkeys. Efficacy studies in lung

cancer models have been extensively validated. We expect the upcoming clinical studies to be informative and establish a firm foundation for evolving these drugs into Phase II/III trials.

Merging tumor targeting and molecular-genetic imaging into an integrated platform is limited by a lack of strategies to enable systemic, ligand-directed delivery and imaging of specific transgenes. Many eukaryotic viruses subserve transgene delivery but require elimination of native tropism for mammalian cells; in contrast, prokaryotic viruses can be adapted to bind to mammalian receptors but are otherwise poor vehicles. We have introduced a system containing cis-elements from adeno-associated virus (AAV) and single-stranded bacteriophage. Our AAV/phage (AAVP) prototype targets ad integrin. We have shown that AAVP provides superior tumor transduction over phage and that incorporation of inverted terminal repeats is associated with an improved fate of the delivered transgene. Moreover, the temporal dynamics and spatial heterogeneity of gene expression mediated by targeted AAVP can be monitored by positron emission tomography. This new class of targeted hybrid viral particles will enable a wide range of applications in biology and medicine. Evaluation of this vector for therapeutic delivery of TNF to tumor-bearing dogs revealed positive results. A clinical trial is planned to bring this vector into the clinic.
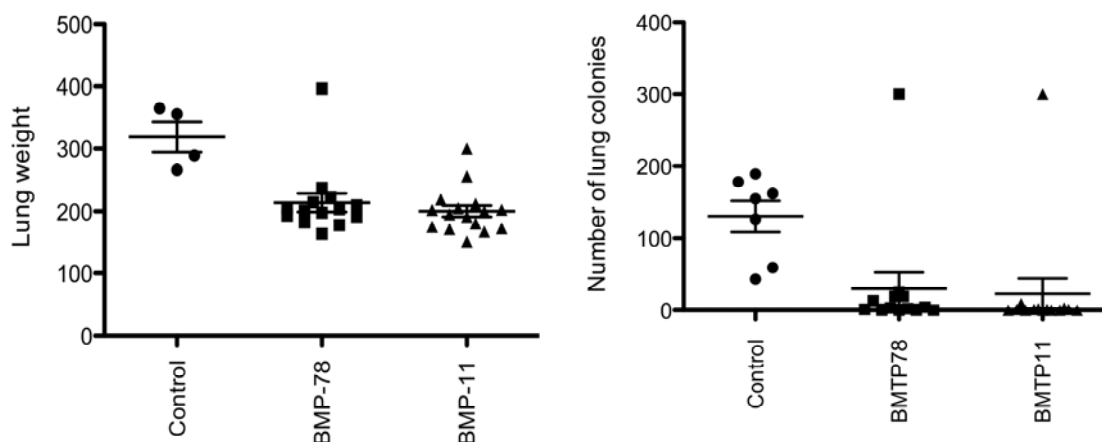
Figure 8: Treatment of tumor-bearing animals with BMTP-11 and BMTP-78. After 4 weeks of treatment, lungs of treated and untreated animals were collect and analyzed for the presence of lung cancer colonies. A significant reduction in lung weight and presence of lung cancer colonies was observed in animals treated with both compounds.
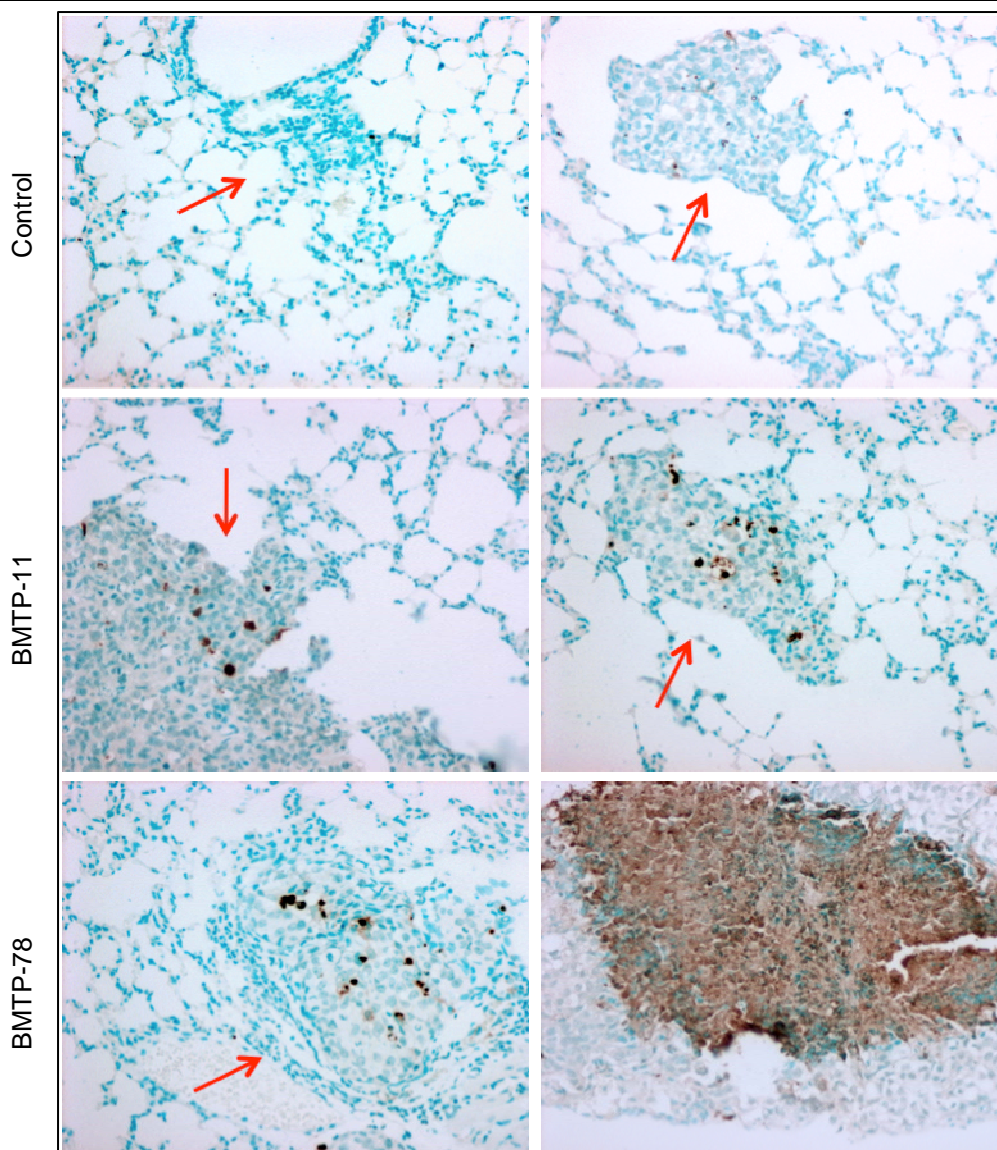
Figure 9: Lung of treated animals were analyzed for the presence of apoptotic cells after treatment with BMTP-11 and BMTP-78. Arrows point to lung cancer colonies containing apoptotic lung cancer cells (brown staining).

Phage-based direct assembly of gold nanoparticles and NIR applications

The integration of phage display-based combinatorial tissue targeting and nanotechnology has emerged from methodology we have established for the direct-assembly of gold (Au) nanoparticles onto phage. Given the challenges for reproducibly building at the nanometer scale, including the need for streamlined and "bottom-up" approaches for assembling nanoparticle architectures, the combination of phage and Au nanoparticles is an ideal system to gather the required expertise to control the fabrication and application of biological assisted nano-assemblies. This work was motivated from the premise that, in nature, the direct-assembly of molecules and particles is often directed by non-specific hydrophobic, van der Walls, and/or electrostatic interactions. We hypothesized that the assembly of phage and Au nanoparticles may also occur spontaneously through similar interactions. The outcome from testing this hypothesis was the design and validation of a method for Au-phage-based nano-assembly without genetic manipulation or complex conjugation chemistry. We have generated stable and

biologically active networks of direct-assembled Au-phage scaffolds, in which we can tune the chemical and physical properties of these biological structures. This tuning capability combined with the programmed tissue targeting property of the phage has proven most valuable, as it has allowed us to integrate multiple functions in a single nano-assembly, serving as a complementary and non-mutually exclusive tool among applications, i.e., near infrared (NIR) surface enhanced Raman scattering (SERS) detection, Au enhanced fluorescence in vitro imaging, MRI and CT scan in vivo imaging, and/or heat deposition for NIR photo-therapy. The identification of vascular markers targeted by circulating ligands continues to shed light on the complex cellular and molecular diversity of the human vasculature. In the near future, the integration of the molecular diversity of blood vessels with nanotechnology will be translated into clinical applications.

Aim 3   To design tools for molecular imaging of lung tumors.

Summary of Research Findings

In this Aim, we hypothesized that molecular addresses within lung tumors can be exploited for imaging and early detection of diseased sites; our goal was to use these biochemical differences to develop targeted imaging agents. We will develop novel tools for intravital imaging at the molecular level in collaboration with the Imaging Core. These devices will be based on labeled peptides and engineered phage particles for targeted systemic delivery of thymidine kinase. The most efficient system will be tested and validated in vivo, in animal models, and ultimately in patients. We look to continue these efforts during the next project period.

Key Research Accomplishments

- Tested peptides, selected by homing to blood vessels in mouse models, as carriers to guide the delivery of cytotoxic drugs, pro-apoptotic peptides, metalloprotease inhibitors, cytokines, fluorophores, and genes.
- Identified vascular receptors that correspond to the selected peptides found in blood vessels of normal organs and tumors.
- Received "safe to proceed" status by the FDA on our BMTP-11-based IND. Human clinical trials will be activated by March 2009.
- Filed a second IND with the FDA to focus on BMTP78.
- Generated stable and biologically active networks of direct-assembled Au-phage scaffolds, in which we can tune the chemical and physical properties of these biological structures.
- Identified vascular markers targeted by circulating ligands to further our knowledge of complex cellular and molecular diversity of the human vasculature.

Conclusions

We propose that the EphA5 receptor expressed on the surface of lung cancer cells controls cells proliferation and survival by activating the MAP kinase signaling. We showed that our EphA5-targeted peptides inhibit phosphorylation of ERK1/2 and JNK. These effects would potentially result in inhibition of lung cancer cell proliferation and induction of apoptosis. Future studies will allow us to use shRNA to inhibit the expression of EphA5 in lung cancer cells and to analyze cell proliferation and survival in vitro and in vivo. We will over-express EphA5 receptor in normal cells and analyze whether the expression of the receptor will cause cell transformation in vitro and in vivo. We will also treat lung cancer tumor-bearing mice with both systemic

injection and nasal inhalation of peptide. These will follow optimization studies for peptide stability, the use of liposome as carriers, and a dose-escalation experiment.

Project 4: Inhibition of bFGF Signaling for Lung Cancer Therapy

(PI: Reuben Lotan, Ph.D.)

The survival of lung cancer patients is poor because this cancer is diagnosed at advanced stages. Therefore, improvements in early detection through the identification of molecular markers for diagnosis and for intervention combined with targeted chemoprevention are urgently needed. While the molecular events involved in lung cancer pathogenesis are being unraveled by ongoing large scale genomics, proteomics, and metabolomics studies, it is already well recognized that proliferation-, survival- and angiogenesis- promoting signaling pathways are amplified in lung cancer. Among the angiogenesis signaling pathways, the basic fibroblast growth factor (bFGF) and its transmembrane tyrosine kinase receptors (FGFRs) are playing important roles in addition to the well-studied vascular endothelial growth factor (VEGF) and its receptors (VEGFRs). Both types of angiogenesis signaling pathways, the VEGF/VEGFR and the bFGF/FGFR, have been detected in NSCLC and associated with lung cancer development. However, most efforts in preclinical and clinical trials have been directed to the VEGF/VEGFR pathway.

We hypothesize that bFGF triggers signaling pathways that contribute to malignant progression of lung cancers by stimulating tumor cell and endothelial cell proliferation and survival and augmenting angiogenesis. Therefore, agents that intervene in this pathway may be useful for lung cancer therapy either alone or in combination with agents that target the VEGF/VEGFR signaling pathways and/or with cytotoxic agents. We will address the following specific aims in order to understand the mechanism(s) underlying the *in vitro* and *in vivo* effects of bFGF on lung cancer and endothelial cells and the ability of bFGF inhibitors to suppress the growth of NSCLC *in vitro* and *in vivo.*

Aim 1   Determine the effects of bFGF on *in vitro* growth, survival, motility, invasion and angiogenesis of NSCLC cells and endothelial cells.

Summary of Research Findings
This aim was completed and summarized in the previous reports.

Aim 2   Evaluate the relative potency of several inhibitors of bFGF binding to receptor (i.e., TMPP and analogs) in inhibiting effects of bFGF detected in Specific Aim 1 and evaluate the effects of these inhibitors in combination with paclitaxel on *in vitro* growth and survival of tumor cells.

Summary of Research Findings

Agents tested during previous reporting periods for inhibition of FGFR signaling were not available in sufficient amounts needed for use in *in vivo* experiments (as detailed in the update for specific aim 3 below), so we tested the potency of additional agents that target FGF receptor signaling. The first agent was 5-Deoxy-5-(methylthio)adenosine (MTA), a naturally occurring sulfur-containing nucleoside present in all mammalian tissues. We have chosen to test MTA because it has been shown to specifically inhibit FGF-2-induced fibroblast proliferation through

binding to the FGF receptor and inhibiting FGF-2-induced FGFR tyrosine kinase activity and autophosphorylation (Fig. 1). Another reason for our interest in this agent was the report that MTA can inhibit the accumulation of the high molecular weight species of bFGF (M. wt. of 24, 22.5, and 22 kDa) in the cell nucleus by suppressing methylation-dependent post-translational modification (Fig. 2). We found that MTA inhibited the growth of the lung tumorigenic cell line 1170-I in a dose-dependent fashion with 50% inhibition that was achieved with about 100 μM MTA (Fig. 1A). The inhibition was due to suppression of the mitogenic effects of bFGF by MTA as indicated by inhibition of the increases S phase (DNA synthesis) caused by bFGF alone compared to bFGF plus MTA (Fig. 1B).

Figure 1: Inhibition of the growth of 1170-I cells by MTA. (A) Cells were treated with the indicated doses of MTA for 72 hours and then cell numbers were assessed by the sulforhodamine B assay in triplicates. (B) Cell cycle analysis was performed after 56 hours of cell growth with no additives (control) or only bFGF, or MTA plus bFGF. The cells were then stained with propidium iodide and processed for cell cycle analysis by flow cytometry.
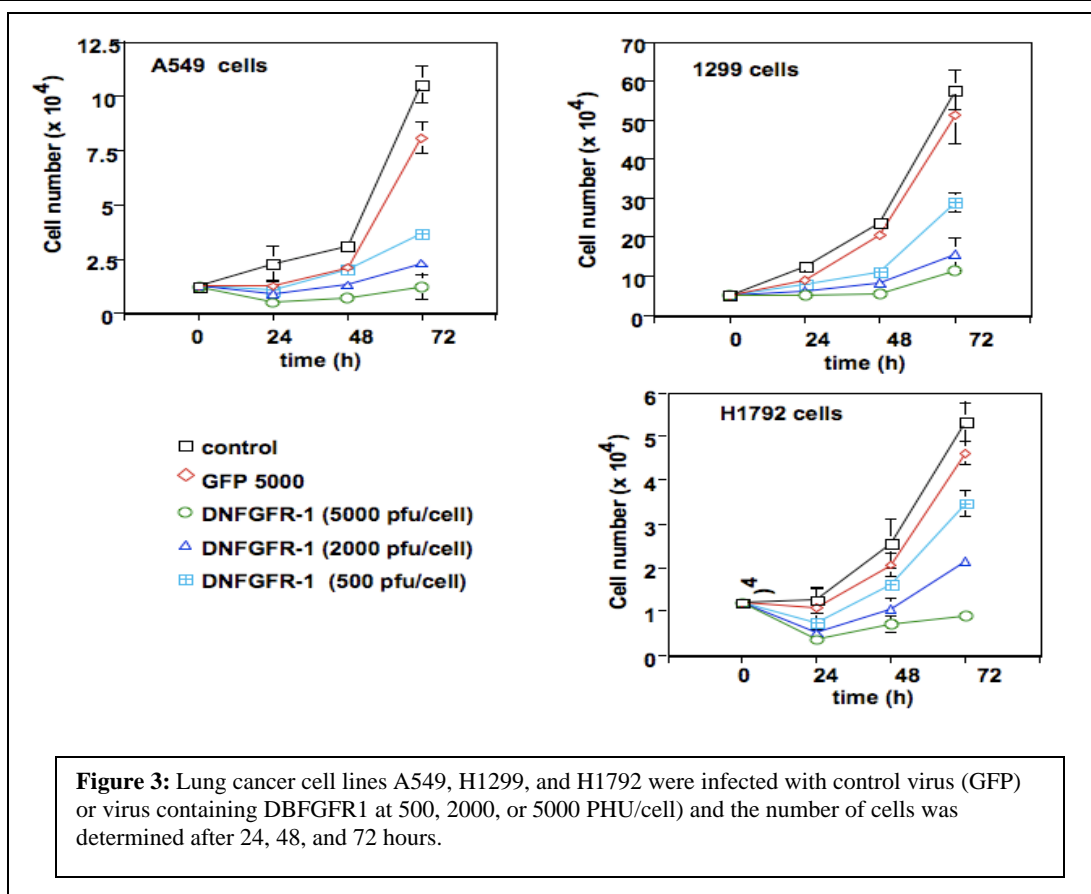
The second agent, Sanofi-Aventis compound SSR128129E, was tested at concentrations of up to 200 nM for 1 to 3 days, with and without 30 ng/ml of bFGF using the following lung tumor cell lines: 1170-I, H441, 2279, PC14PE6, 1799 and BEAS-2B. We found no inhibition of growth with any of these cell lines; we aborted the plans to use this agent. Later, we were informed that Sanofi-Aventis had canceled their own plans to develop this compound.

A third strategy was an alternative to using small molecular weight inhibitors. We previously concluded that infection of lung cancer cells with adenoviral vectors that harbor a dominant negative form of FGF Receptor (DNFGFR1) inhibited cell growth. We have expanded this approach and found that the expression of DNFGFR1 inhibited the growth of several lung cancer cell lines as a function of the amount of the virus used for infection expressed in plaque-forming units (PFU) per cell (Figs. 2 and 3). The results show that expression of DNFGFR1 inhibits the growth of all the cell lines tested and induces cell death as indicated by cell detachment (Fig. 2D), DNA fragmentation detected by the tunnel assay of apoptosis (Fig. 2E), and cleavage of PARP (Fig. 2E). Colony formation in agarose was also suppressed by 76% after treating the cells with the DNFGFR1 viral vector. The expected suppression of FGFR1 kinase activity was confirmed by immunoprecipitation/Western blotting analysis (Fig. 2D).

Figure 2. (A) 1170-I tumorigenic lung cells were infected with adenoviral vector harboring control construct- Green fluorescent protein (GFP) at 10,000 PFU/cell) or virus harboring DNFGFR1 at 1000, 5000, or 10000 PFU/cell. The cell number was determined after 24, 48 and 72 hours. (B) The appearance of the cells treated as in A under the microscope. Note the rounded floating dead cells in culture treated with DNFGFR1 virus for 72 hr. (C) The 1170-I cells were treated with 10000PFU/ml virus with GFP or DNFGFR1 and then assayed for colony formation in agarose. Colony numbers were scored after 6 days under the microscope. Average of 4 fields is presented ±SE. (D) 1170-I cells were infected with adenoviral vector containing GFP or DNFGFR1 and treated with 10 ng/ml bFGF for 30 min before cell lysis and immunoprecipitation with anti-FGFR1 antibodies. The immunoprecipitates were subjected to slab gel electrophoresis and immunoblotting with anti-phosphotyrosine antibodies. (E) Cells were analyzed by the TUNEL assay and PARP cleavage for apoptotic cell death.

Studies on the mechanism by which DNFGFR1 acts to inhibit the growth and induce apoptosis in lung tumor cells are ongoing. Preliminary results indicate that DNFGFR1 increases the cell cycle inhibitors p21 and p27 and decreases the cell cycle regulators cdc25 and Chk1.

Figure 3: Lung cancer cell lines A549, H1299, and H1792 were infected with control virus (GFP) or virus containing DBFGFR1 at 500, 2000, or 5000 PHU/cell) and the number of cells was determined after 24, 48, and 72 hours.

Aim 3   Evaluate anti-tumor activity (growth inhibition, apoptosis, suppression of angiogenesis) of the most effective inhibitor identified in Specific Aim 2 when used alone and in combination with paclitaxel in an orthotopic lung cancer model using luciferase-expressing NSCLC cells for *in vivo* bioluminescence imaging of tumor growth and response to treatment.

Summary of Research Findings

The most appropriate way to pursue our *in vivo* studies, as a prelude to potential clinical trials, is to secure a large source of the drug from our pharmaceutical counterparts. Therefore, from the beginning of this project, we tried to identify agents that target FGF receptor signaling and are under development in pharmaceutical companies. We had identified three companies and tested two of the compounds that they had agreed to provide. Initially, we examined the compound 5,10,15,20-tetrakis(methyl-4-pyridyl)-21H,23H-porphine-tetra-p-tosylate salt (TMPP), which showed inhibitory effects against lung tumor cells, as reported previously. However, the company (Prochon, Rehovot, Israel), which was the source of this agent, decided not to pursue the development of this compound. We contacted Sanofi-Aventis after learning that they had an FGFR inhibitor (SSR128129E). We found that this compound was ineffective in any of our cell lines at concentrations that were relevant for *in vivo* studies. Therefore, we stopped further experiments with this agent, and, as noted, Sanofi-Aventis has also stopped development of this agent due to toxicity.

We contacted Bristol-Mayer-Squibb, who had a dual vascular growth factor receptor (VEGFR) / Fibroblast growth factor receptor (FGFR) inhibitor in development, but we were not able to get

this material for *in vitro* testing. Therefore, we were not able to carry out in vivo experiments with these small molecules. As an alternative, we examined two potential approaches that were described above under specific aim 3, namely the FGFR inhibitor 5'-(methylthio)adenosine and the adenoviral vector expressing dominant negative FGF receptor.

Aim 4   To investigate the expression of bFGF signaling components (bFGF, FGFR-1, FGFR-2, heparan sulfate, syndecan-1, and FGFR-3) by IHC staining of tissue microarrays (TMAs), and correlate the expression of bFGF/bFGFRs between tumor and non-malignant epithelial cells with angiogenesis.

Summary of Research Findings

During the last year, we completed the analysis of the expression patterns of basic fibroblast growth factor (bFGF) and FGF receptors 1, in NSCLC tumors, and premalignant lesions including squamous metaplasia and dysplasia. The publication of these results required some additional experiments (Behrens et al, *Clinical Cancer Research* 2008); final results have demonstrated high expression of bFGF, FGFR1, and FGFR2 in most NSCLC tumors. The pattern of expression for all markers varied according to tumor histologic type and cellular localization. Cytoplasmic expression scores were significantly higher in tumors than in normal epithelia. Nuclear bFGF and FGFR1 levels were significantly higher in women than in men. Although cytoplasmic FGFR1 expression was significantly higher in smokers than in non smokers, nuclear FGFR1 and FGFR2 expression was significantly higher in non smokers. Dysplastic changes showed significantly higher expression of all markers compared with squamous metaplasia.

Key Research Accomplishments

- Suppressed the growth of lung tumor cells by repressing FGFR activation with the FGF receptor inhibitor MTA.
- Demonstrated that dominant negative FGF receptor adenoviral expression vector inhibits the growth of lung cancer cell lines by inducing apoptosis.
- Concluded that bFGF, FGFR1, and FGFR2 are highly expressed in most NSCLC tumors.

Conclusions

During the period of performance, we have shown that MTA, as an effective FGFR inhibitor, is a potent cell growth suppressor and apoptosis inducer, and should be further evaluated in preclinical setting for anti tumor effects. Our research data demonstrated that MTA inhibited the growth of the lung tumorigenic cell line 1170-I in a dose-dependent fashion with 50% inhibition that was achieved in our lab. These findings led us to study adenoviral vectors harboring dominant negative FGFR1 as potential candidates for preclinical *in vivo* studies with aerosolized viral formulation. Studies on the mechanism by which DNFGFR1 acts to inhibit the growth and induce apoptosis in lung tumor cells are ongoing. Our preliminary results indicate that DNFGFR1 increases the cell cycle inhibitors p21 and p27 and decreases the cell cycle regulators cdc25 and Chk1. We look to complete these studies during the next project period to confirm that the bFGF signaling pathway activation may be an early indicator of SCC pathogenesis and a novel target for lung cancer chemopreventive and therapeutic strategies.

Project 5: Targeting mTOR and Ras signaling pathways for lung cancer therapy

(Project Co-leaders: Fadlo R. Khuri, M.D., Shi-Yong Sun, Ph.D.)

Aim 1   To determine whether an mTOR inhibitor inhibits the growth of human NSCLC cells via G1 growth arrest or induction of apoptosis, and to identify the molecular determinants of mTOR inhibitor sensitivity.

This aim was completed and summarized in the previous reports.

Aim 2   To determine whether the effect of mTOR inhibitors on the growth of human NSCLC cells is enhanced in the presence of a PI3K inhibitor or a MAPK inhibitor.

This aim was completed and summarized in the previous reports.

Aim 3   To evaluate the efficacies of the combinations of rapamycin with LY294002 or U0126 in nude mice models of lung cancer xenografts *in vivo*.

Summary of Research Findings

Results from the previous reporting period showed that mTOR inhibitors increase eIF4E phosphorylation in cultured lung cancer cells. Moreover, we determined whether mTOR inhibitors increased p-eIF4E levels *in vivo*. We further detected p-eIF4E levels in lung xenorgafts in mice exposed to RAD001 for 14 days using both Western blotting and immunohistochemistry (IHC). As presented in Figure 1A, p-eIF4E levels in both A549 and H460 xenografts treated with RAD001 detected by the Western blotting were significantly higher than those treated with vehicle control (p <0.001). By IHC, we found that five out of six A549 xenograft tumors did not or expressed very low levels of p-eIF4E. However, six tumors exposed to RAD001 for 14 days exhibited increased levels of p-eIF4E (with various degrees) that were significantly higher than vehicle control tumors (Fig. 1B; $P < 0.01$). Collectively, these results indicate that RAD001 increases eIF4E phosphorylation *in vivo* in lung xenografts.
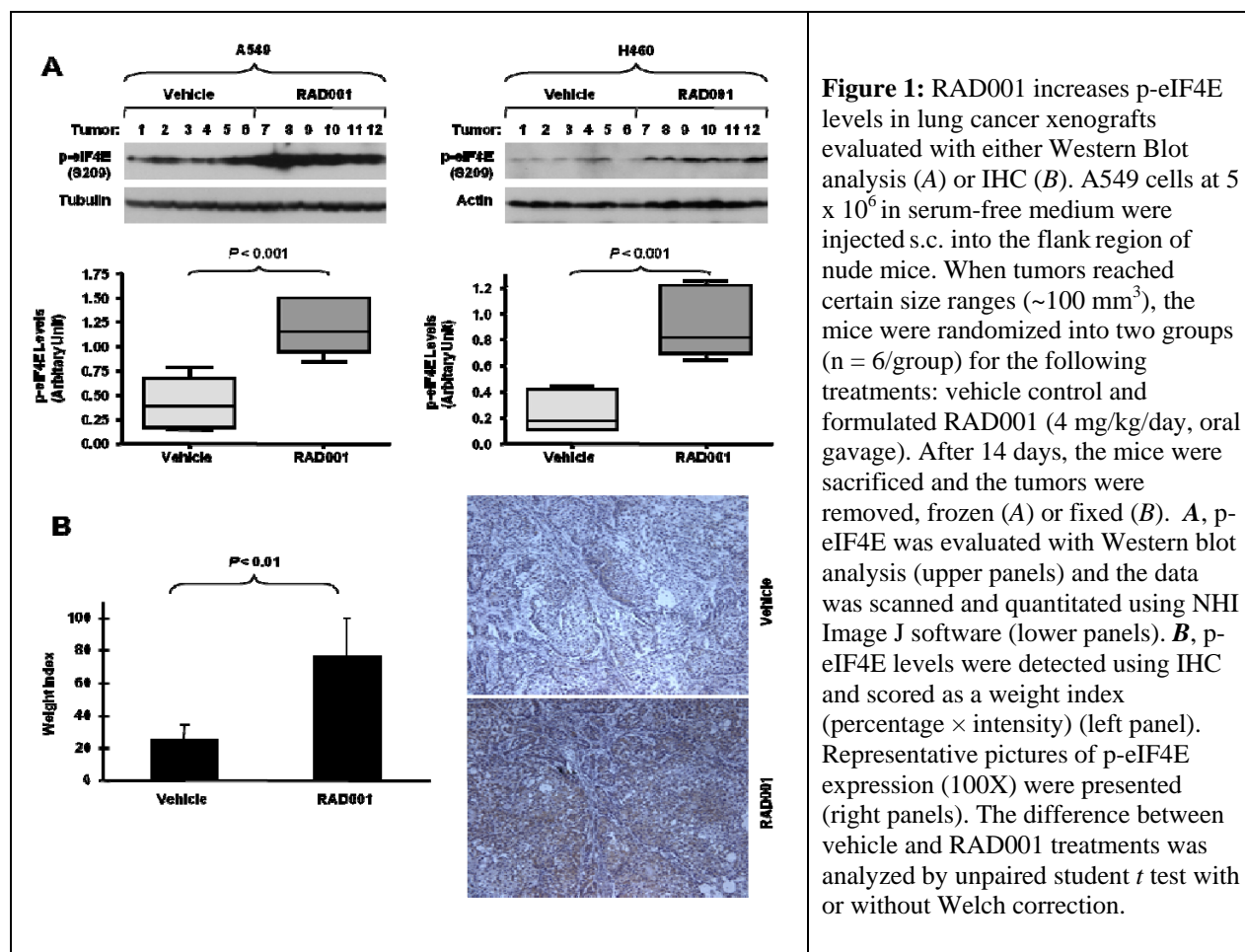
Figure 1: RAD001 increases p-eIF4E levels in lung cancer xenografts evaluated with either Western Blot analysis (*A*) or IHC (*B*). A549 cells at 5 x 10^6 in serum-free medium were injected s.c. into the flank region of nude mice. When tumors reached certain size ranges (~100 mm^3), the mice were randomized into two groups (n = 6/group) for the following treatments: vehicle control and formulated RAD001 (4 mg/kg/day, oral gavage). After 14 days, the mice were sacrificed and the tumors were removed, frozen (*A*) or fixed (*B*). *A*, p-eIF4E was evaluated with Western blot analysis (upper panels) and the data was scanned and quantitated using NHI Image J software (lower panels). *B*, p-eIF4E levels were detected using IHC and scored as a weight index (percentage × intensity) (left panel). Representative pictures of p-eIF4E expression (100X) were presented (right panels). The difference between vehicle and RAD001 treatments was analyzed by unpaired student *t* test with or without Welch correction.

In addition to induction of Akt phosphorylation by mTOR inhibitors, we found that mTOR inhibition also induced activations of the MEK/ERK signaling pathway in some cancer cell lines after a prolonged treatment. The combination of rapamycin with the MEK inhibitor U0126 significantly enhanced growth inhibitory effects of cancer cells, suggesting that MEK/ERK activation may counteract mTOR inhibitors' anticancer efficacy. Similarly, the combination of an mTOR inhibitor with the EGF receptor inhibitor erlotinib synergistically inhibited the growth of both human cancer cells in cell cultures and xenografts in nude mice (Fig. 2). Moreover, the presence of erlotinib suppressed rapamycin-induced phosphorylation of Akt, ERK and eIF4E as well, implying that erlotinib can suppress mTOR inhibition-induced feedback activation of several survival signaling pathways including Akt, ERK and eIF4E. Thus, we suggest a therapeutic strategy for enhancing mTOR-targeted cancer therapy by preventing mTOR inhibition-induced feedback activation of several survival mechanisms. These reportable outcomes were published in *Cancer Biology and Therapy* (Wang et al. 2008).
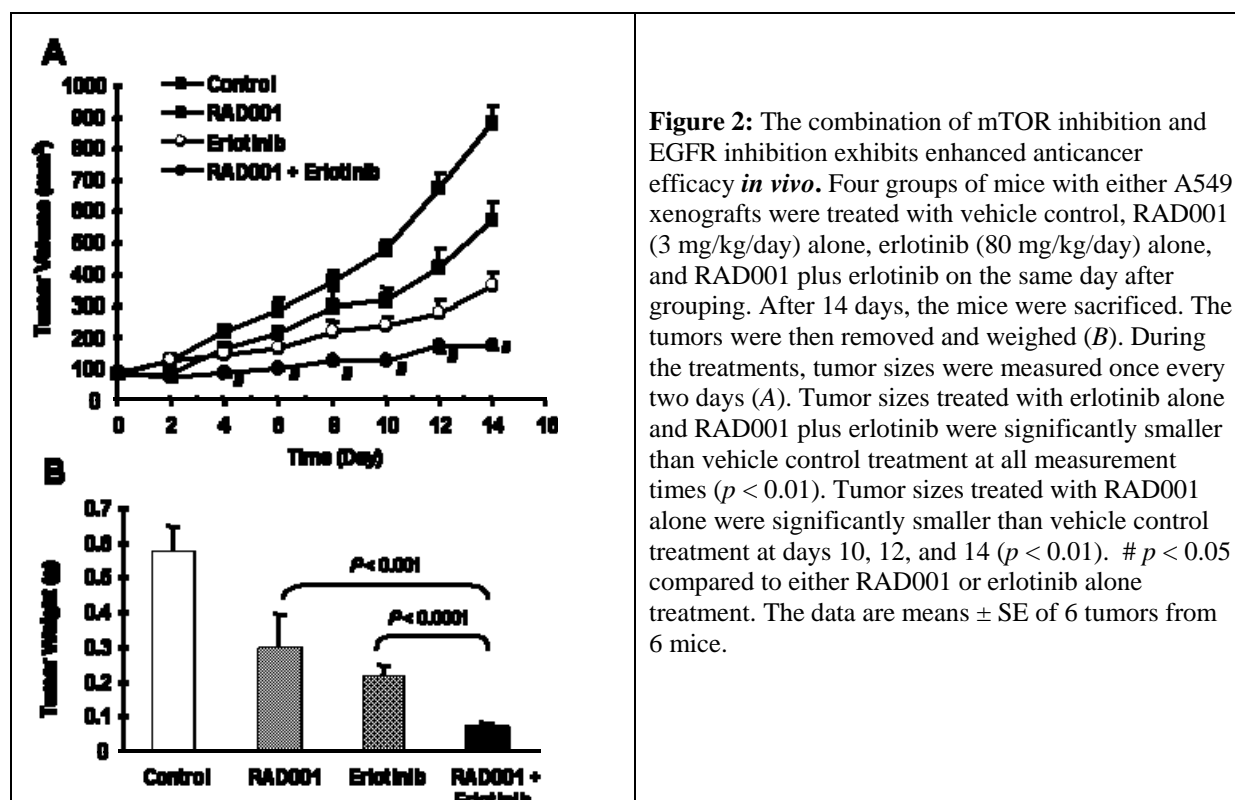
Figure 2: The combination of mTOR inhibition and EGFR inhibition exhibits enhanced anticancer efficacy *in vivo*. Four groups of mice with either A549 xenografts were treated with vehicle control, RAD001 (3 mg/kg/day) alone, erlotinib (80 mg/kg/day) alone, and RAD001 plus erlotinib on the same day after grouping. After 14 days, the mice were sacrificed. The tumors were then removed and weighed (*B*). During the treatments, tumor sizes were measured once every two days (*A*). Tumor sizes treated with erlotinib alone and RAD001 plus erlotinib were significantly smaller than vehicle control treatment at all measurement times ($p < 0.01$). Tumor sizes treated with RAD001 alone were significantly smaller than vehicle control treatment at days 10, 12, and 14 ($p < 0.01$). $\# p < 0.05$ compared to either RAD001 or erlotinib alone treatment. The data are means $\pm$ SE of 6 tumors from 6 mice.

As noted above, the mTOR inhibitor RAD001 increase p-eIF4E levels in vivo (Fig. 1). In xenografts treated with the combination of RAD001 and erlotinib, eIF4E phosphorylation was not increased compared with RAD001-treated tumors. Accordingly, the combination of RAD001 and erlotinib was more potent than each agent alone in inhibiting the growth of lung cancer xenografts. Additionally, we noted that the expression of Mcl-1, which is regulated by cap-dependent translation mechanism and important for eIF4E-mediated oncogenesis, was slightly higher in RAD001-treated tumors, but significantly inhibited in lung tumors treated with the combination of RAD001 and erlotinib. We suggested that erlotinib enhances RAD001's anticancer activity *in vivo* involving abrogation of mTOR inhibition-induced eIF4E phosphorylation. Modulation of eIF4E phosphorylation may serve as a predictive biomarker for RAD001/erlotinib-based cancer therapy. This part of the data will be presented in the upcoming 2009 AACR meeting. The *in vivo* results on the combination of RAD001 and LY294002 in lung cancer xenografts, which were summarized in the last year's report, have been published in Cancer Res (Wang et al. 2008).

Aim 4   To conduct a pilot clinical biochemical induction trial to investigate the effect of RAD001 in operable NSCLC patients and identify molecular determinants of RAD001 sensitivity and prognosis.

Summary of Research Findings

The Phase Ib protocol was activated effective February 2007. After screening 7 eligible patients, with 6 of 7 declining due to the randomization to placebo, we successfully amended the study to remove the placebo arm. Approval was obtained from the FDA, Department of Defense Human Protection Committees as well as Emory's IRB, and we have now accrued 8 total patients on this trial. One of these 8 patients, 3 patients reported drug discontinuation due

to grade 3 nausea and vomiting after 8 days. All other patients have completed the scheduled 3 weeks of therapy and have undergone surgical resection. Overall, there has been a decrease in the FDG uptake on the PET scan in 7 out of 8 patients enrolled to the study. The quantitative reduction in the standardized uptake value (SUV) ranged from 20% to 50% overall; one patient experienced a slight reduction in tumor size with RAD001. Since the last 2 patients enrolled to the study have developed interstitial pneumonitis, we have temporarily halted accrual (effective February 13, 2009) until further information can be obtained about these events. The adverse events appear unlikely related to the study drug and could be a function of the patient's pre-operative pulmonary functions. We are planning to analyze the pre- and post-treatment tumor specimens for molecular markers in the next few weeks.

Key Research Accomplishments

- Indicated that RAD001 increases eIF4E phosphorylation *in vivo* in lung xenografts.
- Demonstrated that mTOR inhibition induced activations of the MEK/ERK signaling pathway in some cancer cell lines after a prolonged treatment.
- Observed co-targeting of mTOR and PI3K/Akt signaling exerts enhanced anticancer activity in lung cancer xenograft models. mTOR inhibitors increase eIF4E phosphorylation in lung cancer xenografts.
- Modulation of eIF4E phosphorylation may serve as a predictive biomarker for RAD001/erlotinib-based cancer therapy.
- Accrued 8 patients on the clinical trial.

Conclusions

Targeting the mTOR axis appears to be a promising strategy against lung cancer. Given the nature of the complexity of lung cancer signaling pathways, including mTOR signaling, it is essential to understand the biology of lung cancer and the mechanism of action for the therapeutics of interest in order to efficiently treat lung cancer through application of mechanism-driven therapeutic regimens. Thus, we have demonstrated the scientific rationale for our effort in pursuing mTOR-targeted lung cancer therapy.

Project 6: Identification and Evaluation of Molecular Markers in Non-Small Cell Lung Cancer (NSCLC)

(PI and co-PI: Ralf Krahe, Ph.D., Li Mao, M.D)

A better understanding of the lung cancer biology and an identification of genes involved in tumor initiation, progression and metastasis are an important first step leading to the development of new prognostic markers and targets for therapy. In the same context, identification of reliable predictive markers for response or resistance to therapy in NSCLC patients is also desperately desired for optimal delivery of targeted therapy and/or standard chemotherapy. The proposed studies aim to identify the two types of markers that would eventually help develop smarter clinical trials, which will selectively recruit patients who are more likely to respond to one regimen over another and lead to improvement of overall therapeutic outcomes.

Aim 1   To expression profile by DNA microarray technology aerodigestive cancers - with primary focus on adenocarcinoma and squamous cell carcinoma (SCC) of the lung, and head and neck squamous cell carcinoma (HNSCC), including primary tumors and normal adjacent tissue, and (where available) metastatic lesions.

Summary of Research Findings

During the current project period, we completed the expression profiling on 8 matched tumor/normal adjacent tissue (T/N) pairs of lung cancers, 5 adenocarcinomas, and 3 squamous cell carcinomas (SCC) from an initial total of 22 NSCLC T/N pairs. However, due to the limited number of samples and limited expression profiling obtained, statistically meaningful conclusions for the lung cancer part of the study and, therefore, meaningful comparisons with the HNSCC part of the study were not possible. We therefore decided to focus our efforts on Aims 2 and 3.

Aim 2   To DNA profile the same samples by complementing DNA approaches to stratify RNA expression profiles on the basis of their corresponding DNA profiles.

Summary of Research Findings

Originally, we proposed to correlate DNA and RNA profiles from the 21 NSCLCs gathered in Aim 1. Due to the issues related to sample procurement, it was not feasible to acquire the necessary number of matching RNA/DNA samples that would result in a significant statistical power. We decided to gather DNA samples without matching RNA samples from 108 NSCLC patients with complete clinical and follow-up data (56 adenocarcinomas, 48 SCC, and 25 other lung cancers) for a total of 129 primary tumor (PT) and 45 matching normal adjacent tissue (NAT/PT) pairs, which we used for genomic profiling.

We performed genomic profiling of the same HNSCC samples on which we performed transcriptomic profiling (see above Aim 1) using the Affymetrix 10K *Xba*l array. Using 24 genetically matched NAT and PT pairs and 12 matching metastatic lymph nodes (MLN), we genotyped a total of 8,430 tag SNPs. Analysis of the genotype data with GeneSpring GTv2 (Agilent) for allelic imbalance (AI), indicative of loss-of-heterozygosity (LOH), showed that the majority of AI events occurred from normal to primary tumor, while the transition from primary tumor to metastasis was marked by few little additional events (0-2%). In the NAT/PT comparison, we identified five regions with significant AI: 9p24.1-p23 (38%), 5q33.3 (25%), 3q25.32-q26.1, 13q14 and 17p13 (all 21%), and 3p23-p22.3 (13%). Our overall objective was to investigate regions of frequent AI in HNSCCs that are shared with NSCLC to identify candidate tumor suppressor genes as well as to assess whether additional "hits" at these loci were present or likely.

Due to limited resolution, we hypothesized that the 10K SNP array probably underestimates LOH, resulting in missed LOH over short genomic segments and poorly defined regional boundaries. To identify additional tumors with smaller losses and to pinpoint the most frequently lost genes within the six most frequently lost regions (9p, 3p, 3q, 5q, 11q, and 17p), we performed LOH analysis in 27 N/P and 14 N/M pairs using a total of 35 microsatellite (MS) markers. In all cases, the MS LOH data confirmed the LOH identified by the SNP array. For all frequently lost regions, the MS data identified loss in additional tumors that were not detected

41

on the SNP array. This was particularly striking for three regions, namely 3p26.1-p25.2, 17p13 and 11q23.2-q23.3. Although SNP LOH at 3p26 and 11q23 was most frequently observed in the NAT/MLN comparison, MS revealed that LOH was much more frequent in N/P. The most frequently lost genes are shown in the table below; all are genes previously reported to be associated with tumorigenesis.

Cytoband	Tumor Suppressor Candidate	Comment
3p26.1-25.2	VHL	Involved in tumor angiogenesis
3q25.31	RARRES1	Down-regulated by methylation in prostate cancer,
5q33.3	CCNJL	Cyclin J-like, cell cycle regulation
9p24.1-p23	PTPRD	Regulates cell growth and transformation
17p13	TP53	Classic tumor suppressor, cell cycle, repair
11q23.2	TAGLN	Transgelin, early marker for transformation

Table 1: Frequently lost gene regions in SNP arrays

The 9p24.1-p23 region was identified in the SNP analysis as the most frequently lost region in this sample set. This region contained only a single gene, *PTPRD*, and we focused on this gene as a candidate tumor suppressor. We compared LOH at *PTPRD* with LOH at *TP53* and *CDKN2A*, both genes reported as being frequently lost early in tumorigenesis. We found that LOH at *PTPRD* in both primary tumors and metastasis (17/26 P=65%, 9/13 M=69%) was as frequent as LOH at *TP53* in primary tumors and even more frequent in metastases (16/26 N/P=62%, 4/13 N/M=31%).

To address the question of whether *PTPRD* was also frequently lost in other tumor types, we compared microsatellite LOH at both *PTPRD* and *TP53* in HNSCC to a set of matched T/N samples from lung and colorectal (CRC) cancers. LOH at *PTPRD* in CRC (3/9=33%) was similar to LOH at *TP53* (4/10=40%)*.* LOH at *PTPRD* in lung cancer (8/20=40%) was even more frequent than at *TP53* (5/20=25%). Thus LOH at *PTPRD*, while not quite as frequent in lung cancer and CRC as in HNSCC, was nevertheless frequently seen. Therefore, *PTPRD* may be a non-specific marker of early tumorigenesis in many epithelial tumors.

As both *PTPRD* and *RARRES1* have CpG islands in their 5' promoter regions that may be subject to epigenetic inactivation by promoter hypermethylation, we investigated hypermethylation as a "hit" that is functionally equivalent to loss (reported in Aim 3).

The genes *TCF21* and *CHD5* had been identified in other studies as possible early markers of tumorigenesis. We also investigated LOH at these two genes in HNSCC and lung cancer samples using MS markers. At *CHD5,* we found little LOH in HNSCC samples (12% in PT and 10% in MLN) and only slightly more in lung cancer (33% of 22 PT). At *TCF21,* LOH in HNSCC was striking (59% of PT and 50% of MLN); lung cancers have somewhat less LOH at this locus (43% of 37 PT).

Aim 3   To evaluate the contribution of promoter hypermethylation and transcriptional inactivation of known cancer genes subject to epigenetic silencing to cancer phenotype.

Summary of Research Findings

Last year, we reported that the transcription factor *TCF21* was the most often hypermethylated (≥30% methylation) gene in both HNSCC (96%, n=24) and NSCLC (95%, n=21). This finding was confirmed when we investigated a second larger validation sample set of 108 NSCLC patients with complete clinical and follow-up data (56 adenocarcinomas, 48 SCC, and 25 other lung cancers) for a total of 129 PT and 45 matching NAT/PT pairs. Overall, 73% of lung cancers showed *TCF21* hypermethylation (n=129). Adenocarcinomas and SCCs together showed hypermethylation in 78% (n=100) of tumors, while other lung cancers showed hypermethylation in 64% of cases (n=25). Adenocarcinomas compared to SCCs showed slightly higher levels of (40%±2.5 vs. 37%±2.7) and more frequent (90% vs. 70%) methylation, respectively.

To determine the effect of *TCF21* promoter hypermethylation on gene expression, we collaborated with Dr. Ignacio Wistuba (Pathology Core) to perform TCF21 protein immunohistochemical (IHC) analysis on a TMA of 300 lung cancer cases. Similar to our DNA-based methylation data, 253 of 300 cases [85%; 166/191 (87%) adenocarcinoma and 87/109 (80%) squamous cell carcinoma] resulted in no or significantly decreased TCF21 expression. Correlation of methylation status with available clinical factors (Biostatistics Core) showed a significant correlation with histology (adenocarcinoma, $p = 0.0026$), sex (females, $p = 0.0209$), and smoking status (never smokers, $p = 0.0476$). However, race, TNM stage, and prognosis were not significantly associated. Given the interesting association of histology, sex, and smoking-status (adenocarcinoma in female never-smokers), which is reminiscent of recent findings for *EGFR* mutations in lung cancer patients, we investigated the possibility that EGFR mutation status might predict TCF21 expression. Multivariate analysis showed that histology, but not gender or smoking status, was associated with low TCF21 expression. However, when adenocarcinoma cases (n=172) were considered alone by both univariate and multivariate analysis, no significant correlation was observed.

A high percentage (85%) of the lung cancers were hypermethylated at *TCF21*. Approximately 35% of samples showed both LOH and hypermethylation. We sequenced the remaining tumors to determine whether mutation might furnish a second hit, but results showed no *TCF21* coding mutations identified. Based on our results, the primary mode of inactivation of *TCF2*1 would appear to be methylation (>85%) followed by deletion (43-59% depending on the tumor type, NSCLC vs. HNSCC). Some tumors have 2 hits (35%), but most tumors would appear to have a single hit (more frequently methylation and less frequently LOH), suggesting that this may be another case of a haploinsufficient tumor suppressor gene. TCF21 is an important basic helix-loop-helix transcription factor that plays an important role in the epithelial-mesenchymal transition (EMT), and haploinsufficiency may be sufficient to be tumorigenic. Based on our methylation profiling, we conclude that *TCF21* promoter hypermethylation and TCF21 expression are good biomarkers of both early lung and head and neck cancer (manuscript in preparation).

We completed the evaluation of methylatable TSG [*PTPRD* and *RARRES1*]. According to Knudson's "two-hit" hypothesis, second hits at tumor suppressor genes are needed for tumorigenesis. In our expression analysis of these same samples, *PTPRD* mRNA was seen to be reduced approximately 2-fold in primary tumors when compared to adjacent normal tissue (T=-2.1527). In order to determine whether the reduced expression of *PTPRD* was due to

haploinsufficiency or hyper-methylation, we used PyroMethA to investigate methylation at both *PTPRD* promoters. The maximum percent methylation seen in any primary tumor for island 1 was 27.8% and for island 2 it was 29.7%. These percentages were not significantly different from maximum levels seen in the matching normal samples (28% for island 1 and 23% for island 2). The largest positive change seen between normal and tumor was 22.7% in primary tumors for island 1 and 21.8% for island 2. However, the mean change was less than 4% and probably within our range of experimental error. Overall, it does not appear that hyper-methylation plays an important role in *PTPRD* loss of function. The observed reduced expression may be entirely due to LOH, and *PTPRD* may therefore be a haplo-insufficient tumor suppressor.

Since *RARRES1* had previously been reported to be hypermethylated in prostate cancer and squamous cell carcinoma of the esophagus, we also investigated promoter hypermethylation at this locus. Approximately 24% of lung cancer and 10% of HNSCC tumors showed significant hypermethylation, as did a number of cancer cell lines.

We also performed global hypomethylation of tumors. Loss of genome-wide methylation is a common feature of cancer, and the degree of hypomethylation has been correlated with genomic instability. Global methylation of repetitive elements possibly arose as a defense mechanism against parasitic DNA elements, including retrotransposons and viral pathogens. Given the alterations of global methylation in both viral infections and cancer, we examined genome-wide methylation levels in HNSCC, in which a specific set of cancers (oropharyngeal) has been causally associated with human papilloma virus (HPV). LINE hypomethylation was more pronounced in HPV-negative than in HPV-positive tumors. Moreover, genomic instability, measured by genome-wide LOH and SNP analysis, was greater in HNSCC samples with more pronounced LINE hypomethylation. Global hypomethylation was variable in HNSCC. Its correlation with both HPV status and degree of LOH as a surrogate for genomic instability may reflect alternative oncogenic pathways in HPV-positive versus HPV-negative tumors.

Aim 4   To determine protein signatures of treatments of erlotinib and other therapeutic agents, alone or in combination, in NSCLC and identify molecular predictors of response.

Summary of Research Findings

During the last project period, we used adenocarcinoma and squamous cell carcinomas to test the expression levels when treated with SAHA (HDAC inhibitor) and 5-Aza-citidine (DNMT inhibitor). Results of these tests suggested that we could use the same tumor models to develop biomarkers able to predict further responses to similar treatment regimens.

In our current study, we used the adenocarcinoma and squamous cell carcinoma models to test a neurotrophic receptor kinase (Trk) inhibitor for similar expression profiles noted in earlier
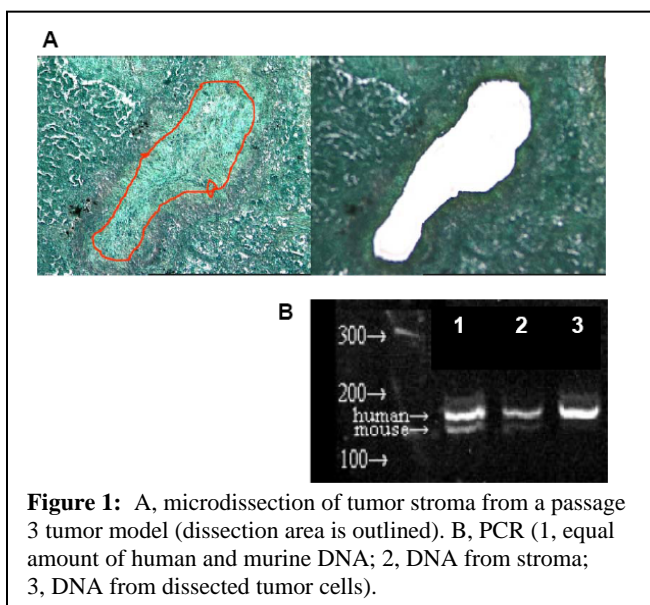
Figure 1: A, microdissection of tumor stroma from a passage 3 tumor model (dissection area is outlined). B, PCR (1, equal amount of human and murine DNA; 2, DNA from stroma; 3, DNA from dissected tumor cells).

44

results. Although expression of Trk can be detected in primary tumors, most of the cancer cell lines lost the expression profile needed for validation of anti-Trk agents. We screened eight of our heterotransplant lung cancer models for expression of Trks (Trk-A, Trk-B, and Trk-C) and their corresponding growth factors (NGF, BDNF, and NT3) using real-time RT-PCR (Table 1). We detected modest expression of certain Trks and their ligands in the tumors.   We then conducted *in vivo* testing using the Trk inhibitor as a single agent to determine a potential anti-tumor effect in the heterotransplant lung cancer models. Five different tumor models were used in the initial testing, using only one animal per treatment group per model to serve for screening purposes. In 100mg/kg dose, the tumor inhibitory effect was observed in 3 of the 5 models, particularly in one of the adenocarcinoma tumor models (model 7) where tumor growth was inhibited by 78% compared to the vehicle-treated control. This model expressed only Trk-B and its ligand, BDNF, but not other Trks and their ligands. We then conducted second stage experiment by focusing on the two models (models 7 and 8) showing signs of tumor inhibition. Five animals were assigned to each treatment group for each model. Although the tumor growth inhibition was minimal for model 8, a similar inhibitory effect (71% inhibition) was observed in model 7 as compared with vehicle treated controls.

Model No.	Histology	TrkA/NGF (2 power - ΔCT x 1E6)	TrkB/BDNF (2 power - ΔCT x 1E6)	TrkC/NT3 (2 power - ΔCT x 1E6)	Response To Trk inhibitor
MDACC1	Adeno	0.1/0.2	1.0/0.3	0/0	No growth inhibitory effect
MDACC2	Poorly dif	0/0	0.2/0.1	0.4/3.9	No growth inhibitory effect
MDACC3	Squamous	0/0	0/0.2	0/0.7	
MDACC4	Squamous	0/0	2.4/0.1	0/1.0	
MDACC5	Adeno	1.9/0.5	0/7.8	0/1.1	
MDACC6	Adeno	0/0	0/0.1	0/0.5	Inhibitory
MDACC7	Adeno	0/0	0.2/3.0	0/0	Inhibitory (78%)
MDACC8	Adeno	0.4/3.0	0/32.8	0/0	Inhibitory
MDACC9	Sqamous	Not tested	Not tested	Not tested	

Table 1: Heterotransplant lung cancer models

In previous studies, it has been shown that early passages of heterotransplant tumors contain infiltrating inflammation cells that disappear in later passages of the tumors. This observation is reasonable because most of the infiltrating inflammation cells are terminally differentiated and are not renewable. However, it is poorly understood whether other tumor stroma cells that may have stem-cell features in the tumors remain of human origin in the tumor models. The presence of tumor-stroma may help evaluate agents that target the tumor microenvironment as part of their mechanisms of action. Our preliminary data from three passages of the tumors suggests the presence of human-origin tumor stroma (Fig. 1). The stroma DNA derived from the tumors showed predominantly human origin whereas DNA from the tumor cells contained no murine component (Fig. 1). Although additional experiments are needed, the result is encouraging.

Aim 5   To determine a clinical utility of the molecular predictors.

Summary of Research Findings

This aim was completed and summarized in previous reports.

Key Research Accomplishments

- Identified shared regions of LOH and allelic imbalance through DNA profiling of HNSCC and NSCLC on matched T/N and T samples.
- Demonstrated that several candidate tumor suppressor genes in these regions are subject to epigenetic silencing by gene-specific hypermethylation in both HNSCC and NSCLC.
- Confirmed *TCF21* promoter hypermethylation and TCF21 expression as promising biomarkers of both early lung and head and neck cancer.
- Observed that early passages of heterotransplant tumors contain infiltrating inflammation cells that disappear in later passages of the tumors.

Conclusions

We performed RNA and DNA profiling on available samples to identify genes and genomic regions that are altered in NSCLC and interrogated additional candidate methylatable genes as potential tumor suppressor genes in NSCLC, to identify their potential as biomarkers. These experiments have generated a list of molecular candidate biomarkers for further investigation in larger sample sets.

Core B: Biostatistics & Data Management Core

(Core Director: J. Jack Lee, Ph.D.)

The Biostatistics and Data Management Core has continued to work with all IMPACT Projects in their research efforts, especially in the area of biostatistical support in clinical trial design, implementation, and analysis of experimental results. We also developed statistical methods to enhance the design and analysis pertinent to the lung cancer research.

Specific Aims:
1. To ensure that the results of all projects are based on well-designed experiments and are appropriately interpreted by providing experimental design; sample size estimates; power calculations; and integrated, comprehensive analysis for each basic science, pre-clinical, and clinical study.
2. To develop a data management system that integrates clinical, pathological, and basic science data while providing data integrity through process tracking and quality control.
3. To provide statistical and data management support for genomic and imaging studies including microarray, proteomics, and molecular targeted imaging.
4. To develop and adapt innovative statistical methods pertinent to biomarker-integrated translational lung cancer studies.
5. To produce statistical reports for all projects.
6. To collaborate and assist all project investigators with the publication of scientific results.

Summary of Research Findings

Core B continues to provide statistical support in the revision and conduct of the clinical trial proposed in Project 1 under the leadership of Dr. Ritsuko Komaki, which has been accruing well in recent months. In addition, we continue to provide statistical support for the clinical trial (ZD6474 in malignant pleural effusion) proposed in the Developmental Research Project 1 under the direction of Drs. Roy Herbst and Carlos Jimenez.

We worked with Dr. Ignacio Wistuba on the statistical analysis of EGFR/EGFR ligand expression in paired primary lung cancer and brain metastasis (Project 5). The biomarkers analyzed include EGF, Amphiregulin, TGF-alpha, p-HER3, HER3, EGFR, pEGFR, and ErbB-2.

We have also worked on the study with GRP78, IL11R and EphA5 on 301 NSCLC patients with Dr. Wistuba and Dr. Masanori Sato (Project 3).

We performed statistical analysis on Dr. Krahe's project involving TCF21 immunohistochemical expression in NSCLC patients. TCF21 is novel candidate tumor suppressor gene, so the abnormality is loss or reduction of expression. We examined the immunohistochemical (IHC) expression of the protein using formalin-fixed and paraffin-embedded tissues from 308 NSCLC patients (adenocarcinoma and squamous cell carcinoma histologies) placed in tissue microarrays (TMA) as performed by the Pathology Core (Dr. Wistuba). In addition, we collaborated with the TCF21/EGFR analyses with 202 patients.

We also worked with Dr. Wistuba on the statistical analyses on immunohistochemical expression of the multiple biomarkers: STAT1, LCK, DUSP6, EGFR, and KRAS with 306 NSCLC patients. It was reported that a five-gene expression signature (DUSP6, MMD, STAT1, HER3, and LCK) was an independent predictor of relapse-free and overall survival in a series of 185 NSCLCs. Our goal was to study the protein IHC expression of 4 of those genes in our large series of NSCLC TMAs and identify if the IHC expression correlated with patients' clinicopathologic features and outcome.

We worked with Dr. Wistuba on statistical analysis on the data for VEGFR and EGFR pathway expression in lung cancer (284 observations), as well as an analysis of IHC expression of stem cell markers associated to NSCLC clinico-pathologic characteristics with Drs. Yuan and Wistuba.

We are also working on HER family analysis including EGFR, Her2 and Her3 and their associated ligands. We will compare the expression of individual markers by IHC to find any link between individual markers and clinical (gender, stage, smoking history, etc) and pathological (total NSCLC, and subtypes adenocarcinoma and squamous cell carcinoma) parameters and survival (recurrence-free survival and overall survival at 5 years).

Key Research Accomplishments

- Continued to provide statistical support in the clinical trials for Project 1 and DRP-1.
- Provided statistical support for Projects 2, 3, 4, 6, and Pathology Core.
- Continued to work closely with the Project 4 PI (Dr. Reuben Lotan) on synergy studies of combination drug treatments in cell lines to determine whether the effect is synergistic, additive, or antagonistic.
- Developed a flexible semi-parametric model and codes, which allows fitting very general interaction patterns for the drug combinations.

- Developed methods and provided codes to construct the confidence interval for the interaction index for the Emax model.
- Developed an additive hazards model with time-varying coefficients.
- Developed a new Bayesian cure rate model to estimate the cure rate and threshold.
- Developed a cure rate model with covariate measurement errors.
- Developed a Bayesian dose-finding trial design with multiple drugs.

Conclusions
Core B continued to provide statistical analysis and data management support for all research projects in the IMPACT study. We will assist the other Projects with their ongoing needs to complete the proposed studies.

Core C: Pathology Core
(Director: Ignacio Wistuba, M.D.)

The IMPACT interdisciplinary research proposal for studying targeted therapy of lung cancers has required extensive histopathologic, IHC, and molecular studies of cell and tissues specimens, which have been assisted, coordinated or performed by the Pathology Core. One of the most important roles of the Pathology Core has been to provide professional technical services for proper procurement, storage and use of human and animal tissues, as well as technical assistance for IHC analysis. In addition, the Pathology Core has provided assistance for collection and evaluation of tissue specimens in IMPACT clinical trials in lung cancer patients.

Aim 1   Develop and maintain repository of tissue, cell and serum specimens from patients with lung neoplasia, as requested by the various component projects.

Summary of Research Findings

During the current project period, we continued the collection of tissue and cell specimens for several IMPACT projects with a large emphasis on the clinical trials:

Project 1. For the IMPACT clinical trial using erlotonib (Tarceva^R), chemotherapy, and radiotherapy in advanced non-small cell lung cancer (NSCLC) patients (Protocol 2005-1023; Principal Investigator: Dr. R. Komaki), the Pathology Core has assisted in the evaluation of tumor tissue specimens of 15 NSCLC cases for biomarker analysis. Of those, 8 cases have been considered adequate for analysis and 6 of them have been examined for *EGFR* (exon 18-21) and *KRAS* (codons 12, 13 and 61) mutations, *EGFR* copy number by fluorescent *in situ* hybridization (FISH), and EGFR protein (total and phosphorylated [p]) expression by immnuhistochemistry. No *EGFR* and *KRAS* mutations were detected in these 8 cases, and one case showed increased *EGFR* copy number (high polysomy). High levels of EGFR and p-EGFR protein expression were detected in two cases.

Project 2. For the IMPACT clinical trial using ZD6474 in NSCLC patients with malignant pleural effusion (Protocol 2005-9029; Principal Investigator: Dr. C. Jimenez), we have collected, processed and banked specimens from the effusions from 13 patients at baseline. In addition, we have collected specimens at 2, 3, 6 and 10 weeks from a total of 31 pleural effusions. From these effusions, we have processed and stored: a) frozen cell pellet; b) formalin-fixed and

paraffin-embedded (FFPE) cell pellets blocks and histology sections; (c) alcohol-fixed and frozen cell smears; e) cell pellets frozen in RNA later; f) cell pellets frozen in DMSO 12%.

Project 6. We have continued collecting fresh NSCLC tumor tissue specimens that have been distributed to Dr. Mao's laboratory for developing mouse tumor heterotransplants. To date, we have provided fresh tissue from 31 lung cancers (18 adenocarcinomas, 9 squamous cell carcinomas and 4 others NSCLCs), and of those, 10 cases have been provided since the last annual report. In all of these cases, FFPE human tissue specimens have been collected, banked and examined (see Project 6 report). In addition, our collaboration on the protein expression and methylation analysis of *TCF21* gene in nSCLC (Project 6, Dr. Krahe) was completed last year.

Other projects. We have completed our work on several other key projects in IMPACT. Project 2, designed to analyze HER and VEGF/R and HIF-1α markers in human NSCLC tissue specimens, was completed in 2007. Project 3 was completed with the analysis of GRP78, IL-11R and Eph5A markers in human NSCLC tissue specimens. Finally, the aim designed to analyze bFGF, receptors FGFR1, and 2 markers (Project 4) in human NSCLC tissue specimens was completed and published (see attached paper).

Aim 2   Develop innovative tissue and cell reagents from lung cancer patients for the investigation and validation of the molecular endpoints relevant to each component project.

Summary of Research Findings

The development of new tissue and cell reagents from lung cancer patients was focused in four different methodologies:

Tissue and cell pellets microarrays (TMA)
The TMAs prepared in previous years (primary lung tumors, paired primary and brain metastasis NSCLC tumors, and cell line pellets) have been utilized for several IHC and FISH analyses, including gene copy number analysis of *EGFR*, *HER2* and *NKX2-1* (*TITF-1*).

Establishment of short-term cultures and cancer cell lines of clinical lung tumor specimens
During last year, our repository of 50 NSCLC cell lines obtained from our DoD grants collaborators, Drs. John Minna and Adi Gazdar (UT-Southwestern Medical Center, Dallas, TX), has been maintained. In addition, we have prepared cell line pellet blocks for IHC and FISH analysis form 47 of these cell lines, including 14 2-core TMAs, that have been used to optimize new antibodies and FISH DNA probes.

Lung cancer heterotransplants using clinical lung tumor samples
As stated above, 10 new specimens have been provided to Dr. Mao's lab (Project 6) to establish these models.

Pleural fluid specimens
In collaboration with Dr. C. Jimenez (Department of Pulmonary Medicine), we have established a large repository of lung cancer malignant pleural fluids (Table 1).

Number	Lung Cancer			Mesothelioma	Other Tumors
	Adenocarcinoma	Squamous Cell Carcinoma	SCLC		
Cases	80	29	8	8	96
Samples					
Supernatant	164	58	16	16	184
Pellets in RNA later	79	26	8	9	85
Cell blocks	96	29	8	10	90
Cryopreserved Cells	63	20	16	22	52
Smears	172	62	9	30	96

Table 1. Number of cases and samples of malignant pleural fluid collected and banked by tumor type.

Aim 3   Process human and animal cell and tissues for histopathological, immunohistochemical (IHC) and molecular analyses, including tissue microdissection, as required by each component project.

Summary of Research Findings

As the previous years, archival and prospectively collected frozen and FFPE cell and tissue specimens from NSCLC patients have been processed and distributed for Projects 1, 2, 3, 4 and 6.

Aim 4   Perform and evaluate IHC analysis in human and animal cell and tissue specimens, as required by the various component projects.

Summary of Research Findings

Most of the studies performed in collaboration with IMPACT research projects have been completed as reported in the previous year. During the current project period, we have expanded our collaboration with Project 1 by continuing to analyze IHC and genetic markers that are relevant to the EGFR and VEGF/R pathways in lung cancer. Three main projects have been performed in the Pathology Core in collaboration with this project:

Analysis of VEGFA and VEGFR-2 copy number and mutation in NSCLC
In collaboration with Dr. R. Herbst (Co-PI Project 1), we previously showed that VEGFR and EGFR pathways are positively correlated in early stage NSCLC and IHC expression of p-VEGF-R2 is an indicator of worse overall survival in stage I-IIIA NSCLC. Recently, we have performed *VEGFA* and *VEGFR-2* gene copy number analysis by quantitative (q)-PCR analysis of DNA extracted from 50 NSCLC cell lines and 101 frozen tumor specimens. In NSCLC cell lines, increased copy numbers of *VEGF* and *VEGFR-2* has been detected in 2% and 5%, respectively. Similar frequencies of increased copy numbers have been detected in tumor specimens for *VEGFA* (3/10, 3%) and *VEGFR-2* (5/101, 5%). A detailed pathological analysis of tumor specimens having these gene abnormalities is being performed, and we plan to characterize, among other markers, the microvascular density (MVD) using tissue specimens.

In addition, mutation analysis of *VEGFR-2* of exons 7, 11, 21, 26 and 30 in NSCLC cell lines and tumor specimens is underway. We have detected two SNPs (exons 11 and 21) in tumor cell lines and only one potentially activating mutation in exon 21 (cgt946cat).

Analysis of the IHC expression of angiogenesis-related markers HIF-1α and carbonic anhydrase IX (CA IX) in tumor specimens from 330 NSCLC patients using TMAs
The IHC analysis of these 2 markers has been completed, and the preliminary statistical analysis demonstrated that NSCLC tumors expressed relatively high levels of cytoplasmic HIF-1α, and cytoplasmic and membrane CAIX. We detected low levels of HIF-1α nuclear expression in tumors. HIF-1α cytoplasmic expression did not correlate with tumor histology and other clinicopathologic features except smoking. Cytoplasmic HIF-1α was significantly ($P<0.001$) higher in smokers compared with never-smokers.

CAIX membrane expression was significantly higher in squamous cell carcinomas than adenocarcinomas ($P<0.001$), and in tumors with more advanced TNM stage ($P=0.001$). Interestingly, patients with positive membrane CAIX had a higher risk of recurrence ($P=0.0096$, HR [95%C] = 2.30 [1.22, 4.30]). After adjusting for lymph node (N) stage, the membrane CAIX effect remains. In addition, patients with positive membrane CAIX had higher risk of recurrence ($P=0.01$, HR [95%CI] = 2.23 [1.19, 4.19]). In multivariate analysis, and aftter adjusting for histology, age, gender, smoking history, N stage and overall TNM stage, patients with higher membrane CAIX had higher risk of death ($P< 0.05$).

Additional IMPACT research activities of the Pathology Core
The Pathology Core has performed independent research activities to better characterize the *EGFR* molecular abnormalities involved in: a) the progression of lung cancer, b) its correlation with other lung cancer molecular abnormalities, and c) to establish their role in the development of lung cancer brain metastasis. During the last year, we completed and submitted some of the studies for publication. As a result of this additional work performed by the Pathology Core, we published one paper and submitted two manuscripts within the last year. We also have data for a third manuscript that is currently in preparation. In addition, four abstracts were presented at the 2008 AACR Annual Meeting (San Diego, CA, April 2008), and one has been accepted for presentation in the 2009 AACR Annual Meeting (Denver, CO, April 2009).

Completed Projects:
a) EGFR abnormalities in the progression of lung adenocarcinomas. A paper by X. Tang et al. was published in Cancer Prevention Research (Cancer Prev Res 1: 192-200, 2008; see attached paper).

b) Association of *EGFR* gene abnormalities with estrogen and progesterone receptors expression. A manuscript authored by G. Raso et al has been submitted to Clinical Cancer Research (see attached manuscript). This manuscript received a favorable review and it will be resubmitted with the revisions in March 2009.

c) Characterization of HER family receptors markers and *EGFR* gene abnormalities in NSCLC primary tumors and brain metastasis. A manuscript authored by M. Sun et al has been submitted to Clinical Cancer Research (see attached manuscript). The manuscript received a favorable review and it will be resubmitted with some new data in March 2009. As requested by the reviewers, we have added information comparing in primary tumors and corresponding brain metastasis the protein expression by IHC of 5 HER ligands, including epiregulin, betacellulin (BTC), heparin-binding epidermal growth factor-like growth factor (HB-EGF), neuroregulin-1 (NRG1), and -2 (NRG2). The new data are currently under statistical analysis by the Biostatistical Core for the resubmission.

Ongoing Projects:

a) Role of *NKX2-1* (*TITF-1*) gene amplification and protein overexpression in lung cancer and its association with *EGFR* abnormalities. Following our data indicating that *NKX2-1* amplification by FISH correlated with outcome in patients with NSCLC, including both adenocarcinoma and squamous cell carcinoma histology (platform presentation in the 2008 AACR Annual Meeting, San Diego, CA), we have expanded our initial observation to a larger set of NSCLC cases and established a DNA q-PCR methodology for analysis of *NKX2-1* copy number analysis. This work has been accepted for platform presentation in the 2009 AACR Annual Meeting, Denver, CO (see attached abstract). A manuscript consolidating all these data is in preparation by Ximing Tang et al.

b) *EGFR* and *HER2* copy analysis by FISH in tumor specimens from 330 NSCLC patients using TMAs, and correlation with *EGFR* and *KRAS* mutations and patients' clinicopathologic features. During the last year we have completed the analysis of the copy number analysis by FISH of these two genes in a large series of NSCLC tumors. Gene mutation and patients' clinicopathologic data are available and the statistical analysis by the Biostatistical Core is in progress. The main aim of this study is to address whether *EGFR* and/or *HER2* gene amplification identify a subset of NSCLC patients with stages I-IIIA with worse outcome and higher incidence of tumor metastasis.

Key Research Accomplishments

- Developed a large repository of lung cancer tissue, cytology and cell lines specimens with annotated clinical data, to be utilized for research projects.
- Developed a series of lung cancer heterotransplants in mice in collaboration with Project 6.
- Characterized the expression (VEGF/VEGFR, HIF-1α/CAIX, and bFGF/receptors) and molecular abnormalities (*VEGFA* and *VEGFR-2*) of angiogenic markers in NSCLC.
- Identified the sequence of *EGFR* abnormalities involved in the progression and metastasis of lung adenocarcinomas.
- Established the correlation between *EGFR* mutations and ER expression in lung adenocarcinomas.
- Characterized the abnormalities of *NKX2-1* (*TITF-1*) in NSCLC and its association with patients' outcome.
- Presented 4 abstracts at the 2008 AACR annual meeting with an additional abstract to presented at the 2009 annual meeting.

Conclusions

The Pathology Core has assisted and collaborated actively with several research projects to perform multiple histopathological, immunohistochemical, and genetic studies in a large series of lung cancer tissue (archival and prospectively collected in the IMPACT clinical trials) specimens. In addition, the Pathology Core has managed to conduct specific research activities, which fully integrate with some of the IMPACT research projects. Due to the direct contribution of the Pathology Core, four abstracts have been presented and one has been accepted for presentation at international meetings, two papers have been published, and two manuscripts are in resubmission process. The Pathology Core has successfully fulfilled the goals proposed for the fourth year of the IMPACT project.

Core D: Imaging Core: Provide Imaging Support for IMPACT Projects
(PI and co-PI: Juri Gelovani, M.D., Ph.D.; Chun Li, Ph.D.)

Summary of Research Findings

Project 2. During the past reporting period, the Imaging Core D completed the development and evaluation of standard operating procedures and chemistry, manufacturing, and control sections of an IND for a Phase I clinical study on PET imaging with ^{18}F-PEG6-IPQA to assess radiation dosimetry and radiolabeled metabolites in patients with NSCLC (Fig. 1). Specifically, the Core developed computer-controlled automated procedures for the radiolabeling of ^{18}F-PEG6-IPQA and QC/QA procedures required for preparation of an IND application to the FDA.

The Core performed a series of PET/CT imaging studies in non-human primates (rhesus macaques) to assess the pharmacokinetics, biodistribution, metabolism, and radiation dosimetry of ^{18}F-PEG6-IPQA, which is required for preparation of an IND application to the FDA. The results of this study are described in the report for Project 2.

Also, the Imaging Core has conducted the final series of ^{18}F-PEG6-IPQA microPET imaging studies in mice bearing different NSCLC xenografts, described in the report for Project 2.

Figure 1: Structure of the novel V-generation agent ^{18}F-PEG6-IPQA with selectivity for active mutant EGFR and improved water solubility.

Project 4. The Imaging Core continued to conduct bioluminescence imaging (BLI) studies in mice bearing s.c. xenografts of A549 carcinomas expressing GFP-Luc (GL) dual-modality reporter gene (previously transfected by the Imaging core). The expression of GL reporter gene in lung carcinoma xenografts growing in mice was assessed by BLI after i.p. injection of D-luciferin (Biosynth, Int., Naperville, IL) substrate at 150 mg/kg per mouse 10 minutes prior to imaging with IVIS200 system (Xenogen, Almeda, CA).

Key Research Accomplishments

- Produced novel ^{18}F-PEG6-IPQA derivative for PET imaging studies in small animals and non-human primates for Project 2.
- Maintained SOPs and performed QC/QA procedures for routine synthesis of ^{111}In-DTPA-PEG-AnnexinV for SPECT/CT imaging in Project I and performed imaging studies.
- Performed microPET/CT imaging (and autoradiography) studies in mice with orthotopic models of different NSCLC using ^{18}F-PEG6-IPQA in Project 2.
- Performed routine synthesis of [^{18}F]FEAU for Project 3 and conducted microPET imaging studies for this project.
- Performed synthesis and ^{64}Cu/^{111}In radiolabeling of novel cyclic nanopeptides for animal imaging studies in Project 3.
- Contracted the GLP studies on toxicology of F-PEG6-IPQA to Charles River Laboratories (MA).

Conclusions

The Imaging Core continues to provide highly specialized imaging support as requested by the project leaders of IMPACT for their designated research projects.

DRP-1: Treatment of Malignant Pleural Effusion with ZD6474, a Novel VEGFR and EGFR TK Inhibitor
(PI and co-PI: Roy Herbst, M.D., Ph.D., Carlos Jimenez, M.D.)

Aim 1   To determine clinical effect of ZD6474.

Aim 2   To investigate biological correlates.

Aim 3   To investigate radiographic correlates.

Aim 4   To assess quality of life.

Summary of Research Findings

The amended single arm, open-label study to evaluate the efficacy of ZD6474 on the management of pleural effusion in NSCLC patients was activated in June of 2007. To date, 17 patients have been enrolled on the study.

Six patients are excluded from the following analysis:

- Five patients did not receive medication:

    - Non-compliance (1)

    - Benign pleural effusion (2)

    - Non-amenable for IPC placement (1)

    - Renal dysfunction (1)

- One patient was not evaluable due to placement of a defective intrapleural catheter.

Days with intrapleural catheter in place
Nine patients have had their intrapleural catheters removed at days 13, 14, 14, 15, 22, 28 67, 68 and 142. One patient with IPC dislodged on day 15 and was removed from the trial on day 23 due to emphysema. The last patient still has the intrapleural catheter in place after 126 days.

Weeks on study and related adverse events
Four patients stopped medication at week 6 due to disease progression. One patient's symptoms stopped the medication at week 6 after developing neurological symptoms and hyponatremia. Another patient with a defective intrapleural catheter was excluded from the study at week 6. One patient stopped the medication at week 7 due to recurrence of QTc prolongation after dose reduction. Four patients completed 10 weeks of treatment, one patient completed 18 weeks of treatment and currently two patients are on medication at weeks 17 and 32.

Response
Six patients had stable disease, one patient had a treatment failure due to emphysema but with stable disease, one patient had a partial response and three patients displayed disease progression.

Correlative studies
In collaboration with Dr. Wistuba (Core C Director), we have been collecting pleural effusion specimens including cryopreserved cell pellets, supernatants, FFPE blocks, smears, and RNA for correlative studies (see Table 2, Core C).

Key Research Accomplishments
- Enrolled 17 out of 25 patients on the clinical trial.
- Collected specimens for correlative analyses on all patients (4 pleural fluid samples and four blood samples per patient).

Conclusions

The trial is enrolling patients; all analyses will be performed after the trial is completed.

DRP-2: TALK - Teens and Young Adults Acquiring Lung Cancer Knowledge

(PI: Alexander V. Prokhorov, M. D., Ph.D.)

Ninety percent of lung cancer cases in adults are direct results of smoking. In children and young adults, tobacco use remains a major public health problem in spite of the recent declines in smoking prevalence among children and adolescents. Over the past 2-3 decades, numerous factors of smoking initiation among adolescents have been thoroughly investigated. A considerable volume of literature is currently available providing important clues with respect to designing tobacco prevention and cessation among youth.

Focusing on this major public health problem – tobacco use among young individuals and lack of in-depth knowledge of lung cancer issues – Project TALK (Teens and Young Adults Acquiring Lung Cancer Knowledge) was conceived and funded as a smoking cessation/prevention pilot project for culturally diverse high-risk young populations that include school drop-outs, economically disadvantaged, and underserved. Using modern technologies, the Departments of Behavioral Science and Thoracic/Head & Neck Medical Oncology have joined their efforts to conduct this developmental project under the leadership of Dr. Alexander V. Prokhorov. The project will assist in making major advances in lung cancer education and prevention among youth. Project TALK will produce a CD-ROM-based education/behavior change for teenagers and young adults (15-24 years of age).

We have thus been devoting our effort in 4 tasks as described in the Statement of Work based on the project timeline:

Task 1. **Develop intervention program.** Focus groups will be held with adolescents and young adults to ensure we are capturing the essence of the program, using the right messages, and employing the appealing video and animated characters. (Years 1-2)

Task 2. **Develop and beta-test CD-ROM.** This includes the design of the animation, illustrations, scripts and accompanying videos. (Years 1-2)

Task 3.   Implement program in agreed upon locations and recruit young adults to participate in the study. (Years 3-4)

Task 4.   Collect and analyze data. (Years 3-4)

Summary of Research Findings

Participant Recruitment
A total of 239 high-risk alternative school students were recruited from the Houston area. Mean age of the participants was 16.2 years (SD=1.0), 79% were male. Thirty-six percent were Hispanic and 49% were African-American. Sixty-eight percent were in high school and 32% in middle school. The majority (70%) were not employed and 30% were employed part-time or full-time. Approximately 25% were current smokers and 29% former smokers.

The recruitment process at Fifth Ward Enrichment Center was assisted by the program's Executive Director; a school counselor at M.R. Wood assisted in recruiting the participants for the study. At M.R. Wood, the students were notified of the project by the school counselor and incoming students were given orientation packages that included the informed consent to be completed and turned in to the teaching staff or counselor. Other students were recruited by Project TALK staff through informal interactions with students who had heard about the game and were interested in participating.

Description of Educational Videogame
The educational videogame, available in both CD-ROM and kiosk form, uses a hospital metaphor in which participants "travel" to different "rooms" to learn about the dangers of tobacco use. The game allows users to personalize the experience by indicating their age, gender, race/ethnicity, smoking status, level of addiction and readiness to quit. Depending on the user's smoking status, the user enters a "nonsmoker" or "smoker" educational track. Each track has a different set of hospital rooms to explore, from which users pick up necessary items required to "escape" from the hospital successfully. The various rooms educate users on the causes of lung cancer, role of smoking in lung cancer development and tobacco cessation/prevention.

Testing
The on-site program testing was completed in May 2008.

Survey
The evaluation instruments of the program have been designed and consist of a baseline survey, 7-day follow-up survey, and 6-month follow-up survey. Both the baseline survey and 7-day follow-up survey were used at the target sites. The 6-month follow-up survey was administered over the phone. Participants are then given the option to leave comments or suggestions with regard to their perception of the program and how it can be improved.

The 6-month follow-up survey contains all the same questions as the 7-day follow-up survey, but was conducted by phone rather than in person.

Seven Day Feasibility Analysis
The primary outcomes for the 7-day feasibility evaluations included: (1) Ease of use and enjoyment of various features of the game; (2) The quality of the interactive multi-media presentations and the environment and their ability to generate interest in smoking and lung cancer prevention; (3) Motivational appeal, educational value and behavior modification post-

completion of game; and (4) Post-completion knowledge of modules in the game. Comparisons of these outcomes by smoking status were done using analysis of variance, chi-square tests and nonparametric methods as appropriate.

Results

The 7-day feasibility survey was completed by 213 participants. The demographic profile of these participants was similar to the demographic profile of the 239 participants at baseline. Mean age of the 213 participants was 16.1 years (SD=1.0), 78% were male. Thirty-six percent were Hispanic and 51% were African-American. Over 50% reported playing the game two or more times. The top three highly rated rooms were surgery/operating theater, patient records and TV/theater rooms. Over 87% of participants reported ease of use with all aspects of the game and the majority of participants enjoyed most features in the game. After playing the game, 94% reported that the materials increased their knowledge about smoking effects and 77% reported that they were inspired never to start or to quit and 70% planned to share the game with family or friends. Post-completion knowledge of modules was assessed. The participants were tested on their knowledge about specific modules and the majority of participants reported that smoking and secondhand smoke is harmful to health, harmful to the unborn child and expensive. However, knowledge regarding nicotine addiction and the more severe consequences of smoking on mortality compared to other addictions was low.

Six-Month Feasibility Analysis

The 6-month survey has been completed by 146 participants. All participants played the game at least once and 40% played twice or more times. Over 85% of participants reported ease of use of this educational tool and the majority of participants enjoyed the experience. After playing the game, 94% reported increased knowledge about the tobacco effects, 82% were inspired never to start or to quit, and 82% planned to share the game with family or friends.

Mediating Variables of Smoking at 6 month Follow-up

The primary outcomes of interest in this study were the mediating determinants of smoking initiation and cessation including the pros and cons of tobacco use, decisional balance and temptations to smoke. These outcomes were analyzed using mixed model regression with time and baseline smoking status and their interaction as fixed effects. There was a significant interaction effect for cons of smoking (F = 5.3; p<.05), decisional balance (F = 8.0; p<.01), and temptations to smoke (F = 7.6; p<.01). For baseline smokers, 6-month temptations to smoke were significantly lower than baseline, and 6-month cons of smoking were significantly higher than baseline. For nonsmokers, these variables did not change significantly.

Smoking Initiation and Cessation

Overall rates of self-reported smoking cessation and initiation at 6-month follow-up were not verified by cotinine or CO validation. Out of 146 participants who responded at 6 months, 34 were baseline smokers (23%) and 112 were non-smokers (77%). At 6 months, 18 (53%) out of 34 baseline smokers reported that they were abstinent and 7 (6%) out of 112 baseline non-smokers reported that they had initiated smoking. When stratified by gender and ethnicity, the results showed that more males and Hispanics quit smoking compared to females and non-Hispanics, although the results were not statistically significant due to small numbers. Those who quit also had significantly lower scores on the pros of smoking, decisional balance, and temptations to smoke compared to those who remained smokers (p<.05).

Key Research Accomplishments

- Performed testing at two sites with a total of 239 participants.

- Completed 7 day follow-up survey with a total of 213 participants.
- Completed 6 month follow-up survey with a total of 146 participants.

Conclusions

Project TALK was successfully developed according to the timeline. It produced an innovative, highly informative, and easy to navigate videogame that was enthusiastically accepted by young individuals at high risk of initiating tobacco use. More than half the smokers who participated had quit smoking at the 6-month follow-up. Overall, results have shown an increased level of awareness regarding the dangers of smoking across the participants enrolled. We aim to place our informational materials in other strategic areas across the community to duplicate results seen in this project.

Career Developmental Project (CDP1): Identification of Membrane Proteins in Bronchial Epithelia Cells as Biomarkers of Early Detection for Lung Cancer

(PI: Shin-Myung Kang, M.D.)

Lung cancer is the leading cause of cancer deaths. Early detection of the malignant lesion leads to an improved 5-year survival rate after surgical resection. Therefore, advanced screening tools are needed urgently to detect lung cancer at an early stage to improve control of such deadly lung cancer.

Aim 1   To isolate membrane proteins uniquely expressed on the surface of squamous metaplasia using organotypically cultured bronchial epithelial cells.

Summary of Research Findings

Membrane proteins were isolated from *in vitro* models of squamous metaplastic bronchial epithelial cells and compared with that of normal mucocilliary bronchial epithelial cells by 2-dimensional polyacrylamide gel electrophoresis. Normal human tracheobronchial epithelial (NHTBE) cells from passage 3 originated from samples collected from smokers and non-smokers; samples were cultured with or without retinoic acid for the formation of in vitro model of squamous metaplasia by air-liquid interface method. Cells were harvested at 12 days after air-liquid formation. Non-small-cell lung cancer cell lines (H226, H2170) were grown on plastic plate in RPMI 1640 containing 10% fetal bovine serum. H226 and H2170 cells were harvested at 80% confluence. Membrane proteins were extracted using ReadyPrep™ Protein Extraction Kit (Membrane I) (Bio-Rad) according to the manufacturer's instruction. To analyze the differentially expressed proteins, 20 µg of membrane protein extracted was subjected to two-dimensional PAGE analysis. The samples were loaded onto 7-cm immobilized pH gradient strips (pH 3-10, nonlinear), which were passively rehydrated for 15 hours. Isoelectric focusing was conducted using a Protein isoelectric focusing cell system for 40,000V/h. After equilibration process, the strips were applied to 10% nongradient SDS-PAGE gel, and the gels were stained using Silver Stain Plus kit (Bio-Rad).

NHTBE	Metaplasia	NSCLC; Sq

Figure 1: 2-D PAGE using membrane proteins from normal human tracheobronchial epithelial (NHTBE) cells, *in vitro* model of squamous metaplasia, and squamous cell carcinomas of lung (H226, H2170). Isoelectric point: 3 - 10 (from left to right)

left upper: NHTBE from smoker
left lower: NHTBE from non-smoker
center upper: squamous metaplasia from smoker
center lower: squamous metaplasia from non-smoker
right upper: H226 (squamous cell carcinoma of lung)
right lower: H2170 (squamous cell carcinoma of lung)

NHTBE	Metaplasia

Figure 2: Highly expressed membrane proteins in squamous metaplasia (arrow) compared to NHTBE cells.

Metaplasia from non-smoker	Metaplasia from smoker

Figure 3: Highly expressed membrane proteins of squamous metaplasia were reproducibly detected in other sample sets.

We compared the expression pattern of membrane proteins of NHTBE cells and squamous metaplasia originating from smokers or non-smokers. There was no significant difference in membrane protein expression on 2-DE between smokers and non-smokers (Fig. 1). We then compared the expression pattern of membrane proteins of NHTBE cells to those of the squamous metaplasia resulting in similar pattern displays. However, some spots had higher expression patterns squamous metaplasia compared to NHTBE cells (Fig. 2). Highly expressed, membrane proteins of squamous metaplasia were reproducibly detected in other sample sets (Fig. 3). Last, we compared expression pattern of membrane proteins of NHTBE cells to those of non-small-cell lung cancer cell lines (H226, H2170; squamous cell carcinoma). Membrane proteins from squamous cell carcinomas displayed very different pattern of expression compared to those from NHTBE cells.

Aim 2   To identify differentially represented proteins using proteomics.

Summary of Research Findings

Using HPLC-tandem Mass Spectrometer in collaboration with the Proteomics Core facility in our institute, we sequenced and determined the specific identity of the proteins isolated in Aim 1. After being excised, the silver-stained spots were destained and digested in gel with 200 ng of modified trypsin (Promega). The resulting peptides were analyzed by nano-liquid chromatography-tandem mass spectrometry with on-line desalting with a Famos autosampler, an Ultimate nano-LC module, and a Switchos precolumn switching device (LC Packings/Dionex).
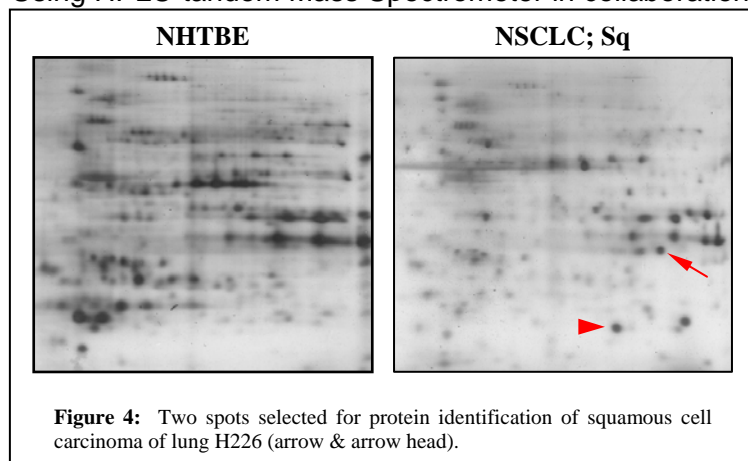
NHTBE	NSCLC; Sq

Figure 4: Two spots selected for protein identification of squamous cell carcinoma of lung H226 (arrow & arrow head).

60

Electrospray ion-trap mass spectrometry was done using an LTQ linear ion-trap mass spectrometer (Thermo). The fragment spectra were analyzed using the National Center for Biotechnology Information nonredundant protein database and the Mascot search engine (Matrix Science).

We decided to compare membrane protein expression of NHTBE cells to that of squamous cell carcinoma (H226). We selected two spots (Fig. 4) which were expressed exclusively in squamous cell carcinoma of lung on 2-DE gel, and we identified these spots (Table 1 and 2). As shown, we did not find any membrane proteins that matched the molecular weight and isoelectric point to the spots. Thus, we are now repeating the identification process by mass spectrometry using the same membrane proteins trypsin-digested. In addition, we are preparing another set of membrane proteins from the NHTBE cells, squamous metaplasia, H226, and H2170 to verify the reproducibility of the expression pattern on 2-DE gel. To minimize the keratin contamination, the pre-cast gradient gels will be used in following experiments.

Protein	Accession no.	pl	M_r (kDa)	Mascot score
Keratin 1	AAG41947	8.16	66.1	609
Unnamed protein product	CAA32649	5.17	59.5	577
Keratin, type II cytoskeletal 2 epidermal (cytokeratin-2e)	P35908	8.07	65.9	265
Electron transfer falvoprotein, alpha polypeptide isoform b	NP_001121188	8.75	30.0	91
Keratin 9	CAA52924	5.14	62.0	81

Table 1. Identified proteins from the upper spot in 2-DE gel of H226 (arrow)

Protein	Accession no.	pl	M_r (kDa)	Mascot score
Unnamed protein product	CAA32649	5.17	59.5	916
Keratin, type II cytoskeletal 2 epidermal (cytokeratin-2e)	P35908	8.07	65.9	911
Keratin, type II cytoskeletal 1	P04264	8.16	66.0	853
Keratin 9	CAA52924	5.14	62.0	455
Chain A, human serum albumin in a complex with myristic acid and tri-iodobenzoic acid	1BKE_A	5.69	66.0	444
Keratin 6A	NP_005545 NP_490596	8.09	60.0	441
Protein	Accession no.	pl	M_r (kDa)	Mascot score
Keratin type II	AAC41769	8.09	60.2	438
Unnamed protein product	BAG64893	5.79	58.9	428
Keratin 5	AAH24292	7.58	62.4	426
Keratin	AAB59562	5.09	51.7	418
Haptoglobin Hp2	1006264A	6.23	41.7	391
Keratin 17	NP_000413	4.97	48.1	251
Complement component 3, isoform CRA-a	EAW69070	8.24	143.7	224
Keratin 1b	CAD91892	5.73	61.8	219
Serpin peptidase inhibitor, class A (alpha-1 antiproteinase, antitrypsin), member 1	AAH15642	5.37	46.7	188
Alpha-fibrinogen precursor	AAA52426	8.27	69.8	144
Fibrinogen gamma chain	AAB59531	5.61	49.5	132
Keratin 19	BAA94608	4.93	11.8	130
Beta-fibrinogen precursor	AAA52429	8.31	54.9	102
Unnamed protein product	BAC05019	8.32	51.6	88
Alpha-2-macroglobulin precursor (alpha-2-M)	P01023	6.00	163.3	85
Transferrin	NP_001054	6.81	77.0	80
Ig kappa chain C rgion (allotype Inv(1,2))	A37927	5.60	11.0	70
G protein-coupled receptor kinase interactor 1 variant	BAD92774	6.63	85.9	45
hCG2020995	EAX01464	6.87	12.4	45

Table 2. Identified proteins from the lower spot in 2-DE gel of H226 (arrow head)

Aim 3   To verify the differentially represented proteins using PCR, Western blotting, and immunocytochemistry.

Summary of Research Findings

Work on this Aim is dependant upon further verification of the results gained in Aim 2 on the differentially expressed membrane proteins. Confirmation will be obtained by real-time PCR, Western blotting analysis, and immunohistochemical staining of the putative biomarkers on lung cancer specimens in tissue microarrays in collaboration with the Pathology Core.

Key Research Accomplishments

- Demonstrated that membrane proteins from squamous cell carcinomas displayed very different pattern of expression compared to those from NHTBE cells.
- Sequenced and determined the specific identity of the proteins isolated from NHTBE and squamous cell carcinomas.

Conclusions

Comparisons of NHTBE cells and squamous metaplasias from smokers and non-smokers have shown that squamous metaplasias display a unique pattern of expression compared to other cell sets in our project. We have sequenced and identified the specific identity of the proteins isolated in Aim 1. Further tests were run with different cell lines to duplicate and confirm these results, but we could not find any specific membrane points that were identified in the earlier studies. Thus, we are now repeating the identification process by mass spectrometry using the same membrane proteins trypsin-digested. In addition, we are preparing another set of membrane proteins from the NHTBE cells, squamous metaplasia, H226, and H2170 to verify the reproducibility of the expression pattern on 2-DE gel. To minimize the keratin contamination, the pre-cast gradient gels will be used in following experiments. We hope that future results will further indicate that unique membrane proteins can be used as biomarkers of early detection for lung cancer.

KEY RESEARCH ACCOMPLISHMENTS

Project 1: Targeting epidermal growth factor receptor signaling to enhance response of lung cancer to therapeutic radiation.

- Entered 22 patients onto the erlotinib (Tarceva) plus radiotherapy for locally advanced NSCLC trial and completed evaluation of 12 of these patients.
- Discovered relationship between the epithelial-to-mesenchymal transition and radiosensitivity of NSCLC cells.
- Demonstrated that pretreatment with gefitinib exerts a radioprotection of H1299-CDH1 cells.
- Demonstrated that small molecule inhibitors of both c-Met and IGF-1R produce a significant radiosensitizing effect on NSCLC cells.
- Completed an assessment of the combination of erlotinib (Tarceva) and radiation in a NSCLC xenograft tumor model.

Project 2: Molecular imaging of EGFR expression and activity in targeted therapy of lung cancer

- Developed the fifth-generation of more water-soluble polyethylene glycol (PEG)-ylated 3-iodo-4-(phenylamino)quinazoline-6-acrylamide (IPQA) derivatives labeled with ^{18}F to simplify the translation of EGFR kinase imaging agents in the clinic in comparison with ^{124}I-JGAP5.
- Discovered [^{18}F]fluoro-hexa-PEG-IPQA has less hepato-biliary clearance and a longer plasma circulation half-time.
- Completed the evaluation of [^{18}F]fluoro-hexa-PEG-IPQA as a novel PET imaging tracer in six rhesus macaques.
- Initiated manufacturing the non-radio labeled (cold) fluoro-hexa-PEG-IPAQ and the precursor with Advanced Biomedical Compounds (ABX). The precursor (compound 9 from scheme 3) will be used to manufacture ^{18}F-fluoro hexa PEG-IPQA clinical dose for phase I study.
- Finalized the toxicology protocol for the proposed rodent study with Charles River Labs.
- Improved lab-scale radiosynthesis to meet cGMP manufacturing guidelines.
- Held a preliminary meeting with oncologists to discuss patient recruitment and study objectives for a future clinical trial.
- Presented study results at the 2008 World Molecular Imaging Congress.

Project 3: Targeted peptide-based systemic delivery of therapeutic and imaging agents to lung tumors

- Tested peptides, selected by homing to blood vessels in mouse models, as carriers to guide the delivery of cytotoxic drugs, pro-apoptotic peptides, metalloprotease inhibitors, cytokines, fluorophores, and genes.
- Identified vascular receptors that correspond to the selected peptides found in blood vessels of normal organs and tumors.
- Received "safe to proceed" status by the FDA on our BMTP-11 based IND. Human clinical trials will be activated by March 2009.
- Filed a second IND with the FDA to focus on BMTP78.

- Generated stable and biologically active networks of direct-assembled Au-phage scaffolds, in which we can tune the chemical and physical properties of these biological structures.
- Identified vascular markers targeted by circulating ligands to further our knowledge of complex cellular and molecular diversity of the human vasculature.

Project 4: Inhibition of bFGF Signaling for Lung Cancer Therapy

- Suppressed the growth of lung tumor cells by repressing FGFR activation with the FGF receptor inhibitor MTA.
- Demonstrated that dominant negative FGF receptor adenoviral expression vector inhibits the growth of lung cancer cell lines by inducing apoptosis.
- Concluded that bFGF, FGFR1, and FGFR2 are highly expressed in most NSCLC tumors.

Project 5: Targeting mTOR and Ras signaling pathways for lung cancer therapy

- Indicated that RAD001 increases eIF4E phosphorylation *in vivo* in lung xenografts.
- Demonstrated that mTOR inhibition induced activations of the MEK/ERK signaling pathway in some cancer cell lines after a prolonged treatment.
- Observed co-targeting of mTOR and PI3K/Akt signaling exerts enhanced anticancer activity in lung cancer xenograft models. mTOR inhibitors increase eIF4E phosphorylation in lung cancer xenografts.
- Modulation of eIF4E phosphorylation may serve as a predictive biomarker for RAD001/erlotinib-based cancer therapy.
- Accrued 8 patients on the clinical trial.

Project 6: Identification and Evaluation of Molecular Markers in Non-Small Cell Lung Cancer (NSCLC)

- Identified shared regions of LOH and allelic imbalance through DNA profiling of HNSCC and NSCLC on matched T/N and T samples.
- Demonstrated that several candidate tumor suppressor genes in these regions are subject to epigenetic silencing by gene-specific hypermethylation in both HNSCC and NSCLC.
- Confirmed *TCF21* promoter hypermethylation and TCF21 expression as good biomarkers of both early lung and head and neck cancer.
- Observed that early passages of heterotransplant tumors contain infiltrating inflammation cells that disappear in later passages of the tumors.

Core B: Biostatistics & Data Management Core

- Continued to provide statistical support in the clinical trials for Project 1 and DRP-1.
- Provided statistical support for Projects 2, 3, 4, 6, and Pathology Core.
- Continued to work closely with the Project 4 PI (Dr. Reuben Lotan) on synergy studies of combination drug treatment in cell lines to determine whether the effect is synergistic, additive, or antagonistic.
- Developed a flexible semi-parametric model and codes which allow fitting very general interaction patterns for the drug combinations.

- Developed methods and provide codes to construct the confidence interval for the interaction index for the Emax model.
- Developed an additive hazards model with time-varying coefficients.
- Developed a new Bayesian cure rate model to estimate the cure rate and threshold.
- Developed a cure rate model with covariate measurement errors.
- Developed a Bayesian dose-finding trial design with multiple drugs.

Core C: Pathology Core

- Developed a large repository of lung cancer tissue, cytology and cell lines specimens with annotated clinical data, to be utilized for research projects.
- Developed a series of lung cancer heterotransplants in mice in collaboration with Project 6.
- Characterized the expression (VEGF/VEGFR, HIF-1α/CAIX, and bFGF/receptors) and molecular abnormalities (*VEGFA* and *VEGFR-2*) of angiogenic markers in NSCLC.
- Identified the sequence of *EGFR* abnormalities involved in the progression and metastasis of lung adenocarcinomas.
- Established the correlation between *EGFR* mutations and ER expression in lung adenocarcinomas.
- Characterized the abnormalities of *NKX2-1* (*TITF-1*) in NSCLC and its association with patients' outcome.
- Presented 4 abstracts at the 2008 AACR annual meeting with an additional abstract to presented at the 2009 annual meeting.

Core D: Imaging Core

- Produced novel ^{18}F-PEG6-IPQA derivative for PET imaging studies in small animals and non-human primates for Project 2.
- Maintained SOPs and performed QC/QA procedures for routine synthesis of ^{111}In-DTPA-PEG-AnnexinV for SPECT/CT imaging in Project I and performed imaging studies.
- Performed microPET/CT imaging (and autoradiography) studies in mice with orthotopic models of different NSCLC using ^{18}F-PEG6-IPQA in Project 2.
- Performed routine synthesis of [^{18}F]FEAU for Project 3 and conducted microPET imaging studies for this project.
- Performed synthesis and ^{64}Cu/^{111}In radiolabeling of novel cyclic nanopeptides for animal imaging studies in Project 3.
- Contracted the GLP studies on toxicology of F-PEG6-IPQA to Charles River Laboratories (MA).

DRP-1: Treatment of Malignant Pleural Effusion with ZD6474, a Novel VEGFR and EGFR TK Inhibitor

- Enrolled 17 out of 25 patients on the clinical trial.
- Collected specimens for correlative analyses on all patients (4 pleural fluid samples and 4 blood samples per patient).

DRP-2: TALK - Teens and Young Adults Acquiring Lung Cancer Knowledge

- Performed testing at two sites with a total of 239 participants.
- Completed 7 day follow-up survey with a total of 213 participants.

- Completed 6 month follow-up survey with a total of 146 participants.

CDP1: Identification of Membrane Proteins in Bronchial Epithelia Cells as Biomarkers of Early Detection for Lung Cancer

- Demonstrated that membrane proteins from squamous cell carcinomas displayed very different pattern of expression compared to those from NHTBE cells.
- Sequenced and determined the specific identity of the proteins isolated from NHTBE and squamous cell carcinomas.

REPORTABLE OUTCOMES

Publications *(attached in Appendix)***:**

Behrens C, Lin HY, Lee JJ, Raso MG, Hong WK, Wistuba II, Lotan R. Immunohistochemical expression of basic fibroblast growth factor and fibroblast growth factor receptors 1 and 2 in the pathogenesis of lung cancer. *Clinical Cancer Research.* 2008 Oct 1;14(19):6014-22. PMID: 18829480.

Cardó-Vila M, Zurita AJ, Giordano RJ, Sun J, Rangel R, Guzman-Rojas L, Anobom CD, Valente AP, Almeida FC, Lahdenranta J, Kolonin MG, Arap W, Pasqualini R. A ligand peptide motif selected from a cancer patient is a receptor-interacting site within human interleukin-11. *PLoS ONE.* 2008;3(10):e3452. PMID: 18941632.

Colella S, Richards KL, Bachinski LL, Baggerly KA, Tsavachidis S, Lang JC, Schuller DE, Krahe R. Molecular signatures of metastasis in head and neck cancer. *Head & Neck.* 2008 Oct;30(10):1273-83. PMID: 18642293.

Hajitou A, Lev DC, Hannay JA, Korchin B, Staquicini FI, Soghomonyan S, Alauddin MM, Benjamin RS, Pollock RE, Gelovani JG, Pasqualini R, Arap W. A preclinical model for predicting drug response in soft-tissue sarcoma with targeted AAVP molecular imaging. *Proceedings of the National Academy of Science U S A.* 2008 Mar 18;105(11):4471-6. PMID: 18337507.

Lee JJ, Kong M. Confidence Interval of Interaction Index for Assessing Multiple Drug Interaction. *Statistics in Biopharmaceutical Research.* 2009 Feb;1(1): 4-17.

Ma, Y. and Yin, G. Cure rate model with mismeasured covariates under transformation. *Journal of the American Statistical Association.* 2008 June;13(483), 743-756.

Nieto-Barajas, L. E. and Yin, G. Bayesian semiparametric cure rate model with an unknown threshold. *Scandinavian Journal of Statistics.* 2008;35(3), 540-556.

Ozawa MG, Zurita AJ, Dias-Neto E, Nunes DN, Sidman RL, Gelovani JG, Arap W, Pasqualini R. Beyond receptor expression levels: the relevance of target accessibility in ligand-directed pharmacodelivery systems. *Trends in Cardiovascular Medicine.* 2008 May;18(4):126-32. PMID: 18555185.

Pathak AK, Bhutani M, Saintigny P, Mao L. Heterotransplant mouse model cohorts of human malignancies: a novel platform for systematic preclinical efficacy evaluation of drugs (SPEED). *American Journal of Translational Research*. 2009 Jan; 1:19-25.

Staquicini FI, Tandle A, Libutti SK, Sun J, Zigler M, Bar-Eli M, Aliperti F, Pérez EC, Gershenwald JE, Mariano M, Pasqualini R, Arap W, Lopes JD. A subset of host B lymphocytes controls melanoma metastasis through a melanoma cell adhesion molecule/MUC18-dependent interaction: evidence from mice and humans. *Cancer Research*. 2008 Oct 15;68(20):8419-28. PMID: 18922915.

Tanaka T, Munshi A, Brooks C, Liu J, Hobbs ML, Meyn RE. Gefitinib radiosensitizes non-small cell lung cancer cells by suppressing cellular DNA repair capacity. *Clinical Cancer Research*. 2008 Feb 15;14(4):1266-73. PMID: 18281562.

Tang X, Varella-Garcia M, Xavier AC, Massarelli E, Ozburn N, Moran C, Wistuba II. EGFR Abnormalities in the Pathogenesis and Progression of Lung Adenocarcinomas. *Cancer Prevention Research*. 2008 Aug;1(3):192-200. PMID: 19138956.

Wang X, Hawk N, Yue P, Kauh J, Ramalingam SS, Fu H, Khuri FR, Sun S-Y. Overcoming mTOR inhibition-induced paradoxical activation of survival signaling pathways enhances mTOR inhibitors' anticancer efficacy. *Cancer Biology & Therapy*. 2008 Dec; 7:1952-8. PMID: 18981735.

Wang X, Yue P, Kim YA, Fu H, Khuri FR, Sun SY. Enhancing mammalian target of rapamycin (mTOR)-targeted cancer therapy by preventing mTOR/raptor inhibition-initiated, mTOR/rictor-independent Akt activation. *Cancer Research.* 2008 Sep 15;68(18):7409-18. PMID: 18794129.

Zhang S, Schafer-Hales K, Khuri FR, Zhou W, Vertino PM, Marcus AI. The tumor suppressor LKB1 regulates lung cancer cell polarity by mediating cdc42 recruitment and activity. *Cancer Research.* 2008 Feb 1;68(3):740-8. PMID: 18245474.

Manuscripts submitted, in revision, or in review

Kong M, Lee JJ. Applying Emax model and Bivariate Thin Plate Splines to Assess Drug Interactions. Revised for Frontiers in Biosciences, 2009.

Lee JJ, Lin HY, Liu DD, and Kong M. Applying Emax model and interaction index for assessing drug interaction in combination studies. Revised for Frontiers in Biosciences, 2009

Massarelli, E., Prudkin, M. L., Ozburn, N., Feng, L., Yin, G., Hong, W. K., O'Reilly, M., Herbst, R. S. and Wistuba, I. I. Correlation between VEGF/VEGFR2 and EGFR immunohistochemical protein expression in early stage non-small cell lung carcinoma. Submitted to ¿, 2009.

Raso MG, Behrens C, Liu S, Prudkin L, Ozburn NO, Woods DM, Tang T, Mehran RJ, Moran C, Lee JJ, and Wistuba I. Immunohistochemical expression of estrogen and progesterone receptors identifies a subset of non-small cell lung carcinomas and correlates with *EGFR* mutation. Submitted to *Clinical Cancer Research* (pending resubmission of the revised manuscript).

Richards KL, Zhang B, Baggerly KA, Colella S, Lang JC, Schuller DE, and Krahe R. Genome-wide hypomethylation in head and neck cancer is more pronounced in HPV-negative tumors and is associated with genomic instability. Submitted to *PLoS One.*

Sun S, Behrens C, Feng L, Ozburn N, Tang X, Yin G, Komaki R, Varella-Garcia M, Hong WK, Aldape KA, and Wistuba I. HER family receptor abnormalities in lung cancer brain metastases and corresponding primary tumors. Submitted to *Clinical Cancer Research* (pending resubmission of the revised manuscript).

Yin G, Lee JJ, Liu DD. Bayesian adaptive randomization using predictive probability. In preparation.

Abstracts *(attached in Appendix)***:**

Fan S, Wang X, Yue P, Kauh J, Ramalingam SS, Fu H, Khuri FR, Sun S-Y. Erlotinib enhances RAD001's anticancer activity *in vivo* involving abrogation of mTOR inhibition-induced eIF4E phosphorylation. AACR Annual Meeting. Denver, Colorado, April 2009.

Prokhorov A.V., Gritz E.R., Marani S. Using an educational videogame to tackle tobacco use among youth. Joint Society for Research on Nicotine & Tobacco and Society for Research on Nicotine & Tobacco-Europe Annual Meeting. Dublin, Ireland, April 2009.

Prudkin L, Liu D, Tchinda J, Woods D, Behrens C, Bekele BN, Moran C, Lee C, Aster JC, Zhou B-B, Wistuba II. NOTCH3/JAGGED1 pathway is involved in non-small cell lung cancer pathogenesis and interacts with EGFR pathway. AACR Annual Meeting. San Diego, California, April 2008.

Raso MG, Behrens C, Liu S, Prudkin L, Denise M. Woods, Natalie Ozburn, Cesar Moran, J. Jack Lee and Ignacio Wistuba. Immunohistochemical expression of estrogen and progesterone receptors identifies a subset of non-small cell lung cancers and correlates with EGFR mutations. AACR Annual Meeting. San Diego, California, April 2008.

Sun M, Massarelli E, Ozburn N, Tang X, Prudkin L, Komaki R, Hong WK, Aldape KD, Moran C, Varella-Garcia M, Wistuba II. *EGFR* increased copy number is frequent in non-small lung cancer with brain metastasis. AACR Annual Meeting. San Diego, California, April 2008.

Tang X, Liu D, Behrens C, He D, Sun M, Rice D, Lee JJ, Hong WK, Wistuba I. *TITF-1* and *EGFR* gene copy variations are associated with prognosis for the patients with non-small cell lung cancer. AACR Annual Meeting. Denver, Colorado, April 2009.

Tang X, Sun M, Behrens C, Prudkin L, Ozburn N, Gazdar AF, Moran C, Varella-Garcia M, Wistuba II. TTF-1 gene amplification and protein expression pattern identify adenocarcinoma of lung with worse prognosis. AACR Annual Meeting. San Diego, California, April 2008.

Tian M, Ogawa K, Yeh H.H., Balatoni J, Mykhopadhyay U, Pal A, Jackson J, Mawlawi O, Wendt R, Uthamanthil R, Borne A, Brammer D, Lepera C.G., Alauddin M, Gelovani J. Pharmacokinetics, Biodistribution, Metabolism, and Radiation Dosimetry of [18F]F-PEG6-IPQA in Non-Human Primates: A pre-IND Study. World Molecular Imaging Congress. Nice, France, September 2008.

Yuan Y, Liu J, Munshi A, Jensen KA, Roberts A, Meyn RE. The epithelial-to-mesenchymal transition (EMT) governs the radiation sensitivity of non-small cell lung cancer (NSCLC) cells. AACR Annual Meeting. Denver, Colorado, April 2009.

Yeh H.H., Ogawa K, Balatoni J, Mukhapadhyay U, Pal A, Yang D, Volgin A, Alauddin M, Gelovani J. Imaging the Expression-Activity and Mutational Status of EGFR in Four Different Non Small Cell Carcinoma Xenografts in Mice using PET with [18F]F-PEG6-IPQA. World Molecular Imaging Congress. Nice, France, September 2008.

Yeh H.H., Nishii R, Balatoni J, Pal A, Soghomonyan S, Flores L, Volgin A, Yang D, Gelovani J. PET with [124I]I-PEG6-IPQA for Imaging Expression-Activity and Mutational Status of EGFR in Four Different Non Small Cell Carcinoma Xenografts in Mice. World Molecular Imaging Congress. Nice, France, September 2008.

CONCLUSIONS

Project 1: We conclude that the epithelial-to-mesenchymal transition (EMT) plays a significant role in governing not just the intrinsic radiosensitivity of NSCLC cells, but also their sensitivity to inhibitors of the epidermal growth factor receptor (EGFR) and the ability of such inhibitors to radiosensitize these cells. It would be useful to assess the EMT status of patients treated with these combinations. In spite of this finding, results suggest that such combinations might be useful in the clinic. In addition, we conclude that targeting other growth factor receptors such as the c-Met and IG-F1R receptors may be an alternative strategy to using EGFR inhibitors.

Project 2: The development of $[^{18}F]$fluoro-hexa-PEG-IPQA into a clinical trial has been actively pursued with clearly defined milestones and timelines. Studies will focus on determining the optimum dosimetry of $[^{18}F]$fluoro-hexa-PEG-IPQA injection based on critical organ safety and detection sensitivity. Data will be obtained on agent distribution, pharmacokientics, radiation dosimetry, and metabolites to build upon our current knowledge base and to shape future studies. We have initiated all fronts of the IND development work to expedite the translational process.

Project 3: We propose that the EphA5 receptor expressed on the surface of lung cancer cells controls cells proliferation and survival by activating the MAP kinase signaling. We showed that our EphA5-targeted peptides inhibit phosphorylation of ERK1/2 and JNK. These effects would potentially result in inhibition of lung cancer cell proliferation and induction of apoptosis.   Future studies will allow us to use shRNA to inhibit the expression of EphA5 in lung cancer cells and to analyze cell proliferation and survival in vitro and in vivo. We will over-express EphA5 receptor in normal cells and analyze whether the expression of the receptor will cause cell transformation in vitro and in vivo. We will also treat lung cancer tumor-bearing mice with both systemic injection and nasal inhalation of peptide. These will follow optimization studies for peptide stability, the use of liposome as carriers, and a dose-escalation experiment.

Project 4: During the period of performance, we have shown that MTA, as an effective FGFR inhibitor, is a potent cell growth suppressor and apoptosis inducer, and should be further evaluated in preclinical setting for anti tumor effects. Our research data demonstrated that MTA inhibited the growth of the lung tumorigenic cell line 1170-I in a dose-dependent fashion with 50% inhibition that was achieved in our lab. These findings led us to study adenoviral vectors harboring dominant negative FGFR1 as potential candidates for preclinical *in vivo* studies with aerosolized viral formulation. Studies on the mechanism by which DNFGFR1 acts to inhibit the growth and induce apoptosis in lung tumor cells are ongoing. Our preliminary results indicate that DNFGFR1 increases the cell cycle inhibitors p21 and p27 and decreases the cell cycle regulators cdc25 and Chk1. We look to complete these studies during the next project period to confirm that the bFGF signaling pathway activation may be an early indicator of SCC pathogenesis and a novel target for lung cancer chemopreventive and therapeutic strategies.

Project 5: Targeting the mTOR axis appears to be a promising strategy against lung cancer. Given the nature of the complexity of lung cancer signaling pathways, including mTOR signaling, it is essential to understand the biology of lung cancer and the mechanism of action for the therapeutics of interest in order to efficiently treat lung cancer through application of mechanism-driven therapeutic regimens. Thus, we have demonstrated the scientific rationale for our effort in pursuing mTOR-targeted lung cancer therapy.

Project 6: We performed RNA and DNA profiling on available samples to identify genes and genomic regions that are altered in NSCLC and interrogated additional candidate methylatable

genes as potential tumor suppressor genes in NSCLC, to identify their potential as biomarkers. These experiments have generated a list of molecular candidate biomarkers for further investigation in larger sample sets.

Biostatistics Core: Core B continued to provide statistical analysis and data management support for all research projects in the IMPACT study. We will assist the other Projects with their ongoing needs to complete the proposed studies.

Pathology Core: The Pathology Core has assisted and collaborated actively with several research projects to perform multiple histopathological, immunohistochemical, and genetic studies in a large series of lung cancer tissue (archival and prospectively collected in the IMPACT clinical trials) specimens. In addition, the Pathology Core has managed to conduct specific research activities, which fully integrate with some of the IMPACT research projects. Due to the direct contribution of the Pathology Core, four abstracts have been presented and one has been accepted for presentation at international meetings, two papers have been published, and two manuscripts are in resubmission process. The Pathology Core has successfully fulfilled the goals proposed for the third year of IMPACT project.

Imaging Core: The Imaging Core continues to provide highly specialized imaging support as requested by the project leaders of IMPACT for their designated research projects.

DRP-1: The trial is enrolling patients; all analyses will be performed after the trial is completed.

DRP-2: Project TALK was successfully developed according to the timeline. It produced an innovative, highly informative, and easy to navigate videogame that was enthusiastically accepted by young individuals at high risk of initiating tobacco use. More than half the smokers who participated had quit smoking at the 6-month follow-up. Overall, results have shown an increased level of awareness regarding the dangers of smoking across the participants enrolled. We aim to place our informational materials in other strategic areas across the community to duplicate results seen in this project.

CDP1: Comparisons of NHTBE cells and squamous metaplasias from smokers and non-smokers have shown that squamous metaplasias display a unique pattern of expression compared to other cell sets in our project. We have sequenced and identified the specific identity of the proteins isolated in Aim 1. Further tests were run with different cell lines to duplicate and confirm these results, but we could not find any specific membrane points that were identified in the earlier studies. Thus, we are now repeating the identification process by mass spectrometry using the same membrane proteins trypsin-digested. In addition, we are preparing another set of membrane proteins from the NHTBE cells, squamous metaplasia, H226, and H2170 to verify the reproducibility of the expression pattern on 2-DE gel. To minimize the keratin contamination, the pre-cast gradient gels will be used in following experiments. We hope that future results will further indicate that unique membrane proteins can be used as biomarkers of early detection for lung cancer.

REFERENCES

Maher, PA. Inhibition of the tyrosine kinase activity of the fibroblast growth factor receptor by the methyltransferase inhibitor 5'-methylthioadenosine. *Journal of Biological Chemistry*. 1993 Feb 25;268(6):4244-9

Pintucci G, Quarto N, Rifkin DB. Methylation of high molecular weight fibroblast growth factor-2 determines post-translational increases in molecular weight and affects its intracellular distribution. *Molecular Biology of the Cell.* 1996 Aug;7(8):1249-58.

Appendix

Confidence Intervals of Interaction Index for Assessing Multiple Drug Interaction

J. JACK LEE and MAIYING KONG

Studies of interactions among biologically active agents have become increasingly important in many branches of biomedical research. We consider that the Loewe additivity model is one of the best general reference models for defining drug interactions. Based on the Loewe additivity model, synergy occurs when the interaction index is less than one, and antagonism occurs when interaction index is greater than one. Starting from the Loewe additivity model and the marginal dose–effect curve for each drug involved in a combination, we first present a procedure to estimate the interaction index and its associated confidence interval at a combination dose with observed effects. Following Chou and Talalay's method for assessing drug interaction based on the plot of interaction indices versus effects for combination doses at a fixed ray, we then construct a pointwise $(1-\alpha) \times 100\%$ confidence bound for the curve of interaction indices versus effects. We found that these methods work better on the logarithm transformed scale than on the untransformed scale of the interaction index. We provide simulations and case studies to illustrate the performances of these two procedures, and present their pros and cons. We also provide S-Plus/R code to facilitate the implementation of these two procedures.

Key Words: Antagonism; Loewe additivity model; Synergy.

1. Introduction

Studies of interactions among biologically active agents, such as drugs, carcinogens, or environmental pollutants, have become increasingly important in many branches of biomedical research. Our research group re-viewed the literature (Lee, Kong, Ayers, and Lotan 2007) and agree with many researchers (e.g., Berenbaum 1985, 1989; Greco, Bravo, and Parsons 1995) that the Loewe additivity model should be considered as the "gold standard" for defining drug interactions

For a combination of k drugs ($k \geq 2$) at $(d_1, \ldots, d_k)$, based on the Loewe additivity model, drug interactions at this combination can be characterized as

$$\frac{d_1}{D_{y,1}} + \cdots + \frac{d_k}{D_{y,k}} \begin{cases} < 1, & \text{synergy;} \\ = 1, & \text{additivity;} \\ > 1, & \text{antagonism.} \end{cases} \quad (1)$$

Here $d_1, \ldots, d_k$ are doses of each drug in the mixture of the k drugs resulting in effect y, and $D_{y,1}, \ldots, D_{y,k}$ are the doses of drugs that result in the effect y for each respective drug given alone. The summation, $\frac{d_1}{D_{y,1}} + \cdots + \frac{d_k}{D_{y,k}}$, is called the interaction index, which is denoted as τ. Based on the Loewe additivity model, the combination dose $(d_1, \ldots, d_k)$ is said to be synergistic if the interaction index is less than the constant number of 1, and additive or antagonistic if the index is equal to or greater than 1, respectively. To give an intuitive idea about the interaction index, we illustrate its meaning in the special case of $k = 2$. Note that the combination dose (d_1, d_2) produces the same effect y as drug 1 alone at dose level $D_{y,1}$, and drug 2 alone at dose level $D_{y,2}$, which implies that 1 unit of drug 2 will produce the same effect as $\frac{D_{y,1}}{D_{y,2}}$ units of drug 1. Thus, the amount of dose at the combination (d_1, d_2) equals to $d_1 + d_2 \frac{D_{y,1}}{D_{y,2}}$

in terms of drug 1 dose. By definition, $\tau = \frac{d_1}{D_{y,1}} + \frac{d_2}{D_{y,2}}$, which implies that $d_1 + d_2 \frac{D_{y,1}}{D_{y,2}} = \tau D_{y,1}$. $\tau < 1$ implies $d_1 + d_2 \frac{D_{y,1}}{D_{y,2}} = \tau D_{y,1} < D_{y,1}$, therefore, the amount of the combination dose (d_1, d_2) to produce the same effect y is less than the amount of dose when single drug is applied, hence, indicating synergy. The smaller τ is, the more is the reduction of the amount of dose in the combination, and the stronger is the synergy. Similarly, $\tau > 1$ implies that $d_1 + d_2 \frac{D_{y,1}}{D_{y,2}} = \tau D_{y,1} > D_{y,1}$, that is, the amount of the combination dose (d_1, d_2) producing the same effect y is more than each single drug dose, hence indicating antagonism. The geometric interpretation of the interaction index can be best shown graphically in Figure 1, panels (A) and (B), where $P = (D_{y,1}, 0)$, $Q = (0, D_{y,2})$, $U = (d_1, d_2)$, all yield the same effect y. If we draw a line $\overline{RS}$ passing through U and parallel to the line $\overline{PQ}$, and draw a line $\overline{OU}$ intercepting with $\overline{PQ}$ at V, then, from the basic geometric properties, the interaction index can be expressed as the ratio of $\frac{\text{length}(\overline{OU})}{\text{length}(\overline{OV})}$. In Figure 1(A), the closer the point U is toward the origin, the less is the amount of combination dose required to produce the same effect as drug 1 alone at $D_{y,1}$ or drug 2 alone at $D_{y,2}$, hence, the stronger is the synergy. By the same token in Figure 1(B), the further the point U is away from the origin, the larger is the amount of combination dose required to produce the same effect as drug 1 alone at $D_{y,1}$ or drug 2 alone at $D_{y,2}$, hence, the stronger is the antagonism. From Figure 1, we conclude that the interaction index can be used to measure the mode and magnitude of drug interactions.

Given the combination dose $(d_1, \ldots, d_k)$ and its effect y, and the marginal dose–effect curves $f_i(D_i)$ for drug i ($i = 1, \ldots, k$), the calculation of the interaction index at a combination dose $(d_1, \ldots, d_k)$ is straightforward. One simply replaces $D_{y,i}$ by $f_i^{-1}(y)$, where f_i^{-1} is the inverse function of f_i ($i = 1, \ldots, k$). However, since the dose–effect curves are usually estimated and the effect y is observed with error, to make valid inferences for drug interactions, one needs to account for all these variabilities. In other words, one needs to consider the estimated interaction indices along with their variances to make valid statistical inferences on drug interaction.

In most settings, the functional form of the marginal dose response curves may not be known and need to be estimated from the data. Chou and Talalay (1984) proposed the median-effect equation which has been widely used to model the dose–effect curve with good success (Chou 2006). In our cell line study (Kong and Lee 2006; Lee et al. 2007), we also find that the median-effect equa-

tion fits the data well. Chou and Talalay's median-effect equation has the following form

$$E = \frac{\left(\dfrac{d}{D_m}\right)^m}{1 + \left(\dfrac{d}{D_m}\right)^m}, \qquad (2)$$

where d is the dose of a drug eliciting effect E, D_m is the median effective dose of a drug, and m is a slope parameter depicting the shape of the curve. When m is negative, the curve described by Equation (2) falls with increasing drug concentration; when m is positive, the curve rises with increasing drug concentration. The median-effect Equation (2) is independent of the drug's mechanisms of action and does not require knowledge of conventional kinetic constants (Chou 2006; Greco et al. 1995). Under the assumption that the dose–effect curves follow Chou and Talalay's median-effect equation, in Section 3 we investigate the characteristics of the interaction index and its logarithmic transformation, and propose a procedure to construct the confidence interval for the estimated interaction index.

Although interaction index can be estimated at each combination dose separately, this approach is not efficient. The result tends to be more varying as it depends on only measurement at a single combination dose level. To gain efficiency, one can assume a model and pool data at various combination doses to form a better estimate of the interaction index. One commonly used approach is applying the ray design. Chou and Talalay (1984) and Chou (1991) proposed a procedure to characterize a two-drug interaction by first fitting marginal dose–effect curves and a dose–effect curve for the combination doses with their components at a fixed ray (i.e., d_1/d_2=a constant, forming a ray in the $d_1 \times d_2$ dose plane), then assessing drug interaction based on the plot of their combination indices versus effects for combination doses at this fixed ray. The confidence intervals for the combination indices were constructed by Monte Carlo techniques (*CalcuSyn* at *http://www.biosoft.com/w/calcusyn.htm*; Belen'kii and Schinazi 1994; *CompuSyn* at *http://www.combosyn.com/*). The combination index has the same form as the interaction index when the combined drugs are mutually exclusive. However, Chou and Talalay's mutual exclusiveness and nonexclusiveness criteria are difficult to evaluate, and the combination index has been criticized by many researchers (Berenbaum 1989; Greco et al., 1995). In Section 3, by adopting the interaction index for Chou and Talalay's method, we extend their method to assess drug interactions among $k (\geq 2)$ drugs, and propose a procedure to construct a pointwise $(1 - \alpha) \times 100\%$ confidence bound for the
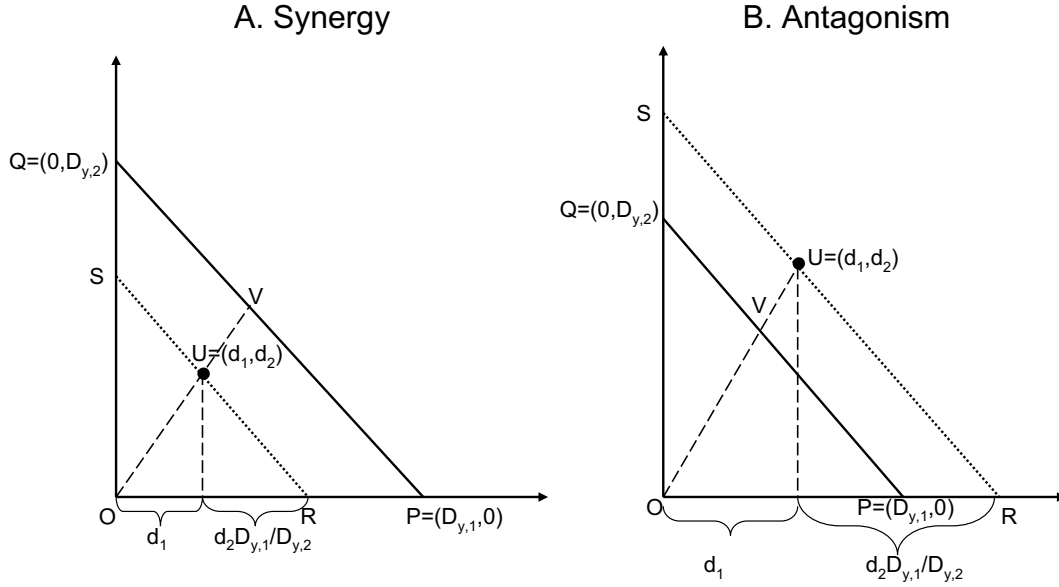
A. Synergy

B. Antagonism

Figure 1. Illustration of the interaction index. $P = (D_{y,1}, 0)$ represents the drug 1 dose producing effect y, $Q = (0, D_{y,2})$ represents the drug 2 dose producing effect y, and $U = (d_1, d_2)$ represents the combination dose producing the same effect y. $\overline{RS}$ is the line passing by U and parallel to $\overline{PQ}$, and V is the intercept of $\overline{OU}$ and $\overline{PQ}$. The interaction index can be expressed as the ratio of $\frac{\text{length}(\overline{OU})}{\text{length}(\overline{OV})}$. Panel A illustrates the case for synergy while Panel B for antagonism.

estimated curve of interaction indices versus effects by accounting for all the variabilities in estimating the dose–effect curves. In Section 4, we present the results from simulations and case studies to show that our proposed procedure performs at least as well as the Monte Carlo procedure in terms of covering the underlying curves and shortening the confidence bound, and performs better in terms of taking less time to compute. The last section is devoted to discussion.

2. Interaction Index and its Confidence Interval at a Combination Dose

In this section, we will present how to construct a confidence interval for interaction index at a combination dose $(d_1, \ldots, d_k)$ with an effect y. Here the dose–effect curve for drug i ($i = 1, \ldots, k$) is estimated from the marginal data with only ith drug being applied. Note that Chou and Talalay's median-effect equation (2) also can be rewritten as

$$\log \frac{E}{1 - E} = m(\log d - \log D_m) = \beta_0 + \beta_1 \log d, \quad (3)$$

where $\beta_0 = -m \log D_m$ and $\beta_1 = m$. The dose producing effect E can be written as either

$$d = D_m \left(\frac{E}{1 - E} \right)^{\frac{1}{m}}, \quad (4)$$

or

$$d = \exp\left(-\frac{\beta_0}{\beta_1} \right) \left(\frac{E}{1 - E} \right)^{\frac{1}{\beta_1}}. \quad (5)$$

Suppose model (3) has the form $\log \frac{E}{1-E} = \beta_0 + \beta_1 \log d + \epsilon$ with ϵ following $N(0, \sigma^2)$, then we may regress $\log \frac{E}{1-E}$ on $\log d$ to get the marginal dose–effect curve $\log \frac{E}{1-E} = \hat{\beta}_{0,i} + \hat{\beta}_{1,i} \log d$ for drug i with $i = 1, \ldots, k$. Meanwhile we may get the variances and covariances for the estimates $\hat{\beta}_{0,i}$ and $\hat{\beta}_{1,i}$ for $i = 1, \ldots, k$. If the observed mean effect at a combination dose $(d_1, \ldots, d_k)$ is y, then, based on (5), the associated interaction index can be estimated by

$$\hat{\tau} = \sum_{i=1}^{k} \frac{d_i}{\hat{D}_{y,i}} = \sum_{i=1}^{k} \frac{d_i}{\exp(-\frac{\hat{\beta}_{0,i}}{\hat{\beta}_{1,i}}) \left(\frac{y}{1-y} \right)^{\frac{1}{\hat{\beta}_{1,i}}}}. \quad (6)$$

The simulations in Section 4 indicate that the distribution of $\log(\hat{\tau})$ is approximately normal, while $\hat{\tau}$ deviates from

a normal distribution for large σ's. Thus, we should apply the delta method (Bickel and Doksum 2001) to $\log \tau$ instead of τ, then we take the exponential transformation to get the confidence interval for τ. By applying delta method to $\log(\hat{\tau})$, we get

$$\text{var}(\log(\hat{\tau}))$$
$$\simeq \frac{1}{\hat{\tau}^2}\text{var}(\hat{\tau})$$
$$\simeq \frac{1}{\hat{\tau}^2}\left(\frac{\partial \hat{\tau}}{\partial \hat{\beta}_{0,1}}, \frac{\partial \hat{\tau}}{\partial \hat{\beta}_{1,1}}, \ldots, \frac{\partial \hat{\tau}}{\partial \hat{\beta}_{0,k}}, \frac{\partial \hat{\tau}}{\partial \hat{\beta}_{1,k}}, \frac{\partial \hat{\tau}}{\partial y}\right)$$
$$\times \Sigma \left(\frac{\partial \hat{\tau}}{\partial \hat{\beta}_{0,1}}, \frac{\partial \hat{\tau}}{\partial \hat{\beta}_{1,1}}, \ldots, \frac{\partial \hat{\tau}}{\partial \hat{\beta}_{0,k}}, \frac{\partial \hat{\tau}}{\partial \hat{\beta}_{1,k}}, \frac{\partial \hat{\tau}}{\partial y}\right)^T ,(7)$$

where

$$\frac{\partial \hat{\tau}}{\partial \hat{\beta}_{0,i}} = \frac{d_i}{\hat{D}_{y,i}}\frac{1}{\hat{\beta}_{1,i}}, \quad \frac{\partial \hat{\tau}}{\partial \hat{\beta}_{1,i}} = \frac{d_i}{\hat{D}_{y,i}}\frac{\log \frac{y}{1-y} - \hat{\beta}_{0,i}}{\hat{\beta}_{1,i}^2}$$

for $i = 1, \ldots, k$, and

$$\frac{\partial \hat{\tau}}{\partial y} = -\frac{1}{y(1-y)}\left(\frac{1}{\hat{\beta}_{1,1}}\frac{d_1}{\hat{D}_{y,1}} + \cdots + \frac{1}{\hat{\beta}_{1,k}}\frac{d_k}{\hat{D}_{y,k}}\right),$$

Σ is the variance–covariance matrix of the $2k$ parameters $(\hat{\beta}_{0,1}, \hat{\beta}_{1,1}, \ldots, \hat{\beta}_{0,k}, \hat{\beta}_{1,k})$ and the observed mean effect y at $(d_1, \ldots, d_k)$. Any two pairs of parameters, $(\hat{\beta}_{0,i}, \hat{\beta}_{1,i})$ and $(\hat{\beta}_{0,j}, \hat{\beta}_{1,j})$ when $i \neq j$ are independent since typically, different experimental subjects was used for drug i alone and for drug j alone, respectively. Further, all those subjects are different from the subjects administrated the combination dose $(d_1, \ldots, d_k)$. Thus, the estimates $(\hat{\beta}_{0,i}, \hat{\beta}_{1,i})$ are independent of the estimates $(\hat{\beta}_{0,j}, \hat{\beta}_{1,j})$ when $i \neq j$, and all of them are independent of the observed mean effect y at $(d_1, \ldots, d_k)$. Therefore, Σ is a block diagonal matrix with the block being a 2×2 matrix except for the last diagonal element $\text{var}(y)$. An approximate variance of $\log(\hat{\tau})$ can be obtained by $\text{var}(\log(\hat{\tau})) \simeq \frac{1}{\hat{\tau}^2}\text{var}(\hat{\tau})$, where

$$\text{var}(\hat{\tau}) \simeq \sum_{i=1}^k \left(\frac{d_i}{\hat{D}_{y,i}}\right)^2$$
$$\times \left(\frac{\text{var}(\hat{\beta}_{0,i})}{\hat{\beta}_{1,i}^2} + \frac{2\text{cov}(\hat{\beta}_{0,i}, \hat{\beta}_{1,i})(\log \frac{y}{1-y} - \hat{\beta}_{0,i})}{\hat{\beta}_{1,i}^3}\right.$$
$$\left.+ \frac{\text{var}(\hat{\beta}_{1,i})(\log \frac{y}{1-y} - \hat{\beta}_{0,i})^2}{\hat{\beta}_{1,i}^4}\right)$$
$$+ \left(\frac{1}{\hat{\beta}_{1,1}}\frac{d_1}{\hat{D}_{y,1}} + \cdots + \frac{1}{\hat{\beta}_{1,k}}\frac{d_k}{\hat{D}_{y,k}}\right)^2$$
$$\times \left(\frac{1}{y(1-y)}\right)^2 \text{var}(y). \qquad (8)$$

We can estimate $\text{var}(y)$ in two ways. When there are replicates at the combination dose $(d_1, \ldots, d_k)$, $\text{var}(y)$ can simply be estimated by the sample variance at (d_1, d_2). Otherwise, we may borrow the information from estimating the marginal dose–effect curves. Note that $\text{var}(\log \frac{y}{1-y}) \simeq (\frac{1}{y(1-y)})^2\text{var}(y)$, thus, we may substitute $(\frac{1}{y(1-y)})^2\text{var}(y)$ by the average of the squared residuals obtained from fitting the median-effect Equation (3) for all drugs involved assuming a constant variance for both the single and combination drug effects. Once the variance is obtained, a $(1 - \alpha) \times 100\%$ confidence interval for $\log(\tau)$ can be formed as

$$\left[\log(\hat{\tau}) - t_{n-2k,\frac{\alpha}{2}}\sqrt{\text{var}(\log(\hat{\tau}))},\right.$$
$$\left.\log(\hat{\tau}) + t_{n-2k,\frac{\alpha}{2}}\sqrt{\text{var}(\log(\hat{\tau}))}\right],$$

where $t_{n-2k,\frac{\alpha}{2}}$ is the $1 - \frac{\alpha}{2}$ percentile of t-distribution with $n - 2k$ degree of freedom, and $n = \sum_{i=1}^k n_i$ with n_i $(i = 1, \ldots, k)$ being the number of observations when drug i is used alone. $2k$ is the total number of estimated parameters involved in estimating the interaction index (6). Thus, a $(1 - \alpha) \times 100\%$ confidence interval for τ can be constructed as:

$$\left[\hat{\tau}\exp\left(-t_{n-2k,\frac{\alpha}{2}}\sqrt{\text{var}(\log(\hat{\tau}))}\right),\right.$$
$$\left.\hat{\tau}\exp\left(t_{n-2k,\frac{\alpha}{2}}\sqrt{\text{var}(\log(\hat{\tau}))}\right)\right]. \quad (9)$$

When $\text{var}(\log(\hat{\tau}))$ is small, we have

$$\hat{\tau}\exp\left(\pm t_{n-2k,\frac{\alpha}{2}}\sqrt{\text{var}(\log(\hat{\tau}))}\right)$$
$$\simeq \hat{\tau}\exp\left(\pm\frac{t_{n-2k,\frac{\alpha}{2}}}{\hat{\tau}}\sqrt{\text{var}(\hat{\tau})}\right)$$
$$\simeq \hat{\tau} \pm t_{n-2k,\frac{\alpha}{2}}\sqrt{\text{var}(\hat{\tau})}.$$

Therefore, if the error in (3) is small, the confidence interval for τ based on (9) is essentially the same as the confidence interval constructed by directly applying the delta method to $\hat{\tau}$, which is

$$\left[\hat{\tau} - t_{n-2k,\frac{\alpha}{2}}\sqrt{\text{var}(\hat{\tau})}, \quad \hat{\tau} + t_{n-2k,\frac{\alpha}{2}}\sqrt{\text{var}(\hat{\tau})}\right]. \quad (10)$$

In Section 4, we illustrate that, for a large error in (3), the confidence interval (9) behaves better than (10) in two aspects: (i) the lower limit is greater than zero all the time; and (ii) the confidence interval has a coverage rate that is closer to the nominal rate. Therefore, the confidence interval (9) is preferred. When $n - 2k$ is large, say $n - 2k \geq 20$, one may use $z_{\frac{\alpha}{2}}$ instead of $t_{n-2k,\frac{\alpha}{2}}$ in estimating the confidence intervals (9) and (10), where $z_{\frac{\alpha}{2}}$ is the $1 - \frac{\alpha}{2}$ percentile of the standard normal distribution.

3. Interaction Indices and Their Confidence Bound at a Fixed Ray

3.1 Two-Drug Combination

Note that the confidence interval (9) is based on a single observation and the marginal dose–effect curves, and the estimated interaction index and its confidence interval are greatly influenced by this single observation. Chou and Talalay (1984) used a ray design to assess drug interactions. The advantage of their method is that it uses all observations with the component doses at a fixed ray. We adopt the interaction index instead of the combination index when using their approach. The basic idea (Chou 1991) is to regress $\log \frac{E}{1-E}$ on $\log D$ for each of the two drugs used alone and regress $\log \frac{E}{1-E}$ on $\log(d_1 + d_2)$ for the combination doses (d_1, d_2) with $\frac{d_2}{d_1} = \frac{\omega_2}{\omega_1}$, say, $\log \frac{E}{1-E} = \beta_{0,c} + \beta_{1,c} \log D_c$. Then for each fixed effect y, one may estimate the interaction index by

$$\hat{\tau}_{CT} = \frac{\hat{D}_{y,c} \frac{\omega_1}{\omega_1 + \omega_2}}{\hat{D}_{y,1}} + \frac{\hat{D}_{y,c} \frac{\omega_2}{\omega_1 + \omega_2}}{\hat{D}_{y,2}}, \quad (11)$$

where $\hat{D}_{y,1} = \exp(-\frac{\hat{\beta}_{0,1}}{\hat{\beta}_{1,1}}) \left(\frac{y}{1-y}\right)^{\frac{1}{\hat{\beta}_{1,1}}}$, $\hat{D}_{y,2} = \exp\left(-\frac{\hat{\beta}_{0,2}}{\hat{\beta}_{1,2}}\right) \left(\frac{y}{1-y}\right)^{\frac{1}{\hat{\beta}_{1,2}}}$, and $\hat{D}_{y,c} = \exp\left(-\frac{\hat{\beta}_{0,c}}{\hat{\beta}_{1,c}}\right)$ $\left(\frac{y}{1-y}\right)^{\frac{1}{\hat{\beta}_{1,c}}}$. Commercial software *CalcuSyn* and *CompuSyn* are available for estimating the interaction indices and their confidence intervals. The confidence intervals for interaction indices in (11) were constructed based on Monte Carlo techniques and the normal assumption on the parameters (Belen'kii and Schinazi 1994). Briefly, the parameters, $(\hat{\beta}_{0,i}, \hat{\beta}_{1,i})$ for $i = 1, 2, c$, and the interaction index (11) are estimated from the observed data, then certain number of random samples (say, 500) of the parameters, $(\hat{\hat{\beta}}_{0,i}, \hat{\hat{\beta}}_{1,i})_j$ for $j = 1, \ldots, 500$ and $i = 1, 2, c$, are generated based on their estimated values and covariances under the normal assumption on each pair of these parameters. Thus, 500 interaction indices, $\hat{\hat{\tau}}_{CT,j}$ ($j = 1, \ldots, 500$), can be calculated and its standard deviation can be estimated as $\hat{\sigma}_\tau^2 = \frac{1}{500} \sum_{j=1}^{500} (\hat{\hat{\tau}}_{CT,j} - \hat{\tau}_{CT})^2$. Consequently, the confidence interval can be constructed as $[\hat{\tau}_{CT} - z_{\frac{\alpha}{2}} \hat{\sigma}_\tau, \ \hat{\tau}_{CT} + z_{\frac{\alpha}{2}} \hat{\sigma}_\tau]$. In the simulation and case studies in Section 4, we used $t_{n_1+n_2+n_c-6, \frac{\alpha}{2}}$ instead of $z_{\frac{\alpha}{2}}$ since the number of observations is small.

In the following subsection, we extend Chou and Talalay's method to $k (\geq 2)$ drugs, estimate drug interaction at a fixed ray, say $d_1 : d_2 : \cdots : d_k = \omega_1 : \omega_2 : \cdots : \omega_k$, and construct a $(1-\alpha) \times 100\%$ confidence interval for the constructed interaction index at each effect y. Thus, by varying y, a pointwise confidence bound for the curve of

interaction indices versus effects with combination doses at the fixed ray can be constructed by using the delta method.

3.2 k-drug combination

Again, we assume that the fitted dose–effect curve is $\log \frac{E}{1-E} = \hat{\beta}_{0,i} + \hat{\beta}_{1,i} \log D_i + \epsilon$ for drug i with $i = 1, \ldots, k$. The fitted dose–effect curve for the mixture with their component doses at a fixed ray with $d_1 : d_2 : \cdots : d_k = \omega_1 : \omega_2 : \cdots : \omega_k$ is $\log \frac{E}{1-E} = \hat{\beta}_{0,c} + \hat{\beta}_{1,c} \log D_c + \epsilon$ with $D_c = d_1 + d_2 + \cdots + d_k$. Then, for each fixed effect y, one may estimate interaction index by

$$\hat{\tau}_{CT} = \frac{\hat{D}_{y,c} \frac{\omega_1}{\omega_1 + \ldots + \omega_k}}{\hat{D}_{y,1}} + \cdots + \frac{\hat{D}_{y,c} \frac{\omega_k}{\omega_1 + \ldots + \omega_k}}{\hat{D}_{y,k}}, \quad (12)$$

where $\hat{D}_{y,i} = \left(\frac{y}{1-y}\right)^{\frac{1}{\hat{\beta}_{1,i}}} \exp\left(-\frac{\hat{\beta}_{0,i}}{\hat{\beta}_{1,i}}\right)$ for $i = 1, \ldots, k, c$. Again, $(\hat{\beta}_{0,i}, \hat{\beta}_{1,i})$ and $(\hat{\beta}_{0,j}, \hat{\beta}_{1,j})$ are independent as long as $i \neq j$ for $i, j = 1, \ldots, k, c$. Based on the delta method (Bickel and Doksum 2001), we can obtain an approximate variance for $\hat{\tau}_{CT}$

$$\begin{aligned}
\text{var}(\hat{\tau}_{CT}) &= \sum_{i=1}^{k} \left(\frac{\partial \hat{\tau}_{CT}}{\partial \hat{D}_{y,i}}\right)^2 \text{var}(\hat{D}_{y,i}) \\
&\quad + \left(\frac{\partial \hat{\tau}_{CT}}{\partial \hat{D}_{y,c}}\right)^2 \text{var}(\hat{D}_{y,c}) \\
&= \sum_{i=1}^{k} \left(-\frac{\omega_i \hat{D}_{y,c}}{(\sum_{i=1}^{k} \omega_i)\hat{D}_{y,i}^2}\right)^2 \text{var}(\hat{D}_{y,i}) \\
&\quad + \left(\frac{1}{\sum_{i=1}^{k} \omega_i}(\sum_{i=1}^{k} \frac{\omega_i}{\hat{D}_{y,i}})\right)^2 \text{var}(\hat{D}_{y,c}) \quad (13)
\end{aligned}$$

with

$$\begin{aligned}
\text{var}(\hat{D}_{y,i}) &= \left(\frac{\partial \hat{D}_{y,i}}{\partial \hat{\beta}_{0,i}}, \frac{\partial \hat{D}_{y,i}}{\partial \hat{\beta}_{1,i}}\right) \Sigma_{\hat{\beta}_{0,i}, \hat{\beta}_{1,i}} \begin{pmatrix} \frac{\partial \hat{D}_{y,i}}{\partial \hat{\beta}_{0,i}} \\ \frac{\partial \hat{D}_{y,i}}{\partial \hat{\beta}_{1,i}} \end{pmatrix} \\
&= \hat{D}_{y,i}^2 \left(-\frac{1}{\hat{\beta}_{1,i}}, \frac{\hat{\beta}_{0,i} - \log \frac{y}{1-y}}{\hat{\beta}_{1,i}^2}\right) \\
&\quad \times \Sigma_{\hat{\beta}_{0,i}, \hat{\beta}_{1,i}} \begin{pmatrix} -\frac{1}{\hat{\beta}_{1,i}} \\ \frac{\hat{\beta}_{0,i} - \log \frac{y}{1-y}}{\hat{\beta}_{1,i}^2} \end{pmatrix}
\end{aligned}$$

for $i = 1, \ldots, k, c$, respectively. Thus, replacing $\text{var}(\hat{D}_{y,i})$ in (13), we can obtain the estimated variance

for $\hat{\tau}_{CT}$:

$$
\begin{aligned}
\text{var}(\hat{\tau}_{CT}) = &\sum_{i=1}^{k} \left(\frac{\omega_i \hat{D}_{y,c}}{(\sum_{i=1}^{k} \omega_i) \hat{D}_{y,i}} \right)^2 \\
&\times \left(\frac{\text{var}(\hat{\beta}_{0,i})}{\hat{\beta}_{1,i}^2} + \frac{2\text{cov}(\hat{\beta}_{0,i}, \hat{\beta}_{1,i})(\log \frac{y}{1-y} - \hat{\beta}_{0,i})}{\hat{\beta}_{1,i}^3} \right. \\
&\left. + \frac{\text{var}(\hat{\beta}_{1,i})(\log \frac{y}{1-y} - \hat{\beta}_{0,i})^2}{\hat{\beta}_{1,i}^4} \right) \\
&+ \left(\frac{\hat{D}_{y,c}}{\sum_{i=1}^{k} \omega_i} \left(\sum_{i=1}^{k} \frac{\omega_i}{\hat{D}_{y,i}} \right) \right)^2 \\
&\times \left(\frac{\text{var}(\hat{\beta}_{0,c})}{\hat{\beta}_{1,c}^2} + \frac{2\text{cov}(\hat{\beta}_{0,c}, \hat{\beta}_{1,c})(\log \frac{y}{1-y} - \hat{\beta}_{0,c})}{\hat{\beta}_{1,c}^3} \right. \\
&\left. + \frac{\text{var}(\hat{\beta}_{1,c})(\log \frac{y}{1-y} - \hat{\beta}_{0,c})^2}{\hat{\beta}_{1,c}^4} \right). \quad (14)
\end{aligned}
$$

Here, we prefer the confidence interval based on the delta method on $\log(\hat{\tau}_{CT})$ since $\log(\hat{\tau}_{CT})$ is more approximately normally distributed than $\hat{\tau}_{CT}$. A $(1 - \alpha) \times 100\%$ confidence interval for $\hat{\tau}_{CT}$ can be constructed by

$$
\left[\hat{\tau}_{CT} \exp\left(\frac{-t_{n+n_c-2k-2, \frac{\alpha}{2}}}{\hat{\tau}_{CT}} \sqrt{\text{var}(\hat{\tau}_{CT})} \right), \right.
$$
$$
\left. \hat{\tau}_{CT} \exp\left(\frac{t_{n+n_c-2k-2, \frac{\alpha}{2}}}{\hat{\tau}_{CT}} \sqrt{\text{var}(\hat{\tau}_{CT})} \right) \right]. (15)
$$

Again $n = \sum_{i=1}^{k} n_i$ and n_i $(i = 1, \dots, k)$ is the number of observations when drug i is used alone, n_c is the number of observations for the combination doses at a fixed ray. By varying y in different values, we can construct a pointwise $(1 - \alpha)100\%$ confidence bound for the curve of interaction indices versus effects. Thus, we can assess drug interactions for combination doses at the fixed ray while considering the stochastic uncertainty in obtaining the observations.

Remark: Comparing the variances of estimated interaction indices in (8) and (14), we note that the first terms in both equations are approximately the same, while the second terms are markedly different. In Sections 2 and 3, the k dose–effect curves for all the drugs involved are estimated. The first terms in both equations describe the uncertainty contributed by estimating the k marginal dose–effect curves. In Section 2, we estimate the interaction index based on the observed mean effect at a single combination dose, and oftentimes, we assume the combination dose is measured without error. Under this setting, the second term in (8) describes the variability contributed by the mean of the observed effects at the combination

(d_1, d_2). In Section 3, we have the observations for combination doses at a fixed ray, then we fit the dose–effect curve for this ray. We estimate the interaction index for each fixed effect, where the combination dose producing such an effect is estimated. Thus, the second term in (14) describes the uncertainty contributed by the variance of the estimated combination dose $\hat{D}_{y,c}$, which could be split into the estimated combination dose

$$
(\hat{d}_1, \dots, \hat{d}_k) = \left(\frac{\omega_1}{\sum_{i=1}^{k} \omega_i} \hat{D}_{y,c}, \dots, \frac{\omega_k}{\sum_{i=1}^{k} \omega_i} \hat{D}_{y,c} \right).
$$

4. Simulations and Case Studies

4.1 Simulations

To examine whether the confidence intervals proposed in Sections 2 and 3 have proper characteristics, we performed simulations in the following two scenarios.

Scenario 1: three drugs, at a single combination dose. In the first scenario, we simulated three drugs that followed the median-effect Equation (2) with the same slope $m = -1$ and different median effective doses: $Dm_1 = 1$, $Dm_2 = 2$, and $Dm_3 = 4$, respectively. We took the combination dose (d_1, d_2, d_3) with each component being one third of its associated median effective dose, that is, $(d_1, d_2, d_3) = (\frac{Dm_1}{3}, \frac{Dm_2}{3}, \frac{Dm_3}{3}) = (\frac{1}{3}, \frac{2}{3}, \frac{4}{3})$. If the combination dose is additive, the expected effect will be 0.5. Let us denote the interaction index at this combination dose as τ, the effect as E, then based on Equation (4), we have

$$
\frac{d_1}{Dm_1 \left(\frac{E}{1-E} \right)^{\frac{1}{m}}} + \frac{d_2}{Dm_2 \left(\frac{E}{1-E} \right)^{\frac{1}{m}}} + \frac{d_3}{Dm_3 \left(\frac{E}{1-E} \right)^{\frac{1}{m}}} = \tau.
$$

Thus, the effect at (d_1, d_2, d_3) can be explicitly expressed as

$$
E = \frac{\left(\tau^{-1} \left(\frac{d_1}{Dm_1} + \frac{d_2}{Dm_2} + \frac{d_3}{Dm_3} \right) \right)^m}{1 + \left(\tau^{-1} \left(\frac{d_1}{Dm_1} + \frac{d_2}{Dm_2} + \frac{d_3}{Dm_3} \right) \right)^m}.
$$

We vary τ among (0.2, 0.4, 0.6, 0.8, 1, 1.25, 1.67, 2.5, 5). The corresponding effect E will be (0.167, 0.286, 0.375, 0.444, 0.5, 0.556, 0.625, 0.714, 0.833), respectively. Note that the slope m is negative, so the dose–effect curve is decreasing. If the effect is less than 0.5, then the combination dose will be synergistic and the interaction index will be less than 1; whereas if the effect is greater than 0.5, the combination dose will be antagonistic and the interaction index will be greater than 1. It is obvious that the farther the interaction index moves away from 1, the stronger is the interaction effect.

Table 1. Simulation results for Scenario 1: a fixed combination dose $(d_1, d_2, d_3) = (\frac{1}{3}, \frac{2}{3}, \frac{4}{3})$ but with varying interaction indices. The three dose–effect curves follow the median-effect equation with $m = -1$ and $(Dm_1, Dm_2, Dm_3) = (1, 2, 4)$.

	τ	0.2	0.4	0.6	0.8	1	1.25	1.67	2.5	5
	mean($\hat{\tau}$)	0.202	0.402	0.601	0.804	1.001	1.266	1.676	2.503	5.022
	Cov.rate	0.950	0.952	0.946	0.947	0.939	0.958	0.951	0.947	0.948
	Cov.rate.log	0.954	0.955	0.950	0.950	0.941	0.953	0.951	0.951	0.954
$\sigma = 0.1$	Len.ci	0.093	0.180	0.266	0.353	0.439	0.555	0.737	1.109	2.276
	Len.ci.log	0.094	0.181	0.268	0.357	0.443	0.560	0.744	1.119	2.298
	Pct.syn.log	100	100	99.4	51.7	3.4	0	0	0	0
	Pct.add.log	0	0	0.6	48.2	94.1	46.4	0.2	0	0
	Pct.ant.log	0	0	0	0.1	2.5	53.6	99.8	100	100
	mean($\hat{\tau}$)	0.220	0.435	0.644	0.879	1.080	1.419	1.850	2.753	5.664
	Cov.rate	0.930	0.933	0.918	0.923	0.916	0.945	0.941	0.920	0.931
	Cov.rate.log	0.956	0.959	0.952	0.952	0.945	0.956	0.953	0.952	0.956
$\sigma = 0.4$	Len.ci	0.397	0.777	1.151	1.562	1.926	2.552	3.381	5.108	10.966
	Len.ci.log	0.463	0.901	1.336	1.812	2.237	2.971	3.972	6.018	13.122
	Pct.syn.log	94.6	52.3	20.8	6.5	3.1	0.5	0.1	0	0
	Pct.add.log	5.4	47.7	79.2	92.2	94.5	91.1	79.2	48.4	5.9
	Pct.ant.log	0	0	0	1.3	2.4	8.4	20.7	51.6	94.1

Under the above setting, we first generated six equally spaced doses, ranging from 0.1 to three-fold of the associated median effective dose for each drug. We then generated the effects based on the model $\log \frac{E}{1-E} = \beta_0 + \beta_1 \log d + \epsilon$ with $\epsilon \sim N(0, \sigma^2)$ for each drug, where $\beta_0 = -m \log D_m$ and $\beta_1 = m$. We generated the observed effect at the combination dose $(\frac{1}{3}, \frac{2}{3}, \frac{4}{3})$ with the same size of the stochastic variation. The total sample size for each simulated experiment was 19 (six observations for each single drug and one observation for the combination dose effect). We fitted each dose–effect curve based on the generated data. Then, for each τ, we estimated the interaction index based on (6), constructed its 95% confidence intervals based on (9) and (10), respectively, calculated the length of the confidence intervals, and counted whether the true τ lies in the respective confidence intervals based on (9) and (10), and whether the confidence interval based on (9) lies below 1, contains 1, or lies above 1. We repeated this procedure 1,000 times, and averaged all the above quantities. We summarized the results in Table 1 under different settings for σ: $\sigma = 0.1$ and $\sigma = 0.4$, respectively. From Table 1, we conclude that (a) the estimation for τ (mean($\hat{\tau}$) in Table 1) is close to the true value and the accuracy decreases as σ increases; (b) the resulting coverage rates (Cov.rate.log) based on confidence interval (9) are closer to the nominal coverage rate of 95% than those (Cov.rate) based on (10), particularly, when σ is larger; (c) the average lengths of the confidence intervals (Len.ci.log) based on (9) and the average lengths of the confidence intervals (Len.ci) based on (10) increase as σ increases with Len.ci.log slightly larger than Len.ci to provide the nom-

inal coverage rate; and (d) the percentage of times the model correctly assesses drug interaction based on (9) as synergy (Pct.syn.log), additivity (Pct.add.log), or antagonism (Pct.ant.log) decreases as σ increases. For each underlying interaction index among (0.2, 0.6, 1, 1.67, 5), we obtained the Q-Q plot of the 1,000 estimated interaction indices (Figure 2, Columns B1 and B3) as well as the Q-Q plot of the 1,000 logarithms of the estimated interaction indices (Figure 2, Columns B2 and B4) under the settings $\sigma = 0.1$ and $\sigma = 0.4$, respectively. From Figure 2, it is clear that for small σ (e.g., $\sigma = 0.1$), both the estimated interaction index and the logarithm of the estimated interaction index are approximately normally distributed. But, when σ becomes large, say $\sigma = 0.4$, the estimated interaction indices deviate from a normal distribution, while the logarithms of the estimated interaction indices are still approximately normally distributed. Therefore, one would expect that the delta method on the logarithm of the interaction index would work better for constructing confidence intervals for interaction indices. This assertion has been verified by the results of the current simulation studies. Thus, we prefer using confidence interval (9) over (10) for the interaction index in Section 2, and using the confidence interval (15) in Section 3.

Scenario 2: Two drugs, with a ray design. The second scenario involves two drugs that have the same dose–effect curves as drug 1 and drug 2 in the first scenario. That is, the two dose–effect curves follow the median-effect Equation (2) with the same slope $m = -1$, and median effective doses: $Dm_1 = 1$ and $Dm_2 = 2$, respectively. We assume that the dose–effect curve for the
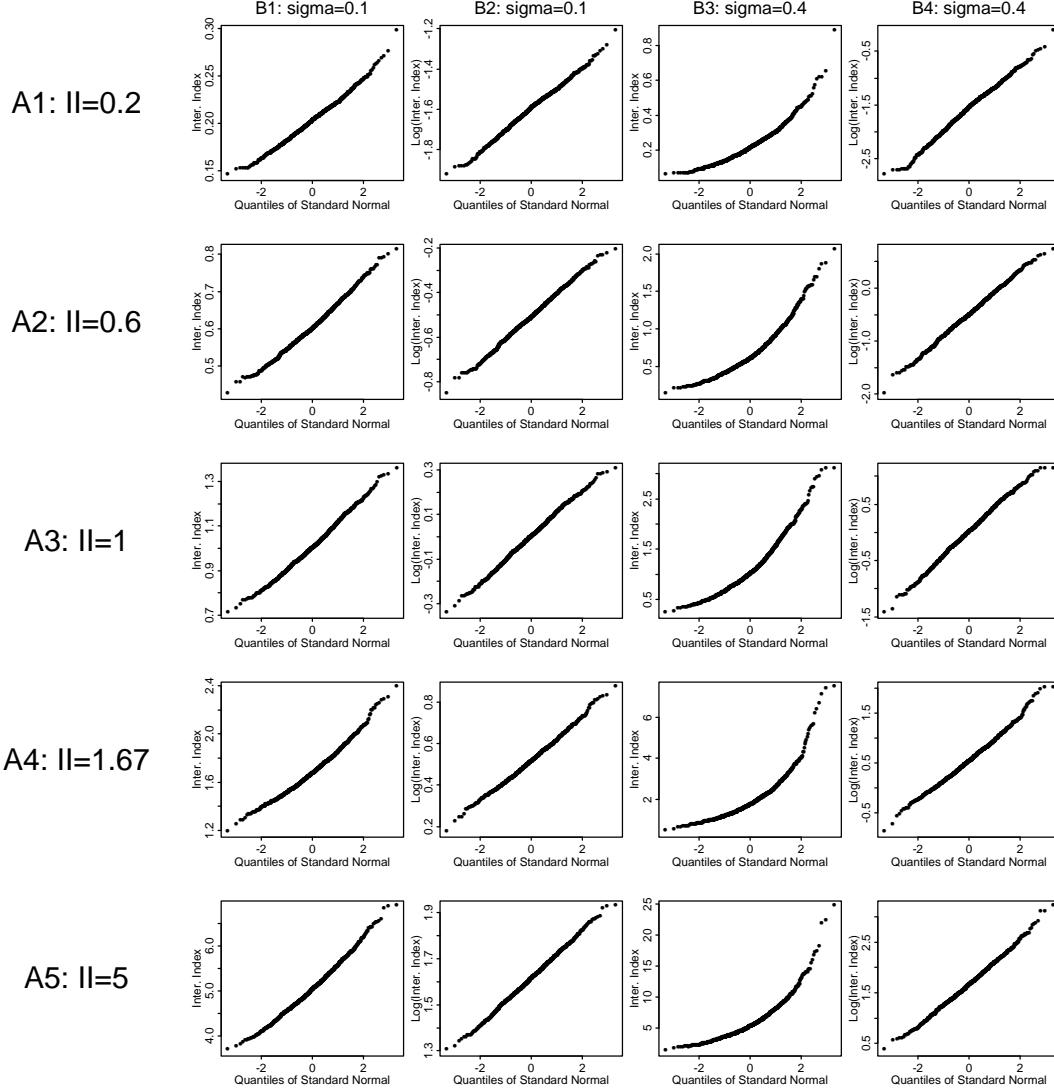
Figure 2.   Q-Q plots of estimated interaction indices (Column B1 and B3) and Q-Q plots of the logarithms of the estimated interaction indices (Column B2 and B4) for 1000 samples under Scenario 1. Columns B1 and B2 show the Q-Q plots under $\sigma = 0.1$, and Column B3 and B4 show the Q-Q plots under $\sigma = 0.4$.

combination doses (d_1, d_2) at the fixed ray, say, $\frac{d_2}{d_1} = \frac{2}{1}$, follows the median-effect Equation (2) with $Dm_{12} = 1.5$ and $m_{12} = -2$.

We generated five equally spaced doses, ranging from 0.1 to three-fold of the associated median effective dose for each of the single drug, and five equally spaced doses, ranging from 0.5 to three-fold of the associated median effective dose for the mixture (d_1, d_2) at the fixed ray with $\frac{d_2}{d_1} = \frac{2}{1}$ and with the dose in the median effect Equation (2) being $d_1 + d_2$. We then generated the effects associated with these generated doses based on the model $\log \frac{E}{1-E} = \beta_0 + \beta_1 \log d + \epsilon$ with $\epsilon \sim N(0, \sigma^2)$ for the two drugs and their mixture under the settings $\sigma = 0.2$ and $\sigma = 0.4$, respectively. The total sample size for each simulated experiment is 15 (five observations for each

single drug and five observations for combination doses). In addition, under each setting for σ, we generated seven samples for illustration. For each sample, we first fitted the dose–effect curves for the two drugs and the mixture, and then performed the following steps: we (a) estimated the interaction indices based on (12) for 42 equally spaced effect levels between the range of 0.1 to 0.95; (b) constructed their confidence intervals based on (15) and on a Monte Carlo simulation proposed by Belen'kii and Schinazi (1994), respectively; and (c) estimated interaction index (6) and constructed the confidence interval (9) for each observed combination dose. Figure 3 illustrates plots of the underlying curve of the interaction index versus effect (solid line), the pointwise 95% confidence bound for this curve based on (15) (dotted lines),

the confidence bound based on the Monte Carlo simulation (dashed lines), and the estimated interaction indices (dots) and their confidence intervals (vertical bars) for the observed doses based on (9) for the seven illustrative samples under each setting for σ. From Figure 3, we conclude that (a) the pointwise 95% confidence bound (dotted lines) embrace the true curve (solid line) well; (b) the pointwise confidence bounds based on (15) (dotted lines) are similar to those based on Monte Carlo simulations (dashed lines) when σ is small, but perform better when σ is large; and (c) the confidence intervals based on single observations (vertical bars) are generally wider than both confidence bounds, and the conclusions based on confidence bounds are more accurate than those based on the confidence intervals (vertical bars) for single observations. In addition, for each sample, we calculated the ratio of the length of the confidence interval based on (9) and the confidence interval based on Monte Carlo simulation described in Section 3 for each of the observed effects at the combination doses at the fixed ray. Under $\sigma = 0.2$, the ratios for the seven samples have a mean 2.05 with standard deviation 0.58, and range from 1.12 to 3.28. Under $\sigma = 0.4$, the ratios for the seven samples have a mean 2.33 with standard deviation 0.92, and range from 1.01 to 4.15 after removing an extreme of the observation with effect close to one (Figure 3, Panel B7). Therefore, when several observations for combination doses at a fixed ray are available, the confidence bound derived in Section 3 using more available information is more efficient, thus preferred. In addition, when we ran this simulation to get the 14 confidence bounds in the 14 panels in Figure 3 by separately using the confidence interval based on (15) and Monte Carlo procedure on an Intel 1.83 GHz computer, the time it took was 10 seconds and 17 minutes, respectively. It is clear that the calculation for the confidence bound based on (15) is much faster than that based on Monte Carlo simulations.

4.2 Case Studies

Our research group (Lee et al. 2007; Kong and Lee 2006) investigated drug interactions between two novel agents, SCH66336 and 4-HPR, in a number of squamous cell carcinoma cell lines (Chun et al. 2003). Here we present the dataset and results from cell line UMSCC22B in Table 2 for investigating drug interaction in combination doses at the fixed ray with $\frac{d_2}{d_1} = \frac{1}{1}$.

We first obtained the dose–effect curves for SCH66336 and 4-HPR by a linear regression of $\log \frac{E}{1-E}$ on $\log d$, based on the data in Table 2. Recall that $\log \frac{E}{1-E} = m(\log d - \log D_m) = \beta_0 + \beta_1 \log d$. The estimates of β_0, β_1, D_m, and $\hat{\sigma}$ for drug 1, drug 2, and the mixture of the drugs with equal concentrations are summarized in the same table.

The transformed data $\log \frac{E}{1-E}$ versus $\log d$ and the median-effect plots are shown in Figure 4(A). This median effect plot indicates that the data follow the median-effect Equation (2) reasonably well. Based on the fitted median-effect equations, we calculated the interaction indices based on (12) for varied effects for combination doses at the fixed ray with $\frac{d_2}{d_1} = \frac{1}{1}$ and constructed their associated confidence bounds based on (15) and on Monte Carlo simulations (Belen'kii and Schinazi 1994), respectively. Figure 4(B) shows the plot of the interaction indices (on the logarithm scale) versus effects (solid line) for combination doses at this fixed ray and the 95% pointwise confidence bounds based on (15) (dotted lines) and on Monte Carlo simulations (dashed lines). Based on the confidence bound (dotted line), we conclude that the combination doses at the fixed ray with $\frac{d_2}{d_1} = \frac{1}{1}$ with effect less than 0.52 are synergistic, and the combination doses at the fixed ray with effect greater than 0.52 are additive. The conclusions based on the confidence bounds obtained from Monte Carlo simulations (dashed lines) are slightly different. We also calculated four interaction indices based on (6) and their confidence intervals based on (9) at the four observed data points (d_1, d_2) as being (0.1, 0.1), (0.5, 0.5), (1, 1), and (2, 2). The four interaction indices were 0.791, 0.609, 0.256, and 0.103, and their corresponding 95% confidence intervals were [0.202, 3.091], [0.169, 2.193], [0.060, 1.087], and [0.018, 0.581], respectively. These pairs of interaction indices versus effects, along with their 95% confidence intervals are shown as vertical bars in Figure 4(B). From these four interaction indices and their confidence intervals, we conclude that the combination doses at the fixed ray with $\frac{d_2}{d_1} = \frac{1}{1}$ are synergistic for doses ≥ 2 μM for each single drug, and additive for doses ≤ 1 μM for each single drug. The conclusions from the two procedures in Section 2 and 3 are slightly different: the combination doses (1, 1) and (0.5, 0.5) with respective observed effect 0.3551 and 0.4919 were identified as additive based on the second and third vertical bar (reading from left to right), while based on the confidence bound (dotted lines), the combination doses were identified as synergistic as each effect was less than 0.52. The relative length of the confidence interval based on (9) versus the monte Carlo confidence interval ranges from 1.27 to 3.72 for the four combination doses at the fixed ray. Once again, this example shows that the confidence interval estimation based on a single observation (9) is not as efficient as the corresponding confidence interval based on model (15) which used more data.

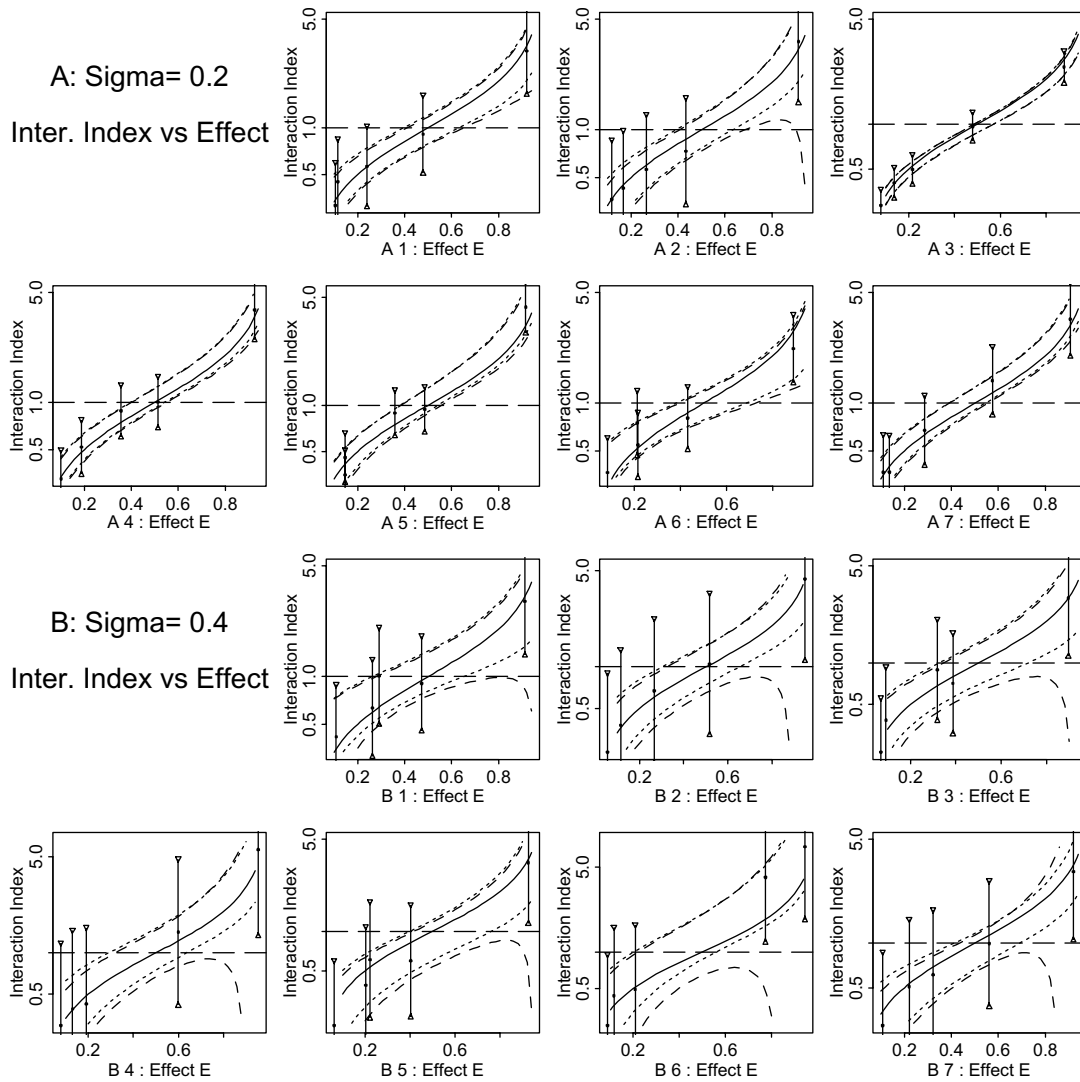We also examined another dataset from a drug combi-

Figure 3. Simulated results under Scenario 2. The solid line is the plot of the underlying true interaction indices versus effects for combination doses at the fixed ray with $\frac{d_2}{d_1} = \frac{2}{1}$, the dotted lines and the dashed lines are the 95% pointwise confidence bounds for the curve of the interaction index versus effect based on the delta method and Monte Carlo simulation under the settings $\sigma = 0.2$ (Panels A) and $\sigma = 0.4$ (Panel B), respectively, and the dots and the vertical bars are the estimated interaction indices and their confidence intervals for observed combinations.

nation study for o-phenanthroline and ADP on the inhibition of horse liver alcohol dehydrogenase, which was analyzed by Chou and Talalay (1984) and by Belen'kii and Schinazi (1994). The dataset and the estimated median-effect parameters are shown in Table 3. The median-effect plots for the two drugs and their mixture (d_1, d_2) at the fixed ray with $\frac{d_2}{d_1} = \frac{1}{17.4}$ are shown in Figure 5(A). The plot of interaction indices versus the fractional inhibitions at this fixed ray are shown as a solid line in Figure 5(B). In the same panel, we illustrate the pointwise confidence bound (dotted lines) based on (15) and the pointwise confidence bound (dashed line) based on

Monte Carlo simulations for this curve, and the estimated interaction indices (dots) and their associated confidence intervals (vertical bars) based on (9) for the combination doses having observed effects. Again, the two 95% confidence bounds are almost the same, the vertical bars are wider than the confidence bound, and the conclusions on drug interactions based on vertical bars and those based on confidence bounds are consistent.

We developed two S-PLUS/R programs. One is used to estimate the interaction index and its confidence interval for a single combination dose of multiple drugs, and the other is used to estimate the pointwise

Table 2. Fractions of squamous cell carcinoma cells (UMSCC22B) surviving after 72 hours of treatment by single and combination dose levels of SCH66336 and 4-HPR and the fitted median-effect parameters.

SCH66336 dose (μM)	4-HPR dose (μM)	Fractional survival	Median-effect parameters
0.1		0.6701	$\hat{\beta}_{0,1} = 0.094(0.085)$
0.5		0.6289	$\hat{\beta}_{1,1} = -0.335(0.066)$
1		0.5577	$\hat{D}m_1 = 1.326$
2		0.4550	$\hat{\sigma}_1 = 0.187$
4		0.3755	
	0.1	0.7666	$\hat{\beta}_{0,2} = 0.217(0.073)$
	0.5	0.5833	$\hat{\beta}_{1,2} = -0.398(0.058)$
	1	0.5706	$\hat{D}m_2 = 1.726$
	2	0.4934	$\hat{\sigma}_2 = 0.129$
0.1	0.1	0.6539	$\hat{\beta}_{0,12} = -0.225(0.092)$
0.5	0.5	0.4919	$\hat{\beta}_{1,12} = -0.596(0.082)$
1	1	0.3551	$\hat{D}m_{12} = 0.686$
2	2	0.2341	$\hat{\sigma}_{12} = 0.182$

Note: The number inside the parentheses in the last column is the standard error of the estimate.
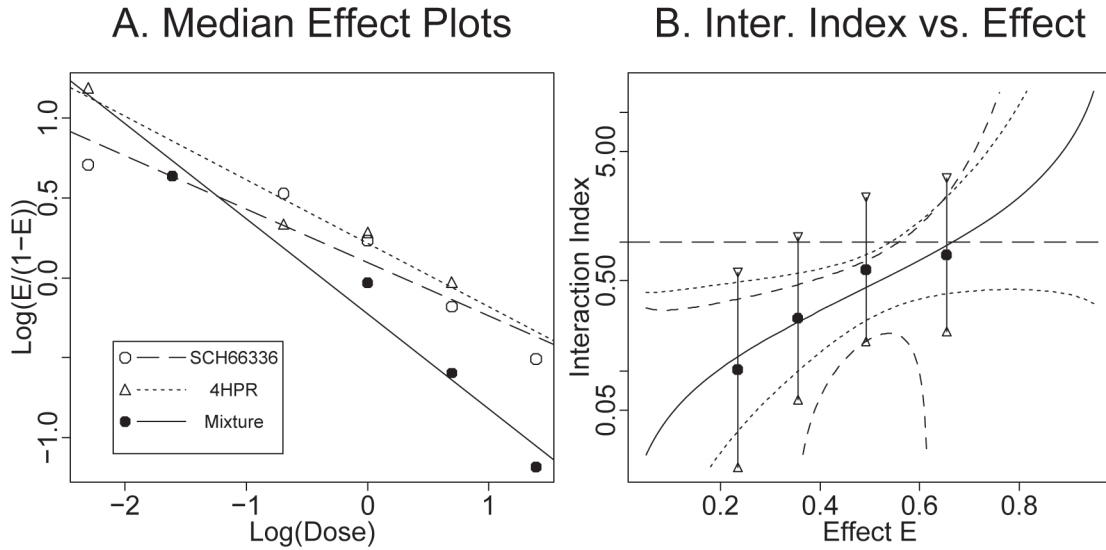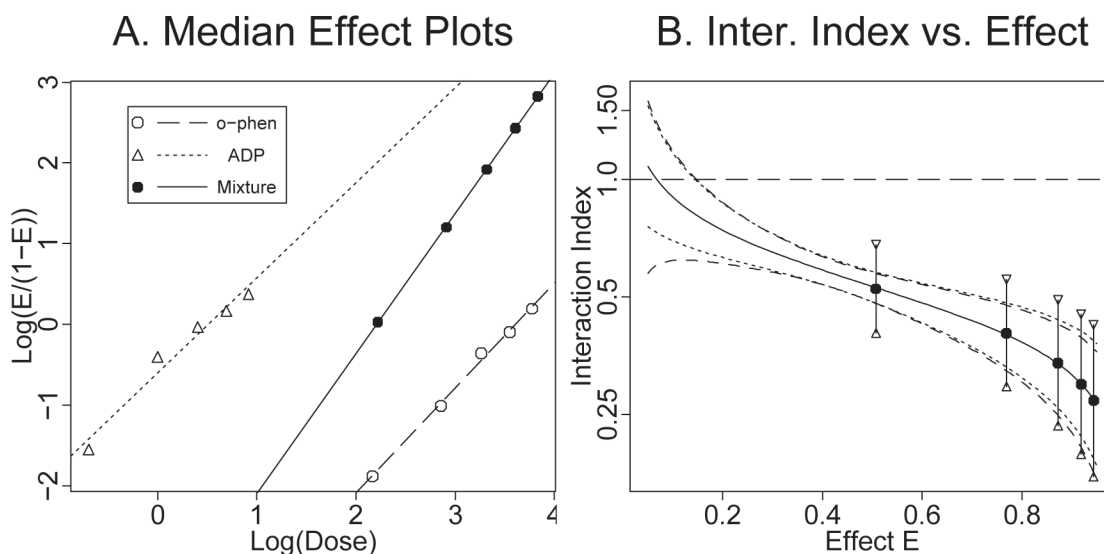

Figure 4. Median-effect plots (Panel A) and the plot of interaction indices versus effects (Panel B) for the combination doses at the fixed ray with $\frac{d_2}{d_1} = \frac{1}{1}$ for SCH66336 and 4HPR. In Panel B, the solid line is the plot of the estimated interaction indices versus effects, the two dotted lines and the two dashed lines are the pointwise 95% confidence bounds for the curve of interaction index versus effect based on the delta method in Section 3 and Monte Carlo simulation, respectively, and the dots and the vertical bars are the estimated interaction indices and their confidence intervals for observed combinations. The four vertical bars from left to right correspond to the combination doses of (2, 2), (1, 1), (0.5, 0.5), and (0.1, 0.1), respectively.

Table 3.   Inhibition of horse liver alcohol dehydrogenase by o-phenanthroline and ADP alone and in combination (Chou and Talalay 1984; Belen'kii and Schinazi 1994).

o-phenanthroline	ADP	Fractional Inhibition	Median-effect parameters
8.7		0.132	$\hat{\beta}_{0,1} = -4.696(0.145)$
17.4		0.267	$\hat{\beta}_{1,1} = 1.302(0.046)$
26.1		0.411	$\hat{D}m_1 = 36.803$
34.8		0.476	$\hat{\sigma}_1 = 0.058$
43.5		0.548	
	0.5	0.175	$\hat{\beta}_{0,2} = -0.601(0.079)$
	1.0	0.400	$\hat{\beta}_{1,2} = 1.178(0.127)$
	1.5	0.492	$\hat{D}m_2 = 1.666$
	2.0	0.542	$\hat{\sigma}_2 = 0.161$
	2.5	0.592	
$9.2 \times \frac{17.4}{18.4}$	$9.2 \times \frac{1}{18.4}$	0.507	$\hat{\beta}_{0,12} = -3.843(0.038)$
$18.4 \times \frac{17.4}{18.4}$	$18.4 \times \frac{1}{18.4}$	0.769	$\hat{\beta}_{1,12} = 1.739(0.012)$
$27.6 \times \frac{17.4}{18.4}$	$27.6 \times \frac{1}{18.4}$	0.872	$\hat{D}m_{12} = 9.117$
$36.8 \times \frac{17.4}{18.4}$	$36.8 \times \frac{1}{18.4}$	0.919	$\hat{\sigma}_{12} = 0.015$
$46.0 \times \frac{17.4}{18.4}$	$46.0 \times \frac{1}{18.4}$	0.944	

Note: The number inside the parentheses in the last column is the standard error of the estimate.

confidence bound for the curve of interaction index versus effect for combination doses at a fixed ray. The S-PLUS/R code and the data example are available in *CI_of_Interaction_Index*, which can be downloaded from *http:// biostatistics.mdanderson.org/SoftwareDownload/*.

5. Discussion

We proposed a procedure in Section 2 to estimate the interaction index and constructed its associated confidence interval for a multiple drug combination. In most cases, the dose–effect for a single agent is known, and investigators are interested in assessing whether drug combinations are synergistic. When resources are limited, the experiment can be conducted in only a limited number of combination doses. We can assess drug interactions for those combination doses based on the procedure provided in Section 2. Note that although the dose–effect curves follow Chou and Talalay's median-effect equation work reasonably well, the model may not work in certain cases. In these cases, other dose–effect models must be sought. For example, Lee et al. (2009) found that the $E_{\max}$ model describes the experimental data there better than Chou and Talalay's median-effect equation; thus, the $E_{\max}$ model was used there. Upon finding the dose–effect curves of any parametric form which fits the data, one may use the same philosophy to estimate the interaction index and construct its associated confidence interval based on the delta method. However, using this "at a

combination dose" method, one can assess drug interactions only at combination doses having observed effects, and the drug interaction tends to be predicted as additivity due to lack of efficiency (i.e., wide confidence intervals) even with nonadditive drug interactions.

Chou and Talalay's method based on a ray design is widely used. We provided a procedure to construct pointwise confidence bound for Chou and Talalay's curve of interaction index versus effect in Section 3. The procedure we provided avoids extensive calculations used in Monte Carlo techniques, which were required in the software *CalcuSyn* and *CompuSyn* and in the method provided by Belen'kii and Schinazi (1994). From the simulations and case studies in Section 4, we find that the confidence bounds provided in Section 3 are at least as good as the confidence bounds constructed using Monte Carlo techniques, while the confidence bounds in Section 3 are much faster to compute. Our limited simulation studies also show that the approximation based on the logarithm transformation and t-statistic works reasonably well when sample size was as low as 19 in one case and 15 in another case.

From simulations and case studies in Section 4, it is clear that the confidence intervals based on single observations (verticals bars in Figures 3, 4, and 5) are wider than the pointwise confidence bounds based on a ray design which use more data. In a ray design, the constructed confidence bound used all the information on this ray, therefore, the estimates based on Section 3 will be more

A. Median Effect Plots

B. Inter. Index vs. Effect

Figure 5. Median-effect plots (Panel A) and the plot of interaction indices versus effects (Panel B) for the combination doses at the fixed ray with $\frac{d_2}{d_1} = \frac{17.4}{1}$ for o-phenanthroline and ADP. In Panel B, the solid line is the plot of the estimated interaction indices versus effects, the two dotted lines and the two dashed lines are the pointwise confidence bounds for the curve of interaction index versus effect based on the delta method and Monte Carlo simulation, respectively, and the dots and the vertical bars are the estimated interaction indices and their confidence intervals for observed combinations.

efficient and more accurate. By examining the curve of interaction indices versus effects on several rays and examining their associated confidence bounds, one may obtain an overall picture of the drug interactions. The limitation is that one can only assess drug interactions for combination doses at these fixed examined rays. When a factorial design or a uniform design (Tan, Fang, Tian, and Houghton 2003) is used, a good strategy is to use response surface models, which use all the information presented in the observed data. We have proposed a generalized response surface model (Kong and Lee 2006) and a semiparametric model (Kong and Lee 2007) to capture drug interaction for all combination doses. However, response surface models for more than three drugs are difficult to construct. Therefore, to assess drug interactions among multiple drugs, the directly calculated interaction index and the plots of interaction indices versus effects at several fixed rays are still feasible and remain appealing methods to use. The confidence intervals we provided in Sections 2 and 3 are easy to calculate, and have a desirable coverage rate. Hence, it suggests that it is not necessary to run extensive Monte Carlo simulations for obtaining these confidence intervals. Based on the result of this article, Lee et al. (2009) constructed the simultaneous confidence interval for interaction indices over a range of treatment effects. The simultaneous confidence interval is also easy to calculate but is more conservative. The proposed confidence intervals can help us to gauge the uncertainties of the interaction indices for combina-

tion doses for two or more drugs and can also be used to provide more in-depth assessment for drug interactions.

References

Belen'kii, M. S., and Schinazi, R. F. (1994), "Multiple Drug Effect Analysis With Confidence Interval," *Antiviral Research*, 25, 1–11.

Berenbaum, M. C. (1985), "The Expected Effect of a Combination of Agents: The General Solution," *Journal of Theoretical Biology*, 114, 413–431.

——— (1989), "What is Synergy?," *Pharmacological Reviews*, 41, 93–141.

Bickel, P. J., and Doksum, K. A. (2001), *Mathematical Statistics: Basic Ideas and Selected Topics*, New Jersey: Prentice Hall, pp. 306–314.

Chou, T. C. (1991), "The Median-Effect Principle and the Combination Index for Quantitation of Synergism and Antagonism," in *Synergism and Antagonism in Chemotherapy*, eds. T. C. Chou and D. C. Rideout, San Diego: Academic Press, pp. 61–101.

——— (2006), "Theoretical Basis, Experimental Design, and Computerized Simulation of Synergism and Antagonism in Drug Combination Studies," *Pharmacological Reviews*, 58, 621–681.

Chou, T. C., and Talalay, P. (1984), "Quantitative Analysis of Dose Effect Relationships: The Combined Effects of Multiple Drugs or Enzyme Inhibitors," *Advances in Enzyme Regulation*, 22, 27–55.

Chun, K. H., Lee, J. J., Ayers, G. D., and Lotan, R. (2003), "Synergistic Induction of Apoptosis in Human Head and Neck Squamous Cell Carcinoma (HNSCC) Cell Lines by the Combination of the Synthetic Retinoid 4HPR and the Farnesyltransferase Inhibitor SCH66336," *Proceedings of American Association for Cancer Research*, 44.

Greco, W. R., Bravo, G., and Parsons, J. C. (1995), "The Search of Synergy: A Critical Review from a Response Surface Perspective," *Pharmacological Reviews*, 47(2), 331–385.

Kong, M., and Lee, J. J. (2006), "A General Response Surface Model with Varying Relative Potency for Assessing Drug Interactions," *Biometrics*, 62(4), 986–995.

——— (2008), "A Semiparametric Response Surface Model for Assessing Drug Interactions," *Biometrics*, 64, 396–405.

Lee, J. J., Kong, M., Ayers, G. D., and Lotan, R. (2007), "Interaction Index and Different Methods for Determining Drug Interaction in Combination Therapy," *Journal of Biopharmaceutical Statistics*, 17, 461–480.

Lee, J. J., Lin, H. Y., Liu, D. D., and Kong, M. (2009), "Applying E_{max} Model and Interaction Index for Assessing Drug Interaction in Combination Studies," *Frontiers in Biosciences*, in press.

Tan, M., Fang, H., Tian, G., and Houghton, P. J. (2003), "Experimental Design and Sample Size Determination for Testing Synergism in Drug Combination Studies Based on Uniform Measures," *Statistics in Medicine*, 22, 2091–2100.

About the Authors

J. Jack Lee, Department of Biostatistics, The University of Texas M. D. Anderson Cancer Center, Houston, TX (E-mail: *jjlee@mdanderson.org*). Maiying Kong, Department of Biostatistics, The University of Texas M. D. Anderson Cancer Center, Houston, TX, and Department of Bioinformatics and Biostatistics, University of Louisville, Louisville, KY (E-mail: *maiying.kong@louisville.edu*).

Cure Rate Model With Mismeasured Covariates Under Transformation

Yanyuan MA and Guosheng YIN

Cure rate models explicitly account for the survival fraction in failure time data. When the covariates are measured with errors, naively treating mismeasured covariates as error-free would cause estimation bias and thus lead to incorrect inference. Under the proportional hazards cure model, we propose a corrected score approach as well as its generalization, and implement a transformation on the mismeasured covariates toward error additivity and/or normality. The corrected score equations can be easily solved through the backfitting procedure, and the biases in the parameter estimates are successfully eliminated. We show that the proposed estimators for the regression coefficients are consistent and asymptotically normal. We conduct simulation studies to examine the finite-sample properties of the new method and apply it to a real data set for illustration.

KEY WORDS: Cure model; Errors-in-variables problem; Proportional hazards model; Semiparametric method; Survival fraction.

1. INTRODUCTION

In oncology studies, it is often observed that a certain percentage of subjects are either cured following treatment or are unsusceptible to the event of interest and thus will never experience the failure (e.g., disease relapse). To explicitly incorporate the survival fraction for such data, cure rate models have been proposed and extensively investigated. The two-component mixture cure model (Berkson and Gage 1952) naturally separates the entire population into cured and noncured subjects,

$$S(t|\mathbf{X}) = \theta(\mathbf{X}) + \{1 - \theta(\mathbf{X})\}S^*(t|\mathbf{X}),$$

where $\theta(\mathbf{X})$ is the cure probability and $S^*(t|\mathbf{X})$ is a proper survival function for the uncured population, that is, $\lim_{t \to \infty} S^*(t|\mathbf{X}) = 0$. Its intuitive structure and ease of interpretation has made this mixture cure model the focus of much attention (see, e.g., Gray and Tsiatis 1989; Sposto, Sather, and Baker 1992; Laska and Meisner 1992; Kuk and Chen 1992; Maller and Zhou 1996; Sy and Taylor 2000; Lu and Ying 2004; Li, Tiwari, and Guha 2007). But the mixture cure model lacks certain desirable properties, as pointed out by Chen, Ibrahim, and Sinha (1999). Moreover, the numerical computation can be quite challenging due to the additive structure of the cured and uncured components.

Alternatively, the proportional hazards cure rate model developed by Yakovlev and Tsodikov (1996) and Tsodikov (1998a) integrates the survival times of the cured and noncured subjects into one single formulation of the survival function,

$$S(t|\mathbf{X}) = \exp\{-\theta(\mathbf{X})F(t)\}, \tag{1}$$

where $\theta(\mathbf{X})$ is a known link function and $F(t)$ is an unknown baseline cumulative distribution function (cdf). The corresponding cure rate is $S(\infty|\mathbf{X}) = \exp\{-\theta(\mathbf{X})\}$, and the hazard function is $\lambda(t|\mathbf{X}) = \theta(\mathbf{X})f(t)$, where $f(t) = dF(t)/dt$. When $\theta(\mathbf{X}) = \exp(\mathbf{X}^T\boldsymbol{\beta})$ and $\boldsymbol{\beta}$ contains an intercept b, model (1) becomes the usual Cox proportional hazards model (Cox 1972) subject to the restriction of a bounded baseline cumulative hazard function, given by $\Lambda_0(t) = F(t)\exp(b)$. Thus a cure rate model has a bounded cumulative hazard, leading to an improper survival function [i.e., $S(\infty|\mathbf{X}) > 0$], whereas a noncure model, such as the Cox model, has an unbounded cumulative hazard, thus resulting in a proper survival function [i.e., $S(\infty|\mathbf{X}) = 0$]. Yakovlev and Tsodikov (1996) and Chen et al. (1999) provided a sound biological derivation for model (1), and Tsodikov, Ibrahim, and Yakovlev (2003) provided a comprehensive review.

In reality, it is often the case that the covariate $\mathbf{X}$ can be measured only approximately or indirectly, leading to an errors-in-variables problem. If covariates with measurement errors are naively taken as error-free, then severe bias can be induced in the parameter estimates. Fuller (1987) and Carroll, Ruppert, Stefanski, and Crainiceanu (2006) explored various methods for correcting the bias. The observed variable, denoted by $\mathbf{W}$, is typically related to the true covariate $\mathbf{X}$ through a model $p_{\mathbf{W}|\mathbf{X}}(\mathbf{W}|\mathbf{X}, \boldsymbol{\xi})$, where $\boldsymbol{\xi}$ can be an unknown parameter. It is common to assume a normal additive error structure, that is, $\mathbf{W}$ equals $\mathbf{X}$ plus a normal random noise. When this normality assumption does not hold, one needs to either adapt the methodology to treat the nonnormal error or transform the covariates $\mathbf{X}$ and $\mathbf{W}$ into a normal error form (Nusser, Carriquiry, Dodd, and Fuller 1996; Eckert, Carroll, and Wang 1997).

The Cox model with measurement errors, has been studied extensively in, for example, the induced partial likelihood approach (Prentice 1982); joint models of survival times and longitudinal covariates measured with errors (Tsiatis, DeGruttola, and Wulfsohn 1995; Wulfsohn and Tsiatis 1997; Tsiatis and Davidian 2001), the regression calibration method (Wang, Hsu, Feng, and Prentice 1997), pseudo–partial likelihood methods (Zucker 2005) and in the presence of a validation set (Zhou and Pepe 1995; Zhou and Wang 2000; Hu and Lin 2002). Hu, Tsiatis, and Davidian (1998) and Song, Davidian, and Tsiatis (2002) studied semiparametric likelihood-based methods to relax the distributional assumption on the covariates. Various correction estimators and corrected scores have been provided by Stefanski (1989), Nakamura (1990, 1992), Kong and Gu (1999), Buzas (1998), Huang and Wang (2000), Augustin (2004), Gorfine, Hsu, and Prentice (2004), and Song and Huang (2005). Moreover, measurement error problems have been addressed in other contexts: Kulich and Lin (2000) explored these problems in the additive hazards model; Cheng

Yanyuan Ma is Professor, Institute of Statistics, University of Neuchâtel, Switzerland (E-mail: *yanyuan.ma@unine.ch*). Guosheng Yin is Assistant Professor, Department of Biostatistics, M. D. Anderson Cancer Center, University of Texas, Houston, TX 77030 (E-mail: *gsyin@mdanderson.org*).

and Wang (2001), linear transformation models; Li and Ryan (2004), with heterogeneous covariate errors; and Li and Lin (2000), Greene and Cai (2004), and Hu and Lin (2004), in extensions to multivariate failure time data.

Although there is a rich body of literature dealing with measurement errors in censored survival data, all the aforementioned research work cannot be directly applied to the case with a cure fraction. To the best of our knowledge, measurement error issues in semiparametric cure rate models have not been addressed to date, and this is the first work to deal with estimation and inference in this regard. We can appreciate the difficulties involved in such models due to various unspecified components and their interactions, including the distributions of the unobservable variables, the censoring distribution, and the baseline distribution function. In fact, we have found that a general semiparametric method requires one to either assume covariate-independent censoring or directly model the censoring mechanism, neither of which is considered a satisfactory approach.

This research is motivated by a recent lung cancer study, in which the objective was to assess the association of patient survival with a certain biomarker expression in the tumor cell cytoplasm. For each patient, we had either one reading or two readings of biomarker expression by different pathologists to reduce the subjectivity of the evaluation. However, neither of the two measurements of biomarker expression could be considered precise. Our interest lies in investigating the potential of the biomarker as a new prognostic marker and therapeutic target for lung cancer. Figure 1 shows the Kaplan–Meier survival curves stratified by tumor histology (adenocarcinoma or squamous cell carcinoma). After approximately 7 years of follow-up, we can see a stable plateau at the tails of the survival curves, which indicates the existence of a possible cure fraction.

In this article we consider the proportional hazards cure rate model in (1), where $\mathbf{X}$ is measured with errors. The error structure is not necessarily normal additive, and multiple measurements may exist for $\mathbf{X}$. Without making any assumptions on the distribution of $\mathbf{X}$, we propose a corrected score approach based on the nonparametric maximum likelihood estimator (NPMLE) and a new transformation on the contaminated covariates. We show that the estimators for $\boldsymbol{\beta}$ and $F(t)$ are strongly consistent and converge to a Gaussian process at a root-n rate. Due to the complex natures of such functional measurement error problem and NPMLE, the derivations of these asymptotic properties are very involved. Furthermore, the proposed nonparametric transformation on the covariates to improve the error normality and additivity is very different from the Box–Cox or spline transformation described by Eckert et al. (1997). We show that our transformation, which can be broadly applied in general measurement error problems, is effective and easy to use. On the other hand, we note that the corrected score itself can be generalized to accommodate nonnormal error structure. Due to the proportional hazard structure, the NPMLE and partial likelihood estimator are equivalent, and thus the same estimator can be derived from the partial likelihood instead of NPMLE. A more detailed discussion of this issue is given in Section 6.

The rest of the article is organized as follows. In Section 2 we introduce notation and propose a computationally effective estimation procedure when covariates are measured with normal additive errors. In Section 3 we derive the asymptotic properties of the proposed estimators for $\boldsymbol{\beta}$ and $F(t)$, and in Section 4 we propose a general transformation to handle the nonnormal and nonadditive measurement error structure. In Section 5 we report the results of simulation studies that we conducted to evaluate the finite-sample properties of the estimators, along with our application of the proposed model to the lung cancer data set. We give some concluding remarks in Section 6 and outline the technical details of the proofs of the theorems in the Appendix.
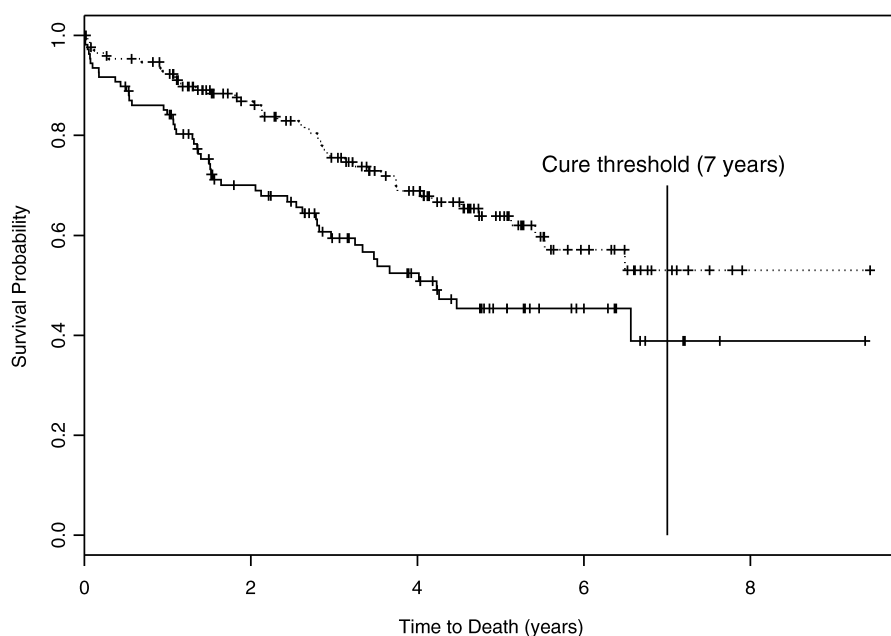

Figure 1. Estimated Kaplan–Meier survival curves for patients with lung cancer, stratified by tumor histology (———— squamous; ·········· adenocarcinoma).

2. METHODOLOGY

For $i = 1, \ldots, n$, let T_i be the failure time, let C_i be the censoring time for subject i, and, correspondingly, let a q-vector $\mathbf{X}_i$ denote the covariates, the first component of which is 1. We assume that $(Y_i, \Delta_i, \mathbf{X}_i)$ are independent and identically distributed (iid), where $Y_i = \min(T_i, C_i)$ and $\Delta_i = I(T_i \leq C_i)$ is the censoring indicator. Furthermore, T_i is conditionally independent of C_i given covariate $\mathbf{X}_i$. The follow-up time is infinite and a proportion of subjects never experience failure or right-censoring, that is $Y_i = \infty$ with probability one for those subjects. To claim a subject cured, we need to choose a threshold and then set $Y_i = \infty$ if Y_i is larger than this threshold. In practice, a typical threshold is the largest observed event time.

For simplicity of description, we assume a classical measurement error model structure, where the error is additive and follows a mean-0 normal distribution. The treatment of the nonnormal and/or nonadditive error case is given in Section 4. We formulate the cure rate model with covariate measurement errors as

$$S(t|\mathbf{X}) = \exp\{-F(t)e^{\mathbf{X}^T\boldsymbol{\beta}}\}, \qquad \mathbf{W} = \mathbf{X} + \mathbf{U},$$

where the error $\mathbf{U} \sim N(\mathbf{0}, \mathbf{V})$. The observations are of the form $\{(Y_i, \Delta_i, \mathbf{W}_{i1}, \ldots, \mathbf{W}_{ir_i}), i = 1, \ldots, n\}$; that is, for each unobservable $\mathbf{X}_i$, we have r_i replicated observations of $\mathbf{W}_{ij}$'s ($j = 1, \ldots, r_i$). The number of replicates is allowed to vary across different subjects, and it also may occur that $r_i = 1$. The case where some covariates are error-free is accommodated in our model by setting the relevant terms in $\mathbf{V}$ to be 0. We further make the typical surrogacy assumption that $\mathbf{W}$ and Y are independent conditional on $\mathbf{X}$. Thus, given the unobserved true covariate $\mathbf{X}$, the observed covariate $\mathbf{W}$ does not contain any additional information.

Write the survival function and the probability density function for the event of interest as $S_e(Y|\mathbf{X}) = \exp\{-F(Y)e^{\mathbf{X}^T\boldsymbol{\beta}}\}$ and $f_e(Y|\mathbf{X}) = \exp\{-F(Y)e^{\mathbf{X}^T\boldsymbol{\beta}}\} f(Y)e^{\mathbf{X}^T\boldsymbol{\beta}}$. Similarly, for the censoring times, let $S_c(Y|\mathbf{X}) = \Pr(C \geq Y|\mathbf{X})$ and $f_c(Y|\mathbf{X}) = -\partial S_c(Y|\mathbf{X})/\partial Y$. Under the cure rate model, we know that $S_e(\infty|\mathbf{X}) = \exp(-e^{\mathbf{X}^T\boldsymbol{\beta}}) > 0$ and $S_c(\infty|\mathbf{X}) > 0$.

If $\mathbf{X}$ is observed, then the likelihood of a single observation (Y, Δ) given $\mathbf{X}$ can be written as

$$f(Y, \Delta|\mathbf{X})$$
$$= \left[\{f_e(Y|\mathbf{X})S_c(Y|\mathbf{X})\}^\Delta \{f_c(Y|\mathbf{X})S_e(Y|\mathbf{X})\}^{1-\Delta} \right]^{I(Y<\infty)}$$
$$\times \{S_e(\infty|\mathbf{X})S_c(\infty|\mathbf{X})\}^{I(Y=\infty)}.$$

Similar to the work of Zeng, Yin, and Ibrahim (2006), we construct a sieve of the distribution function F, and thus the log-likelihood is given by

$$\log f(Y, \Delta|\mathbf{X}) = \Delta I(Y<\infty)\{-F(Y)e^{\mathbf{X}^T\boldsymbol{\beta}} + \log F\{Y\}$$
$$+ \mathbf{X}^T\boldsymbol{\beta} + \log S_c(Y|\mathbf{X})\}$$
$$+ (1 - \Delta)I(Y<\infty)$$
$$\times \{\log f_c(Y|\mathbf{X}) - F(Y)e^{\mathbf{X}^T\boldsymbol{\beta}}\}$$
$$+ I(Y=\infty)\{\log S_c(\infty|\mathbf{X}) - e^{\mathbf{X}^T\boldsymbol{\beta}}\},$$

where $F\{Y\}$ denotes the jump size of $F(\cdot)$ at Y and $F(\cdot)$ is a right-continuous function with jumps at event times only. For

ease of exposition, we write $p_i \equiv F\{Y_i\}$, denote the ordered distinct failure times as $(Y_{(1)}, \ldots, Y_{(m)})$, and denote the corresponding jump sizes as $(p_{(1)}, \ldots, p_{(m)})$, where m is the number of distinct failure times. Under the constraint $\sum_{i=1}^m p_{(i)} = 1$, we introduce a Lagrange multiplier, λ, and maximize

$$\sum_{i=1}^n \log f(Y_i, \Delta_i|\mathbf{X}_i) - n\lambda \left(\sum_{i=1}^m p_{(i)} - 1 \right)$$

with respect to $(\boldsymbol{\beta}, \lambda, p_{(1)}, \ldots, p_{(m)})$. Collecting only the terms containing the unknown parameters $(\boldsymbol{\beta}, \lambda, F)$, this is equivalent to maximizing

$$\sum_{i=1}^n \left[-F(Y_i)e^{\mathbf{X}_i^T\boldsymbol{\beta}} + \Delta_i I(Y_i < \infty)(\log F\{Y_i\} + \mathbf{X}_i^T\boldsymbol{\beta}) \right]$$
$$- n\lambda \left(\sum_{i=1}^m p_{(i)} - 1 \right), \quad (2)$$

where $F(Y_i) = \sum_{Y_j \leq Y_i, \Delta_j = 1} F\{Y_j\}$ and $F(\infty) = 1$.

As opposed to using a profile likelihood approach (see Zeng et al. 2006), we take a backfitting procedure to maximize the log-likelihood. To be more specific, we solve for the $p_{(i)}$'s and λ by fixing $\boldsymbol{\beta}$, and solve for $\boldsymbol{\beta}$ by fixing the $p_{(i)}$'s and λ. The derivatives of (2) with respect to the $p_{(i)}$'s and λ are

$$\frac{1}{p_{(i)}} = \sum_{j=1}^n I(Y_{(i)} \leq Y_j < \infty)e^{\mathbf{X}_j^T\boldsymbol{\beta}} + n\lambda, \qquad i = 1, \ldots, m, \quad (3)$$

and

$$\sum_{i=1}^m p_{(i)} = 1. \quad (4)$$

Therefore, we can iterate between (3), (4), and

$$\sum_{i=1}^n \{\Delta_i I(Y_i < \infty) - F(Y_i)e^{\mathbf{X}_i^T\boldsymbol{\beta}}\}\mathbf{X}_i = \mathbf{0} \quad (5)$$

to obtain the estimators.

When $\mathbf{X}$ is not observable but the $\mathbf{W}$'s are observed instead, we modify the estimating equations so that they are functions of the observed data and yield consistent estimators. We keep (4) unchanged. Following the corrected score approach, we modify the m equations in (3) by replacing $e^{\mathbf{X}_i^T\boldsymbol{\beta}}$ with $e^{\mathbf{W}_i^T\boldsymbol{\beta} - \boldsymbol{\beta}^T\mathbf{V}\boldsymbol{\beta}/2}$,

$$\frac{1}{p_{(i)}} = \sum_{j=1}^n \frac{1}{r_j} \sum_{k=1}^{r_j} I(Y_{(i)} \leq Y_j < \infty)e^{\mathbf{W}_{jk}^T\boldsymbol{\beta} - \boldsymbol{\beta}^T\mathbf{V}\boldsymbol{\beta}/2} + n\lambda,$$
$$i = 1, \ldots, m. \quad (6)$$

An alternative way to handle multiple measurements is to take an average of the $\mathbf{W}_{ik}$'s for each i a priori to form a single "better" observation, that is, using

$$\frac{1}{p_{(i)}} = \sum_{j=1}^n I(Y_{(i)} \leq Y_j < \infty)e^{\bar{\mathbf{W}}_j^T\boldsymbol{\beta} - \boldsymbol{\beta}^T\mathbf{V}_j\boldsymbol{\beta}/2} + n\lambda$$

to replace (3), where $\bar{\mathbf{W}}_i = r_i^{-1}\sum_{k=1}^{r_i}\mathbf{W}_{ik}$ and $\mathbf{V}_i = r_i^{-1}\mathbf{V}$. In practice, we have found that the two treatments of the $\mathbf{W}_{ik}$'s

yield very similar results. To modify (5), we replace $\mathbf{X}_i$ with $\mathbf{W}_i$ and $e^{\mathbf{X}_i^T \boldsymbol{\beta}} \mathbf{X}_i$ with $e^{\mathbf{W}_i^T \boldsymbol{\beta} - \boldsymbol{\beta}^T \mathbf{V} \boldsymbol{\beta}/2}(\mathbf{W}_i - \mathbf{V}\boldsymbol{\beta})$ to obtain

$$\sum_{i=1}^{n} \frac{1}{r_i} \sum_{k=1}^{r_i} \Big\{ \Delta_i I(Y_i < \infty) \mathbf{W}_{ik}$$
$$- F(Y_i) e^{\mathbf{W}_{ik}^T \boldsymbol{\beta} - \boldsymbol{\beta}^T \mathbf{V} \boldsymbol{\beta}/2} (\mathbf{W}_{ik} - \mathbf{V}\boldsymbol{\beta}) \Big\} = \mathbf{0}. \quad (7)$$

The final estimators under the corrected scores can be obtained by solving (4), (6), and (7) simultaneously.

3. ASYMPTOTIC PROPERTIES

For ease of exposition, we focus on the situation in which we have one surrogate $\mathbf{W}$ for the true unobserved $\mathbf{X}$. We first introduce some notation and define $l^\infty(\mathcal{H})$ as the space of all bounded linear functionals on $\mathcal{H}$, where

$$\mathcal{H} = \{(\mathbf{h}_1, h_2) : \mathbf{h}_1 \in \mathcal{R}^q, \|\mathbf{h}_1\| < 1,$$
$$h_2 \text{ is a function in } [0, \infty) \text{ with } \|h_2\|_V \leq 1\}$$

and $\|h_2\|_V$ is the total variation of h_2. Let $l(\boldsymbol{\beta}, F)$ be the log-likelihood conditional on $\mathbf{X}$,

$$l(\boldsymbol{\beta}, F) = -F(Y) e^{\mathbf{X}^T \boldsymbol{\beta}} + \Delta I(Y < \infty) \{\log f(Y) + \mathbf{X}^T \boldsymbol{\beta}\},$$

where we omit the part of $l(\boldsymbol{\beta}, F)$ that does not involve $\boldsymbol{\beta}$ or F. Denote the derivative of $l(\boldsymbol{\beta}, F)$ with respect to $\boldsymbol{\beta}$ as $\mathbf{l}_{\boldsymbol{\beta}}(\boldsymbol{\beta}, F)$ and write $l_F(\boldsymbol{\beta}, F)[\int Q_F(h_2) \, dF]$ as the derivative of $l(\boldsymbol{\beta}, F)$ along the path $(\boldsymbol{\beta}, F_\epsilon = F + \epsilon \int Q_F(h_2) \, dF), \epsilon \in (-\epsilon_0, \epsilon_0)$ for a small constant $\epsilon_0 > 0$, where $Q_F(h_2) = h_2(t) - \int_0^\infty h_2(t) \, dF(t)$. This operation ensures that $Q_F(h_2)$ integrates to 0, and thus the perturbed F remains a valid cdf. This restriction plays the same role as the Lagrange multiplier. The corrected scores can be constructed by replacing the terms involving $\mathbf{X}$ in $\mathbf{l}_{\boldsymbol{\beta}}(\boldsymbol{\beta}, F)$ and $l_F(\boldsymbol{\beta}, F)[\int Q_F(h_2) \, dF]$ with those involving $\mathbf{W}$. We denote the expressions after such replacement as $\mathbf{S}_{\boldsymbol{\beta}}(\boldsymbol{\beta}, F)$ and $S_F(\boldsymbol{\beta}, F)[\int Q_F(h_2) \, dF]$. Note that $\int Q_F(h_2) \, dF$ does not involve $\mathbf{X}$ or $\mathbf{W}$. Straightforward calculation yields that

$$\mathbf{S}_{\boldsymbol{\beta}}(\boldsymbol{\beta}, F) = -F(Y) e^{\mathbf{W}^T \boldsymbol{\beta} - \boldsymbol{\beta}^T \mathbf{V} \boldsymbol{\beta}/2}(\mathbf{W} - \mathbf{V}\boldsymbol{\beta}) + \Delta I(Y < \infty) \mathbf{W}$$

and

$$S_F(\boldsymbol{\beta}, F)\left[\int Q_F(h_2) \, dF\right]$$
$$= -\int_0^Y Q_F(h_2) \, dF(t) \, e^{\mathbf{W}^T \boldsymbol{\beta} - \boldsymbol{\beta}^T \mathbf{V} \boldsymbol{\beta}/2}$$
$$+ \Delta I(Y < \infty) Q_F\{h_2(Y)\}.$$

Let $\mathbb{P}_n$ and $\mathbb{P}$ denote the empirical measure of n iid observations and the expectation; that is, for any measurable function $g(Y, \Delta, \mathbf{X})$ in $L_2(P)$,

$$\mathbb{P}_n[g(Y, \Delta, \mathbf{X})] = \frac{1}{n} \sum_{i=1}^{n} g(Y_i, \Delta_i, \mathbf{X}_i) \qquad \text{and}$$

$$\mathbb{P}[g(Y, \Delta, \mathbf{X})] = E[g(Y, \Delta, \mathbf{X})].$$

We assume that our model is identifiable and that the following regularity conditions are satisfied:

(C1) The covariate $\mathbf{W}$ is bounded with probability 1.

(C2) Conditional on $\mathbf{X}$, the censoring time C is independent of T, and $P(C = \infty | \mathbf{X}) > 0$.

(C3) The true parameter $\boldsymbol{\beta}_0$ belongs to the interior of a known compact set $\mathcal{B}_0$, and the true cdf F_0 is differentiable with its first derivative $f_0(t) > 0$ for all $t \in \mathcal{R}^+$.

These are rather mild conditions that are routinely made in cure rate models. We now present the asymptotic properties of the estimators, including strong consistency, asymptotic normality, and the variance estimation formula.

Theorem 1. Under the regularity conditions, assume the limiting estimating equation

$$\mathbb{P}\left\{\mathbf{S}_{\boldsymbol{\beta}}(\boldsymbol{\beta}, F)^T \mathbf{h}_1 + \mathbf{S}_F(\boldsymbol{\beta}, F)\left[\int Q_F(h_2) \, dF\right]\right\} = 0$$

has a unique zero. With probability 1, the estimators $\hat{\boldsymbol{\beta}}_n$ and $\hat{F}_n(t)$ of (4), (6), and (7) satisfy

$$|\hat{\boldsymbol{\beta}}_n - \boldsymbol{\beta}_0| \to \mathbf{0} \qquad \text{and} \qquad \sup_{t \in \mathcal{R}^+} |\hat{F}_n(t) - F_0(t)| \to 0.$$

Theorem 2. Under the regularity conditions, $\sqrt{n}(\hat{\boldsymbol{\beta}}_n - \boldsymbol{\beta}_0, \hat{F}_n - F_0)$ converges weakly to a mean-0 Gaussian process in $l^\infty(\mathcal{H})$.

The proofs of these two theorems depend heavily on the empirical process theory (van der Vaart and Wellner 2000), which are outlined in the Appendix.

Theorem 3. Under the regularity conditions, the estimator $\hat{\boldsymbol{\beta}}_n$ satisfies

$$\sqrt{n}(\hat{\boldsymbol{\beta}}_n - \boldsymbol{\beta}_0) \to N(\mathbf{0}, \mathbf{A}^{-1}\mathbf{B}(\mathbf{A}^{-1})^T)$$

in distribution as $n \to \infty$, where

$$\mathbf{A} = E\Bigg(e^{\mathbf{W}^T \boldsymbol{\beta} - \boldsymbol{\beta}^T \mathbf{V} \boldsymbol{\beta}/2}\Big[F_0(Y)\{\mathbf{V} - (\mathbf{W} - \mathbf{V}\boldsymbol{\beta})(\mathbf{W} - \mathbf{V}\boldsymbol{\beta})^T\}$$
$$- (\mathbf{W} - \mathbf{V}\boldsymbol{\beta})\int_0^Y \mathbf{b}_4(y)^T \, dF_0(y) \Big] \Bigg)^T,$$

$$\mathbf{B} = \left\{ \mathbf{S}_{\boldsymbol{\beta}}(\boldsymbol{\beta}_0, F_0) + S_F(\boldsymbol{\beta}_0, F_0)\left[\int_0^Y \mathbf{b}_4(y) \, dF_0(y)\right] \right\}^{\otimes 2},$$

and $\mathbf{b}_4$ is given in (A.5) in the Appendix.

The derivation of the variance sandwich formula with covariate measurement errors is very different from that without measurement errors, as shown in the Appendix.

4. NONNORMAL AND NONADDITIVE ERROR

Measurement error models often require transforming covariates toward the error normality and additivity. Considering one component of $\mathbf{W}$ and $\mathbf{X}$, we need to find a suitable transformation function ϕ so that $\phi(W) = \phi(X) + U$, where U follows a mean-0 normal distribution. When the transformation ϕ belongs to a parametric family indexed by $\boldsymbol{\gamma}$, for the case with duplicates ($r_i = 2$), we have that

$$\phi(W_1, \boldsymbol{\gamma}) = \phi(X, \boldsymbol{\gamma}) + U_1, \qquad \phi(W_2, \boldsymbol{\gamma}) = \phi(X, \boldsymbol{\gamma}) + U_2,$$

where U_1 and U_2 are independent mean-0 normal variables. We can estimate the parameter $\boldsymbol{\gamma}$ through the maximum likelihood approach based on $\{\phi(W_{i1}, \boldsymbol{\gamma}) - \phi(W_{i2}, \boldsymbol{\gamma})\}/\sqrt{2}$, for

$i = 1, \ldots, n$. But in many practical situations, a standard transformation family, such as the Box–Cox or power transformation, may not be sufficient to achieve the desired normal and additive error structure. Eckert et al. (1997) proposed a class of transformations based on piecewise cubic spline functions. This family of transformation is nonparametric and versatile and often performs superior to the Box–Cox transformation. However, its implementation can be difficult, and the transformation contains several ad hoc procedures.

To enhance the flexibility of our model, we propose a transformation that is easy to use and completely data-driven. We first sort all of the W_{ij}'s in an increasing order, denoted as $(W_{(1)}, W_{(2)}, \ldots, W_{(2n)})$. Let $b_i = \phi(W_{i1}) - \phi(W_{i2})$, $b_{(i)}$'s be the order statistics, and let $(q_1, q_2, \ldots, q_n)$ correspond to the $(.5/n, 1.5/n, \ldots, 1 - .5/n)$ quantiles of the standard normal distribution. Then we search for the set of $\phi(W_{ij})$'s that minimizes $\sum_{i=1}^{n}[\{b_{(i)} - \mu_b\}/\sigma_b - q_i]^2$, where μ_b and σ_b^2 are the sample mean and sample variance of the b_i's. The minimization is performed under a monotonic constraint that the $\phi(W_{ij})$'s follow exactly the same order as the W_{ij}'s, that is, $\phi(W_{(1)}) \leq \phi(W_{(2)}) \leq \cdots \leq \phi(W_{(2n)})$. The basic intuition behind this operation is that we want to find a transformation ϕ so that the resulting n sample quantiles are the closest to the expected quantiles in terms of the mean squared error (MSE). Other than monotonicity, we impose no constraints on ϕ; thus this transformation is more flexible than those proposed in the literature. For convenience, we use the MSE as the evaluation criterion for the transformation; one certainly could opt for other criteria, such as the mean absolute deviation or a weighted average, which may emphasize the central part more than the tail part of the data or may focus only on the maximum distance.

The proposed transformation is rank-preserving but cannot make a distinction between ϕ and $a_0 + a_1\phi$ for any constants a_0 and a_1. Thus, to ensure identifiability, we set the first two values, $\phi(W_{(1)})$ and $\phi(W_{(2)})$, to two constants, say $\phi(W_{(1)}) = 1$ and $\phi(W_{(2)}) = 2$. Our original problem involves an order-constrained minimization, which often requires rather specialized optimization routines. If we reparameterize and take $\phi(W_{(i)}) = \sum_{j=1}^{i} e^{\tau_j}$, then we can minimize $\sum_{i=1}^{n}[\{b_{(i)} - \mu_b\}/\sigma_b - q_i]^2$ without constraints to obtain the τ_j's and hence the $\phi(W_{ij})$'s. Note that a single value change in any of the τ_j's would cause changes in μ_b and σ_b; thus the optimization cannot be simplified by investigating each individual term separately. In addition, the fixed order of $\phi(W_{ij})$'s does not imply a fixed order of b_i's; thus the objective function may not be differentiable at the τ_j values at which a change in the order of b_i's occurs. Because of these considerations, we use a large-scale Nelder–Mead simplex method as the optimization procedure, in combination with multiple sets of dispersed starting values for τ_j's, to avoid convergence to local minima. It is worth pointing out that although the optimal solution gives the best transformation toward normality, in reality, we would be content as long as the resulting $\phi(W_{i1}) - \phi(W_{i2})$ was sufficiently close to normality. Various procedures can be used to examine the performance of the transformation. We formulate the Pearson-type statistic in the form of $\sum_{k=1}^{K}(E_k - O_k)^2/E_k$, where K is the number of partitions of the data space, and E_k and O_k are the expected and observed bin counts. Under the null model in

which $(b_i - \mu_b)/\sigma_b$ follows the standard normal distribution, the Pearson statistic asymptotically follows a chi-squared distribution with degrees of freedom $K - 1$ (see, e.g., Rao 1973). The proposed nonparametric transformation is straightforward and is quite effective, as we show in our numerical studies. Once we obtain the $\phi(W_{ij})$'s, the variance V can be easily estimated using the sample variance of $\{\phi(W_{i1}) - \phi(W_{i2})\}/\sqrt{2}$, $i = 1, \ldots, n$.

In general, there is no guarantee that a normal additive error can always be achieved. In cases where the normal error cannot be obtained, the estimating equations (3) and (5) should be corrected by replacing $\mathbf{X}_j$, $e^{\mathbf{X}_j^T \boldsymbol{\beta}}$ with $\mathbf{W}_j - E(\mathbf{U}_j)$, $e^{\mathbf{W}_j^T \boldsymbol{\beta}}/E(e^{\mathbf{U}_j^T \boldsymbol{\beta}})$ and $\mathbf{X}_j e^{\mathbf{X}_j^T \boldsymbol{\beta}}$ with $\mathbf{W}_j e^{\mathbf{W}_j^T \boldsymbol{\beta}}/E(e^{\mathbf{U}_j^T \boldsymbol{\beta}}) - e^{\mathbf{W}_j^T \boldsymbol{\beta}} E(\mathbf{U}_j e^{\mathbf{U}_j^T \boldsymbol{\beta}})/E(e^{\mathbf{U}_j^T \boldsymbol{\beta}})^2$.

5. NUMERICAL STUDIES

5.1 Simulation

We conducted three sets of simulation studies to examine the small-sample performance of the proposed methods. First, we studied a cure rate model function,

$$S(t|X_1, X_2) = \exp\{-\exp(\beta_0 + \beta_1 X_1 + \beta_2 X_2)F(t)\}, \quad (8)$$

where X_1 is a uniformly distributed random variable on $[0, 1]$ and subject to measurement errors and X_2 is a Bernoulli random variable that takes a value of 0 or 1 with equal probability. We took the true parameters $\beta_0 = .5$, $\beta_1 = 1$, $\beta_2 = -.5$, and $F(t) = 1 - \exp(-t)$. The measurement error model was formulated as $W = X_1 + U$, where U was a normal random variable with mean 0 and standard deviation σ. We considered $\sigma = .1$ and $.2$ to examine the impact of the measurement error on the estimators. When the censoring time was generated from an exponential distribution with mean 1, designated as exp(1), the resulting data set had an approximate censoring rate of 17%, and a cure rate of 8%; and when the censoring time was generated from exp(.1), it yielded a censoring rate of 33%. We took sample sizes of $n = 200$ and 300, and performed 1,000 simulations under each configuration. For each data replicate, we implemented the backfitting procedure to estimate β_0, β_1, and β_2 and the corresponding variances. The corrected estimating equations were solved using the Newton–Raphson algorithm, which converged very fast and was quite robust to the initial values. For comparison, we also carried out a naive estimation procedure, in which the measurement error was ignored and W was treated as X_1. The simulation results are presented in Tables 1 and 2, corresponding to censoring rates of 17% and 33%. As we can see, even with a small measurement error scale, $\sigma = .1$, the naive estimator of β_0 was biased upward and that of β_1 was biased downward, and these biased increased severely as the measurement error increased to $\sigma = .2$. The corresponding coverage probabilities of 95% confidence intervals were under the nominal level, especially for the cases with $\sigma = .2$. Interestingly, because covariate X_2 was measured precisely, the estimator of β_2 under the naive method performed well; the bias was negligible, and the coverage probability was close to 95%. In contrast, the proposed estimator successfully corrected the bias under all of the scenarios. Moreover, the estimated variances based on the asymptotic normal approximation formula

Table 1. Simulation results under model (8) with 17% censoring

σ	n	Estimate	Proposed method			Naive method		
			β_0	β_1	β_2	β_0	β_1	β_2
.1	200	Bias	−.011	.031	.002	.041	−.089	.006
		Empirical variance	.039	.095	.031	.035	.072	.030
		Estimated variance	.037	.098	.028	.031	.073	.027
		95% cv	.941	.956	.936	.923	.927	.929
	300	Bias	−.005	.021	−.001	.046	−.096	.003
		Empirical variance	.028	.066	.019	.025	.050	.018
		Estimated variance	.025	.064	.018	.020	.048	.018
		95% cv	.932	.939	.956	.901	.926	.950
.2	200	Bias	−.007	.028	−.003	.152	−.336	.007
		Empirical variance	.054	.164	.032	.033	.058	.030
		Estimated variance	.052	.156	.040	.026	.055	.027
		95% cv	.941	.946	.944	.805	.687	.936
	300	Bias	−.008	.026	−.004	.148	−.331	.005
		Empirical variance	.034	.103	.020	.022	.038	.018
		Estimated variance	.033	.100	.019	.017	.037	.018
		95% cv	.943	.952	.951	.764	.576	.950

NOTE: 95% CV represents the coverage probability of 95% confidence intervals.

were quite close to the empirical variances, and our method produced satisfactory coverage probabilities at the 95% nominal level. When σ increased, the estimated variances for the β's increased as more variability was incorporated into the model and the estimation procedure. However, the opposite was true for the naive estimators. Because W was treated as the true covariate X_1, more variation in the covariate would produce better estimators; the variances using the naive method were in fact smaller for $\sigma = .2$ compared with those with $\sigma = .1$. At a higher censoring rate, as shown in Table 2, similar conclusions can be drawn. The estimated variances increased as the censoring percentage increased and decreased as the sample size grew large.

Our second simulation was designed to study a scenario with replicates for mismeasured covariates. We considered a cure rate model,

$$S(t|X_1, X_2, X_3, X_4) = \exp\{-\exp(\beta_0 + \beta_1 X_1 + \beta_2 X_2 + \beta_3 X_3 + \beta_4 X_4) F(t)\}, \quad (9)$$

where both X_1 and X_2 are Bernoulli random variables that take a value of 1 with probabilities of .5 and .6, and X_3 and X_4 are generated from uniform distributions on $[-.5, .5]$ and $[0, 1]$. Here X_4 was unobservable; instead, we observed two replicates (W_1, W_2), where each replicate was X_4 plus a normal error with mean 0 and standard deviation $\sigma = .2$. The true parameters were $\beta_0 = .5$, $\beta_1 = .5$, $\beta_2 = -.5$, $\beta_3 = 1$, $\beta_4 = -1$, and $F(t) = 1 - \exp(-t)$. The censoring times were generated independently from exp(1), yielding an approximate censoring

Table 2. Simulation results under model (8) with 33% censoring

σ	n	Estimate	Proposed method			Naive method		
			β_0	β_1	β_2	β_0	β_1	β_2
.1	200	Bias	−.006	.016	−.003	.046	−.104	.000
		Empirical variance	.054	.135	.038	.047	.102	.037
		Estimated variance	.050	.126	.036	.041	.093	.034
		95% cv	.949	.946	.937	.928	.924	.935
	300	Bias	−.005	.006	.003	.046	−.110	.006
		Empirical variance	.035	.085	.025	.031	.065	.024
		Estimated variance	.033	.082	.024	.028	.062	.023
		95% cv	.939	.950	.945	.917	.921	.944
.2	200	Bias	−.025	.078	−.008	.141	−.312	.007
		Empirical variance	.063	.207	.042	.038	.071	.038
		Estimated variance	.070	.205	.038	.036	.070	.034
		95% cv	.958	.951	.938	.863	.776	.934
	300	Bias	−.001	.032	−.009	.155	−.331	.003
		Empirical variance	.048	.149	.026	.030	.055	.024
		Estimated variance	.044	.128	.025	.023	.047	.023
		95% cv	.943	.932	.946	.790	.646	.950

NOTE: 95% CV represents the coverage probability of 95% confidence intervals.

Table 3. Simulation results under model (9) with 25% censoring

		Proposed method					Naive method				
n	Estimate	β_0	β_1	β_2	β_3	β_4	β_0	β_1	β_2	β_3	β_4
Average $\bar{W}$											
200	Bias	.021	.009	−.013	.028	−.037	−.091	.005	−.008	.020	.184
	Empirical variance	.078	.044	.042	.134	.182	.060	.042	.040	.130	.108
	Estimated variance	.069	.042	.042	.128	.173	.053	.041	.040	.123	.099
	95% cv	.931	.952	.953	.946	.948	.920	.950	.953	.946	.896
300	Bias	.012	.002	−.006	.013	−.023	−.096	−.002	−.001	.006	.189
	Empirical variance	.051	.030	.028	.082	.115	.039	.030	.027	.081	.069
	Estimated variance	.045	.028	.027	.084	.110	.035	.027	.027	.081	.065
	95% cv	.926	.948	.950	.960	.953	.912	.947	.952	.958	.869
Replicates (W_1, W_2)											
200	Bias	.023	.009	−.012	.028	−.040	−.162	.002	−.005	.014	.325
	Empirical variance	.080	.044	.042	.135	.187	.051	.042	.039	.129	.073
	Estimated variance	.069	.042	.042	.128	.182	.046	.041	.040	.122	.068
	95% cv	.929	.950	.955	.944	.956	.877	.954	.954	.945	.745
300	Bias	.012	.002	−.006	.013	−.024	−.166	−.005	.002	.001	.327
	Empirical variance	.052	.030	.028	.082	.117	.034	.029	.027	.080	.047
	Estimated variance	.045	.028	.027	.084	.114	.030	.027	.026	.081	.045
	95% cv	.926	.946	.951	.959	.952	.835	.945	.953	.956	.654

NOTE: 95% CV represents the coverage probability of 95% confidence intervals.

rate of 25%. We implemented two different treatments of the replicates: averaging W_1 and W_2 to obtain a single "better" measurement, $\bar{W} = (W_1 + W_2)/2$, and incorporating each individual measurement (W_1, W_2) in the estimation as in (6) and (7). The simulation results, given in Table 3, show that the estimates using $\bar{W}$ or (W_1, W_2) were comparable. In particular, the bias could be corrected satisfactorily compared with the naive method, the asymptotic variance provided a good approximation of the empirical variance, and the 95% coverage probability closely matched the nominal level. As the sample size increased, the bias and variance decreased. But the naive method had obvious biases in the estimates of β_0 and β_4, whereas the parameter estimates for the precisely measured covariates X_1, X_2, and X_3 were satisfactory. Furthermore, it is interesting that using the duplicates (W_1, W_2) led to much worse biases and coverage probabilities than those resulting from using the average $\bar{W}$ based on the naive method. The averaged covariate values could offset the effect of measurement errors to a certain extent, because the random noise would diminish by averaging over multiple replicates.

In the third simulation, we conducted a sensitivity analysis to demonstrate the effectiveness of the proposed transformation and the robustness of our model to the misspecified normal additive error. We examined model (8) with measurement error structure $W = \exp(X_1 + U)$, where we generated U from a normal, a Student t with degrees of freedom 10 and 5, and a uniform distribution. We set the mean of U to 0 and the standard deviation of U to .2 for all of the scenarios. We implemented the proposed transformation on the covariate, even though for all cases but the first, whether or not a normal additive error structure could be obtained is not clear. Table 4 shows that the proposed method performed well by imposing our transformation when W is linked to X through a nonnormal and nonadditive error. We could capture the true transformation that recovered the normal additive error structure. When the normality

assumption was violated, our estimation procedure appeared to be quite robust and still produced estimates with very small biases. As the degree of freedom of the t distribution decreased to 5, the performance deteriorated slightly. In the simulations not reported here, we also explored other transformations, such as $W = (X_1 + U)^3$, and found similar results.

In the foregoing simulations, the censoring distribution has an infinite support. Because in reality the censoring time is always finite, we also conducted simulations in which the censoring distribution was finitely supported. Here a subject is considered cured if the subject is censored and the corresponding censoring time is larger than the largest observed event time. The estimator remains consistent, and the variance estimation and the 95% coverage probability are satisfactory as well.

5.2 Lung Cancer Data

As an illustration, we applied the cure rate model with measurement errors to the lung cancer data set. The study group comprised 280 patients. The covariates of interest included either one or two readings of biomarker expression, tumor histology (61% adenocarcinoma = 1; 39% squamous cell carcinoma = 0), and patient age (range, 34 to 90 years; mean, 66 years) and sex (52% female = 1; 48% male = 0). The covariate age was standardized to have mean 0 and variance 1. The underlying true expression of the biomarker could not be measured precisely. For half of the patients, only one reading of biomarker expression was available, whereas for the other half, two different readings were recorded, with no preference given to either reading.

For the 140 patients with 2 readings of biomarker expression, we took the difference of the logarithm of the 2 readings and found that the original observations of biomarker expression did not satisfy the normal additive error structure. After carrying out our transformation on the readings of biomarker

Table 4. Transformation and sensitivity analysis of the error structure under model (8)

n	Error	Estimate	Proposed method			Naive method		
			β_0	β_1	β_2	β_0	β_1	β_2
200	Normal	Bias	−.017	.047	−.003	.147	−.334	.008
		Empirical variance	.055	.163	.032	.034	.057	.029
		Estimated variance	.052	.159	.030	.026	.056	.028
		95% cv	.952	.951	.938	.808	.695	.943
	t_{10}	Bias	−.015	.044	−.006	.147	−.334	.009
		Empirical variance	.057	.173	.033	.035	.061	.030
		Estimated variance	.051	.159	.030	.026	.056	.028
		95% cv	.939	.942	.946	.812	.690	.946
	t_5	Bias	−.084	.203	−.011	.120	−.273	.007
		Empirical variance	.066	.220	.033	.036	.067	.030
		Estimated variance	.062	.203	.031	.027	.061	.028
		95% cv	.948	.939	.946	.847	.780	.947
	Uniform	Bias	−.017	.047	−.003	.145	−.329	.007
		Empirical variance	.054	.150	.031	.035	.055	.029
		Estimated variance	.052	.158	.030	.026	.057	.028
		95% cv	.954	.957	.952	.803	.718	.944
300	Normal	Bias	−.006	.017	−.001	.150	−.341	.009
		Empirical variance	.035	.106	.020	.022	.041	.019
		Estimated variance	.033	.100	.019	.017	.037	.018
		95% cv	.936	.944	.951	.762	.578	.948
	t_{10}	Bias	−.009	.027	−.002	.147	−.333	.007
		Empirical variance	.033	.103	.022	.021	.039	.020
		Estimated variance	.033	.099	.019	.017	.037	.018
		95% cv	.950	.941	.934	.756	.586	.937
	t_5	Bias	−.075	.180	−.006	.120	−.272	.006
		Empirical variance	.038	.128	.023	.022	.042	.020
		Estimated variance	.039	.124	.020	.018	.040	.018
		95% cv	.952	.941	.935	.816	.729	.937
	Uniform	Bias	−.006	.021	−.003	.147	−.331	.007
		Empirical variance	.032	.099	.020	.021	.038	.019
		Estimated variance	.033	.098	.019	.017	.037	.018
		95% cv	.957	.945	.941	.768	.567	.951

NOTE: 95% CV represents the coverage probability of 95% confidence intervals.

expression, we can see that the error structure was much closer to normal based on the quantile–quantile plot in Figure 2. We also performed the Pearson chi-squared test, under which we obtained a p value $> .7$ for K ranging from 4 to 10; thus a normal error structure after the transformation was quite convincing. For patients with duplicated readings of biomarker expression, we used the averaged value $\bar{W}$ and the individual observations (W_1, W_2) for the analysis. Table 5 shows that ignoring the measurement error could cause severe bias, particularly in the estimates of the intercept and the biomarker expression effect. We found that biomarker expression significantly affected patient survival; a higher expression was associated with a shorter survival time. The naive method tended to underestimate the variance and produce a downward bias for the biomarker effect. As for other error-free covariates, the proposed method and the naive method yielded similar estimates. Patients with a tumor histology of adenocarcinoma had a significantly better survival rate than those with squamous cell carcinoma; moreover, younger patients could be expected to live longer at a lower risk of death. There was no significant difference in survival across

sex in this study population, although there was a trend that women might live longer.

The cure threshold in our model could be determined through consultation with physicians, which is a medical issue based on the patient population and disease status. Because such a threshold is restricted to lie to the right of the largest failure time, we conducted a sensitivity analysis by taking the cure threshold at 7, 7.5, or 8 years. We found that the parameter estimates were not sensitive to the specification of the threshold, because it only affected the censored observations at the right tail.

6. DISCUSSION

We have proposed a semiparametric cure rate model with covariate measurement errors. The model inherits the well-known proportional hazards structure, with the corrected score functions derived based on NPMLE to estimate β and $F(t)$. The asymptotic consistency and root-n convergence of the estimators were established through modern empirical process techniques. Simulation studies showed that the corrected score approach produced consistent estimators, whereas the naive estimation typically led to severe biases.
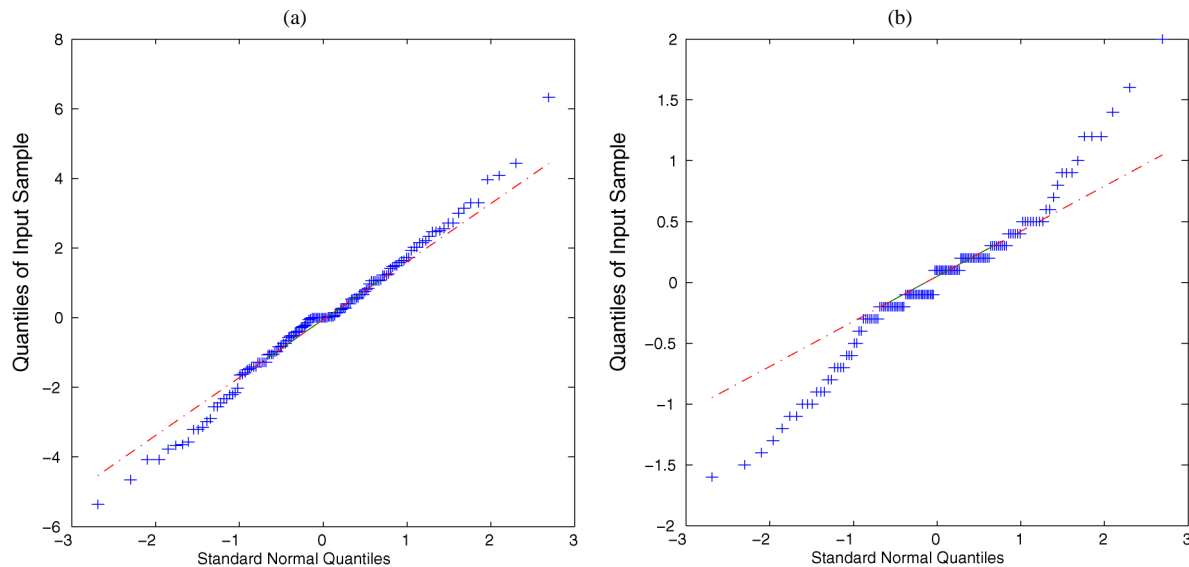
Figure 2. Quantile–quantile plots of the error with the transformed readings of biomarker expression (a) and the original observations (b) for the lung cancer data.

For the proportional hazard cure model, the NPMLE and partial likelihood estimator were in fact identical. This can be verified by assigning $n\lambda$ in NPMLE to $\sum_{Y_j=\infty} e^{\mathbf{X}_j^T \boldsymbol{\beta}}$. The details of this derivation are given in the Appendix. Naturally, the corrected score estimator thus also can be derived equivalently through the partial likelihood approach. In our view, using NPMLE has several advantages. First, consistency is self-evident through a conditional distribution argument. Second, the cure rate model and the Cox model are fundamentally different; therefore, to estimate the intercept b using the partial likelihood procedure, we need to reparameterize the model by taking $b = \log \Lambda_0(\infty)$. Third, the partial likelihood approach is restricted only to the proportional hazards structure, whereas NPMLE is much more general. For example, the proportional odds cure model can be easily handled by NPMLE, whereas the partial likelihood is not applicable (see Zeng et al. 2006). Even though finding a corrected score is not always straightforward or even possible, a general Monte Carlo–corrected score method can be implemented in practice. In this regard,

$\mathbf{W}_i$ can be augmented with $\tilde{\mathbf{U}}_i \sqrt{-1}$ to form $\tilde{\mathbf{W}}_i$, where $\tilde{\mathbf{U}}_i$ has the same distribution as the measurement error $\mathbf{U}_i$; calculate the score function using $\tilde{\mathbf{W}}_i$; and set the real part to 0 to solve for $\boldsymbol{\beta}$. Although the Monte Carlo–corrected score approach does not always guarantee a consistent estimator, in the case when a true corrected score does exist, it will be consistent; thus it can be viewed as a numerical way of finding a corrected score. Further exploration in these areas should be worthwhile.

The corrected-score method belongs to the family of functional approaches that make no distributional assumptions on the unobservable true covariates, as opposed to structural models that specify a distribution of $\mathbf{X}$. However, the corrected score and its generalized form depend on the additive error structure. Because in reality not all measurements can be transformed to normality and/or additivity, the more general semiparametric approach proposed by Tsiatis and Ma (2004) is worth exploring. Preliminary studies toward this end have uncovered several modeling and computational issues, including the need to estimate the censoring mechanism or strong assumptions, such as censoring, independent of the covariates. These same difficulties also prevent us from absorbing the transformation inside of the estimation procedure itself.

An alternative approach in functional measurement error models is based on the simulation-extrapolation (SIMEX) method (Cook and Stefanski 1994; Stefanski and Cook 1995; Li and Lin 2003; Greene and Cai 2004). SIMEX first simulates data sets with an increasing amount of measurement errors and then extrapolates back to the nonerror case. Because the correct extrapolation function is generally unknown, in theory SIMEX can produce only approximately consistent estimates. However, in practice its performance is often satisfactory, and sometimes it even outperforms the asymptotically "correct" methods. It would be interesting to implement SIMEX under the cure rate models with measurement errors.

In contrast to the usual classical measurement error structure, where $\mathbf{W} = \mathbf{X} + \mathbf{U}$, $\mathbf{U}$ is independent of $\mathbf{X}$, in another class of

Table 5. Regression coefficient estimates and estimated variances for the lung cancer data, using the averaged and individual reading of biomarker expression

Estimate	Intercept	Histology	Age	Sex	Biomarker
Averaged reading $\bar{W}$					
Proposed estimate	−.2904	−.5622	.4352	−.0687	.0505
Estimated variance	.2990	.0639	.0138	.0450	.0077
Naive estimate	−.1672	−.5306	.4337	−.0748	.0299
Estimated variance	.1347	.0489	.0130	.0426	.0026
Individual reading (W_1, W_2)					
Proposed estimate	−.2648	−.5555	.4348	−.0697	.0462
Estimated variance	.2885	.0624	.0138	.0450	.0074
Naive estimate	−.1448	−.5248	.4334	−.0758	.0261
Estimated variance	.0923	.0476	.0134	.0434	.0020

errors, called Berkson error, $\mathbf{X} = \mathbf{W} + \mathbf{U}$ and $\mathbf{U}$ is independent of $\mathbf{W}$. Berkson error models are often relatively easier to deal with, because the distribution of the unobservable variable $\mathbf{X}$ does not appear in the likelihood. In the Cox model framework, Zucker (2005) considered such an error structure and proposed a consistent estimator. Similar estimators can be developed for the cure rate model. Further consideration in the presence of a mixture of classical and Berkson errors may be also of interest.

APPENDIX: PROOFS

Proof of Theorem 1

Multiplying (6) by $\hat{p}_{(i)} = \hat{F}_n\{Y_i\}$ on both sides and summing over the m equations, we have

$$\hat{\lambda}_n = \frac{1}{n} \sum_{i=1}^{n} \Delta_i I(Y_i < \infty) - \int_0^{\infty} H_n(y, \hat{\boldsymbol{\beta}}_n) \, d\hat{F}_n(y), \qquad \text{(A.1)}$$

where

$$H_n(y, \hat{\boldsymbol{\beta}}_n) = \frac{1}{n} \sum_{Y_j < \infty} I(Y_j \geq y) e^{\mathbf{W}_j^T \hat{\boldsymbol{\beta}}_n - \hat{\boldsymbol{\beta}}_n \mathbf{V} \hat{\boldsymbol{\beta}}_n / 2}.$$

Thus $\hat{F}_n\{Y_i\} = \Delta_i / n\{\hat{\lambda}_n + H_n(Y_i, \hat{\boldsymbol{\beta}}_n)\}$. Obviously, from (A.1), $\hat{\lambda}_n$ should be bounded by a constant with probability 1; therefore, by choosing a subsequence, still indexed by $\{n\}$, we assume that $\hat{\lambda}_n \to \lambda^*$. By choosing a further subsequence, we assume that $\hat{\boldsymbol{\beta}}_n \to \boldsymbol{\beta}^*$ and $\hat{F}_n \to F^*$ pointwise.

Note that the classes $\{\mathbf{W}\}$ and $\{I(Y \geq y)\}$ are P–Donsker, because of their monotonicity and uniform boundedness. Under the continuously differentiable operation of taking the exponential and the algebraic operation of multiplication, the class

$$\{I(\infty > Y \geq y) e^{\mathbf{W}^T \boldsymbol{\beta} - \boldsymbol{\beta}^T \mathbf{V}\boldsymbol{\beta}/2} : \boldsymbol{\beta} \in \mathcal{B}_0\}$$

also is P–Donsker (see van der Vaart and Wellner 2000, thms. 2.7.5, 2.10.6, and 2.10.8) and thus is Glivenko–Cantelli. Due to the Glivenko–Cantelli theorem and the bounded convergence theorem, we conclude that uniformly in y, $H_n(y, \hat{\boldsymbol{\beta}}_n) \to H^*(y)$, where

$$H^*(y) = E\{I(\infty > Y \geq y) e^{\mathbf{W}^T \boldsymbol{\beta}^* - \boldsymbol{\beta}^* \mathbf{V}\boldsymbol{\beta}^*/2}\}.$$

Moreover, the right side of (A.1) converges to

$$\lambda^* = E\{\Delta I(Y < \infty)\} - E\left\{I(Y < \infty) \int_0^Y H^*(y) \, dF^*(y)\right\}.$$

We next show that $|\lambda^* + H^*(y)|$ is bounded away from 0. Because each $\hat{F}_n\{Y_i\}$ is nonnegative and $\sum_{i=1}^{n} \hat{F}_n\{Y_i\} = 1$, we have

$$1 = \sum_{i=1}^{n} \frac{I(Y_i < \infty)\Delta_i}{n(\hat{\lambda}_n + H_n(Y_i, \hat{\boldsymbol{\beta}}_n))} = \sum_{i=1}^{n} \frac{I(Y_i < \infty)\Delta_i}{n|\hat{\lambda}_n + H_n(Y_i, \hat{\boldsymbol{\beta}}_n)|}$$

$$\geq \frac{1}{n} \sum_{i=1}^{n} \frac{I(Y_i < \infty)\Delta_i}{|\hat{\lambda}_n + H_n(Y_i, \hat{\boldsymbol{\beta}}_n)| + \epsilon},$$

for any positive constant ϵ. Because $H_n(y, \hat{\boldsymbol{\beta}}_n)$ converges uniformly to $H^*(y)$, we have

$$\frac{1}{n} \sum_{i=1}^{n} \frac{I(Y_i < \infty)\Delta_i}{|\hat{\lambda}_n + H_n(Y_i, \hat{\boldsymbol{\beta}}_n)| + \epsilon} - \frac{1}{n} \sum_{i=1}^{n} \frac{I(Y_i < \infty)\Delta_i}{|\lambda^* + H^*(Y_i)| + \epsilon} \to 0.$$

Then, after taking limits on both sides, we obtain $1 \geq E\{\Delta I(Y < \infty)/(|\lambda^* + H^*(Y)| + \epsilon)\}$. Let $\epsilon \to 0$; then we have

$$1 \geq \int_0^{\infty} \frac{c_0 \, dy}{|\lambda^* + H^*(y)|}, \qquad \text{(A.2)}$$

where c_0 is a positive constant. This implies that there exists a $\delta^* > 0$ such that $|\lambda^* + H^*(y)| > \delta^*$, because otherwise, we have that $\inf_y |\lambda^* + H^*(y)| = 0$. If $H^*(\infty) + \lambda^* = 0$, then $H^*(\infty) = -\lambda^* = 0$. In this case, $|\lambda^* + H^*(y)| = H^*(y) < 1$ for sufficiently large y, which contradicts (A.2). If $\lambda^* = -H^*(y_0)$ for a finite y_0, then (A.2) becomes $1 \geq c_0 \int_0^{\infty} 1/|H^*(y_0) - H^*(y)| \, dy$. This is impossible, because $H^*(y)$ is continuously differentiable in a neighborhood of y_0. Furthermore, $|\lambda^* + H^*(y)| > \delta^*$ implies that when n is large, $|\hat{\lambda}_n + H_n(y, \hat{\boldsymbol{\beta}}_n)| > \delta^*$. Note that $\hat{F}_n(y) = n^{-1} \sum_{i=1}^{n} \Delta_i I(Y_i \leq y)/|\hat{\lambda}_n + H_n(Y_i, \hat{\boldsymbol{\beta}}_n)|$ so $\hat{F}_n(y)$ converges uniformly to $F^*(y) = E\{\Delta I(Y \leq y)/|\lambda^* + H^*(Y)|\}$.

Based on the definitions of $\mathbf{S}_{\boldsymbol{\beta}}(\boldsymbol{\beta}, F)$ and $S_F(\boldsymbol{\beta}, F)[\int Q_F(h_2) \, dF]$, we have

$$\mathbb{P}_n\left\{\mathbf{S}_{\boldsymbol{\beta}}(\hat{\boldsymbol{\beta}}_n, \hat{F}_n)^T \mathbf{h}_1 + S_F(\hat{\boldsymbol{\beta}}_n, \hat{F}_n)\left[\int Q_{\hat{F}_n}(h_2) \, d\hat{F}_n\right]\right\} = 0$$

for any $(\mathbf{h}_1, h_2) \in \mathcal{H}$. Using the uniform convergence of $(\hat{\boldsymbol{\beta}}_n, \hat{F}_n)$ to $(\boldsymbol{\beta}^*, F^*)$, as $n \to \infty$, we obtain

$$\mathbb{P}\left\{\mathbf{S}_{\boldsymbol{\beta}}(\boldsymbol{\beta}^*, F^*)^T \mathbf{h}_1 + S_F(\boldsymbol{\beta}^*, F^*)\left[\int Q_{F^*}(h_2) \, dF^*\right]\right\} = 0.$$

On the other hand, we also have

$$\mathbb{P}\left\{\mathbf{S}_{\boldsymbol{\beta}}(\boldsymbol{\beta}_0, F_0)^T \mathbf{h}_1 + S_F(\boldsymbol{\beta}_0, F_0)\left[\int Q_{F_0}(h_2) \, dF_0\right]\right\}$$

$$= \mathbb{P}\left\{\mathbf{l}_{\boldsymbol{\beta}}(\boldsymbol{\beta}_0, F_0)^T \mathbf{h}_1 + l_F(\boldsymbol{\beta}_0, F_0)\left[\int Q_{F_0}(h_2) \, dF_0\right]\right\}$$

$$= 0, \qquad \text{(A.3)}$$

because of our construction. Based on the uniqueness assumption and continuity of F_0, we obtain $\boldsymbol{\beta}_0 = \boldsymbol{\beta}^*$ and $F^* = F_0$.

Proof of Theorem 2

Following the definition of $\mathcal{H}$, $\sqrt{n}(\hat{\boldsymbol{\beta}}_n - \boldsymbol{\beta}_0, \hat{F}_n - F_0)$ can be treated as a linear functional in the metric space $l^{\infty}(\mathcal{H})$, which is defined as

$$\sqrt{n}(\hat{\boldsymbol{\beta}}_n - \boldsymbol{\beta}_0, \hat{F}_n - F_0)(\mathbf{h}_1, h_2)$$

$$= \sqrt{n}(\hat{\boldsymbol{\beta}}_n - \boldsymbol{\beta}_0)^T \mathbf{h}_1 + \sqrt{n} \int h_2(t) \, d(\hat{F}_n - F_0).$$

We next establish the asymptotic distribution of $\sqrt{n}(\hat{\boldsymbol{\beta}}_n - \boldsymbol{\beta}_0, \hat{F}_n - F_0)$ in $l^{\infty}(\mathcal{H})$.

We denote the derivative of $\mathbf{S}_{\boldsymbol{\beta}}(\boldsymbol{\beta}, F)$ with respect to $\boldsymbol{\beta}$ as $\mathbf{S}_{\boldsymbol{\beta}\boldsymbol{\beta}}(\boldsymbol{\beta}, F)$, the derivative of $\mathbf{S}_{\boldsymbol{\beta}}(\boldsymbol{\beta}, F)$ with respect to F along the path $F_{\epsilon} = F + \epsilon(\hat{F}_n - F)$ as $\mathbf{S}_{\boldsymbol{\beta}F}(\boldsymbol{\beta}, F)[\hat{F}_n - F]$, the derivative of $S_F(\boldsymbol{\beta}, F)[\int Q_F(h_2) \, dF]$ with respect to $\boldsymbol{\beta}$ as $\mathbf{S}_{F\boldsymbol{\beta}}(\boldsymbol{\beta}, F) \times [\int Q_F(h_2) \, dF]$, and the derivative of $S_F(\boldsymbol{\beta}, F)[\int Q_F(h_2) \, dF]$ with respect to F along the path $F_{\epsilon} = F + \epsilon(\hat{F}_n - F)$ as $S_{FF}(\boldsymbol{\beta}, F) \times [\int Q_F(h_2) \, dF, \hat{F}_n - F]$. Explicitly, we have

$$\mathbf{S}_{\boldsymbol{\beta}\boldsymbol{\beta}}(\boldsymbol{\beta}, F)$$

$$= F(Y) e^{\mathbf{W}^T \boldsymbol{\beta} - \boldsymbol{\beta}^T \mathbf{V}\boldsymbol{\beta}/2} \{\mathbf{V} - (\mathbf{W} - \mathbf{V}\boldsymbol{\beta})(\mathbf{W} - \mathbf{V}\boldsymbol{\beta})^T\},$$

$$\mathbf{S}_{F\boldsymbol{\beta}}(\boldsymbol{\beta}, F)\left[\int Q_F(h_2) \, dF\right]$$

$$= -\int_0^Y Q_F(h_2) \, dF(t) e^{\mathbf{W}^T \boldsymbol{\beta} - \boldsymbol{\beta}^T \mathbf{V}\boldsymbol{\beta}/2} (\mathbf{W} - \mathbf{V}\boldsymbol{\beta}),$$

$$\mathbf{S}_{\boldsymbol{\beta}F}(\boldsymbol{\beta}, F)[\hat{F}_n - F]$$

$$= -\{\hat{F}_n(Y) - F(Y)\} e^{\mathbf{W}^T \boldsymbol{\beta} - \boldsymbol{\beta}^T \mathbf{V}\boldsymbol{\beta}/2} (\mathbf{W} - \mathbf{V}\boldsymbol{\beta}),$$

and

$$S_{FF}(\boldsymbol{\beta}, F)\left[\int Q_F(h_2)\, dF, \hat{F}_n - F\right]$$

$$= -e^{\mathbf{W}^T\boldsymbol{\beta} - \boldsymbol{\beta}^T\mathbf{V}\boldsymbol{\beta}/2} \int_0^Y Q_F(h_2)\, d(\hat{F}_n - F)$$

$$+ \left\{e^{\mathbf{W}^T\boldsymbol{\beta} - \boldsymbol{\beta}^T\mathbf{V}\boldsymbol{\beta}/2} F(Y) - I(Y < \infty)\Delta\right\} \int_0^\infty h_2(t)\, d(\hat{F}_n - F).$$

Our estimating equations require that

$$\mathbb{P}_n\left\{\mathbf{S}_{\boldsymbol{\beta}}(\hat{\boldsymbol{\beta}}_n, \hat{F}_n)^T\mathbf{h}_1 + S_F(\hat{\boldsymbol{\beta}}_n, \hat{F}_n)\left[\int Q_{\hat{F}_n}(h_2)\, d\hat{F}_n\right]\right\} = 0.$$

Noting (A.3), we obtain

$$\sqrt{n}(\mathbb{P}_n - \mathbb{P})\left\{\mathbf{S}_{\boldsymbol{\beta}}(\hat{\boldsymbol{\beta}}_n, \hat{F}_n)^T\mathbf{h}_1 + S_F(\hat{\boldsymbol{\beta}}_n, \hat{F}_n)\left[\int Q_{\hat{F}_n}(h_2)\, d\hat{F}_n\right]\right\}$$

$$= -\sqrt{n}\mathbb{P}\left\{\mathbf{S}_{\boldsymbol{\beta}}(\hat{\boldsymbol{\beta}}_n, \hat{F}_n)^T\mathbf{h}_1 + S_F(\hat{\boldsymbol{\beta}}_n, \hat{F}_n)\left[\int Q_{\hat{F}_n}(h_2)\, d\hat{F}_n\right]\right\}$$

$$+ \sqrt{n}\mathbb{P}\left\{\mathbf{S}_{\boldsymbol{\beta}}(\boldsymbol{\beta}_0, F_0)^T\mathbf{h}_1 + S_F(\boldsymbol{\beta}_0, F_0)\left[\int Q_{F_0}(h_2)\, dF_0\right]\right\}.$$

$$(A.4)$$

We now examine the left and right sides of (A.4). For the left side, we note that the classes $\{\mathbf{W}\}$ and $\{F(Y)\}$ are P–Donsker, because of their monotonicity and uniform boundedness. Under the continuously differentiable operation of taking the exponential, and the algebraic operation of multiplication, the class

$$\left\{e^{\mathbf{W}^T\boldsymbol{\beta} - \boldsymbol{\beta}^T\mathbf{V}\boldsymbol{\beta}/2}, e^{\mathbf{W}^T\boldsymbol{\beta} - \boldsymbol{\beta}^T\mathbf{V}\boldsymbol{\beta}/2}(\mathbf{W} - \mathbf{V}\boldsymbol{\beta}),\right.$$

$$e^{\mathbf{W}^T\boldsymbol{\beta} - \boldsymbol{\beta}^T\mathbf{V}\boldsymbol{\beta}/2}(\mathbf{W} - \mathbf{V}\boldsymbol{\beta})F(Y):$$

$$\left.\|\boldsymbol{\beta} - \boldsymbol{\beta}_0\| < \delta_0, \sup_y |F(y) - F_0(y)| < \delta_0\right\}$$

also is P–Donsker (see van der Vaart and Wellner 2000, thms. 2.7.5, 2.10.6, and 2.10.8). In addition, the class $\{h_2, Q_F(h_2), \int_0^Y Q_F(h_2)\, dF : \|h_2\|_V \le 1, \sup_y |F(y) - F_0(y)| < \delta_0\}$ contains functions of Y with bounded variations, and so also is P–Donsker. Therefore, from the explicit expressions of $\mathbf{S}_{\boldsymbol{\beta}}$ and S_F, the preservation of the Donsker classes under algebraic operations implies that the class

$$\mathcal{A} = \left\{\mathbf{S}_{\boldsymbol{\beta}}(\boldsymbol{\beta}, F)^T\mathbf{h}_1 + S_F(\boldsymbol{\beta}, F)\left[\int Q_F(h_2)\, dF\right]:\right.$$

$$\left.\|\mathbf{h}_1\| \le 1, \|h_2\|_V \le 1, \|\boldsymbol{\beta} - \boldsymbol{\beta}_0\| + \sup_y |F(y) - F_0(y)| < \delta_0\right\}$$

is P–Donsker. On the other hand, based on the consistency of $\hat{\boldsymbol{\beta}}$ and $\hat{F}_n$, the bounded norm of $\mathbf{h}_1$ and the bounded total variation of h_2, it is straightforward to show that

$$\mathbf{S}_{\boldsymbol{\beta}}(\hat{\boldsymbol{\beta}}_n, \hat{F}_n)^T\mathbf{h}_1 + S_F(\hat{\boldsymbol{\beta}}_n, \hat{F}_n)\left[\int Q_{\hat{F}_n}(h_2)\, d\hat{F}_n\right]$$

$$\to \mathbf{S}_{\boldsymbol{\beta}}(\boldsymbol{\beta}_0, F_0)^T\mathbf{h}_1 + S_F(\boldsymbol{\beta}_0, F_0)\left[\int Q_{F_0}(h_2)\, dF_0\right]$$

uniformly in $(\mathbf{h}_1, h_2) \in \mathcal{H}$. Thus the left side of (A.4) is equal to

$$\sqrt{n}(\mathbb{P}_n - \mathbb{P})\left\{\mathbf{S}_{\boldsymbol{\beta}}(\boldsymbol{\beta}_0, F_0)^T\mathbf{h}_1 + S_F(\boldsymbol{\beta}_0, F_0)\left[\int Q_{F_0}(h_2)\, dF_0\right]\right\}$$

$$+ o_p(1),$$

where $o_p(1)$ is a random variable that converges to 0 in probability in $l^\infty(\mathcal{H})$. As a result, the left side of (A.4) converges weakly to a mean-0 Gaussian process in $l^\infty(\mathcal{H})$.

For the right side, simple algebra shows that uniformly in $(\mathbf{h}_1, h_2) \in \mathcal{H}$,

$$\left|\mathbf{S}_{\boldsymbol{\beta}}(\hat{\boldsymbol{\beta}}_n, \hat{F}_n)^T\mathbf{h}_1 + S_F(\hat{\boldsymbol{\beta}}_n, \hat{F}_n)\left[\int Q_{\hat{F}_n}(h_2)\, d\hat{F}_n\right]\right.$$

$$- \mathbf{S}_{\boldsymbol{\beta}}(\boldsymbol{\beta}_0, F_0)^T\mathbf{h}_1 - S_F(\boldsymbol{\beta}_0, F_0)\left[\int Q_{F_0}(h_2)\, dF_0\right]$$

$$- \left\{(\hat{\boldsymbol{\beta}}_n - \boldsymbol{\beta}_0)^T\mathbf{S}_{\boldsymbol{\beta}\boldsymbol{\beta}}(\boldsymbol{\beta}_0, F_0)\mathbf{h}_1\right.$$

$$+ (\hat{\boldsymbol{\beta}}_n - \boldsymbol{\beta}_0)^T\mathbf{S}_{F\boldsymbol{\beta}}(\boldsymbol{\beta}_0, F_0)\left[\int Q_{F_0}(h_2)\, dF_0\right]$$

$$+ \mathbf{h}_1^T\mathbf{S}_{\boldsymbol{\beta}F}[\hat{F}_n - F_0]$$

$$\left.+ S_{FF}(\boldsymbol{\beta}_0, F_0)\left[\int Q_{F_0}(h_2)\, dF_0, \hat{F}_n - F_0\right]\right\}\right|$$

$$\le o_p\{\|\hat{\boldsymbol{\beta}}_n - \boldsymbol{\beta}_0\| + \|\hat{F}_n - F_0\|_{l^\infty(\mathcal{H})}\}.$$

Thus, combining this with the expressions of $\mathbf{S}_{\boldsymbol{\beta}\boldsymbol{\beta}}, \mathbf{S}_{\boldsymbol{\beta}F}, \mathbf{S}_{F\boldsymbol{\beta}}$, and S_{FF}, we obtain that the right side of (A.4) equals

$$-\sqrt{n}\left\{(\hat{\boldsymbol{\beta}}_n - \boldsymbol{\beta}_0)^T\boldsymbol{\Omega}_{\boldsymbol{\beta}}(\mathbf{h}_1, Q_{F_0}(h_2))\right.$$

$$\left.+ \int_0^\infty \Omega_F(\mathbf{h}_1, Q_{F_0}(h_2))\, d(\hat{F}_n - F_0)(y)\right\}$$

$$+ o_p\{\sqrt{n}(\|\hat{\boldsymbol{\beta}}_n - \boldsymbol{\beta}_0\| + \|\hat{F}_n - F_0\|_{l^\infty(\mathcal{H})})\},$$

where

$$\boldsymbol{\Omega}_{\boldsymbol{\beta}}(\mathbf{h}_1, Q_{F_0}(h_2))$$

$$= E\left[F_0(Y)e^{\mathbf{W}^T\boldsymbol{\beta} - \boldsymbol{\beta}^T\mathbf{V}\boldsymbol{\beta}/2}\{\mathbf{V} - (\mathbf{W} - \mathbf{V}\boldsymbol{\beta})(\mathbf{W} - \mathbf{V}\boldsymbol{\beta})^T\}\mathbf{h}_1\right]$$

$$- E\left[e^{\mathbf{W}^T\boldsymbol{\beta} - \boldsymbol{\beta}^T\mathbf{V}\boldsymbol{\beta}/2}(\mathbf{W} - \mathbf{V}\boldsymbol{\beta})\int_0^Y Q_{F_0}(h_2)\, dF_0(t)\right]$$

and

$$\Omega_F(\mathbf{h}_1, Q_{F_0}(h_2))$$

$$= E\left\{e^{\mathbf{W}^T\boldsymbol{\beta} - \boldsymbol{\beta}^T\mathbf{V}\boldsymbol{\beta}/2}F_0(Y) - I(Y < \infty)\Delta\right\}Q_{F_0}\{h_2(y)\}$$

$$- E\left(I(y \le Y)e^{\mathbf{W}^T\boldsymbol{\beta} - \boldsymbol{\beta}^T\mathbf{V}\boldsymbol{\beta}/2}[(\mathbf{W} - \mathbf{V}\boldsymbol{\beta})^T\mathbf{h}_1 + Q_{F_0}\{h_2(y)\}]\right)$$

$$+ \int_0^\infty E\left(I(y \le Y)e^{\mathbf{W}^T\boldsymbol{\beta} - \boldsymbol{\beta}^T\mathbf{V}\boldsymbol{\beta}/2}\right.$$

$$\left.\times [(\mathbf{W} - \mathbf{V}\boldsymbol{\beta})^T\mathbf{h}_1 + Q_{F_0}\{h_2(y)\}]\right) dF_0(y).$$

Note that the last term in the foregoing expression is added to ensure that $\int \Omega_F(\mathbf{h}_1, Q_{F_0}(h_2))\, dF_0 = 0$. We now show that $(\boldsymbol{\Omega}_{\boldsymbol{\beta}}, \Omega_F)$, which is a linear operator on a subspace of $\mathcal{H}$ to itself, with mean-0 Ω_F under F_0, is invertible. Note that

$$\boldsymbol{\Omega}_{\boldsymbol{\beta}}(\mathbf{h}_1, Q_{F_0}(h_2))$$

$$= E\left\{\mathbf{S}_{\boldsymbol{\beta}\boldsymbol{\beta}}\mathbf{h}_1 + \mathbf{S}_{F\boldsymbol{\beta}}\left[\int Q_{F_0}(h_2)\, dF_0\right]\right\}$$

$$= E\left[E\left\{\frac{\partial \mathbf{S}_{\boldsymbol{\beta}}}{\partial \boldsymbol{\beta}}\mathbf{h}_1 + \frac{\partial S_F[\int Q_{F_0}(h_2)\, dF_0]}{\partial \boldsymbol{\beta}}\Big|\mathbf{X}, Y, \Delta\right\}\right]$$

$$= E\left\{\frac{\partial E(\mathbf{S}_{\boldsymbol{\beta}}|\mathbf{X}, Y, \Delta)}{\partial \boldsymbol{\beta}}\mathbf{h}_1 + \frac{\partial E(S_F[\int Q_{F_0}(h_2)\, dF_0]|\mathbf{X}, Y, \Delta)}{\partial \boldsymbol{\beta}}\right\}$$

$$= E\left(\mathbf{l}_{\boldsymbol{\beta}\boldsymbol{\beta}}\mathbf{h}_1 + \mathbf{l}_{F\boldsymbol{\beta}}\left[\int Q_{F_0}(h_2)\, dF_0\right]\right)$$

$$= -E\left(\mathbf{l}_{\boldsymbol{\beta}}\mathbf{l}_{\boldsymbol{\beta}}^T\mathbf{h}_1 + l_F\left[\int Q_{F_0}(h_2)\,dF_0\right]\mathbf{l}_{\boldsymbol{\beta}}\right)$$

and, similarly,

$$\int_0^\infty \Omega_F\big(\mathbf{h}_1, Q_{F_0}(h_2)\big)\,dG(y)$$

$$= E\left(\mathbf{h}_1^T\mathbf{S}_{\boldsymbol{\beta}F}[G] + S_{FF}\left[\int Q_{F_0}(h_2)\,dF_0, G\right]\right)$$

$$= E\left\{E\left(\mathbf{h}_1^T\mathbf{S}_{\boldsymbol{\beta}F}[G] + S_{FF}\left[\int Q_{F_0}(h_2)\,dF_0, G\right]\bigg| \mathbf{X}, Y, \Delta\right)\right\}$$

$$= E\left(\mathbf{h}_1^T\mathbf{l}_{\boldsymbol{\beta}F}[G] + l_{FF}\left[\int Q_{F_0}(h_2)\,dF_0, G\right]\right)$$

$$= -E\left(\mathbf{h}_1^T\mathbf{l}_{\boldsymbol{\beta}}l_F[G] + l_F\left[\int Q_{F_0}(h_2)\,dF_0\right]l_F[G]\right)$$

for an arbitrary function G such that $\int_0^\infty dG(y) = 0$. In particular, for $G = \int Q_{F_0}(h_2)\,dF_0$, we obtain

$$\int_0^\infty \Omega_F\big(\mathbf{h}_1, Q_{F_0}(h_2)\big)Q_{F_0}(h_2)\,dF_0$$

$$= -E\left\{\mathbf{h}_1^T\mathbf{l}_{\boldsymbol{\beta}}l_F\left[\int Q_{F_0}(h_2)\,dF_0\right] + \left(l_F\left[\int Q_{F_0}(h_2)\,dF_0\right]\right)^2\right\}.$$

If for certain $(\mathbf{h}_1, h_2)$ and an arbitrary G satisfying $\int_0^\infty dG(y) = 0$, we have

$$\Omega_{\boldsymbol{\beta}}\big(\mathbf{h}_1, Q_{F_0}(h_2)\big) = \mathbf{0} \qquad \text{and}$$

$$\int_0^\infty \Omega_F\big(\mathbf{h}_1, Q_{F_0}(h_2)\big)\,dG(y) = 0,$$

then we obtain

$$0 = \mathbf{h}_1^T\Omega_{\boldsymbol{\beta}}\big(\mathbf{h}_1, Q_{F_0}(h_2)\big) + \int_0^\infty \Omega_F\big(\mathbf{h}_1, Q_{F_0}(h_2)\big)Q_{F_0}(h_2)\,dF_0$$

$$= -\mathbf{h}_1^T E\left(\mathbf{l}_{\boldsymbol{\beta}}\mathbf{l}_{\boldsymbol{\beta}}^T\mathbf{h}_1 + l_F\left[\int Q_{F_0}(h_2)\,dF_0\right]\mathbf{l}_{\boldsymbol{\beta}}\right)$$

$$- E\left\{\mathbf{h}_1^T\mathbf{l}_{\boldsymbol{\beta}}l_F\left[\int Q_{F_0}(h_2)\,dF_0\right] + \left(l_F\left[\int Q_{F_0}(h_2)\,dF_0\right]\right)^2\right\}$$

$$= -E\left\{(\mathbf{h}_1^T\mathbf{l}_{\boldsymbol{\beta}})^2 + 2\mathbf{h}_1^T\mathbf{l}_{\boldsymbol{\beta}}l_F\left[\int Q_{F_0}(h_2)\,dF_0\right]\right.$$

$$\left. + \left(l_F\left[\int Q_{F_0}(h_2)\,dF_0\right]\right)^2\right\}$$

$$= -E\left\{\left(\mathbf{h}_1^T\mathbf{l}_{\boldsymbol{\beta}} + l_F\left[\int Q_{F_0}(h_2)\,dF_0\right]\right)^2\right\};$$

therefore, with probability 1, $\mathbf{h}_1^T\mathbf{l}_{\boldsymbol{\beta}} + l_F[\int Q_{F_0}(h_2)\,dF_0] = 0$. When $Y = \infty$, $l_F[\int Q_{F_0}(h_2)\,dF_0] = 0$, and thus we obtain $\mathbf{h}_1 = \mathbf{0}$. Subtracting l_F evaluated at $(Y < \infty, \Delta = 1)$ by its value at $(Y < \infty, \Delta = 0)$, we obtain $l_F[\int Q_{F_0}(h_2)\,dF_0](Y, \Delta = 1) - l_F[\int Q_{F_0}(h_2)\,dF_0](Y, \Delta = 0) = Q_{F_0}\{h_2(Y)\} = 0$ for any $Y < \infty$, and thus $h_2 = 0$. Therefore, we have shown that $(\Omega_{\boldsymbol{\beta}}, \Omega_F)$ is indeed invertible. Denoting its inverse $(\Omega_{\boldsymbol{\beta}}^{-1}, \Omega_F^{-1})$, we can rewrite (A.4) as

$$\sqrt{n}\left\{(\hat{\boldsymbol{\beta}}_n - \boldsymbol{\beta}_0)^T\mathbf{h}_1 + \int_0^\infty Q_{F_0}(h_2)\,d(\hat{F}_n - F_0)\right\}$$

$$= -\sqrt{n}(\mathbb{P}_n - \mathbb{P})\left\{\mathbf{S}_{\boldsymbol{\beta}}(\boldsymbol{\beta}_0, F_0)^T\Omega_{\boldsymbol{\beta}}^{-1}\big(\mathbf{h}_1, Q_{F_0}(h_2)\big)\right.$$

$$\left. + S_F(\boldsymbol{\beta}_0, F_0)\left[\int \Omega_F^{-1}\big(\mathbf{h}_1, Q_{F_0}(h_2)\big)\,dF_0\right]\right\}$$

$$+ o_p\{\sqrt{n}(\|\hat{\boldsymbol{\beta}}_n - \boldsymbol{\beta}_0\| + \|\hat{F}_n - F_0\|_{l\infty})\} + o_p(1)$$

for all $(\mathbf{h}_1, h_2) \in \mathcal{H}$. So, $\sqrt{n}\{(\hat{\boldsymbol{\beta}}_n - \boldsymbol{\beta}_0)^T\mathbf{h}_1 + \int_0^\infty Q_{F_0}(h_2)\,d(\hat{F}_n - F_0)\} = O_p(1)$ for all $(\mathbf{h}_1, h_2) \in \mathcal{H}$, and thus $\{\sqrt{n}(\|\hat{\boldsymbol{\beta}}_n - \boldsymbol{\beta}_0\| + \|\hat{F}_n - F_0\|_{l\infty})\} = O_p(1)$. As an immediate result,

$$\sqrt{n}\left\{(\hat{\boldsymbol{\beta}}_n - \boldsymbol{\beta}_0)^T\mathbf{h}_1 + \int_0^\infty Q_{F_0}(h_2)\,d(\hat{F}_n - F_0)\right\}$$

$$= -\sqrt{n}(\mathbb{P}_n - \mathbb{P})\left\{\mathbf{S}_{\boldsymbol{\beta}}(\boldsymbol{\beta}_0, F_0)^T\Omega_{\boldsymbol{\beta}}^{-1}\big(\mathbf{h}_1, Q_{F_0}(h_2)\big)\right.$$

$$\left. + S_F(\boldsymbol{\beta}_0, F_0)\left[\int \Omega_F^{-1}\big(\mathbf{h}_1, Q_{F_0}(h_2)\big)\,dF_0\right]\right\}$$

$$+ o_p(1),$$

and thus the proof of the theorem is complete.

Proof of Theorem 3

From the proof of Theorem 2, if we take $Q_{F_0}(h_2) = 0$, then we obtain that

$$\sqrt{n}(\hat{\boldsymbol{\beta}}_n - \boldsymbol{\beta}_0)^T\mathbf{h}_1$$

$$= -\sqrt{n}(\mathbb{P}_n - \mathbb{P})\left\{\mathbf{S}_{\boldsymbol{\beta}}(\boldsymbol{\beta}_0, F_0)^T\Omega_{\boldsymbol{\beta}}^{-1}(\mathbf{h}_1, 0)\right.$$

$$\left. + S_F(\boldsymbol{\beta}_0, F_0)\left[\int \Omega_F^{-1}(\mathbf{h}_1, 0)\,dF_0\right]\right\} + o_p(1).$$

Write

$$\mathbf{b}_1(y) = E\{I(y \le Y)e^{\mathbf{W}^T\boldsymbol{\beta} - \boldsymbol{\beta}^T\mathbf{V}\boldsymbol{\beta}/2}(\mathbf{W} - \mathbf{V}\boldsymbol{\beta})\},$$

$$\mathbf{b}_2 = \int_0^\infty \mathbf{b}_1(y)\,dF_0(y),$$

$$c_1 = E\{e^{\mathbf{W}^T\boldsymbol{\beta} - \boldsymbol{\beta}^T\mathbf{V}\boldsymbol{\beta}/2}F_0(Y) - I(Y < \infty)\Delta\},$$

$$c_2(y) = E\{I(y \le Y)e^{\mathbf{W}^T\boldsymbol{\beta} - \boldsymbol{\beta}^T\mathbf{V}\boldsymbol{\beta}/2}\},$$

$$\mathbf{b}_3 = \left[\int_0^\infty \{c_1 - c_2(y)\}^{-1}\,dF_0(y)\right]^{-1} \tag{A.5}$$

$$\times \left[\int_0^\infty \{\mathbf{b}_1(y) - \mathbf{b}_2\}/\{c_1 - c_2(y)\}\,dF_0(y)\right],$$

$$\mathbf{b}_4(y) = \{c_1 - c_2(y)\}^{-1}\{\mathbf{b}_1(y) - \mathbf{b}_2 - \mathbf{b}_3\},$$

$$\mathbf{a}_1 = E[F_0(Y)e^{\mathbf{W}^T\boldsymbol{\beta} - \boldsymbol{\beta}^T\mathbf{V}\boldsymbol{\beta}/2}\{\mathbf{V} - (\mathbf{W} - \mathbf{V}\boldsymbol{\beta})(\mathbf{W} - \mathbf{V}\boldsymbol{\beta})^T\}],$$

$$\mathbf{a}_2 = E\left[e^{\mathbf{W}^T\boldsymbol{\beta} - \boldsymbol{\beta}^T\mathbf{V}\boldsymbol{\beta}/2}(\mathbf{W} - \mathbf{V}\boldsymbol{\beta})\int_0^Y \mathbf{b}_4(y)^T\,dF_0(y)\right].$$

It can be verified that

$$\Omega_{\boldsymbol{\beta}}^{-1}(\mathbf{h}_1, 0) = (\mathbf{a}_1 - \mathbf{a}_2)^{-1}\mathbf{h}_1 = (\mathbf{A}^{-1})^T\mathbf{h}_1$$

and

$$\Omega_F^{-1}(\mathbf{h}_1, 0) = \mathbf{b}_4(y)^T(\mathbf{A}^{-1})^T\mathbf{h}_1,$$

where $\mathbf{A} = (\mathbf{a}_1 - \mathbf{a}_2)^T$. Thus

$$\sqrt{n}(\hat{\boldsymbol{\beta}}_n - \boldsymbol{\beta}_0)^T\mathbf{h}_1$$

$$= -\sqrt{n}(\mathbb{P}_n - \mathbb{P})\left[\left\{\mathbf{S}_{\boldsymbol{\beta}}(\boldsymbol{\beta}_0, F_0)^T + S_F(\boldsymbol{\beta}_0, F_0)\left[\int \mathbf{b}_4(y)^T\,dF_0\right]\right\}\right.$$

$$\left. \times (\mathbf{A}^{-1})^T\mathbf{h}_1\right] + o_p(1).$$

Denote

$$\mathbf{B} = \left\{\mathbf{S}_{\boldsymbol{\beta}}(\boldsymbol{\beta}_0, F_0) + S_F(\boldsymbol{\beta}_0, F_0)\left[\int \mathbf{b}_4(y)\,dF_0\right]\right\}^{\otimes 2},$$

where $\mathbf{a}^{\otimes 2} = \mathbf{a}\mathbf{a}^T$ for a vector $\mathbf{a}$. Then the result follows.

Equivalence of the NPMLE and Partial Likelihood Estimator

The partial likelihood estimator for the proportional hazards cure rate model can be obtained by solving

$$\sum_{i=1}^{n} \Delta_i I(Y_i < \infty) \left\{ \tilde{\mathbf{X}}_i - \frac{\sum_{j \in R_i} \tilde{\mathbf{X}}_j e^{\tilde{\mathbf{X}}_j^T \tilde{\boldsymbol{\beta}}}}{\sum_{j \in R_i} e^{\tilde{\mathbf{X}}_j^T \tilde{\boldsymbol{\beta}}}} \right\} = \mathbf{0} \qquad \text{(A.6)}$$

and

$$\sum_{i=1}^{n} \frac{\Delta_i I(Y_i < \infty)}{\sum_{j \in R_i} e^{\tilde{\mathbf{X}}_j^T \tilde{\boldsymbol{\beta}}}} - e^b = 0, \qquad \text{(A.7)}$$

where R_i is the risk set at Y_i and $\tilde{\mathbf{X}}_i$ and $\tilde{\boldsymbol{\beta}}$ represent $\mathbf{X}$ and $\boldsymbol{\beta}$ with the first component (corresponding to the intercept b) excluded (see, e.g., Tsodikov 1998b).

In the NPMLE, setting the Lagrange multiplier $n\lambda = \sum_{Y_j = \infty} e^{\mathbf{X}_j^T \boldsymbol{\beta}}$, from (3), we immediately obtain

$$p_i = \frac{\Delta_i I(Y_i < \infty)}{\sum_{j \in R_i} e^{\mathbf{X}_j^T \boldsymbol{\beta}}} \qquad \text{and} \qquad F(Y_i) = \sum_{Y_k \leq Y_i} \frac{\Delta_k I(Y_k < \infty)}{\sum_{j \in R_k} e^{\mathbf{X}_j^T \boldsymbol{\beta}}},$$

and thus

$$\sum_{i=1}^{n} e^{\mathbf{X}_i^T \boldsymbol{\beta}} \mathbf{X}_i F(Y_i) = \sum_{i=1}^{n} \sum_{Y_k \leq Y_i} \frac{e^{\mathbf{X}_i^T \boldsymbol{\beta}} \mathbf{X}_i \Delta_k I(Y_k < \infty)}{\sum_{j \in R_k} e^{\mathbf{X}_j^T \boldsymbol{\beta}}}$$

$$= \sum_{k=1}^{n} \Delta_k I(Y_k < \infty) \frac{\sum_{j \in R_k} e^{\mathbf{X}_j^T \boldsymbol{\beta}} \mathbf{X}_j}{\sum_{j \in R_k} e^{\mathbf{X}_j^T \boldsymbol{\beta}}},$$

and, from (5), we obtain

$$\sum_{i=1}^{n} \Delta_i I(Y_i < \infty) \left(\mathbf{X}_i - \frac{\sum_{j \in R_i} e^{\mathbf{X}_j^T \boldsymbol{\beta}} \mathbf{X}_j}{\sum_{j \in R_i} e^{\mathbf{X}_j^T \boldsymbol{\beta}}} \right),$$

equivalent to (A.6). From (4), we have

$$\sum_{i=1}^{n} \frac{\Delta_i I(Y_i < \infty)}{\sum_{j \in R_i} e^{\mathbf{X}_j^T \boldsymbol{\beta}}} = 1,$$

equivalent to (A.7).

[Received September 2007. Revised February 2008.]

REFERENCES

Augustin, T. (2004), "An Exact Corrected Log-Likelihood Function for Cox's Proportional Hazards Model Under Measurement Error and Some Extensions," *Scandinavian Journal of Statistics*, 31, 43–50.

Berkson, J., and Gage, R. P. (1952), "Survival Curve for Cancer Patients Following Treatment," *Journal of the American Statistical Association*, 47, 501–515.

Buzas, J. S. (1998), "Unbiased Scores in Proportional Hazards Regression With Covariate Measurement Error," *Journal of Statistical Planning & Inference*, 67, 247–257.

Carroll, R. J., Ruppert, D., Stefanski, L. A., and Crainiceanu, C. (2006), *Measurement Error in Nonlinear Models: A Modern Perspective* (2nd ed.), London: CRC Press.

Chen, M. H., Ibrahim, J. G., and Sinha, D. (1999), "A New Bayesian Model for Survival Data With a Surviving Fraction," *Journal of the American Statistical Association*, 94, 909–919.

Cheng, S. C., and Wang, N. (2001), "Linear Transformation Models for Failure Time Data With Covariate Measurement Error," *Journal of the American Statistical Association*, 96, 706–716.

Cook, J. R., and Stefanski, L. A. (1994), "Simulation-Extrapolation Estimation in Parametric Measurement Error Models," *Journal of the American Statistical Association*, 89, 1314–1328.

Cox, D. R. (1972), "Regression Models and Life Tables" (with discussion), *Journal of the Royal Statistical Society*, Ser. B, 34, 187–220.

Eckert, R. S., Carroll, R. J., and Wang, N. (1997), "Transformations to Additivity in Measurement Error Models," *Biometrics*, 53, 262–272.

Fuller, W. A. (1987), *Measurement Error Models*, New York: Wiley.

Gorfine, M., Hsu, L., and Prentice, R. L. (2004), "Nonparametric Correction for Covariate Measurement Error in a Stratified Cox Model," *Biostatistics*, 5, 75–87.

Gray, R. J., and Tsiatis, A. A. (1989), "A Linear Rank Test for Use When the Main Interest Is in Differences in Cure Rates," *Biometrics*, 45, 899–904.

Greene, W. F., and Cai, J. (2004), "Measurement Error in Covariates in the Marginal Hazards Model for Multivariate Failure Time Data," *Biometrics*, 60, 987–996.

Hu, C., and Lin, D. Y. (2002), "Cox Regression With Covariate Measurement Error," *Scandinavian Journal of Statistics*, 29, 637–655.

——— (2004), "Semiparametric Failure Time Regression With Replicates of Mismeasured Covariates," *Journal of the American Statistical Association*, 99, 105–118.

Hu, P., Tsiatis, A. A., and Davidian, M. (1998), "Estimating the Parameters in the Cox Model When Covariate Variables Are Measured With Error," *Biometrics*, 54, 1407–1419.

Huang, Y., and Wang, C. Y. (2000), "Cox Regression With Accurate Covariates Unascertainable: A Nonparametric-Correction Approach," *Journal of the American Statistical Association*, 95, 1209–1219.

Kong, F. H., and Gu, M. (1999), "Consistent Estimation in the Cox Proportional Hazards Model With Covariate Measurement Errors," *Statistica Sinica*, 9, 953–970.

Kuk, A. Y. C., and Chen, C. H. (1992), "A Mixture Model Combining Logistic Regression With Proportional Hazards Regression," *Biometrika*, 79, 531–541.

Kulich, M., and Lin, D. Y. (2000), "Additive Hazards Regression With Covariate Measurement Error," *Journal of the American Statistical Association*, 95, 238–248.

Laska, E. M., and Meisner, M. J. (1992), "Nonparametric Estimation and Testing in a Cure Rate Model," *Biometrics*, 48, 1223–1234.

Li, Y., and Lin, X. (2000), "Covariate Measurement Errors in Frailty Models for Clustered Survival Data," *Biometrika*, 87, 849–866.

——— (2003), "Functional Inference in Frailty Measurement Error Models for Clustered Survival Data Using the SIMEX Approach," *Journal of the American Statistical Association*, 98, 191–203.

Li, Y., and Ryan, L. (2004), "Survival Analysis With Heterogeneous Covariate Measurement Error," *Journal of the American Statistical Association*, 99, 724–735.

Li, Y., Tiwari, R., and Guha, S. (2007), "Mixture Cure Survival Models With Dependent Censoring," *Journal of the Royal Statistical Society*, Ser. B, 69, 285–306.

Lu, W., and Ying, Z. (2004), "On Semiparametric Transformation Cure Models," *Biometrika*, 91, 331–343.

Maller, R., and Zhou, X. (1996), *Survival Analysis With Long-Term Survivors*, New York: Wiley.

Nakamura, T. (1990), "Corrected Score Function for Errors-in-Variables Models: Methodology and Application to Generalized Linear Models," *Biometrika*, 77, 127–137.

——— (1992), "Proportional Hazards Model With Covariates Subject to Measurement Error," *Biometrics*, 48, 829–838.

Nusser, S. M., Carriquiry, A. L., Dodd, K. W., and Fuller, W. A. (1996), "A Semiparametric Transformation Approach to Estimating Usual Daily Intake Distributions," *Journal of the American Statistical Association*, 91, 1440–1449.

Prentice, R. L. (1982), "Covariate Measurement Errors and Parameter Estimation in a Failure Time Regression Model," *Biometrika*, 69, 331–342.

Rao, C. R. (1973), *Linear Statistical Inference and Its Applications* (2nd ed.), New York: Wiley.

Song, X., and Huang, Y. (2005), "On Corrected Score Approach for Proportional Hazards Model With Covariate Measurement Error," *Biometrics*, 61, 702–714.

Song, X., Davidian, M., and Tsiatis, A. A. (2002), "An Estimator for the Proportional Hazards Model With Multiple Longitudinal Covariates Measured With Error," *Biostatistics*, 3, 511–528.

Sposto, R., Sather, H. N., and Baker, S. A. (1992), "A Comparison of Tests of the Difference in the Proportion of Patients Who Are Cured," *Biometrics*, 48, 87–99.

Stefanski, L. A. (1989), "Unbiased Estimation of a Nonlinear Function of a Normal Mean With Application to Measurement Error Models," *Communications in Statistics, Part A—Theory and Methods*, 18, 4335–4358.

Stefanski, L. A., and Cook, J. R. (1995), "Simulation-Extrapolation: The Measurement Error Jackknife," *Journal of the American Statistical Association*, 90, 1247–1256.

Sy, J. P., and Taylor, J. M. G. (2000), "Estimation in a Cox Proportional Hazards Cure Model," *Biometrics*, 56, 227–236.

Tsiatis, A. A., and Davidian, M. (2001), "A Semiparametric Estimator for the Proportional Hazards Model With Longitudinal Covariates Measured With Error," *Biometrika*, 88, 447–458.

Tsiatis, A. A., and Ma, Y. (2004), "Locally Efficient Semiparametric Estimators for Functional Measurement Error Models," *Biometrika*, 91, 835–848.

Tsiatis, A. A., DeGruttola, V., and Wulfsohn, M. S. (1995), "Modeling the Relationship of Survival to Longitudinal Data Measured With Error: Applications to Survival and CD4 Counts in Patients With AIDS," *Journal of the American Statistical Association*, 90, 27–37.

Tsodikov, A. (1998a), "A Proportional Hazards Model Taking Account of Long-Term Survivors," *Biometrics*, 54, 1508–1516.

⸻ (1998b), "Asymptotic Efficiency of a Proportional Hazards Model With Cure," *Statistics and Probability Letters*, 39, 237–244.

Tsodikov, A. D., Ibrahim, J. G., and Yakovlev, A. Y. (2003), "Estimating Cure Rates From Survival Data: An Alternative to Two-Component Mixture Models," *Journal of the American Statistical Association*, 98, 1063–1078.

van der Vaart, A. W., and Wellner, J. A. (2000), *Weak Convergence and Empirical Processes*, New York: Springer.

Wang, C. Y., Hsu, L., Feng, Z. D., and Prentice, R. L. (1997), "Regression Calibration in Failure Time Regression," *Biometrics*, 53, 131–145.

Wulfsohn, M. S., and Tsiatis, A. A. (1997), "A Joint Model for Survival and Longitudinal Data Measured With Error," *Biometrics*, 53, 330–339.

Yakovlev, A. Y., and Tsodikov, A. D. (1996), *Stochastic Models of Tumor Latency and Their Biostatistical Applications*, Hackensack, NJ: World Scientific.

Zeng, D., Yin, G., and Ibrahim, J. G. (2006), "Semiparametric Transformation Models for Survival Data With a Cure Fraction," *Journal of the American Statistical Association*, 101, 670–684.

Zhou, H., and Pepe, M. S. (1995), "Auxiliary Covariate Data in Failure Time Regression," *Biometrika*, 82, 139–149.

Zhou, H., and Wang, C.-Y. (2000), "Failure Time Regression With Continuous Covariates Measured With Error," *Journal of the Royal Statistical Society*, Ser. B, 62, 657–665.

Zucker, D. M. (2005), "A Pseudo-Partial Likelihood Method for Semiparametric Survival Regression With Covariate Errors," *Journal of the American Statistical Association*, 100, 1264–1277.

Bayesian Semiparametric Cure Rate Model with an Unknown Threshold

LUIS E. NIETO-BARAJAS

Department of Statistics, ITAM

GUOSHENG YIN

Department of Biostatistics, M.D. Anderson Cancer Center

ABSTRACT. We propose a Bayesian semiparametric model for survival data with a cure fraction. We explicitly consider a finite cure time in the model, which allows us to separate the cured and the uncured populations. We take a mixture prior of a Markov gamma process and a point mass at zero to model the baseline hazard rate function of the entire population. We focus on estimating the cure threshold after which subjects are considered cured. We can incorporate covariates through a structure similar to the proportional hazards model and allow the cure threshold also to depend on the covariates. For illustration, we undertake simulation studies and a full Bayesian analysis of a bone marrow transplant data set.

Key words: Bayesian non-parametrics, cure model, cure threshold model, discrete Markov gamma process, mixture prior, survival analysis

1. Introduction

In the study of time-to-event data for certain diseases, there exists a positive probability of not observing the failure event. In other words, there exists a fraction of the population that is cured of or insusceptible to the disease, who thus will never experience the failure. The survival models that incorporate a cure fraction are often referred to as *cure rate models*.

Most methods for modelling survival data with a cure fraction have been rooted in two main model formulations: the standard (mixture) cure rate model of Berkson & Gage (1952) and the alternative (proportional hazards) cure rate model of Yakovlev & Tsodikov (1996), which was later studied by Chen *et al.* (1999) in a Bayesian context. The standard cure rate model (Berkson & Gage, 1952) is a mixture model defined by

$$S_{\text{pop}}(t) = \pi + (1-\pi)S(t), \tag{1}$$

where $\pi \in (0,1)$ and $S(t)$ is a proper survival function. Note that $\lim_{t \to 0} S_{\text{pop}}(t) = 1$ and $\lim_{t \to \infty} S_{\text{pop}}(t) = \pi > 0$, and therefore $S_{\text{pop}}(t)$ is an improper survival function. If we ignore the impropriety of $S_{\text{pop}}(t)$, and carry on with the traditional relationship between a survival function and a cumulative hazard function, we have

$$H_{\text{pop}}(t) = -\log S_{\text{pop}}(t) = -\log\{\pi + (1-\pi)S(t)\},$$

which satisfies that $\lim_{t \to 0} H_{\text{pop}}(t) = 0$ and $\lim_{t \to \infty} H_{\text{pop}}(t) = -\log \pi > 0$. If we proceed and take the first derivative, then the hazard rate is

$$h_{\text{pop}}(t) = \frac{\mathrm{d}}{\mathrm{d}t} H_{\text{pop}}(t) = \frac{(1-\pi)f(t)}{\pi + (1-\pi)S(t)}, \tag{2}$$

where $f(t)$ is the density function corresponding to $S(t)$. Now, $h_{\text{pop}}(t)$ has the following properties: $\lim_{t \to 0} h_{\text{pop}}(t) = (1-\pi)f(0)$ and $\lim_{t \to \infty} h_{\text{pop}}(t) = 0$. Extensive research has been

conducted for the standard cure rate model in the literature (Kuk & Chen, 1992; Maller & Zhou, 1992, 1995; Sy & Taylor, 2000; Lu & Ying, 2004; among others).

The alternative cure rate model of Yakolev & Tsodikov (1996) is defined by

$$S_{\mathrm{pop}}(t) = \exp\{-\theta F(t)\}, \tag{3}$$

where $\theta > 0$ and $F(t)$ is a proper cumulative distribution function. This model satisfies the conditions that $\lim_{t\to 0} S_{\mathrm{pop}}(t) = 1$ and $\lim_{t\to\infty} S_{\mathrm{pop}}(t) = e^{-\theta}$; therefore, $S_{\mathrm{pop}}(t)$ is not a proper survival function. Regardless of the improper condition, the cumulative hazard function is given by

$$H_{\mathrm{pop}}(t) = -\log S_{\mathrm{pop}}(t) = \theta F(t)$$

which leads to $\lim_{t\to 0} H_{\mathrm{pop}}(t) = 0$ and $\lim_{t\to\infty} H_{\mathrm{pop}}(t) = \theta > 0$. If we take its first derivative, then the hazard rate is

$$h_{\mathrm{pop}}(t) = \frac{\mathrm{d}}{\mathrm{d}t} H_{\mathrm{pop}}(t) = \theta f(t), \tag{4}$$

where $f(t)$ is the density function corresponding to $F(t)$. We have that $\lim_{t\to 0} h_{\mathrm{pop}}(t) = \theta f(0)$ and $\lim_{t\to\infty} h_{\mathrm{pop}}(t) = 0$. This alternative model can be derived within a biological context related to metastasis-competent tumour cells, and thus can facilitate a nice interpretation. More recently, Ibrahim *et al.* (2001a) and Tsodikov *et al.* (2003) have given a comprehensive review and discussion of the current development of the cure rate model (3) from both the frequentist and Bayesian perspectives. Relevant work includes that of Gray & Tsiatis (1989), Peng & Dear (2000), Betensky & Schoenfeld (2001), Tsodikov (2002), Lam & Xue (2005), and Yin & Ibrahim (2005), among others.

In the semiparametric cure rate models, one usually concentrates on modelling the hazard rate function $h(t)$ of the uncured group, corresponding to $S(t)$ in (1) and $F(t)$ in (3), respectively. Ibrahim *et al.* (2001b) proposed a piecewise constant hazard function to model the baseline hazard $h(t)$. More specifically, for the uncured subjects,

$$h(t) = \sum_{j=1}^{J} \lambda_j I(s_{j-1} < t \le s_j),$$

where $0 < s_1 < \cdots < s_J$ with $s_J > t_i$, for $i = 1, \ldots, n$. The number J controls the degree to which the model is non-parametric (its 'non-parametricity' or flexibility). If $J = 1$, $h(t)$ is a constant hazard rate and the larger the J the more non-parametric (flexible) the model. In addition, the prior is adjusted in such a way that the degree of parametricity in the right tail is controlled by a smoothing parameter. However, the hazard rate $h(t)$ is not associated with that of the cured group, and thus the implication with respect to the hazard rate of the entire population is not clear; and the intervals that define the finite partition of the time axis are taken to be data driven.

In all cure models known in the literature, the researchers model a positive cure probability, but do not explicitly quantify the finite cure time, which would provide very useful information with direct application to the clinical management of the disease. If the follow-up of a patient is long enough, it is reasonable to consider the patient cured from the disease after a certain time point. In this paper, we introduce a new cure rate model that allows us to separate the cured from the uncured group by explicitly modelling a finite cure threshold. For this purpose, we define a hazard rate with a cure threshold for the entire population, including both cured and uncured subjects. Inference of the model is driven by a mixture non-parametric prior for the hazard rate. This prior is established from a mixed gamma process with the marginal distribution at each partition time defined by a mixture of a gamma

distribution and a point mass at zero. In particular, the new modelling scheme allows us to determine the subject-specific threshold after which an individual may be considered cured.

A brief description of the paper is as follows. In section 2, we define the new cure rate model and propose the non-parametric prior based on the mixture of the Markov gamma process and a point mass at zero, and develop its properties. In section 3, we present the prior to posterior analysis, and derive the full conditional distributions for Gibbs sampling. In section 4, we extend the new method to cope with covariates through a specification similar to the proportional hazards model. In section 5, we illustrate our model with simulation studies and carry out a full Bayesian analysis of a real data set from a bone marrow transplant study. We conclude with a brief discussion in section 6.

2. Cure threshold model

In order to formulate a meaningful cure rate model, we examine the conditions that are required for the hazard function of the entire population in the aforementioned cure rate models: $H_{\text{pop}}(t)$ satisfies (i) $\lim_{t \to 0} H_{\text{pop}}(t) = 0$ and (ii) $\lim_{t \to \infty} H_{\text{pop}}(t) = const. < \infty$. If we define $h_{\text{pop}}(t) = \mathrm{d}H_{\text{pop}}(t)/\mathrm{d}t$, a necessary condition for (i) and (ii) to be satisfied is that $\lim_{t \to \infty} h_{\text{pop}}(t) = 0$.

After a sufficient follow-up, the uncured subjects would have experienced the event, while the cured ones would be either censored or still 'alive' in the study. That is, after the cure threshold, the remaining subjects in the study are risk free of the event. Following this route, we propose a new cure rate model for the population hazard rate function that vanishes when t exceeds a certain threshold, say τ, that is

$$h_{\text{pop}}(t) = h(t)I(t \leq \tau), \tag{5}$$

with $h(t)$ a non-negative function. This new specification of the hazard function can be interpreted as either a mixture cure model (1) or a proportional hazards cure model (3) by constraining the event time of the uncured group, say T^u, right-bounded by the threshold τ, $\mathrm{P}(T^u \leq \tau) = 1$. In practical applications, it is more realistic to let the hazard rate drop to zero after the cure threshold as the subjects who have survived up to τ would become risk-free of the event. The cure threshold hazard model (5) defines a valid cure rate model that allows us to completely identify the cured and the uncured groups.

In the Bayesian paradigm, we define a non-parametric prior for $h(t)$ as in Walker & Mallick (1997),

$$h(t) = \sum_{k=1}^{\infty} \lambda_k I(\tau_{k-1} < t \leq \tau_k),$$

where $0 = \tau_0 < \tau_1 < \cdots$ forms a partition of the time axis, and $\{\lambda_k\}$ is a discrete time independent gamma process, i.e. $\lambda_k \overset{\text{ind}}{\sim} \text{Ga}(\alpha_k, \beta_k)$, where $\text{Ga}(\alpha, \beta)$ denotes a Gamma distribution with mean α/β. If we combine this prior process with the constraint in model (5), then the cure time τ will only occur in discrete periods, which can be accurately estimated with a fine partition. Denoting τ_z as the discretized cure time, then condition $t \leq \tau_z$ can be replaced by $k \leq z$, and thus the prior on the entire population becomes

$$h_{\text{pop}}(t) = \sum_{k=1}^{\infty} \lambda_k I(k \leq z)I(\tau_{k-1} < t \leq \tau_k). \tag{6}$$

Moreover, we can take a prior on τ_z by considering a prior on z. If we denote the prior on z by $f(z)$, then the new process $\{\lambda_k^*\}$ with $\lambda_k^* = \lambda_k I(k \leq z)$, can be characterized by

$$f(\lambda_k^* | z) = \text{Ga}(\lambda_k^* | \alpha_k, \beta_k)I(k \leq z) + I(\lambda_k^* = 0)I(k > z).$$

Marginalizing over z, the prior distribution of λ_k^* becomes

$$f(\lambda_k^*) = \eta_k \mathrm{Ga}(\lambda_k^* \,|\, \alpha_k, \beta_k) + (1 - \eta_k) I(\lambda_k^* = 0),$$

with $\eta_k = \mathrm{P}(z \geq k)$, i.e. λ_k^* has a prior distribution given by a mixture of a Gamma distribution and a point mass at zero.

The first and second moments of the process $\{\lambda_k^*\}$ are the following:

$$\mathrm{E}(\lambda_k^*) = \eta_k \left(\frac{\alpha_k}{\beta_k} \right)$$

and

$$\mathrm{Var}(\lambda_k^*) = \eta_k (1 - \eta_k) \left(\frac{\alpha_k}{\beta_k} \right)^2 + \eta_k \frac{\alpha_k}{\beta_k^2}.$$

Due to the existence of z, λ_k^* and λ_{k+1}^* are not independent, in fact, the covariance is given by

$$\mathrm{Cov}(\lambda_{k+1}^*, \lambda_k^*) = \eta_{k+1}(1 - \eta_k) \left(\frac{\alpha_{k+1}}{\beta_{k+1}} \right) \left(\frac{\alpha_k}{\beta_k} \right). \tag{7}$$

It is worth noting that this non-parametric prior differs substantially from other non/semi-parametric constructions for cure rate models. In light of the new model (5), we non-parametrically model the hazard rate of the entire population, whereas Ibrahim *et al.* (2001b), for instance, model the hazard rate for the non-cured subjects only. If $\eta_k = 1$, i.e. the time interval k lies before the cure index z, $\mathrm{E}(\lambda_k^*) = \alpha_k / \beta_k$, $\mathrm{Var}(\lambda_k^*) = \alpha_k / \beta_k^2$ and $\mathrm{Cov}(\lambda_{k+1}^*, \lambda_k^*) = 0$, which reduces to the independent piecewise exponential model.

To enhance the dependence in the process $\{\lambda_k\}$ and to further model trends in the hazard, we can consider the Markov gamma process of Nieto-Barajas & Walker (2002) for the λ_k's instead of taking them to be independent. As a result, we induce a stronger correlation within the λ_k^*'s. The Markov gamma process $\{\lambda_k\}$ is defined through a latent process $\{u_k\}$ in the following way: start the process with

$$\lambda_1 \sim \mathrm{Ga}(\alpha_1, \beta_1)$$

and then take

$$u_k \,|\, \lambda_k \sim \mathrm{Po}(c_k \lambda_k)$$

and

$$\lambda_{k+1} \,|\, u_k \sim \mathrm{Ga}(\alpha_{k+1} + u_k, \beta_{k+1} + c_k)$$

for $k = 1, 2, \ldots$. Here, $\mathrm{Po}(c)$ denotes a Poisson distribution with intensity c. If we take α_k and β_k to be constant, then the process $\{\lambda_k\}$ is stationary with marginals $\lambda_k \sim \mathrm{Ga}(\alpha, \beta)$ and correlation $\mathrm{Corr}(\lambda_{k+1}, \lambda_k) = c_k / (\beta + c_k)$.

Clearly, if $z \geq k$ for all k with probability 1 (w.p.1), i.e. there is no (finite) cure time, the prior (6) reduces to the case of Nieto-Barajas & Walker (2002). If $c_k = 0$ for all k, then $u_k = 0$ w.p.1, which implies that $\{\lambda_k^*\}$ reduces to the previous case in (7) where the dependence is very weak. This formulation of the prior represents a new generalization of the independent gamma process (Walker & Mallick, 1997). It enhances the flexibility and capability of the hazard structure to model survival data with a possible cure fraction.

The prior modelling, given by equation (6), implies that the cure fraction π defined as the proportion of the population that will never experience the failure, is given by

$$\pi = \lim_{t \to \infty} S_{\mathrm{pop}}(t) = \exp\left\{ -\sum_{k=1}^{z} \lambda_k (\tau_k - \tau_{k-1}) \right\},$$

since λ_k is taken to be zero for $k > z$. Note that the sum in the expression for π is a finite summation bounded by z. This is due to the fact that the paths of our non-parametric prior characterize that the hazard rate takes the value of zero from τ_z onwards, whereas in the standard mixture and the proportional hazards cure rate models, the hazard rate vanishes asymptotically or decays toward zero.

One needs to specify a prior distribution for z, which has a support on $\{1, 2, \ldots\}$. A natural option is to consider a positive Poisson prior distribution, i.e. $z \sim \text{Po}^+(\mu)$, for $\mu > 0$, where $\text{Po}^+(c)$ is a positive Poisson distribution with parameter c, that is, if $x \sim \text{Po}^+(c)$ then $x - 1 \sim \text{Po}(c)$. Although the sample paths of our prior $h_{\text{pop}}(t)$ are piecewise constant almost surely (a.s.), the sample paths of the corresponding cumulative hazard function $H_{\text{pop}}(t)$ (integrated process) are continuous a.s. Therefore, the non-parametric prior $S_{\text{pop}}(t) = e^{-H_{\text{pop}}(t)}$ assigns a positive probability to the set of continuous (improper) survival functions, which allows for a finite cure time.

3. Prior to posterior analysis

Let $h_{\text{pop}}(t)$ be the prior hazard rate as in (6). Then, the cumulative hazard function $H_{\text{pop}}(t)$ has the form of

$$H_{\text{pop}}(t_i) = \sum_{k=1}^{\infty} \lambda_k I(k \le z) w_{ki},$$

where

$$w_{ki} = \begin{cases} \tau_k - \tau_{k-1}, & t_i > \tau_k \\ t_i - \tau_{k-1}, & t_i \in (\tau_{k-1}, \tau_k] \\ 0, & \text{otherwise.} \end{cases} \tag{8}$$

Through $f_{\text{pop}}(t_i) = h_{\text{pop}}(t_i) e^{-H_{\text{pop}}(t_i)}$, the density function $f_{\text{pop}}(t)$ can be easily derived.

Let $\boldsymbol{\lambda}$ and $\mathbf{u}$ denote the vectors of λ_k and u_k, $\boldsymbol{\lambda}_{(-k)}$ and $\mathbf{u}_{(-k)}$ denote the rest after deleting the kth component, respectively. The joint prior distribution of $(\boldsymbol{\lambda}, \mathbf{u}, z)$ can be written as

$$f(\boldsymbol{\lambda}, \mathbf{u}, z) = f(\boldsymbol{\lambda}, \mathbf{u}) f(z),$$

with

$$f(\boldsymbol{\lambda}, \mathbf{u}) = \text{Ga}(\lambda_1 | \alpha_1, \beta_1) \prod_{k=1}^{\infty} \{\text{Po}(u_k | c_k \lambda_k) \text{Ga}(\lambda_{k+1} | \alpha_{k+1} + u_k, \beta_{k+1} + c_k)\} \tag{9}$$

and $f(z) = \text{Po}^+(z \mid \mu)$.

Let $\mathbf{T} = (T_1, \ldots, T_n)$ denote a sample of size n from $f_{\text{pop}}(t)$ with possibly right-censored observations. Without loss of generality, let us assume that $(T_1, \ldots, T_{n_u})$ are exact failure observations and $(T_{n_u+1}, \ldots, T_n)$ are right-censored. Thus, the likelihood for $(\boldsymbol{\lambda}, \mathbf{u}, z)$ is

$$\text{lik}(\boldsymbol{\lambda}, \mathbf{u}, z \mid \mathbf{t}) = \prod_{i=1}^{n_u} h_{\text{pop}}(t_i) \prod_{i=1}^{n} e^{-H_{\text{pop}}(t_i)},$$

which can be expressed as

$$\text{lik}(\boldsymbol{\lambda}, \mathbf{u}, z \mid \mathbf{t}) = \prod_{k=1}^{\infty} \{\lambda_k I(k \le z)\}^{r_k} e^{-I(k \le z) m_k \lambda_k}, \tag{10}$$

where

$$r_k = \sum_{i=1}^{n_u} I(\tau_{k-1} < t_i \le \tau_k) \quad \text{and} \quad m_k = \sum_{i=1}^{n} w_{ki}, \tag{11}$$

with w_{ki} given in (8).

Therefore, the derivation of the posterior full conditional distributions is straightforward. The posterior conditional distribution of λ_k is

$$f(\lambda_k | \boldsymbol{\lambda}_{(-k)}, \mathbf{u}, z, \mathbf{t}) = \mathrm{Ga}(\lambda_k | \alpha_k + u_{k-1} + u_k + r_k, \beta_k + c_{k-1} + c_k + m_k I(k \leq z)) \qquad (12)$$

with $c_0 = 0$ and $u_0 = 0$ w.p.1. The latent variables $\mathbf{u}$ do not appear in the likelihood; thus, their posterior conditional distributions are the same as the prior conditional distributions, i.e.

$$f(u_k | \boldsymbol{\lambda}, \mathbf{u}_{(-k)}) \propto \frac{1}{\Gamma(1+u_k)\Gamma(\alpha_{k+1}+u_k)} \{ c_k(\beta_{k+1} + c_k)\lambda_k \lambda_{k+1} \}^{u_k} I_{\{0,1,\dots\}}(u_k). \qquad (13)$$

Finally, the posterior conditional distribution of z is given by

$$f(z | \boldsymbol{\lambda}, \mathbf{t}) \propto f(z) \exp\left\{ -\sum_{k=1}^{\infty} m_k I(k \leq z) \lambda_k \right\} I(k^* \leq z). \qquad (14)$$

Note that the likelihood, given in (10), imposes a constraint on the possible values of z. The likelihood is zero for all values of z such that there exists a $k > z$ that $r_k \neq 0$. Thus, the full conditional distribution is different than zero only for $k^* \leq z$, where k^* is the largest value of k such that the interval $(\tau_{k-1}, \tau_k]$ has at least one exact observation.

The parameter z plays a critical role in the model. In particular, z determines the threshold τ_z, such that if a patient survives up to that time, then the patient can be considered cured of the disease. Remember that *a priori* $z \sim \mathrm{Po}^+(\mu)$, to let the data drive the posterior inference for μ, we take a hierarchical model by assigning a hyper-prior distribution for μ. If we take $\mu \sim \mathrm{Ga}(a_0, b_0)$, then the posterior conditional distribution of μ given all other parameters in the model only depends on z and is given by

$$f(\mu | z) = \mathrm{Ga}(\mu | a_0 + z - 1, b_0 + 1).$$

Finally, we can estimate τ_z with $\tau_{\hat{z}}$, where $\hat{z}$ is the posterior median, or to be conservative, $\hat{z}$ could be an upper quantile of the posterior distribution of z, i.e. $\hat{z}$ is the smallest value s such that $P(z \leq s) = 1 - \alpha$, for a small α. Hence, in order to obtain posterior inferences, a Gibbs sampler (see, for example, Smith & Roberts, 1993) with these full conditional distributions needs to be implemented.

4. Covariate information

In the standard mixture and proportional hazards cure rate models, covariates can be incorporated by modelling π or θ as a function of the covariates. For the mixture cure rate model, Kuk & Chen (1992) modelled π with a logistic regression model, which, according to Chen *et al.* (1999), has several drawbacks: it does not have a proportional hazards structure for the entire population and yields improper posterior distributions for some non-informative improper priors. For the proportional hazards cure model, Chen *et al.* (1999) introduced covariates through the parameter θ, in order to have a proportional hazards structure for the entire population.

To conduct a covariate analysis, we propose a semiparametric model which is, in spirit, similar to the proportional hazards model of Cox (1972). The 'baseline' hazard is modelled by (6) to explicitly impose a cure fraction and a cure threshold. In addition, we equip the model with more flexibility in such a way that each individual can have a different cure time indexed by z_i. Then, for individual i with a possibly time-dependent p-covariate vector $\mathbf{x}_i(t)$, we propose the hazard function to be of the form

$$h_i(t\,|\,\mathbf{x}_i, z_i) = h(t\,|\,z_i)\,\mathrm{e}^{\gamma'\mathbf{x}_i(t)},\tag{15}$$

where γ is a vector of regression parameters and $h(t\,|\,z_i)$ is the 'baseline' hazard function. We assign $h(t\,|\,z_i)$ a non-parametric mixture prior that is capable of modelling a cure fraction and a cure time, i.e.

$$h(t\,|\,z_i) = \sum_{k=1}^{\infty} \lambda_k I(k \leq z_i) I(\tau_{k-1} < t \leq \tau_k),$$

where $\{\lambda_k\}$ is a Markov gamma process common to all subjects and z_i is the cure threshold index for subject i. Our non-parametric prior on $h(t\,|\,z_i)$ allows a patient to be considered at risk before time τ_{z_i}, and to be considered cured if the patient survives beyond time τ_{z_i}.

Model (15) is not a proportional hazards model due to different cure thresholds indexed by z_i. This distinctive feature allows us to estimate the subject-specific threshold by assigning a prior distribution $f(z_i)$ dependent on the covariates, for instance

$$z_i \sim \mathrm{Po}^+\,(\mathrm{e}^{\delta'\mathbf{y}_i}),$$

where δ is a vector of unknown coefficients and $\mathbf{y}_i$ is a q-vector of fixed covariates. Note that $\mathbf{x}_i$ and $\mathbf{y}_i$ may share common covariates.

In this case, the cumulative hazard function becomes

$$H_i(t\,|\,\mathbf{x}_i, z_i) = \sum_{k=1}^{\infty} \lambda_k I(k \leq z_i) w_{ki}(t, \mathbf{x}_i, \gamma),$$

where

$$w_{ki}(t, \mathbf{x}_i, \gamma) = \begin{cases} \int_{\tau_{k-1}}^{\tau_k} \exp\{\gamma'\mathbf{x}_i(s)\}\,\mathrm{d}s, & t > \tau_k \\ \int_{\tau_{k-1}}^{t} \exp\{\gamma'\mathbf{x}_i(s)\}\,\mathrm{d}s, & t \in (\tau_{k-1}, \tau_k] \\ 0, & \text{otherwise.} \end{cases}$$

Given a sample of size n, let n_u be the number of failures, i.e. $(T_1, \ldots, T_{n_u})$ are the observed event times, and $(T_{n_u+1}, \ldots, T_n)$ are right-censored observations. The likelihood function is

$$\mathrm{lik}(\lambda, \mathbf{u}, \mathbf{z}, \gamma\,|\,\mathrm{data}) = \left\{ \prod_{i=1}^{n_u} h_i(t_i\,|\,\mathbf{x}_i, z_i) \right\} \left\{ \prod_{i=1}^{n} \mathrm{e}^{-H_i(t_i\,|\,\mathbf{x}_i, z_i)} \right\},$$

which can be re-expressed as

$$\mathrm{lik}(\lambda, \mathbf{u}, \mathbf{z}, \gamma\,|\,\mathrm{data}) = \exp\left\{ \sum_{i=1}^{n_u} \gamma'\mathbf{x}_i(t_i) \right\} \prod_{k=1}^{\infty} \left[\lambda_k^{r_k}\,\mathrm{e}^{-m_k(\gamma, \mathbf{z})\lambda_k} \prod_{i=1}^{n_u} I(k \leq z_i)^{I(\tau_{k-1} < t_i \leq \tau_k)} \right],$$

where

$$r_k = \sum_{i=1}^{n_u} I(\tau_{k-1} < t_i \leq \tau_k) \quad \text{and} \quad m_k(\gamma, \mathbf{z}) = \sum_{i=1}^{n} I(k \leq z_i) w_{ki}(t_i, \mathbf{x}_i, \gamma).$$

Then, we can obtain the posterior full conditional distributions, which are needed for the implementation of Gibbs sampling. The full conditional distributions of λ_k and u_k are given in a form similar to the non-parametric case without covariates, i.e. the conditional distribution of λ_k given the rest is

$$f(\lambda_k\,|\,\gamma, \lambda_{(-k)}, \mathbf{u}, \mathrm{data}) = \mathrm{Ga}(\lambda_k\,|\,\alpha_k + u_{k-1} + u_k + r_k, \beta_k + c_{k-1} + c_k + m_k(\gamma, \mathbf{z}))$$

with $c_0 = 0$ and $u_0 = 0$ w.p.1, and

$$f(u_k\,|\,\gamma, \lambda, \mathbf{u}_{(-k)}, \mathbf{z}, \mathrm{data}) = f(u_k\,|\,\lambda, \mathbf{u}_{(-k)}),$$

given by equation (13). The full conditional distribution of z_i is

$$f(z_i|\boldsymbol{\delta},\boldsymbol{\gamma},\boldsymbol{\lambda},\text{data}) \propto \exp\left\{-\sum_{k=1}^{\infty}\lambda_k I(k \le z_i) w_{ki}(t_i,\mathbf{x}_i,\boldsymbol{\gamma})\right\}\text{Po}^+(z_i|e^{\boldsymbol{\delta}'\mathbf{y}_i})I(k_i \le z_i).$$

Note that the likelihood imposes a lower bound k_i for z_i, where k_i is the interval where the observation t_i occurred. If t_i is censored then there is no lower bound, so $k_i = 1$. Let $f(\boldsymbol{\gamma})$ be the prior distribution for $\boldsymbol{\gamma}$, then

$$f(\boldsymbol{\gamma}|\boldsymbol{\lambda},\mathbf{z},\text{data}) \propto f(\boldsymbol{\gamma})\exp\left\{\sum_{i=1}^{n_u}\boldsymbol{\gamma}'\mathbf{x}_i(t_i) - \sum_{k=1}^{\infty}m_k(\boldsymbol{\gamma},\mathbf{z})\lambda_k\right\}.$$

Finally, we assign a hyper-prior distribution, $f(\boldsymbol{\delta})$, for the vector of coefficients $\boldsymbol{\delta}$, so that the data can help us to determine the covariate effects on the cure threshold. Then, the full conditional distribution of $\boldsymbol{\delta}$ only depends on the cure threshold index z_i, given by

$$f(\boldsymbol{\delta}|\mathbf{z}) \propto f(\boldsymbol{\delta})\exp\left\{\sum_{i=1}^{n}\left(\boldsymbol{\delta}'\mathbf{y}_i(z_i-1) - e^{\boldsymbol{\delta}'\mathbf{y}_i}\right)\right\}.$$

As in the case without covariates, the cure time τ_{z_i}, after which an individual would be considered cured, can be estimated by $\tau_{\hat{z}_i}$, where $\hat{z}_i$ is an upper quantile of the posterior distribution of z_i, which can be determined by the covariates.

Based on the semiparametric model (15), the probability of not experiencing failure for an individual with covariates $\mathbf{x}_i(t)$ and cure threshold z_i, is given by $\pi_i = \lim_{t\to\infty}S_i(t|\mathbf{x}_i,z_i)$, and more precisely,

$$\pi_i = \exp\left\{-\sum_{k=1}^{z_i}\lambda_k\int_{\tau_{k-1}}^{\tau_k}e^{\boldsymbol{\gamma}'\mathbf{x}_i(s)}\,\mathrm{d}s\right\}.$$

This gives us a way to characterize the covariate effects on the cure fraction π_i. A negative regression coefficient $\boldsymbol{\gamma}$, for example, leads to a larger probability of not experiencing the failure (i.e. a higher cure fraction) when increasing the value of the corresponding covariate.

5. Numerical study

We demonstrate the properties of our cure threshold model with simulation studies in examples 1 and 2, and then illustrate its application to a bone marrow transplant data set in example 3.

Example 1. First, we simulated data from the proportional hazards cure rate model of Yakolev & Tsodikov (1996) by taking a baseline density with a bounded support. We took a triangular distribution $\text{Tri}(a,c,b)$ as the baseline density, which puts a probability of one to the interval $[a,b]$ and the mode at c. In particular, we chose $a=0$, $c=1$ and $b=4$. The censoring time was independently generated from a uniform distribution to yield a 30% censoring rate. We took the sample size $n=100$ and the cure proportion $e^{-\theta}=0.20$.

We took a fixed time partition with $\tau_0=0$ and $\tau_k=\tau_{k-1}+\Delta$, with $\Delta=0.10$, for $k=1,\ldots,100$. We considered different values of (α_k,β_k,c_k) and for the hyper-prior distribution on μ we took $a_0=b_0=0.01$ in order to be vague. In all scenarios, we ran the Gibbs sampler for 10,000 iterations with a burn-in period of 1000.

We used the logarithm of the pseudo-marginal likelihood (LPML) statistic as a model selection criterion (see, for example, Sinha & Dey, 1997). Table 1 summarizes this statistic as well as several other posterior estimates for different sets of the hyper-parameters when fitting our semiparametric model (6) to the simulated sample.

Table 1. *Posterior estimates of LPML, cure threshold, posterior mean and 95% credible interval (CI) for π, for a simulated sample of size $n = 100$ with a triangular baseline density*

α_k	β_k	c_k	LPML	$\tau_{\hat{z}}$	$\hat{\pi}$	95% CI
0.01	0.01	0	−153.11	7.1	0.188	(0.110, 0.272)
0.1	0.1	0	−149.91	4.2	0.176	(0.105, 0.259)
1	1	0	−134.42	3.6	0.133	(0.082, 0.193)
1	1	5	−130.35	3.8	0.169	(0.103, 0.246)
1	1	20	−127.33	4.0	0.173	(0.098, 0.254)
1	1	50	−125.48	4.1	0.178	(0.111, 0.259)

Table 1 shows that, according to the LPML statistics, the best fit is achieved with either one of the last two sets of hyper-parameters at the bottom of the table, which correspond to $\alpha_k = \beta_k = 1$ and $c_k = 20$ and 50. With our mixture prior for λ_k^*, $\alpha_k = \beta_k = 1$ makes the continuous part of the mixture very different from the point mass at zero, and thus the model can easily capture the change point z. Otherwise, if α_k and β_k are very small to induce a large prior variance, the model may not distinguish well between the continuous part and the point mass at zero. The posterior estimate of the cure time τ_z is based on the 95% quantile of the posterior distribution of z, i.e. $\tau_{\hat{z}} = \Delta \times \hat{z}$ where $\hat{z}$ is the 95% quantile. We can see that the two best fitting models according to the LPML statistic can accurately estimate the true cure time, 4, and the true cure rate, 0.20. For a comparison with other (frequentist) methods, we computed the estimate of the cure proportion based on the work of Maller & Zhou (1992) and obtained $\hat{\pi} = 0.182$ with a 95% confidence interval (0.102, 0.263), which is comparable to our estimates.

In Fig. 1, we present the hazard rate estimates for the last four sets of parameters in Table 1, and include 95% credible intervals together with the true hazard. The credible
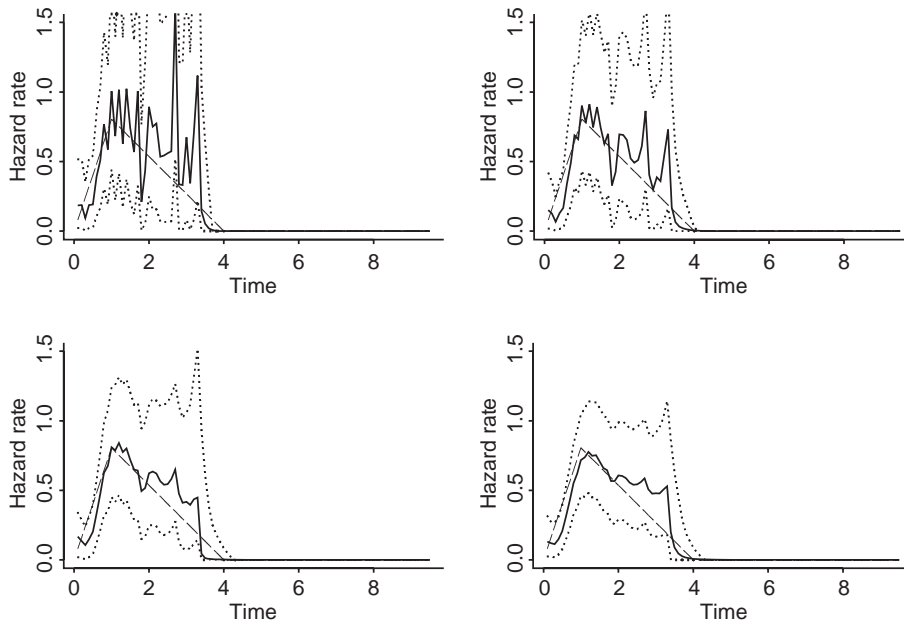
Fig. 1. Posterior hazard rate estimates (solid line) together with 95% credibility intervals (dotted line). The dashed line corresponds to the true hazard. Top-left $c_k = 0$, top-right $c_k = 5$, bottom-left $c_k = 20$ and bottom-right $c_k = 50$.
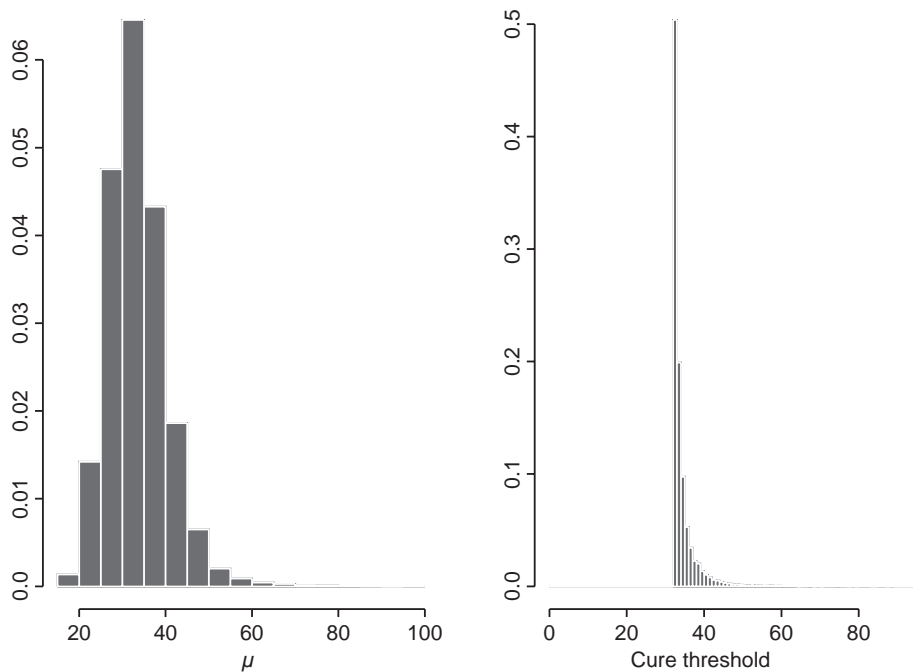
Fig. 2. Posterior distributions: μ (left panel) and z (right panel).

intervals were calculated as the 2.5% and 97.5% quantiles of the posterior distributions. We can see that the hazard estimates are smoother as c_k increases and the credible bands become narrower. The posterior distributions of μ and the cure threshold z are reported in Fig. 2. These graphs correspond to the last set of hyper-parameters in Table 1, that is $(\alpha_k, \beta_k, c_k) = (1, 1, 50)$. The posterior median of μ is 32.8, which is located near the lower bound of the distribution of z, 33. This suggests that the 50% of the mass in the lower part of the distribution of μ collapses into one single point (the lower bound) in the distribution of z due to the constraint at the last exact observation.

To examine the frequentist properties of our estimates, we calculated the coverage percentage of the 95% credible intervals for τ_z and π based on 500 samples of size 100. If we take $(\alpha_k, \beta_k, c_k) = (1, 1, 50)$, then the coverage rate of the 95% credible interval is 91.7% for τ_z, and 94.8% for π. Therefore, our Bayesian credible intervals preserve the desirable frequentist properties.

Example 2. In the second example, we intend to compare the proposed model with the traditional cure rate models that cannot model the finite cure time. We simulated data from the proportional hazards cure model of Yakolev & Tsodikov (1996) with the baseline density given by an exponential distribution with mean 1. In contrast to example 1, the hazard gradually decays to zero instead of dropping to zero at a finite cure time. We applied the proposed cure threshold model so as to capture a finite cure time in this 'traditional' case. The censoring time was independently generated from a uniform distribution to yield 25% of the censoring times, and we took a sample size of $n = 100$ and a cure proportion $e^{-\theta} = 0.25$.

Table 2. *Posterior estimates of LPML, cure threshold, posterior mean and 95% CI for π, for a simulated sample of size n = 100 with an exponential baseline density*

α_k	β_k	c_k	LPML	$\tau_{\hat{z}}$	$\hat{\pi}$	95% CI
0.01	0.01	0	−120.73	10.2	0.249	(0.166, 0.340)
0.1	0.1	0	−120.13	5.9	0.229	(0.151, 0.317)
1	1	0	−117.40	5.1	0.124	(0.075, 0.182)
1	1	5	−111.09	5.4	0.193	(0.127, 0.269)
1	1	20	−108.77	5.9	0.219	(0.143, 0.302)
1	1	50	−107.47	6.3	0.232	(0.152, 0.321)

We partitioned the time axis by setting $\tau_0 = 0$ and $\tau_k = \tau_{k-1} + \Delta$, with $\Delta = 0.15$, for $k = 1, \ldots, 100$. We took $a_0 = b_0 = 0.01$ for the prior on μ and considered different sets of hyper-parameters for the Markov gamma process of the baseline hazard. We ran the Gibbs sampler for 10,000 iterations with a burn-in period of 1000. Table 2 summarizes the model selection statistic LPML and posterior estimates of τ_z and π. According to the LPML statistic, the best fitting models are obtained when $\alpha_k = \beta_k = 1$ and $c_k = 20$ or 50.

For the last three cases at the bottom of Table 2, the 95% credible intervals for π contain the true value of the cure rate, 0.25. If we compute the estimate of the cure proportion by Maller & Zhou (1992), we obtain a value of 0.249 with a 95% confidence interval (0.160, 0.337). Although our cure threshold model does not exactly match the model that generated the data, due to the difference in the existence of a cure threshold or not, our model managed to correctly estimate the cure rate.

Furthermore, the hazard and the survival functions are also well estimated. In Fig. 3, we can see that the true hazard and survival functions lie between the 95% credible bands when taking $(\alpha_k, \beta_k, c_k) = (1, 1, 50)$.
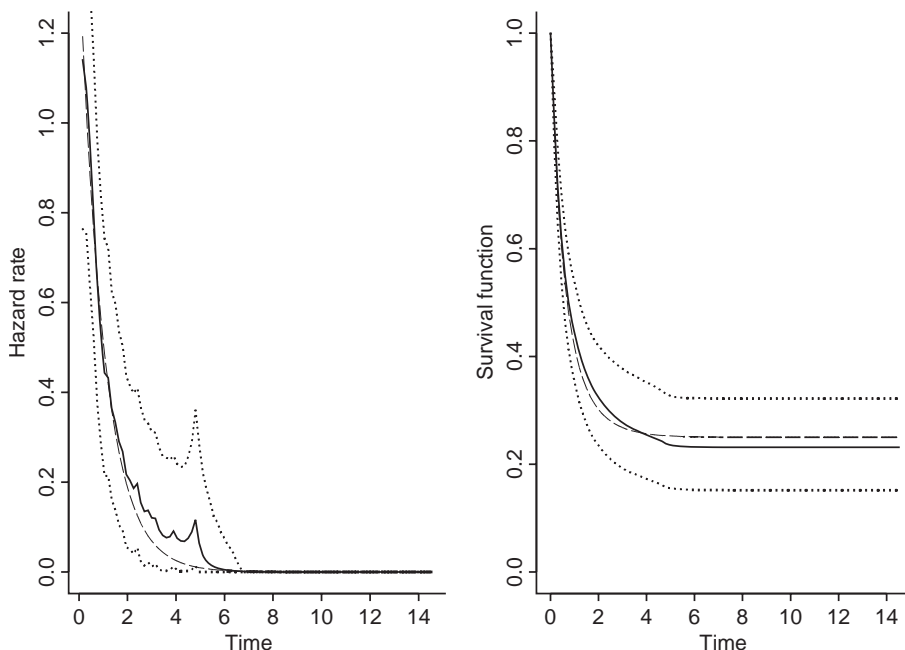
Fig. 3. Posterior estimates (solid line) and 95% CI (dotted line): Hazard rate (left panel) and survival function (right panel). The dashed line corresponds to the true hazard/survival function.

Considering the last parameter specification in Table 2, and noting that the data were simulated from the model with no cure threshold, then an estimated cure time of 6.3 corresponds to the 99.94% quantile of the uncured group. This would mean that there is a probability of 0.0006 of observing an event after this estimated 'cure time'. Therefore, if a patient has survived up to τ_2, the patient is practically cured. In practice, a cure threshold would provide very useful information and guidance for the clinical management of the disease. In other words, our model is able to adequately estimate the cure proportion, as well as providing additional information about the possible cure time.

Example 3. As a final illustration, we applied the proposed method to a bone marrow transplantation (BMT) data set (Avalos *et al.*, 1993). BMT is a procedure to restore stem cells by replacing bone marrow that has been destroyed as a result of treatment with high doses of anticancer drugs or radiation therapy. The goal is for the healthy, transplanted stem cells to restore the bone marrow's ability to produce functioning blood cells in numbers that are adequate for good health.

Patients represented in the data set had been diagnosed with Hodgkin's disease or with non-Hodgkin's lymphoma, and had undergone one of two types of BMT: (i) allogeneic BMT (infusion of bone marrow from a matched sibling donor), or (ii) autogeneic BMT (reinfusion of the patient's own marrow that had been removed prior to marrow-destroying treatment). Of 43 BMT patients, 16 had undergone an allogeneic transplant ($x_1 = 1$) and 27 an autogeneic transplant ($x_1 = 0$). The objective of the study was to evaluate the leukaemia-free survival difference between the two BMT groups. Time to death or relapse was recorded in days. Patients were also categorized by their diagnosis of Hodgkin's disease ($x_2 = 1$) or non-Hodgkin's lymphoma ($x_2 = 0$). Other covariates included in the analysis were the Karnofsky score at transplant (x_3) and the waiting time in months from diagnosis to transplant (x_4). The Karnofsy score provides a general indication of a patient's wellness or level of disability due to disease or illness.

In Fig. 4, we show the estimated Kaplan–Meier survival curves stratified by the transplant groups. For the BMT patients, there is a clear stable plateau after approximately one and a half years of follow-up. This is strong empirical evidence that some percentage of patients in this population might be cured.
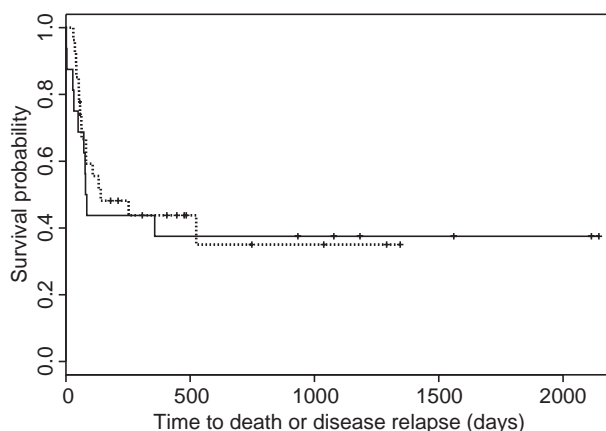
Fig. 4. Kaplan–Meier survival curves stratified by transplant groups: (—) allogeneic group and (···) autogeneic group.

We implemented our semiparametric model described in section 4 with the four covariates $(x_1, \ldots, x_4)$ in the multiplicative part of the hazard, and the same four covariates to determine the cure threshold for each patient, i.e. $y_j = x_j$ for $j = 1, \ldots, 4$. We defined a fixed time partition of the form, $\tau_0 = 0$ and $\tau_k = \tau_{k-1} + \Delta$, with $\Delta = 30$ (days) for $k = 1, \ldots, 72$. We considered different sets of hyper-parameters (α_k, β_k, c_k) and assigned vague independent priors to the regression parameters γ_s, that is, $\gamma_s \stackrel{\text{ind}}{\sim} N(0, 100)$ for $s = 1, \ldots, 4$, and vague independent priors for the coefficients δ_j, i.e. $\delta_j \stackrel{\text{ind}}{\sim} N(0, 100)$ for $j = 1, \ldots, 4$.

Simulating from the posterior full conditional distributions of λ, $\mathbf{u}$ and $\mathbf{z}$ is straightforward. However, in order to simulate γ_s and δ_j, we implemented Metropolis–Hastings steps (see, for example, Tierney, 1994), described as follows:

(i) M–H step for γ_s: At iteration $r + 1$, we simulated γ_s^* from $N(\gamma_s^{(r)}, \sigma^2)$, and took $\gamma_s^{(r+1)} = \gamma_s^*$ with probability $p(\gamma_s^*, \gamma_s^{(r)})$ or $\gamma_s^{(r+1)} = \gamma_s^{(r)}$ with probability $1 - p(\gamma_s^*, \gamma_s^{(r)})$, where

$$p(\gamma_s^*, \gamma_s^{(r)}) = \min\left\{1, \frac{f(\gamma_s^*)}{f(\gamma_s^{(r)})} \exp\left[\sum_{i=1}^{n_u} (\gamma_s^* - \gamma_s^{(r)}) x_{si}(t_i) + \sum_{k=1}^{\infty} \{m_k(\boldsymbol{\gamma}^{(r)}, \mathbf{z}) - m_k(\boldsymbol{\gamma}^*, \mathbf{z})\} \lambda_k\right]\right\},$$

with $\boldsymbol{\gamma}^* = (\gamma_1^{(r+1)}, \ldots, \gamma_{s-1}^{(r+1)}, \gamma_s^*, \gamma_{s+1}^{(r)}, \ldots)$.

(ii) M–H step for δ_j: At iteration $r + 1$, we simulated δ_j^* from $N(\delta_j^{(r)}, \sigma^2)$, and took $\delta_j^{(r+1)} = \delta_j^*$ with probability $q(\delta_j^*, \delta_j^{(r)})$ or $\delta_j^{(r+1)} = \delta_j^{(r)}$ with probability $1 - q(\delta_j^*, \delta_j^{(r)})$, where

$$q(\delta_j^*, \delta_j^{(r)}) = \min\left\{1, \frac{f(\delta_j^*)}{f(\delta_j^{(r)})} \exp\left[\sum_{i=1}^{n} (\delta_j^* - \delta_j^{(r)}) y_{ji}(z_i - 1) - \left(e^{\boldsymbol{\delta}^{*\prime} \mathbf{y}_i} - e^{\boldsymbol{\delta}^{(r)\prime} \mathbf{y}_i}\right)\right]\right\},$$

with $\boldsymbol{\delta}^* = (\delta_1^{(r+1)}, \ldots, \delta_{j-1}^{(r+1)}, \delta_j^*, \delta_{j+1}^{(r)}, \ldots)$.

We carried out a random walk algorithm with $\sigma^2 = 25$ for the variance of the proposal distribution in each case. We ran the Gibbs sampler for 100,000 iterations using a burn-in of 20,000. The posterior estimates of the LPML statistic are summarized in Table 3, from which we can see that there is little difference in the model fit for different specifications of the hyper-parameters. In fact, for the last two cases where $(\alpha_k, \beta_k) = (2, 2)$ and $c_k = 20, 50$, the fitting of the model is basically the same. At the bottom of Table 3, we have included the LPML statistic for the semiparametric model proposed by Chen *et al.* (1999) when using a partition of $J = 5$ intervals in such a way that the number of failures in each partition is approximately the same. We took the prior distributions $\lambda_j \sim \text{Ga}(0.01, 0.01)$ for the baseline hazard, and independent $N(0, 100)$ priors for the regression coefficients in their proportional hazards structure. Clearly, based on the LPML statistics, the model by Chen *et al.* (1999) does not perform as well as our model.

The covariates appear in our semiparametric model (15) via two different ways: (i) in a multiplicative manner affecting the 'baseline' hazard and (ii) in the Poisson mean of z_i affecting the cure threshold. Posterior estimates of the covariate effects on the 'baseline' hazard, $\hat{\boldsymbol{\gamma}}$,

Table 3. *Posterior estimates of the LPML statistics for the BMT data set*

α_k	β_k	c_k	LPML
1	1	0	-163.33
2	2	0	-162.85
2	2	5	-162.61
2	2	20	-161.74
2	2	50	-161.52
Model of Chen *et al.*			-165.50

Table 4. *Estimated covariate effects on the hazard for the BMT data*

	Our model		Model of Chen *et al.*	
Covariate	Post. mean	95% CI	Post. mean	95% CI
Intercept	−	−	4.59	(2.79, 6.42)
Transplant type	−0.03	(−0.92, 0.86)	0.27	(−0.62, 1.14)
Hodgkin's disease	1.17	(0.14, 2.15)	1.02	(0.0003, 2.05)
Karnofsky score	−0.07	(−0.08, −0.05)	−0.06	(−0.08, −0.04)
Waiting time	−0.01	(−0.03, 0.008)	−0.01	(−0.03, 0.006)

Table 5. *Estimated covariate effects on the cure threshold for the BMT data*

Covariate	Post. mean	95% CI
Transplant type	0.10	(−0.73, 0.88)
Hodgkin's disease	−0.74	(−1.70, −0.001)
Karnofsky score	0.03	(0.02, 0.04)
Waiting time	0.004	(−0.01, 0.02)

are presented in Table 4, when taking $(\alpha_k, \beta_k, c_k) = (2, 2, 50)$. We see that the type of transplant (autogeneic or allogeneic) and the waiting time had no significant effects on the hazard, while a diagnosis of Hodgkin's disease and the Karnofsky score did. The risk of death or disease relapse was approximately twice higher for patients with Hodgkin's disease than those with non-Hodgkin's lymphoma. The Karnofsky score imposed a significant negative effect on the hazard, i.e. a decrease of 10 units in the Karnofsky scale would increase by 50% the risk of death or disease relapse.

In Table 4, we have also included the estimated covariate effects when fitting the model of Chen *et al.* (1999). Comparing the results of the two models, we can see that the posterior estimates for the Karnofsky score and waiting time are the same, while those for the transplant type and Hodgkin's disease are slightly different. Using the model by Chen *et al.* (1999), we can obtain the same conclusion regarding the covariate effects in the hazard as that with our model. A diagnosis of the Hodgkin's disease and Karnofsky score had significant effects on the hazard. This supports the fact that even though the models are different, they provide similar results.

One major advantage of our model is that we can estimate the cure threshold. We present the covariate effects in the Poisson mean to model the cure times in Table 5. We can see that the covariates with a significant effect on the cure threshold are, a diagnosis of Hodgkin's disease, and the Karnofsky score. A patient with Hodgkin's disease would have a reduction of 50% in the mean cure time compared to a patient with non-Hodgkin's lymphoma. It might not seem sensible that a patient with a more serious condition would experience a cure sooner. However, because the presence of Hodgkin's disease increases the hazard twice as much, this implies that patients diagnosed with Hodgkin's disease are likely to die more quickly than patients diagnosed with non-Hodgkin's lymphoma. Therefore, once a patient with Hodgkin's disease survives beyond a relatively shorter threshold of time, then he/she would be considered cured. Similarly, 10 points more in the Karnofsky scale would increase 35% the mean cure time.

Once we have estimated the parameters of the model, we can obtain predictive estimates of other quantities of interest, such as the hazard and survival functions, cure thresholds and cure rates. Toward this goal, we considered four hypothetical patients with differing Karnofsky scores and differing diagnoses of Hodgkin's disease or non-Hodgkin's lymphoma, which are the two covariates with significant effects in the model. Table 6 shows the covariates for the four new patients together with estimates for the cure times (based on 95% quantiles) and cure

Table 6. *Predictive cure thresholds and cure proportions for new patients in the BMT data*

Patient (x_1, x_2, x_3, x_4)	τ_z 95% quantile	π Post. mean
(0, 0, 90, 36)	34 months	0.64
(0, 1, 90, 36)	24 months	0.50
(0, 0, 60, 36)	15 months	0.27
(0, 1, 60, 36)	10 months	0.15

probabilities when setting $(\alpha_k, \beta_k, c_k) = (2, 2, 50)$. As expected, patients with Hodgkin's disease have shorter cure times (15 and 10 months) than patients with non-Hodgkin's lymphoma (34 and 24 months), for Karnofsky scores of 90 and 60, respectively. On the other hand, patients with a larger Karnofsky score have a larger probability of being cured from the disease.

Finally, in Figs 5 and 6, we present the predictive hazard and survival function estimates for the four patients, respectively. The hazard rate for patients with Hodgkin's disease and a
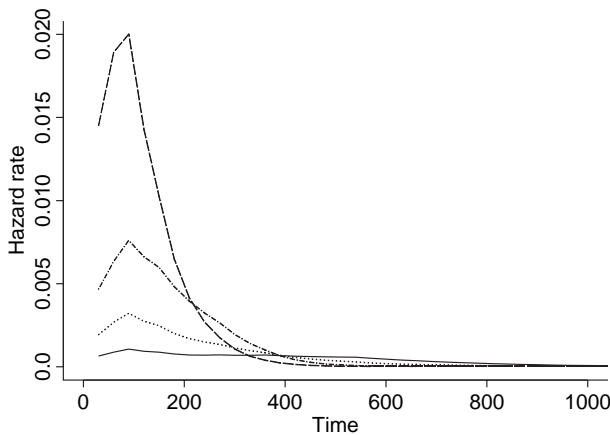
Fig. 5. Predictive hazard rate estimates for four patients with covariates (x_1, x_2, x_3, x_4): solid line (0, 0, 90, 36), dotted line (0, 1, 90, 36), dashed-dotted line (0, 0, 60, 36) and dashed line (0, 1, 60, 36).
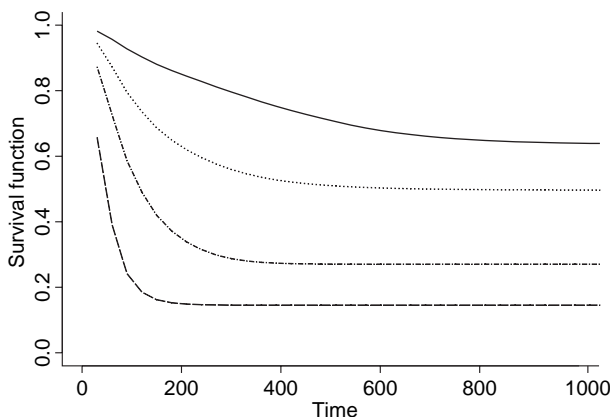
Fig. 6. Predictive survival function estimates for four patients with covariates (x_1, x_2, x_3, x_4): solid line (0, 0, 90, 36), dotted line (0, 1, 90, 36), dashed-dotted line (0, 0, 60, 36) and dashed line (0, 1, 60, 36).

low Karnofsky score is higher than that for patients with non-Hodgkin's lymphoma and a high Karnofsky score. In the predictive survival curve estimates, we can see that the Karnofsky score strongly affects the probability of being cured. When the Karnofsky score increases from 60 to 90, the cure rate increases from 15% to 50%, for patients with Hodgkin's disease, and from 27% to 64%, for patients with non-Hodgkin's lymphoma.

6. Conclusions

We have proposed a new cure rate model that explicitly incorporates a parameter that determines the time after which a patient can be considered cured. This is in contrast to other cure rate models with which the estimation of a cure time is not possible. In reality, after the cure threshold, the hazard drops to zero, as the susceptible or non-cured subjects would have already experienced the event, and the rest of the subjects in the population would be considered risk free. This is a distinct and attractive feature of our model compared with other cure rate models in the literature, which allows the hazard to slowly decay to zero regardless of the cure threshold.

For making inference, we have proposed a semiparametric prior distribution based on a mixture of a Markov gamma process and a point mass at zero. This allows us to model the cured and uncured groups at the same time, whereas the two groups are modelled separately as a mixture in other cure models. We have extended our proposal to cope with covariates in a Bayesian semiparametric cure threshold model. Our semiparametric construction includes an exponential link function of the covariates in a multiplicative way, as well as allows each patient to have a different cure time depending on the covariates. Implementation of our model is straightforward via a Gibbs sampler.

In a frequentist approach, estimation of the threshold parameter τ in (5) might be challenging when leaving the non-negative function $h(t)$ completely unknown. The partial likelihood method by taking $h(t)$ as a nuisance parameter does not appear to be promising, especially for model (15). Alternative approaches for studying the frequentist properties of (5) would be required.

References

Avalos, B. R., Klein, J. L., Kapoor, N., Tutsckha, P. J., Klein, J. P. & Copelan, E. A. (1993). Preparation for marrow transplantation in Hodgkin's and non-Hodgkin's lymphoma using Bu/CY. *Bone Marrow Transplant*. **13**, 133–138.

Betensky, R. A. & Schoenfeld, D. A. (2001). Nonparametric estimation in a cure model with random cure times. *Biometrics* **57**, 282–286.

Berkson, J. & Gage, R. P. (1952). Survival curve for cancer patients following treatment. *J. Amer. Statist. Assoc.* **47**, 501–515.

Chen, M. H., Ibrahim, J. G. & Sinha, D. (1999). A new Bayesian model for survival data with a surviving fraction. *J. Amer. Statist. Assoc.* **94**, 909–919.

Cox, D. R. (1972). Regression models and life-tables (with discussion). *J. Roy. Statist. Soc. Ser. B* **34**, 187–220.

Gray, R. J. & Tsiatis, A. A. (1989). A linear rank test for use when the main interest is in differences in cure rates. *Biometrics* **45**, 899–904.

Ibrahim, J. G., Chen, M. H. & Sinha, D. (2001a). *Bayesian survival analysis*. Springer, New York.

Ibrahim, J. G., Chen, M. H. & Sinha, D. (2001b). Bayesian semiparametric models for survival data with a cure fraction. *Biometrics* **57**, 383–388.

Kuk, A. Y. C. & Chen, C. H. (1992). A mixture model combining logistic regression with proportional hazards regression. *Biometrika* **79**, 531–541.

Lam, K. F. & Xue, H. (2005). A semiparametric regression cure model with current status data. *Biometrika* **92**, 573–586.

Lu, W. & Ying, Z. (2004). On semiparametric transformation cure models. *Biometrika* **91**, 331–343.

Maller, R. A. & Zhou, S. (1992). Estimating the proportion of immunes in a censored sample. *Biometrika* **79**, 731–739.

Maller, R. A. & Zhou, S. (1995). Testing for the presence of immune or cured individuals in censored survival data. *Biometrics* **51**, 1197–1205.

Nieto-Barajas, L. E. & Walker, S. G. (2002). Markov beta and gamma processes for modelling hazard rates. *Scand. J. Statist.* **29**, 413–424.

Peng, Y. & Dear, K. B. G. (2000). A nonparametric mixture model for cure rate estimation. *Biometrics* **56**, 237–243.

Sinha, D. & Dey, D. K. (1997). Semiparametric Bayesian analysis of survival data. *J. Amer. Statist. Assoc.* **92**, 1195–1212.

Smith, A. F. M. & Roberts, G. O. (1993). Bayesian computations via the Gibbs sampler and related Markov chain Monte Carlo methods. *J. R. Statist. Soc. Ser. B* **55**, 3–23.

Sy, J. P. & Taylor, J. M. G. (2000). Estimation in a Cox proportional hazards cure model. *Biometrics* **56**, 227–236.

Tierney, L. (1994). Markov chains for exploring posterior distributions. *Ann. Statist.* **22**, 1701–1722.

Tsodikov, A. (2002). Semi-parametric models of long- and short-term survival: an application to the analysis of breast cancer survival in Utah by age and stage. *Statist. Med.* **21**, 895–920.

Tsodikov, A., Ibrahim, J. G. & Yakovlev, A. Y. (2003). Estimating cure rates from survival data: an alternative to two-component mixture models. *J. Amer. Statist. Assoc.* **98**, 1063–1078.

Walker, S. G. & Mallick, B. K. (1997). Hierarchical generalized linear models with Bayesian nonparametric mixing. *J. R. Statist. Soc. Ser. B* **59**, 845–860.

Yakovlev, A. Y. & Tsodikov, A. D. (1996). *Stochastic models of tumor latency and their biostatistical applications*. World Scientific, New Jersey.

Yin, G. & Ibrahim, J. (2005). Cure rate models: a unified approach. *Can. J. Statist.* **33**, 559–570.

Luis E. Nieto-Barajas, Department of Statistics, ITAM, Rio Hondo 1, Tizapan San Angel, 01000, Mexico D.F., Mexico.
E-mail: lnieto@itam.mx

Review Article
Heterotransplant mouse model cohorts of human malignancies: A novel platform for Systematic Preclinical Efficacy Evaluation of Drugs (SPEED)

Ashutosh K. Pathak[1,3], Manisha Bhutani[1,2], Pierre Saintigny[1], Li Mao[1]

[1]Department of Thoracic/Head and Neck Medical Oncology, University of Texas M. D. Anderson Cancer Center Houston, TX 77030; [2]Internal Medicine, Michigan State University, East Lansing, MI 48824; and [3]Discovery Medicine & Clinical Pharmacology (DMCP) Oncology/Immunology, Bristol-Myers Squibb Company, Princeton, NJ 08543, USA

Abstract: Advances in molecular biology demonstrate that cancer is heterogeneous disease necessitating a personalized management approach. This is introducing a paradigm shift in clinical trial designs where molecular characterization of cancers is assuming importance equal to (or even more than) the traditional histologic diagnosis as the eligibility criterion for randomized clinical trials of new therapies. Recommendations have been made to gather the molecular information from clinical phase II trials distinguishing responding from non responding tumors for subsequent planning of large scale phase III trials. However by the time we reach phase II level, more than a billion dollars apart from years of research have been invested. It would be therefore prudent to conceptualize laboratory based platforms to obtain the proof of concept as early as possible, even before embarking upon the pivotal clinical trials. In this regard, we hereby propose and detail a novel preclinical platform incorporating the existing mouse models to address the issue of tumor heterogeneity in a systematic manner through creation of a setting similar to phase II trials in human patients. By providing critical information about a drug's efficacy and the molecular determinants of response early on, this platform would potentially provide a solid foundation to build avant-garde clinical trials integrating recent advances in molecular medicine.

Introduction

The approval rates for the Investigational New Drugs (INDs) have been decreasing whereas the developmental cost and duration are increasing exponentially [1,2]. It is estimated that approximately 90% of the INDs fail to get US FDA approval and this situation is even worse in the oncology field, with over 95% failure rate 3. What is more worrisome is more than 70% of the anti-cancer drug candidates fail in Phase II and approximately 60% of those entered into Phase III fail, causing enormous loss of time and resources [3,4]. The major cause of Phase II / III failures is lack of efficacy of the testing agents 4 with 80% of phase III failures in oncology attributed to lack of efficacy [5].

While lack of efficacy has been traditionally attributed to ineffective drugs, in the post genomic era it has been realized that many potentially effective agents fail because we fail to address the molecular subtypes and signatures accounting for variations in response to treatment and survival among patients [6,7]. This results in erroneous clinical trial design/ analysis, enormous wastage of patient and monetary resources, addition of another failed therapy to the graveyard, and demise of potentially effective therapies as exemplified by the failure of Gefitinib to improve outcome in non–small-cell lung cancer when added to chemotherapy. On the other hand, brilliant successes of Trastuzumab and Imatinib suggest that integration of

molecular determinants of response in clinical trials is a promising strategy to test the intrinsic efficacy of an IND against a specific patient subgroup. Recommendations have therefore been made for enrichment trial design by limiting enrollment to patients (over)expressing a molecular target or putative predictors of response [7,8]. However, at the time of clinical studies, such predictors are either hypothetical or we need another clinical trials of other drugs affecting the same target to reach a validated predictor.

To address these issues, experts have recommended utilizing phase II trial analysis to identify the molecular markers distinguishing responders and non responders for subsequent planning of randomized trials evaluating INDs [9,10]. It should however be remembered that by the time the we reach phase II level, approximately billion dollars and years of research has been invested [11]. Considering the slow pace of clinical trials, the high rates of compound attrition late in clinical phase, the relatively small number of patients available for trials and the finite R&D budgets of the biopharmaceutical industry, solving the challenges of personalized therapies requires low-cost, preferably laboratory based model systems to test an IND's efficacy and identify and validate molecular predictors of response even before we embark upon the clinical trials. Fortified with such a data, we would be able to design our clinical trials with greater confidence and save enormous amount of time, money and patient resources. We believe that a potential solution lies in the innovative use of mouse models of human cancer with an aim to facilitate the identification of the efficacious drugs, as well as predictors of response. However, to ferret out the most appropriate mouse model from amongst the existing ones, it is imperative to understand the advantages and pitfalls of available mouse models.

The recent unraveling of complete mouse genome sequence has strengthened our capability to study the parallels and contrasts between the pharmacology of drug stability, metabolism and action between mouse and human studies and have thus reinvigorated our interests in mice models [12]. While the development of genetically engineered mouse models has contributed greatly towards understanding the process of carcinogenesis and target selection, the xenograft models,

established by injecting 0.5–1.0 million cultured cancer cells subcutaneously in a nude / SCID mice, have been more popular for drug screening purposes due to its ease, low cost, and faster establishment. Almost every successful cancer therapy developed in the modern era has undergone xenograft testing, however many agents that show consistent and potent anticancer efficacy in xenografts, fail in the clinical trials due to lack of efficacy. This might be due to reliance of xenografts on small numbers of homogeneous cell lines adapted to the artificial culture conditions and acquisition of biological characteristics significantly different from the original natural clone over serial passages in culture.

In an attempt to circumvent this flaw, investigators have tried transplanting fresh cells or tissues obtained directly from the cancer patients into the nude / SCID mice, called heterotransplants. This approach has demonstrated superior correlation of chemosensitivity and specificity data for individualized therapy [13-18]. Amongst these approaches, studies where intact tissue from the patient was transplanted into the mice have shown the excellent patient response prediction rates of 90% and 97% for chemosensitivity and chemoresistance, respectively [19]. We have previously reported the response rate of 21% (95% CI, 9–38%) to paclitaxel in a series of 34 NSCLC heterotransplants, comparable to the response rates observed in chemotherapy-naïve NSCLC patients [20]. As the original microenvironment of the human tumor is retained, the crucial interplay of human stroma - neoplastic components is recapitulated to a greater extent in heterotransplants. This contributes to better replication of pharmacogenomic profiles, histology, chromosome complement, antigen expression, and gene expression of human tumors [19-21], accounting for their better preclinical predictive value as compared to cell line based xenografts. Therefore out of the available models, heterotransplants seem closest to an 'ideal' model to establish a novel platform for Systematic Preclinical Efficacy Evaluation of Drugs (SPEED).

The SPEED approach is designed to address the fundamental uncoupling or disconnection between the bench scientist, who may not understand the intricacies of clinical efficacy trials, and the clinical scientist, who may find it
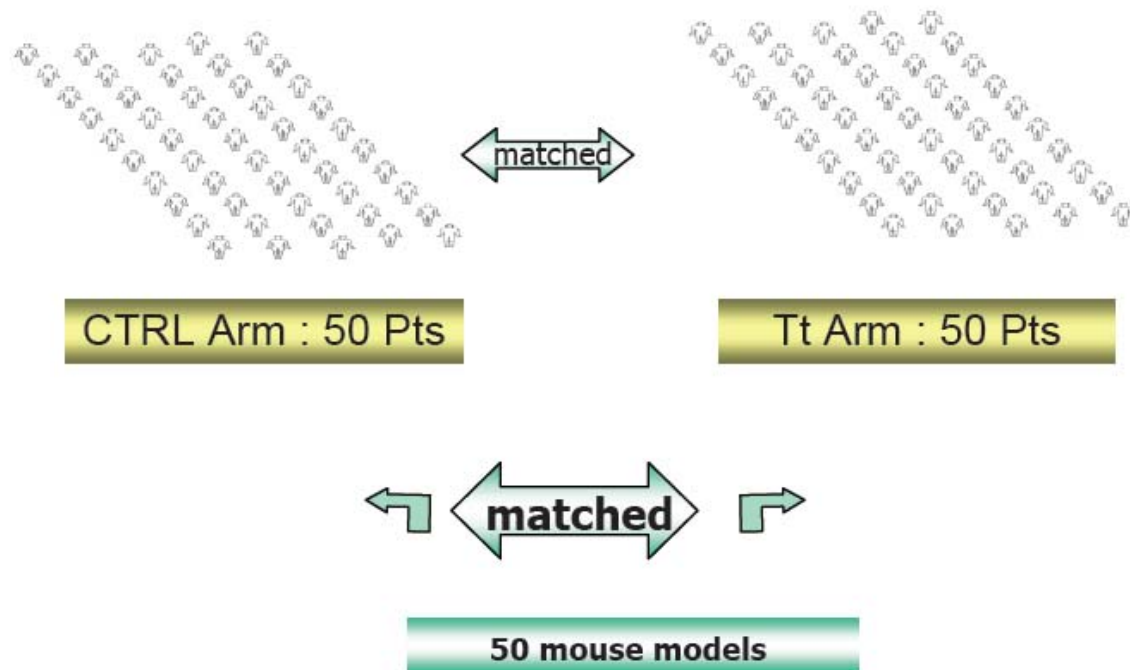
Figure 1: A mouse cohort prepared from 50 models for a specific malignancy would be equivalent to 100 patients enrolled in a clinical trial. Both test (Tt) and controls (CTRL) arms of the mouse cohort can be generated readily at a fraction of cost and time compared to clinical trials. The two arms of mouse cohort are adequately matched with regard to various biological properties.

difficult to make calculated translation of bench side discoveries. For SPEED, a reasonable number (close to the number needed for clinical phase II studies) of well characterized and validated heterotransplant mouse models would be established to make perpetual cohorts comprising of various histologies (**Figure 1**). These cohorts would be used to carry out preclinical IND efficacy studies in a systematic manner (replicating clinical phase II trials) to gauge an agent's possible clinical efficacy and identify the molecular markers of response.

We must understand that as of now, the efficacy criteria used to advance an agent in preclinical studies are different from those in the clinical setting. For example, the NCI criterion for assessing a drug response in mice models is 58% inhibition of tumor growth. In a clinical trial, however, this would define a Progressive Disease. Alternatively, animals are treated immediately after transplantation, before the development of overt tumors; in essence, studying a form of chemoprevention

which is of limited therapeutic relevance. Therefore the efficacy results of mice studies frequently do not translate into standard clinical results.

Moreover, these preclinical efficacy results, usually obtained in a limited number of mice, are often considered exciting enough to initiate pivotal clinical trials, not surprisingly leading to more than 90% failure rates. Until we systematically test the drugs at preclinical stage within a framework of convincing statistical power/ design, we might not emerge of the current situation where success in drug development depends more upon chance rather than scientific and robust foundation. In this regard, The SPEED platform provides us an opportunity to apply the principles of biostatistics to meticulously design the preclinical studies in a systematic manner. The required number of models according to the power of study can be created and not only the clinical criteria of 'response' but also the 'response rates' can be measured in the mouse cohort to gauge the clinical efficacy of the INDs. A careful sample size calculation

Figure 2: A sample of fresh tumors are obtained from lung cancer patients at the time of surgery and transplanted subcutaneously into 4- 6 weeks old female nu+/nu+ mice under anesthesia by a small incision in bilateral axillary area. On reaching a size of 1,500 mm3, the tumors are harvested and propagated further in 2nd batch of mice. After these tumors are established, tumor tissue is harvested, cryopreserved, and can be used to prepare mouse cohorts as and when required. Multiple cohorts may be generated simultaneously to test various drugs, doses, or combinations.

should help us achieve the scientific objectives and extract information from the preclinical data to translate into clinical setting.

As a first step in this regard, we have initiated to establish a cohort of heterotransplant models from primary non small cell lung cancer (NSCLC) tumors of unrelated patients. The tumors are propagated in mice for limited number of passages to retain the human components of the tumor as much as possible. Because tumor pieces can be cryopreserved and re-implanted with high success rates as and when required [21], each model will allow expansion of early passage materials for hundreds of mice tests (**Figure 2**). By enabling us to collect data on modulations in biology, molecular profiles, and response to various interventions in these close- to- human mouse models, SPEED approach has significant potential for anticancer research.

SPEED approach can be utilized to discover molecular markers of response and evaluate targeted agents for suitability to modern personalized clinical trials. In numerous cases

the excellent preclinical results with INDs do not translate in the clinical practice because we do not have guiding examples of where a class of agents would be most effective. Most trials of targeted agents are still conducted empirically and 'fail' because many participants did not express the target or the molecular predictor(s) of response [6,22]. In this respect, SPEED approach can guide us by providing preclinical information to enrich trial cohorts by selecting appropriate patients expressing molecular signatures predictive of response and bring on a paradigm shift from the current template approach to the cutting edge personalized approach in clinical trials.

SPEED approach can address many other clinical questions. For, example, there are questions about the prognostic value of costly or invasive post-therapy analysis of residual tumors, which can be addressed using comparable mouse models exposed to the same therapy. We can establish a mouse cohort from patients with residual or progressive/ metastatic tumors to define the molecular/ genetic determinants of response
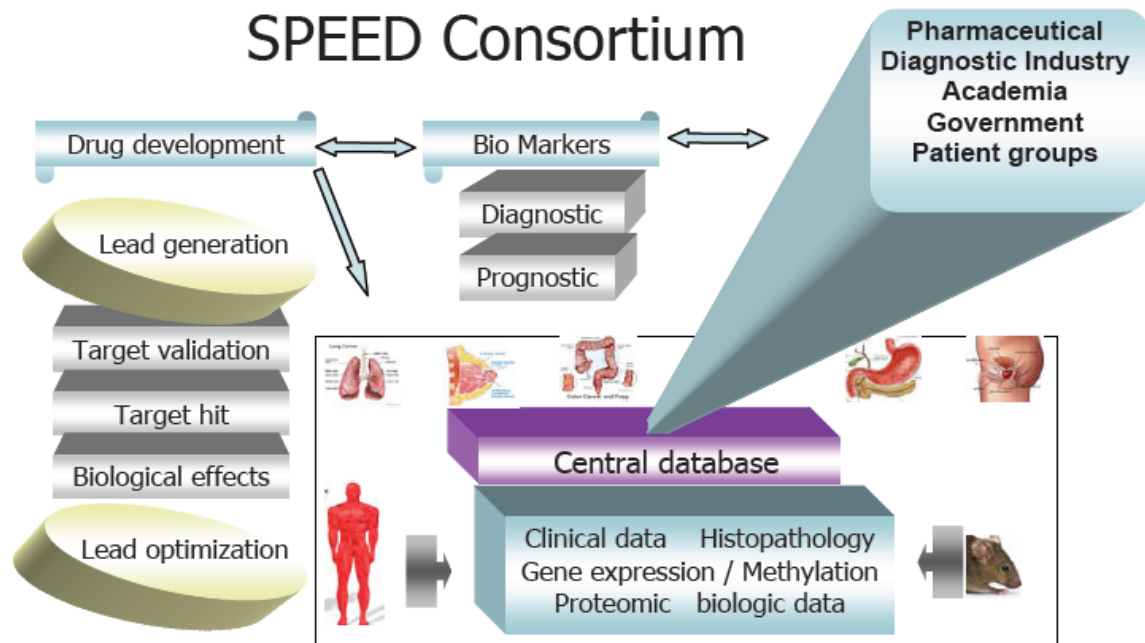
Figure 3: SPEED Consortium proposes the key stakeholders including academia, industry, government bodies, and philanthropic groups to join hands and leverage all resources (financial, data and information, scientific expertise) to expedite anticancer drug development process.

or resistance. Yet another key potential role of these cohorts is to evaluate for differences in the molecular signatures of tumor cells and stroma cells to delineate the patterns of host-tumor microenvironment that occur during cancer regression or progression. These cohorts can be used to test new delivery systems, including those enabled by recent advances in nanotechnology. In addition, these cohorts could aid in development of novel imaging agents, mathematical modeling, and data reconstruction and visualization to address the questions about human cancers.

A core constituent of SPEED would be the central database housing histopathologic, genetic, expression profiling, methylation profiling, proteomic and other biologic data about heterotransplant tumors (in early, intermediate, and later passages) and their human counterparts as an integrated source of information. Its later version would include information about the SPEED results testing therapeutic agents and experimental protocols and may have free public access for widespread utilization.

There are some caveats and biases of heterotransplant models to be considered during the drug development approaches. Heterotransplants usually involve non-orthotopic tumors and might select out angiogenic clones capable of sustained tumor growth after transplantation. It may not fully capture the genetic diversity of metastatic disease, a major biological issue challenging the efficacy of targeted therapeutics in the deadly solid tumors. Also, in our own experience only approximately 50% heterotransplanted human tumors actually achieve engraftment in mice. Therefore these models may provide efficacy data only against those tumors growing in mice. As the host (SCID and nude) mice have profound defects in their immune response, it would preclude the testing of immunomodulatory agents in the system. Also because SCID mice show defects in DNA repair (which could limit testing of some cytotoxics) and nude mice show an overall frailty, it can limit their capacity to tolerate novel treatments. There may be further limitations of heterotransplant models but we should remember that in view of more than 90% drug failure rates, it is imperative to explore novel approach to use existing models

while continuing our search for the better models. Till the time we find one, the SPEED approach may well be based on heterotransplant mouse models. Future clinical trials based on this approach would guide us to refine this preclinical strategy further and the knowledge build up would help in the evolution of a more scientific and robust foundation of IND development process.

Future Directions

The scientific scope of SPEED may be expanded to include other malignancies through concerted efforts of interested groups and stakeholders to institute a consortium (**Figure 3**). The primary goal of the SPEED consortium would be to provide accurate, faithful, and reproducible mouse model cohorts to the research community for further investigation and explorations. SPEED consortium through development of promising agents and biomarkers could also guide federal regulatory bodies on their use and quality control for cancer treatment. Moreover, the consortium illustrates the exceptional potential for development of evidence to improve understanding of the biology of cancer.

In conclusion, the high attrition rates compel us to revisit the science, strategy and processes currently used in drug development. There is a need for scientific and technological innovations to obtain early readouts for proof of concept to decrease drug attrition rates at a later stage. In this regard SPEED paradigm, fostering meticulous statistical modus operandi, provides a perfect launch pad to the mouse models to leap into an exciting new era of drug development and provides a robust keystone to decrease current drug attrition rates in clinical trials.

Acknowledgements

Please address correspondences to: Li Mao, MD, Molecular Biology Laboratory, Department of Thoracic/Head and Neck Medical Oncology, Unit 432, The University of Texas M.D. Anderson Cancer Center, P.O. Box 301402, Houston, TX 77030, USA, Phone: 713-792-6363, Fax: 713-796-8655, E-mail: lmao@mdanderson.org.

References

[1] Owens J: 2006 drug approvals: finding the niche. Nat Rev Drug Discov 2007;6:99-101.
[2] Mullin R: Drug development costs about $1.7 billion. Chem. Eng. News 81, 2003
[3] Kola I, Landis J: Can the pharmaceutical industry reduce attrition rates? Nat Rev Drug Discov 2004;3:711-5.
[4] Elias TG, M. Singh, N. & Zemmel, R.: Why products fail in phase III. in vivo 2006;24:49-54.
[5] Kola I: The state of innovation in drug development. Clin Pharmacol Ther 2008; 83:227-30.
[6[Betensky RA, Louis DN, Cairncross JG: Influence of unrecognized molecular heterogeneity on randomized clinical trials. J Clin Oncol 2002;20:2495-9.
[7] Kopetz S, Overman M, Chang DZ, Glover KY, Shureiqi I, Wolff RA, Abbruzzese JL, Eng C: Systematic survey of therapeutic trials for metastatic colorectal cancer: room for improvement in the critical pathway. J Clin Oncol 2008;26:2000-5.
[8] Benson AB, 3rd: From silos to a critical path of new agent development: a paradigm to revolutionize clinical research. J Clin Oncol 2008;26:1924-5.
[9] Mandrekar SJ, Grothey A, Goetz MP, Sargent DJ: Clinical trial designs for prospective validation of biomarkers. Am J Pharmacogenomics 2005;5:317-25.
[10] Sargent DJ, Conley BA, Allegra C, Collette L: Clinical trial designs for predictive marker validation in cancer treatment trials. J Clin Oncol 2005;23:2020-7.
[11] Gilbert J HP, Singh A: Rebuilding Big Pharma's Business Model. in Vivo 21, 2003
[12] Consortium: Genome sequence of the Brown Norway rat yields insights into mammalian evolution. Nature 2004;428:493-521.
[13] Salmon SE, Hamburger AW, Soehnlen B, Durie BG, Alberts DS, Moon TE: Quantitation of differential sensitivity of human-tumor stem cells to anticancer drugs. N Engl J Med 1978;298:1321-7.
[14] Sanfilippo O, Daidone MG, Costa A, Canetta R, Silvestrini R: Estimation of differential in vitro sensitivity of non-Hodgkin lymphomas to anticancer drugs. Eur J Cancer 1981;17:217-26.
[15] Gazdar AF, Steinberg SM, Russell EK, Linnoila RI, Oie HK, Ghosh BC, Cotelingam JD, Johnson BE, Minna JD, Ihde DC: Correlation of in vitro drug-sensitivity testing results with response to chemotherapy and survival in extensive-stage small cell lung cancer: a prospective clinical trial. J Natl Cancer Inst 1990;82:117-24.
[16] Fruehauf JP BA: In vitro determination of drug response: A discussion of clinical applications, in DeVita VT Jr HS, Rosenberg SA (eds) (ed): Principles and Practice of Oncology Updates

(ed 4). Philadelphia, PA, JB Lippincott,, 1993, p 1-16

[17] Poupon MF, Arvelo F, Goguel AF, Bourgeois Y, Jacrot M, Hanania N, Arriagada R, Le Chevalier T: Response of small-cell lung cancer xenografts to chemotherapy: multidrug resistance and direct clinical correlates. J Natl Cancer Inst 1993;85:2023-9.

[18] Shaw GL, Gazdar AF, Phelps R, Linnoila RL, Ihde DC, Johnson BE, Oie HK, Pass HI, Steinberg HM, Ghosh BC, Walsh TE, Nesbitt JC, Cotelingam JD, Minna JD, and Mulshine JL: Individualized chemotherapy for patients with non-small cell lung cancer determined by prospective identification of neuroendocrine markers and in vitro drug sensitivity testing. Cancer Res 1993;53:5181-7.

[19] Fiebig HH, Maier A, Burger AM: Clonogenic assay with established human tumour xenografts: correlation of in vitro to in vivo activity as a basis for anticancer drug discovery. Eur J Cancer 2004;40:802-20.

[20] Perez-Soler R, Kemp B, Wu QP, Mao L, Gomez J, Zeleniuch-Jacquotte A, Yee H, Lee JS, Jagirdar J, Ling YH: Response and determinants of sensitivity to paclitaxel in human non-small cell lung cancer tumors heterotransplanted in nude mice. Clin Cancer Res 2000;6:4932-8.

[21] Rubio-Viqueira B, Jimeno A, Cusatis G, Zhang X, Iacobuzio-Donahue C, Karikari C, Shi C, Danenberg K, Danenberg PV, Kuramochi H, Tanaka K, Singh S, Salimi-Moosavi H, Bouraoud N, Amador ML, Altiok S, Kulesza P, Yeo C, Messersmith W, Eshleman J, Hruban RH, Maitra A, Hidalgo M: An in vivo platform for translational drug development in pancreatic cancer. Clin Cancer Res 2006;12:4652-61.

[22] Castro M: The simpleton's error in drug development. J Clin Oncol 2002;20:4606-7.

Correlation between VEGF/VEGFR2 and EGFR immunohistochemical protein expression in early stage non-small cell lung carcinoma.

Erminia Massarelli, Maria L. Prudkin, Natalie Ozburn, Lei Feng, Guosheng Yin,

Waun Ki Hong, Michael O'Reilly, Roy S. Herbst, Ignacio I. Wistuba

Several lines of evidence indicate that activation of Vascular Endothelial Growth Factor Receptor (VEGFR) and Epidermal Growth Factor Receptor (EGFR) pathways are critical for non-small cell lung cancer (NSCLC) development, growth and progression. Despite the availability of new biological compounds targeting both signaling pathways in NSCLC, data about the co-expression of these two pathways in a large cohort of NSCLC tumor samples are not available. To better understand the correlation between VEGFR and EGFR pathways expression, we investigated in a large series of surgically resected NSCLC tumor tissues placed in tissue microarrays the tumor immunohistochemical (IHC) protein expression of: VEGF-A, VEGF-R2, p-VEGF-R2 (phosphorylated VEGF-R2), EGFR and p-EGFR (phosphorylated EGFR). Correlations between VEGF-A, VEGFR2, p-VEGFR2 and clinicopathologic information and survival analysis were examined. In a subset of NSCLSs with adenocarcinoma histology, mutation status of *EGFR* and *KRAS* genes was correlated with IHC expression. Two hundred eighty-four surgically resected tumors, including 179 adenocarcinomas and 105 squamous cell carcinomas from patients with stage I-II-IIIA NSCLC were studied. A semi-quantitative analysis of nuclear, cytoplasmic and membranous localization of IHC expression was performed for each marker. Lung adenocarcinomas demonstrated higher expression of cytoplasmic VEGF-A (p=0.0001), membranous (p=0.005) and cytoplasmic (p=0.03) VEGF-R2, and membranous p-VEGF-R2 (p=0.0002) compared to squamous cell carcinomas. Lower VEGF-A (p=0.0009), membranous (p=0.01) and cytoplasmic VEGF-R2 (p=0.02) expression was statistically associated with non-smoking history. With a median follow up of 4.28 years, 91 deaths occurred. Independent of age, histology and stage, cytoplasmic p-VEGF-R2 expression was found to have a prognostic role for worse overall survival (p=0.01, HR=1.047, 95% CI=1.01, 1.085). Of interest, significant increase of cytoplasmic and membranous p-EGFR expression was detected in tumors showing higher levels of cytoplasmic VEGF-A (p=0.01 and p=0.0001, respectively), VEGF-R2 (p=0.0001 and p=0.0001), and p-VEGF-R2 (p=0.0001 and p=0.0003). In the 15 *EGFR*-mutated cases a significant lower membranous VEGF-R2 expression was observed (p=0.02). Higher membranous VEGF-R2 expression was observed in the 9 *KRAS* mutated cases, but this did not reach statistical significance. In summary, our findings indicate that VEGFR and EGFR pathways are positively correlated in early stage NSCLC and IHC expression of p-VEGF-R2 is an indicator of worse overall survival in stage I-IIIA NSCLC (Grant IMPACT W81XWH-05-0027).

Immunohistochemical Expression of Estrogen and Progesterone Receptors Identifies a Subset of Non-small Cell Lung Carcinomas and Correlates with *EGFR* Mutation

Maria Gabriela Raso,[1] Carmen Behrens,[2] Suyu Liu,[3] Ludmila Prudkin,[1] Natalie C. Ozburn,[2]

Denise M. Woods,[1] Ximing Tang,[2] Reza J. Mehran,[4] Cesar Moran,[1,2] J. Jack Lee,[3]

and Ignacio I. Wistuba[1,2]

Authors' Affiliations: Departments of [1]Pathology, [2]Thoracic/Head and Neck Medical

Oncology, [3]Biostatistics, and [4]Thoracic Surgery, The University of Texas M. D. Anderson

Cancer Center, Houston, TX 77030

Running title: ER and PR expression in NSCLC

Abbreviations: EGFR, epidermal growth factor receptor; NSCLC, non-small cell lung carcinoma; ER, estrogen receptor; PR, progesterone receptor.

Key words: Estrogen receptors, Progesterone receptor, *EGFR* mutation, Field cancerization

Requests for reprints:
Ignacio I. Wistuba
Department of Pathology
The University of Texas M. D. Anderson Cancer Center
1515 Holcombe Blvd., Unit 85
Houston, TX 77030-4009
Telephone: (713) 563-9184
Fax: (713) 792-0309
E-mail: iiwistuba@mdanderson.org

Statement of Clinical Relevance.

A better understanding of the signaling pathways that lead to tumor growth may help in the development of new and more effective strategies for targeted chemoprevention and treatment of lung cancer. Our finding of frequent overexpression of ER and PR in NSCLC suggests that the activation of these pathways is an attractive novel target for lung cancer chemopreventive and therapeutic strategies. The correlation between ER and *EGFR* mutation in lung adenocarcinoma suggests that it might be important to target both pathways simultaneously for lung cancer therapy.

ABSTRACT

Purpose: To determine the frequency of estrogen receptors (ER) α and β and progesterone receptor (PR) immunohistochemical expression in a large set of NSCLC specimens, and to compare our results with those for some of the same antibodies that have provided inconsistent results in previously published reports.

Experimental Design: Using multiple antibodies, we investigated the immunohistochemical expression of ERα and β and PR in 317 NSCLCs placed in tissue microarrays and correlated their expression with patients' clinicopathologic characteristics, and in adenocarcinomas, with *EGFR* mutation status.

Results: ERα and β were detected in the nucleus and cytoplasm of NSCLC cells; however, the frequency of expression (nucleus: α, 5%–36%, and β, 42%–56%; cytoplasm: α, <1%–42%, and β, 20%–98%) varied among the different antibodies tested. PR was expressed in 63% of tumor cell nuclei. ERα nuclear expression significantly correlated with adenocarcinoma histology, female gender, and history of never smoking ($P = 0.0048$ to <0.0001). In NSCLC, higher cytoplasmic ERα expression significantly correlated with worse RFS (HR 1.77, 95% CI, 1.12, 2.82; $P = 0.015$) in multivariate analysis. In adenocarcinomas, ERα expression correlated with *EGFR* mutation ($P = 0.0029$ to <0.0001). ERβ and PR, but not ERα, expressed in the normal epithelium adjacent to lung adenocarcinomas.

Conclusions: Both ER antibodies and PR are frequently expressed in NSCLC. ERα expression distinguishes a NSCLC subset that has defined clinicopathologic and genetic features. The correlation between ER and *EGFR* mutation in lung adenocarcinoma suggests that it might be important to target both pathways simultaneously in lung cancer therapy.

INTRODUCTION

Lung cancer is the most common cause of cancer mortality worldwide, with over 1 million deaths each year (1). Lung cancer includes several histological types, the most frequently occurring of which are two types of non-small cell lung carcinoma (NSCLC): adenocarcinoma and squamous cell carcinoma (2). During the last two decades, mortality rates associated with cancer have continued to decrease across all major sites in both men and women; however, the rates for lung cancer in females have continued to increase (3, 4). Despite global statistics estimating that 15% of lung cancer in men and 53% in women are not attributable to smoking (1), smoking remains the primary risk factor for lung cancer. The higher proportion of lung cancer in females who have never smoked compared with males who have never smoked suggests a possible role for gender-dependent hormones in the development of lung cancer (5).

Estrogen receptors (ER) α and β are expressed in normal lung tissue and in lung tumors in both men and women (6), yet the data are inconsistent as to whether ER expression is gender biased (6-9) or associated with NSCLC overall survival (9-11). The data reported on the immunohistochemical expression for both ER receptors in NSCLC remain controversial. ERα has been reported to be expressed in the nucleus (0%−45%) and cytoplasm (0%−73%) of malignant lung cancer cells in the cases examined (9, 10, 12, 13). The percentages for ERβ are more consistent, with 46%−60% of NSCLC cases showing only nuclear expression (9-14). Similarly, two reports suggested that progesterone receptor (PR) is frequently (47%) expressed in NSCLC tumor cells, and this expression correlated with better patient outcome (12, 15).

Several *in vitro* and *in vivo* studies have provided evidence supporting a biological role for estrogens in lung carcinogenesis by direct promotion of cell proliferation—estrogens stimulate the proliferation of NSCLC cells through estrogen receptor-mediated signaling,

4

whereas anti-estrogens inhibit the growth of NSCLC cells (6, 7, 13, 16, 17). Estrogen can directly stimulate the transcription of estrogen-responsive genes in the nucleus of lung cells and can also transactivate growth factor-signaling pathways—the epidermal growth factor receptor (EGFR) pathway, in particular (13, 18). In estrogen stimulation of lung cancer cells, EGFR ligands are rapidly released, activating the EGFR and mitogen-activated protein kinase 1 (MAPK1) growth pathways (19). Activation of the EGFR pathway appears to play an important role in the pathogenesis and progression of NSCLC (20). In lung cancer cells, the constitutive activation of EGFR is achieved by several mechanisms, including increased production of ligands, increased levels of the receptor, and mutation of the *EGFR* tyrosine kinase domain (20-22). Of interest, EGFR protein expression is downregulated in response to estrogens and upregulated in response to anti-estrogens, suggesting that a reciprocal control mechanism exists between the EGFR and ER pathways (19).

The purpose of the current study was to determine the frequency of ERα and β and PR protein immunohistochemical expression in a large set of NSCLCs placed in tissue microarray (TMA) specimens and to compare our results with those for some of the same antibodies that have provided inconsistent results in previously published reports (9-14). In addition, the receptor-expression results were correlated with patients' clinicopathologic features, including NSCLC histology, gender, smoking history, and patient outcome, and in adenocarcinoma with tumors' *EGFR* activating mutation status. Finally, to understand ERα and β and PR protein expression role in the early pathogenesis of lung cancer, we investigated the characteristics of ERα and β and PR protein expression in the non-malignant respiratory epithelium adjacent to tumors taken from a subset of our retrospectively reviewed lung adenocarcinoma cases.

MATERIALS AND METHODS

  Case selection and TMA construction. We obtained archived, formalin-fixed, paraffin-embedded (FFPE) tissue from surgically resected (with curative intent) lung cancer specimens (lobectomies and pneumonectomies) containing tumor and adjacent normal epithelium tissues from the Lung Cancer Specialized Program of Research Excellence Tissue Bank at The University of Texas M. D. Anderson Cancer Center (Houston, TX), which has been approved by the institutional review board. The tissue had been collected from 1997 to 2001, and the tissue specimens were histologically examined and classified using the 2004 World Health Organization classification system (2). We selected 317 NSCLC tissue samples (201 adenocarcinomas and 116 squamous cell carcinomas) for our TMAs. TMAs were constructed using triplicate 1-mm diameter cores per tumor, and each core included central, intermediate, and peripheral tumor tissue. Detailed clinical and pathologic information, including demographics, smoking history (never- and ever-smokers), and smoking status (never, former, and current), clinical and pathologic tumor-node-metastasis (TNM) stage, overall survival (OS) duration, and time to recurrence was available for most cases (Supplementary Table 1). Patients who had smoked at least 100 cigarettes in their lifetime were defined as smokers, and smokers who quit smoking at least 12 months before their lung cancer diagnosis were defined as former smokers. Tumors were pathologic TNM stages I–IV according to the revised International System for Staging Lung Cancer (23).

  To assess the immunohistochemical expression of ERα and β and PR markers in the non-malignant respiratory epithelium adjacent to lung tumors, we selected whole histology sections containing tumor and adjacent lung tissue from 64 adenocarcinomas that were included in our TMAs.

Immunohistochemical staining and evaluation. The following antibodies against ERα

and β and PR were purchased: 1) ERα-1, clone 6F11, Novocastra, Leica Microsystems Inc.

(Bannockburn, IL); 2) ERα-2, clone 6F11, Chemicon, Millipore Corporate (Billerica, MA); 3)

ERα-3, clone HC20, Santa Cruz Biotechnology Inc. (Santa Cruz, CA); 4) ERα-4, clone 1D5,

Lab Vision Corporation (Fremont, CA); 5) ERβ-1, clone H150, Santa Cruz Biotechnology

(Santa Cruz, CA); 2) ERβ-2, clone 14C8, GeneTex Inc (San Antonio, TX); and 6) PR, clone

SP2, Lab Vision Corporation (Fremont, CA). Details on immunohistochemistry conditions and

characteristics of the antibodies are listed in Supplementary Table 2. Immunohistochemical

staining was performed as follows: 5-µM FFPE tissue sections were deparaffinized, hydrated,

heated in a steamer for 10 minutes with 10 mM sodium citrate (pH 6.0) for antigen retrieval, and

washed in Tris buffer. Peroxide blocking was done with 3% H_2O_2 in methanol at room

temperature for 15 min, followed by 10% fetal bovine serum in tris-buffered saline-t for 30 min.

The slides were incubated with primary antibody at an ambient temperature for 60 min for all

antibodies; the exception was ERβ 14C8 (ERβ-2), which was incubated overnight at 4°C,

washed with phosphate-buffered saline, and incubated with biotin-labeled secondary antibody

(Envision Dual Link +, DAKO, Carpinteria, CA) for 30 min. Staining for the slides was

developed with 0.05% 3', 3-diaminobenzidine tetra hydrochloride, which had been freshly

prepared in 0.05 mol/L Tris buffer at pH 7.6 containing 0.024% H_2O_2, and then the slides were

counterstained with hematoxylin, dehydrated, and mounted. FFPE normal breast tissue was used

as the positive control. For the negative control, we used the same specimens used for the

positive controls but replaced the primary antibody with phosphate-buffered saline.

Two observers (M.G.R. and I.I.W.) jointly quantified the immunohistochemical

expression of ERs and PR using light microscopy (magnification 20×). Both nuclear and

cytoplasmic expressions were quantified using a four-value intensity score (0, 1+, 2+, and 3+) and the percentage (0% to 100%) of reactivity. We defined the intensity categories as follows: 0 = no appreciable staining; 1+ = barely detectable staining in epithelial cells compared with the stromal cells; 2+ = readily appreciable staining; and, 3+ = dark brown staining of cells. Next, an expression score was obtained by multiplying the intensity and reactivity extension values (range, 0–300).

EGFR mutation analysis. Exons 18–21 of EGFR were polymerase chain reaction (PCR)-amplified using intron-based primers as previously described (24, 25). Approximately 200 microdissected FFPE cells were used for each PCR amplification. All PCR products were directly sequenced using the Applied Biosystems PRISM dye terminator cycle sequencing method. All sequence variants were confirmed by independent PCR amplifications from at least two independent microdissections and DNA extraction, and the variants were   sequenced in both directions, as previously reported (24, 25).

Statistical analysis. The immunohistochemical expression and clinicopathologic data were summarized using standard descriptive statistics and frequency tabulations. BLiP plots were generated to summarize the distribution of ER and PR expressions. Associations between the marker expression and patients' clinical and demographical variables (including age, sex, smoking history, histology type, and pathologic stage) were assessed using appropriate methods including the chi-square or Fisher exact test for categorical variables, and Wilcoxon rank sum or Kruskal-Wallis test for continuous variables. The Spearman rank correlation coefficient was used to estimate the correlation between immunohistochemistry markers. Kaplan-Meier survival curves for patient OS and RFS were also generated. The log-rank test was used to identify the difference between the patient groups for both overall and RFS. For univariate and multivariate

analyses for immunohistochemical expressions, the Cox proportional hazard model was used. Two-sided P values less than 0.05 were considered statistically significant.

RESULTS

Correlation of expression of ER antibodies. We examined four commercially available antibodies against ERα: two using the same clone (6F11) and two antibodies against ERβ (Supplementary Table 2). Using the scores of expression generated from all NSCLCs we analyzed the correlation of the expression in the malignant cells for the four ERα and the two ERβ antibodies tested. All four of the ERα antibodies showed nuclear staining, and two of the four antibodies also detected expression in the cytoplasm of malignant cells (ERα-3, clone HC20, and ERα–4, clone 1D5). The two ERα clone 6F11 antibodies (ERα-1 and ERα-2), obtained from two different companies, demonstrated only nuclear staining. All four of the ERα antibodies significantly correlated with each other at nuclear expression (Spearman rank correlation: $r = 0.32$ to 0.48; $P < 0.0001$; Supplementary Table 3). Also, significant correlation was detected in the staining of the two ERα antibodies, showing cytoplasmic expression ($r = 0.43$; $P < 0.0001$). There was no statistically significant correlation between both of the ERβ antibodies examined in their nuclear expression; although they significantly correlated at their cytoplasmic expression, the correlation coefficient was very low ($r = 0.17$; $P = 0.005$).

Frequency of ER and PR expression in NSCLC specimens by histology. We analyzed the frequency of any ER and PR immunohistochemical expression (positive cases, score >0) for each antibody tested by NSCLC tumor histology, and the data are summarized in Table 1. Representative microphotographs of the expression of ER and PR with some of the antibodies tested are shown in Fig. 1. ERs and PR were detected in the nucleus of malignant cells by all of the corresponding antibodies tested. However, when expressed, the percentage of malignant cells

9

showing staining was low in general, with an average percentage of positive expression of: 19% (range 2-90%) for ERα-1 nuclear; 13% (range 2-93%) for ERα-2 nuclear; 21% (range 1-60%) and 19% (range 3-73%) for ERα-3 nuclear and cytoplasmic, respectively; and, 11% (range 3-97%) and 7% (range 3-30%) for ERα-4 nuclear and cytoplasmic, respectively. The average percentages of positive cells expressing ERβ were 37 % (range 3-90%) and 37% (range 3-97%) for ERβ-1 nuclear and cytoplasmic, respectively; and, 13 % (range 1-77) and 24 % (range 3-67) for ERβ–2 nuclear and cytoplasmic, respectively.

Although there are important variations in the frequency of expression between the nuclear ERα antibodies tested, adenocarcinoma histology showed significantly higher frequency of expression than squamous cell carcinomas for all ERα antibodies ($P < 0.0001–0048$; Table 1). For nuclear expression of ERβ, the data obtained with both antibodies tested were relatively consistent, and the adenocarcinoma histology demonstrated a significantly higher frequency of expression than the squamous cell carcinoma did with the ERβ-2 antibody ($P = 0.0069$). Two of the ERα (ERα-3 and ERα-4) and both ERβ antibodies also detected ER expression in the cytoplasm of NSCLC cells (Table 1). While the ERβ-2 antibody was expressed in the cytoplasm of a subset of NSCLCs, the ERβ-1 antibody was expressed in nearly all of the tumors. Cytoplasmic expression—only for the ERα-3 antibody—was significantly higher in adenocarcinomas when compared with squamous cell carcinomas ($P = 0.0064$).

In the NSCLC tissues, PR expression was frequently detected in the nuclei of malignant cells only. Squamous cell carcinoma histology showed a marginally significant higher frequency of expression than that of the adenocarcinomas ($P = 0.05$; Table 1).

Correlation between ER and PR expression in NSCLC and patients' clinicopathologic features. We correlated expression of ERs and PR for each antibody tested with the patients'

clinicopathologic characteristics, including histology, gender, tobacco history, and TNM

pathological stage using the expression score as a continuous variable. Using this type of

analysis, adenocarcinoma histology also showed a statistically significant higher nuclear

expression for all ERα antibodies and for the ERβ-2 antibody than squamous histology (Table

2). Of great interest was the fact that the NSCLC tissues obtained from females and never

smokers demonstrated statistically significant higher expression of nuclear ERα and β for

several of the antibodies used (Table 2). No correlations between the expression of PR and the

clinicopathologic characteristics were found.

We performed OS and recurrence-free survival (RFS) analyses to determine the

expression of ERs and PR for each antibody tested by using specimens from 317 patients with

NSCLC with a median follow-up of 6.1 years for OS and 4.2 years for RFS. No association was

detected between the expression of ER and PR and OS. Of interest, any expression of

cytoplasmic ERα, using ERα-4 antibody, and nuclear ERβ, using the ERβ-1 antibody, conferred

to patients a significantly worse RFS in the both univariate and multivariate analysis (Fig. 2 and

Table 3). However, only the cytoplasmic expression of ERα-4 correlated with worse RFS when

dichotomized score being used (HR 1.77; 95% CI, 1.11–2.81; $P = 0.0156$; Table 3).

Correlation between ER and PR expression in NSCLC and tumor EGFR mutation

status. Among 182 adenocarcinoma cases, *EGFR* mutations of the tyrosine kinase domain

(exons 18–21) were detected in 31 (17%) cases. Most (88%) *EGFR* mutations were detected in

the exons 19 and 21, and we did not find correlation between the location of the mutation and ER

α and β expression. We correlated the ER and PR scores and any expression (positive cases,

score >0) with *EGFR* mutation status. Interestingly, *EGFR* mutant adenocarcinomas

demonstrated statistically significant higher expression than wild-type tumors of nuclear ERα,

11

cytoplasmic ERα, and nuclear ERβ when tested with antibodies ERα-3, ERα-4, and ERβ-1, respectively (Table 4 and Fig. 3). Because there was a higher incidence of *EGFR* mutation in lung adenocarcinoma cases from patients with a history of never smoking, Asian ethnicity, or female characteristics (data not shown), we adjusted the effects of age, gender, smoking history, ethnicity, and pathological stage in the correlation of ERα and β with *EGFR* mutation status. After linear regression analysis, all the significant correlations remained statistical significant. There was no correlation between PR expression and *EGFR* mutation status.

  ER and PR immunohistochemical expression in the lung respiratory airway adjacent to adenocarcinoma cases. To characterize the pattern of expression of ER and PR in the respiratory airway field in patients with lung cancer, we selected 64 adenocarcinoma cases (35 females and 29 males; 19 never smoked, 13 current smokers, and 32 former smokers), and we studied the immunohistochemical expression of ERα and β and PR in the respiratory cells lining the small bronchi (n = 35 cases), bronchioles (n = 83 cases), and alveoli exhibiting Type II cells hyperplastic changes (n = 15 cases) using the same semi quantitative scoring system used in the TMAs. For ERs, we tested the ERα-4 and ERβ-1 antibodies. From each case, we used immunohistochemistry to examine whole tissue sections from a mean of three different paraffin blocks (range 3–6) containing tumor and adjacent normal lung tissue. We found that ERα was not expressed in the airway epithelium adjacent to lung adenocarcinomas, including epithelial samples from 21 positive tumors (Supplementary Table 4). In contrast, ERβ was widely expressed in the cytoplasm of respiratory cells: 91% of bronchi, 84% of bronchioles, and 29% of the hyperplastic alveoli. ERβ nuclear immunostaining was found less frequently: 5% of bronchi, 10% of bronchioles, and none of the hyperplastic alveolar cells. Noticeably, in the bronchial cells, we identified two patterns of cytoplasmic immunostaining: a homogeneous staining in all

types of bronchial cells and heterogeneous staining comprising only ciliated cells with mainly

supranuclear or apical expression (Fig. 1). PR was found in the nucleus of 56% of bronchi, 61%

of bronchioles, and 33% of hyperplastic alveoli. Of interest, there was a high level of correlation

(28/33 comparisons, 85%) between the expression of PR in the normal epithelium and the

corresponding tumors. Twenty (95%) out of 21 cases with PR positive in the normal epithelium

were detected in patients with tumors that also expressed this receptor.

DISCUSION

ERα and β frequently expressed in our NSCLC cases, and ERα expression distinguished

a subset of NSCLC that has defined clinicopathologic and genetic features. Although the

immunohistochemical expression of ERα and β has been reported in tumor tissue specimens

from surgically resected NSCLCs, the data on the fraction of tumors expressing ER are still

controversial. Previous studies on ERα immunohistochemical expression in formalin-fixed and

paraffin-embedded NSCLC specimens using seven different antibodies identified nuclear

expression in malignant cells in frequencies that ranged from none (10, 14) to 18% (26) and 38%

(12). Similarly, in other studies, the frequency of ERα cytoplasmic expression in NSCLC ranged

from 0%–3% (12, 26) to 35% (11) and 73% (27). In the current study, using four different

commercially available ERα antibodies, we also identified a wide range of percentages in the

frequency of NSCLCs exhibiting any expression of ERα in the nucleus (7%–54%) and in the

cytoplasm (0%–42%) of tumor cells. However, in our study, when the scores of

immunohistochemical expression were analyzed as continuous variables, all of the

ERα antibodies significantly correlated with each other at nuclear and cytoplasmic locations.

A similar situation is observed when the ERβ immunohistochemical expression data are

examined in NSCLC. Several previous studies, using six different antibodies, have reported

frequencies of ERβ expression in tumors with a wide range of percentages at the nuclear location—0% (9), 34%47% (10, 12, 14), and 61%–84% (9, 11) —but not in the cytoplasm of malignant cells, where most of the studies have shown no reactivity (9, 10, 12, 14); some expression was seen in a small number of cases (6) or low frequency of expression in a large number of cases (10%) (11). In the present study using two antibodies, any ERβ nuclear expression was detected in about half (56% and 42%) of the NSCLCs, and cytoplasmic expression was found in a wider range (20%–98%) of our cases. We do not have a definitive explanation to the high levels of expression of ERβ in NSCLC cells in our study, and the discordance with previous reports. However, immunohistochemical analysis has shown the distribution of ERβ to be much more widespread than ERα (28-30). Several studies have reported that ERβ immunohistochemical expression is frequently detected in the nucleus and cytoplasm of normal respiratory cells (28). While expression has been questioned by suggestions that this observation is based on non-specific binding produced by unpurified antibodies (31), multiple reports have shown the presence of a non-nuclear pool of ERs in normal and malignant cells (32-35). Yang et al (35) used one of the same ERβ antibodies that we used (ERβ-1) and demonstrated mitochondrial localization of this receptor in several normal human and murine cells, suggesting a role for ERβ receptor in the cytoplasm of cells. Our finding of high frequency of ERβ expression, using ERb-1 antibody, in the cytoplasm of normal respiratory cells from our lung adenocarcinoma patients are consistent with these findings.

Several discrepancies were observed when we compared our results with those published previously (6, 9, 10, 12) using the same antibodies, especially for ERα. For example, our ERα-3 antibody, raised against the COOH-terminus region of the protein, detected any nuclear and cytoplasmic expressions in 54% and 42% of our NSCLC cases, respectively. Using this

14

antibody, nuclear expression was reported in a small number of NSCLC tumors by Stabile et al (6) and in none of the 130 tumors examined by Kawai et al (10). At the cytoplasmic location of malignant cells, both studies reported positive immunostaining (6, 10), with up to 73% of cases in the study performed by Kawai et al (10).

Why these inconsistent results on the immunohistochemical expression of ER α and β occur raises a very important question. Clearly the reasons for the inconsistent results include the use of different antibodies manufactured from different clones and by different companies. Indeed, some of these antibodies have been made against different parts of the protein: full length, NH_2-terminues, and COOH-terminus regions. It has been suggested that several mRNA splicing variants of ERα have been detected in lung cancer cell lines, and antibodies raised against epitopes in the deleted exons of ER may give conflicting results (6). In addition, it is important to note that there are multiple criteria reported to assess ERα and β positivity in NSCLC tissues. Although most studies considered different levels of intensity (usually a scale 0–3+) of expression at nuclear and cytoplasmic locations combined with the percentage of malignant cells expressing a given intensity, the cutoff levels of expression vary significantly between studies (e.g., 1+ in >10% of cells; 1+ in 1%–25% of cells; >50% of cells; score "0–8", etc) (6, 9-12, 14, 26).

Because there were different levels of ERα and β immunohistochemical expression detected using different antibodies in ours and the previous studies (6, 9-12, 14, 26), we correlated the expression of ER using all of the antibodies we tested with the patients' clinicopathological features and the tumors' *EGFR* mutation status. The evaluation of multiple antibodies for ER expression adds strength to our findings. In our study, we analyzed the immunohistochemical scores as continuous and dichotomized variables, and a significantly

higher expression of nuclear ERα was detected with all four antibodies tested in adenocarcinoma than squamous cell carcinoma histology—three out of the four antibodies tested in tumors obtained from females compared with males and from people who had never smoked compared with smokers. The two previous studies reporting ERα nuclear expression in NSCLC, which examined a relatively large series of cases, did not address differences of expression based on histology types or patients' clinicopathologic features (12, 26). In the NSCLC tissues that we reviewed, higher expression of ERβ correlated significantly with tumor adenocarcinoma histology and the patients' female gender for ERβ-1 antibody, and correlated with the patients' history of never smoking with the ERβ-2 antibody.

Few studies have shown inconsistent results on whether ER expression is biased to any gender using different types of specimens and assays (6-9). Schwartz et al (9), using a different antibody than ours, reported that NSCLCs obtained from females were 46% less likely to have ERβ-positive tumors than males in a multivariate analysis. In addition, mRNA expression of ERα has been reported to be significantly higher in lung tumors from women than from men (8). In a small number of NSCLC tumor tissue specimens, ERα and β gene transcripts have been found to be expressed in similar levels when comparing samples obtained from females and males (7). Adenocarcinoma of the lung, which shows a weaker association with tobacco smoking than with other types of lung cancer, is also found predominantly in women, suggesting a possible role for female hormones in the pathogenesis of this type of lung cancer (5).

In previous studies, ERβ expression in NSCLC tumors has been associated with improved survival (9-11), whereas the immunohistochemical expression of ERα has been shown to be a poor prognostic factor (9). Thus, both ERs have been proposed to play opposite roles in cell proliferation, with ERα promoting proliferation and ERβ having an anti-proliferative effect

16

(36, 37). In our study, we did not find a correlation between OS and RFS and ERβ expression, but we did find that only the expression of cytoplasmic ERα (using one antibody) conferred to patients a significantly worse RFS, but not OS, in multivariate analysis.

Several studies have shown that estrogen signaling plays a role in the development of the epithelium in the lung and that estrogen could potentially promote lung cancer (6, 7, 13, 16, 17). Additionally, anti-estrogen drugs have been suggested to have a role in the therapy of lung cancer (6, 19). NSCLC cell lines and *in vivo* tumor xenographts have been shown to respond to estrogens, and tumor growth can be inhibited up to 40% by the anti-estrogen fulvestrant (6). In the past few years, significant advances have been made in the development of new molecularly targeted agents for lung cancer (38). The identification of the subset of patients with NSCLC who will benefit with targeted therapy is a key element in the development of personalized treatment approaches in this disease. A pilot study of combined therapy using fulvestrant and gefitinib in advanced NSCLC has shown to be well tolerated and has demonstrated some tumor responses (39). Our study results strongly suggest that NSCLC tumors obtained from patients with adenocarcinoma histology, female gender, and history of never smoking have a higher chance of expressing ERs and have the potential to respond positively to anti-estrogen therapy.

To the best of our knowledge, our study is the first to report an association between *EGFR* mutation and ERα and β expression in lung adenocarcinomas. Importantly, we have demonstrated that the correlation between ER expression and *EGFR* mutation is independent of the clinicopathological features associated with both abnormalities, such as adenocarcinoma histology, female gender, and history of never smoking (40). Based on the interactions between ER and EGFR-signaling pathways, there is evidence showing that targeting both pathways by using anti-estrogens (fulvestrant) and EGFR tyrosine kinase inhibitors (gefitinib), the antitumor

effect in *in vitro* and *in vivo* lung cancer models of the drug combination is higher than in treatment with each drug alone (19). Thus, our findings of an association between the activation of both pathways further strengthens the concept of combined anti-estrogen and EGFR inhibitor therapy for a selected group of patients with lung adenocarcinoma.

Although PR expression has been reported to be present in NSCLC cell lines and tumor specimens, the data are controversial like those for ERs (11, 12, 15, 41, 42). Out of four studies reporting on immunohistochemical expression of PR in surgical resected and formalin-fixed NSCLC tissue specimens using different antibodies, there were two studies that reported a relatively high frequency of PR expression in tumors (39% and 47%) (12, 15); the remaining two reports showed no expression (11, 42). In the present study, PR was frequently (63%) detected in the nuclei of malignant NSCLC, with a trend to higher expression in squamous cell carcinoma histology. We did not find a correlation between PR and any of the clinicopathologic characteristics we studied, including survival. In contrast, Ishibashi et al reported that PR immunohistochemical expression was higher in NSCLCs obtained from females and correlated with better OS in stages I–III tumors (12). In breast cancer, transcription of the PR gene is well known to be regulated by estrogenic actions through estrogen receptors, and a positive PR status is generally regarded as one of the markers of functional estrogenic pathways. In our study, we found no statistical correlation between PR and any of the ER antibodies studied. *In vitro* and *in vivo* studies have shown that administration of progesterone inhibits the growth of PR-positive NSCLC cell lines, which is similar to what has been shown to happen in breast and endometrial carcinomas (12).

Lung cancer is believed to develop from a series of preneoplastic lesions in the respiratory mucosa, and these abnormalities are frequently extensive and multifocal throughout

18

the respiratory epithelium, indicating a field-effect or field-cancerization phenomenon (43). Our findings of relatively frequent expression of nuclear PR and lack of expression of ERα in the normal epithelium adjacent to adenocarcinomas expressing these receptors suggest that PR, but not ERα expression, may represent a field-effect phenomenon. Of interest, all but one case with normal epithelium expression of PR showed expression of this receptor in the corresponding tumor. The frequent finding of cytoplasmic ERβ in normal epithelium may represent a constitutive expression in normal respiratory cells and is probably not related to the carcinogenesis process (35).

In summary, our findings show that ERα and β and PR are frequently expressed in NSCLC, and ER expression distinguishes a subset of NSCLC that has defined clinicopathologic and genetic features. The correlation between ER and EGFR mutation in lung adenocarcinoma suggests that it might be important to target both pathways simultaneously for lung cancer chemoprevention and therapy.

References

1.   Parkin DM, Bray F, Ferlay J, Pisani P. Global cancer statistics, 2002. CA Cancer J Clin 2005; 55:74-108.

2.   Travis WD, Brambilla E, Muller-Hermelink HK, Harris CC. Tumours of the lung. In: Travis WD, Brambilla E, Muller-Hermelink HK, Harris CC, editors. Pathology and Genetics: Tumours of the Lung, Pleura, Thymus and Heart. Lyon: International Agency for Research on Cancer (IARC); 2004. p. 9-124.

3.   Brennan P, Bray I. Recent trends and future directions for lung cancer mortality in Europe. Br J Cancer 2002; 87:43-8.

4.   Jemal A, Siegel R, Ward E, et al. Cancer statistics, 2008. CA Cancer J Clin 2008; 58:71-96.

5.   Sun S, Schiller JH, Gazdar AF. Lung cancer in never smokers--a different disease. Nat Rev Cancer 2007; 7:778-90.

6.   Stabile LP, Davis AL, Gubish CT, et al. Human non-small cell lung tumors and cells derived from normal lung express both estrogen receptor alpha and beta and show biological responses to estrogen. Cancer Res 2002; 62:2141-50.

7.   Mollerup S, Jorgensen K, Berge G, Haugen A. Expression of estrogen receptors alpha and beta in human lung tissue and cell lines. Lung Cancer 2002; 37:153-9.

8.   Fasco MJ, Hurteau GJ, Spivack SD. Gender-dependent expression of alpha and beta estrogen receptors in human nontumor and tumor lung tissue. Mol Cell Endocrinol 2002; 188:125-40.

9.   Schwartz AG, Prysak GM, Murphy V, et al. Nuclear estrogen receptor beta in lung cancer: expression and survival differences by sex. Clin Cancer Res 2005; 11:7280-7.

10.   Kawai H, Ishii A, Washiya K, et al. Estrogen receptor alpha and beta are prognostic factors in non-small cell lung cancer. Clin Cancer Res 2005; 11:5084-9.

11.   Skov BG, Fischer BM, Pappot H. Oestrogen receptor beta over expression in males with non-small cell lung cancer is associated with better survival. Lung Cancer 2008; 59:88-94.

12.   Ishibashi H, Suzuki T, Suzuki S, et al. Progesterone receptor in non-small cell lung cancer--a potent prognostic factor and possible target for endocrine therapy. Cancer Res 2005; 65:6450-8.

13.   Marquez-Garban DC, Chen HW, Fishbein MC, Goodglick L, Pietras RJ. Estrogen receptor signaling pathways in human non-small cell lung cancer. Steroids 2007; 72:135-43.

14.   Wu CT, Chang YL, Shih JY, Lee YC. The significance of estrogen receptor beta in 301 surgically treated non-small cell lung cancers. J Thorac Cardiovasc Surg 2005; 130:979-86.

15.   Su JM, Hsu HK, Chang H, et al. Expression of estrogen and progesterone receptors in non-small-cell lung cancer: immunohistochemical study. Anticancer Res 1996; 16:3803-6.

16.   Pietras RJ, Marquez DC, Chen HW, Tsai E, Weinberg O, Fishbein M. Estrogen and growth factor receptor interactions in human breast and non-small cell lung cancer cells. Steroids 2005; 70:372-81.

17.   Hershberger PA, Vasquez AC, Kanterewicz B, Land S, Siegfried JM, Nichols M. Regulation of endogenous gene expression in human non-small cell lung cancer cells by estrogen receptor ligands. Cancer Res 2005; 65:1598-605.

18.   Stabile LP, Siegfried JM. Estrogen receptor pathways in lung cancer. Curr Oncol Rep 2004; 6:259-67.

19.   Stabile LP, Lyker JS, Gubish CT, Zhang W, Grandis JR, Siegfried JM. Combined targeting of the estrogen receptor and the epidermal growth factor receptor in non-small cell lung cancer shows enhanced antiproliferative effects. Cancer Res 2005; 65:1459-70.

20.   Sequist LV, Lynch TJ. EGFR tyrosine kinase inhibitors in lung cancer: an evolving story. Annu Rev Med 2008; 59:429-42.

21.   Herbst RS, Bunn PA, Jr. Targeting the epidermal growth factor receptor in non-small cell lung cancer. Clin Cancer Res 2003; 9:5813-24.

22.   Fujimoto N, Wislez M, Zhang J, et al. High expression of ErbB family members and their ligands in lung adenocarcinomas that are sensitive to inhibition of epidermal growth factor receptor. Cancer Res 2005; 65:11478-85.

23.   Mountain CF. Revisions in the International System for Staging Lung Cancer. Chest 1997; 111:1710-7.

24.   Shigematsu H, Lin L, Takahashi T, et al. Clinical and biological features associated with epidermal growth factor receptor gene mutations in lung cancers. J Natl Cancer Inst 2005; 97:339-46.

25.   Tang X, Shigematsu H, Bekele BN, et al. EGFR tyrosine kinase domain mutations are detected in histologically normal respiratory epithelium in lung cancer patients. Cancer Res 2005; 65:7568-72.

26.   Lau SK, Chu PG, Weiss LM. Immunohistochemical expression of estrogen receptor in pulmonary adenocarcinoma. Appl Immunohistochem Mol Morphol 2006; 14:83-7.

27.   Kawai H, Ishii A, Washiya K, et al. Combined overexpression of EGFR and estrogen receptor alpha correlates with a poor outcome in lung cancer. Anticancer Res 2005; 25:4693-8.

28.   Taylor AH, Al-Azzawi F. Immunolocalisation of oestrogen receptor beta in human tissues. J Mol Endocrinol 2000; 24:145-55.

29.   Jarvinen TA, Pelto-Huikko M, Holli K, Isola J. Estrogen receptor beta is coexpressed with ERalpha and PR and associated with nodal status, grade, and proliferation rate in breast cancer. Am J Pathol 2000; 156:29-35.

30.   Skliris GP, Carder PJ, Lansdown MR, Speirs V. Immunohistochemical detection of ERbeta in breast cancer: towards more detailed receptor profiling? Br J Cancer 2001; 84:1095-8.

31.   Saunders PT. Does estrogen receptor beta play a significant role in human reproduction? Trends Endocrinol Metab 2005; 16:222-7.

32.   Collins P, Webb C. Estrogen hits the surface. Nat Med 1999; 5:1130-1.

33.   Razandi M, Oh P, Pedram A, Schnitzer J, Levin ER. ERs associate with and regulate the production of caveolin: implications for signaling and cellular actions. Mol Endocrinol 2002; 16:100-15.

34.   Speirs V, Carder PJ, Lane S, Dodwell D, Lansdown MR, Hanby AM. Oestrogen receptor beta: what it means for patients with breast cancer. Lancet Oncol 2004; 5:174-81.

35.   Yang SH, Liu R, Perez EJ, et al. Mitochondrial localization of estrogen receptor beta. Proc Natl Acad Sci U S A 2004; 101:4130-5.

36.   Lindberg MK, Moverare S, Skrtic S, et al. Estrogen receptor (ER)-beta reduces ERalpha-regulated gene transcription, supporting a "ying yang" relationship between ERalpha and ERbeta in mice. Mol Endocrinol 2003; 17:203-8.

37.   Stettner M, Kaulfuss S, Burfeind P, et al. The relevance of estrogen receptor-beta expression to the antiproliferative effects observed with histone deacetylase inhibitors and phytoestrogens in prostate cancer treatment. Mol Cancer Ther 2007; 6:2626-33.

38.   Lynch TJ, Bonomi PD, Butts C, et al. Novel agents in the treatment of lung cancer:

Fourth Cambridge Conference. Clin Cancer Res 2007; 13:s4583-8.

39.   Traynor AM, Schiller JH, Stabile LP, et al. Pilot study of gefitinib and fulvestrant in the

treatment of post-menopausal women with advanced non-small cell lung cancer. Lung Cancer

2008.

40.   Shigematsu H, Gazdar AF. Somatic mutations of epidermal growth factor receptor

signaling pathway in lung cancers. Int J Cancer 2006; 118:257-62.

41.   Kaiser U, Hofmann J, Schilli M, et al. Steroid-hormone receptors in cell lines and tumor

biopsies of human lung cancer. Int J Cancer 1996; 67:357-64.

42.   Di Nunno L, Larsson LG, Rinehart JJ, Beissner RS. Estrogen and progesterone receptors

in non-small cell lung cancer in 248 consecutive patients who underwent surgical resection. Arch

Pathol Lab Med 2000; 124:1467-70.

43.   Wistuba, II. Genetics of preneoplasia: lessons from lung cancer. Curr Mol Med 2007;

7:3-14.

Figure Legends

Fig. 1. Fig. 1. Microphotographs showing representative examples of immunohistochemical expression of estrogen receptors (ER) α (panels *A*, *B*, and *C*) and β (panels *D*, *E* and *F*) and progesterone receptor (PR; panels *G*, *H* and *I*), in tissue specimens of non-small cell lung carcinoma (NSCLC) tumors and bronchial epithelium (panels *A*, *D*, and *G*) adjacent to adenocarcinomas. The two NSCLC histologies are represented: adenocarcinoma (panels *B*, *E* and *H*), and squamous cell carcinoma (panels *C*, *F* and *I*). ER α and β expressions are shown using antibodies ER-α4 and ER-β1, respectively. Examples of nuclear expression and cytoplasmic expressions are indicated by red and blue arrows, respectively. Normal epithelia show nuclear expression of ER-β and PR, and cytoplasmic expression of ER-β. Adenocarcinomas show nuclear expression for all three markers and cytoplasmic staining for ER-β. Squamous cell carcinomas show nuclear staining for PR, and both nuclear and cytoplasmic for ER-β. The magnification of the microphotographs is 200x for normal epithelium and 400x for tumors.

Fig. 2. Kaplan-Meier curves showing recurrence free survival (RFS) of NSCLC patients for ERα cytoplasmic (panel *A*) and ERβ nuclear (panel *B*) expression.

Fig. 3. Representative examples of ERα and β immunohistochemical expression (*upper figures*) and epidermal growth factor receptor *(EGFR)* mutations (*lower figures*) in lung adenocarcinomas. Panel *A*: ERα (antibody ERα-4) positive in the nucleus of malignant cells and sequencing chromatograms showing the presence of mutant form of *EGFR* (15 bp deletion in exon 19; arrow indicates in-frame deletion mutation sequence). Panel *B*: ERβ (antibody ERβ-1)

positive in the nucleus of malignant cells and sequencing chromatograms showing the presence

of mutant *EGFR* (L858R point mutation in exon 21; arrow indicates C<u>T</u>G to C<u>G</u>G mutation).

Panel *C*: ER α and β (same antibodies than panels *A* and *B*) with negative expression in the

malignant cells and sequencing chromatograms showing the presence of wild-type form for

EGFR exon 19 (line indicates sequence 746 to 750).

Table 1. Frequency of ER and PR immunohistochemical expression[*] in NSCLC tissue specimens

Marker	Location	Adenocarcinoma		Squamous cell carcinoma		
		Number of cases	Positive N (%)	Number of cases	Positive N (%)	*P* value
ERα-1	Nucleus	187	20 (11)	109	2 (2)	0.0048
	Cytoplasm	187	0	108	0	--[†]
ERα-2	Nucleus	186	84 (45)	110	23 (21)	<0.0001
	Cytoplasm	185	1 (<1)	111	0	1.000
ERα-3	Nucleus	191	16 (8)	114	0	0.0007
	Cytoplasm	190	92 (48)	114	37 (33)	0.0064
ERα-4	Nucleus	185	74 (40)	109	25 (23)	0.0028
	Cytoplasm	185	35 (19)	109	18 (17)	0.6043
ERβ-1	Nucleus	189	102 (54)	112	66 (59)	0.4022
	Cytoplasm	189	185 (98)	112	110 (98)	1.0000
ERβ-2	Nucleus	174	83 (48)	100	31 (31)	0.0069
	Cytoplasm	172	37 (22)	100	16 (16)	0.2685
PR	Nucleus	177	103 (58)	112	78 (70)	0.05
	Cytoplasm	176	0	112	0	--[†]

[*]Any expression score >0 is considered positive.

[†]Not tested.

Abbreviations: ER, estrogen receptor; PR, progesterone receptor; NSCLC, non-small cell lung cancer; ERα, estrogen receptor-α; ERβ, estrogen receptor-β.

Table 2. Significant correlations between immunohistochemical expression of ER and PR[*] and NSCLC patients' clinicopathological features.

Estrogen Receptor	Histology ADCA (n = 201) > SCC (n = 116)	Gender Female (n = 167) > Male (n = 150)	Tobacco History Never (n = 54) > Ever (n = 262)
ERα-1 nucleus	0.0048	0.0051	ns[†]
ERα-2 nucleus	<0.0001	0.0109	0.0006
ERα-3 nucleus	0.0015	ns	0.0242
ERα-4 nucleus	0.0004	0.0148	0.0044
ERβ-1 nucleus	ns	ns	0.0290
ERβ-2 nucleus	0.0016	0.044	ns

*ER and PR were tested using expression score.

[†]ns = not statistically significant.

Abbreviations: ER, estrogen receptor; PR, progesterone receptor; NSCLC, non-small cell lung cancer; ADCA, adenocarcinoma SCC, squamous cell carcinoma; ERα, estrogen receptor-α; ERβ, estrogen receptor-β.

Table 3. Multivariate RFS analysis using Cox regression model in NSCLC patients[*]

Variable	Hazard ratio	95% CI of HR		*P* value
		Lower limit	Upper limit	
ER as continuous variable				
ERα-4 cytoplasm	1.05	1.01	1.08	0.0068
ERβ-1 nucleus	1.01	1.00	1.02	0.0034
Stage II vs. I	1.90	1.14	3.18	0.0145
Stage III/IV vs. I	3.17	1.98	5.08	<.0001
ER dichotomized				
ERα-4 cytoplasm: >0 vs. 0	1.77	1.11	2.81	0.0156
ERβ-1 nucleus: >0 vs. 0	1.36	0.91	2.05	0.1388
Stage II vs. I	1.79	1.08	2.99	0.0250
Stage III/IV vs. I	3.13	1.97	4.99	<.0001

*With only significant covariates.

Abbreviations: NSCLC, non-small cell lung cancer; CI, confidence interval; HR, hazard ratio; ER, estrogen receptor; ERα, estrogen receptor-α; ERβ, estrogen receptor-β.

Table 4. Significant correlations between immunohistochemical expression of ER and *EGFR* mutation status in adenocarcinoma

ER expression by antibody	*EGFR* mutation status		
	Wild-type N positive/total (%)	Mutant N positive/total (%)	*P* value
ERα-3 nucleus	9/146 (6)	7/28 (25)	0.0016
ERα-3 cytoplasm	68/146 (47)	21/27 (78)	0.0029
ERα-4 nucleus	50/143 (35)	18/27 (67)	0.0020
ERα-4 cytoplasm	20/143 (14)	13/27 (48)	<0.0001
ERβ-1 nucleus	70/145 (48)	22/27 (82)	0.00015

*ER and PR were tested using expression score.

Abbreviations: ER, estrogen receptor; EGFR, epidermal growth factor receptor; PR, progesterone receptor; ERα, estrogen receptor-α; ERβ, estrogen receptor-β.
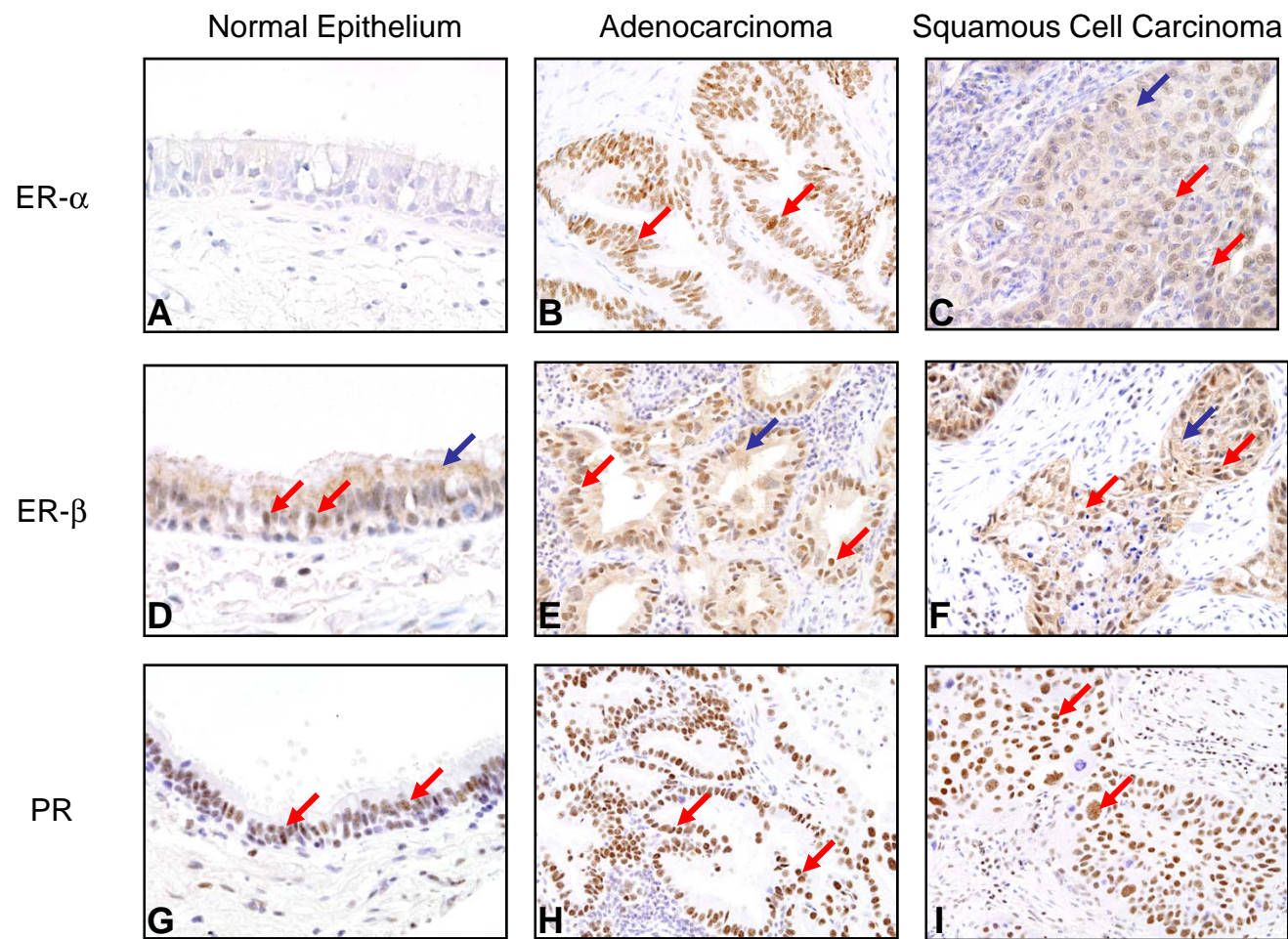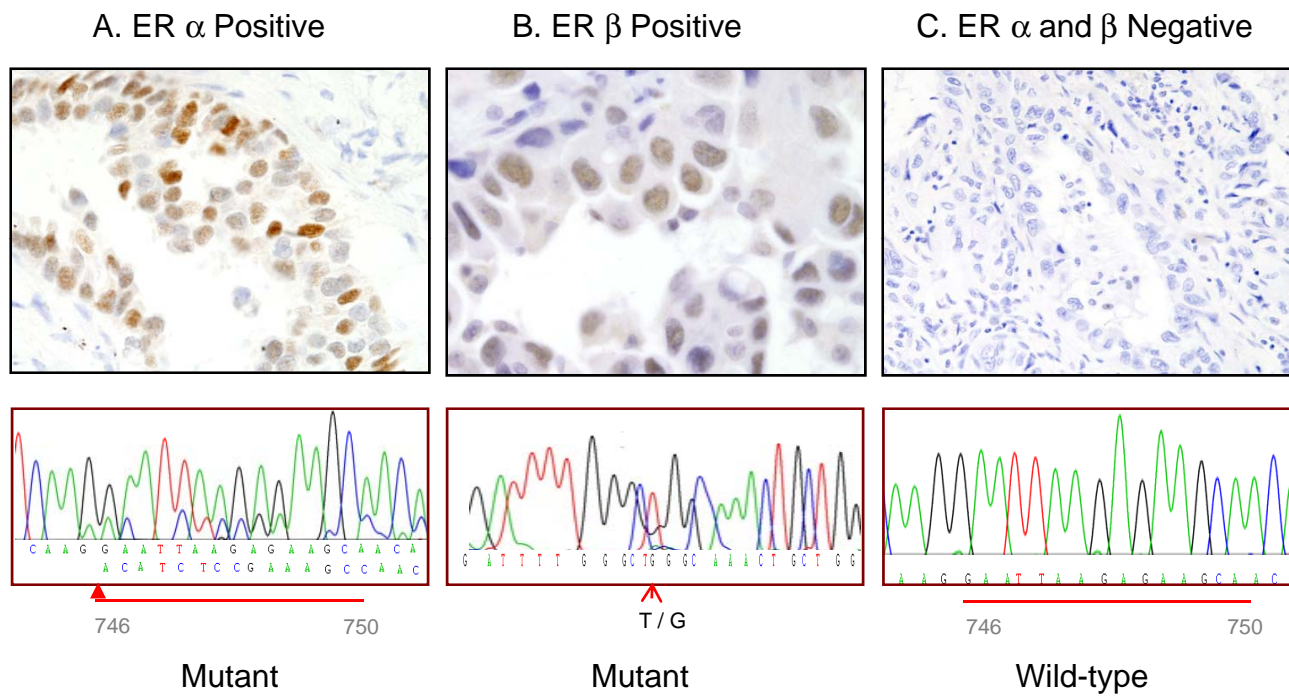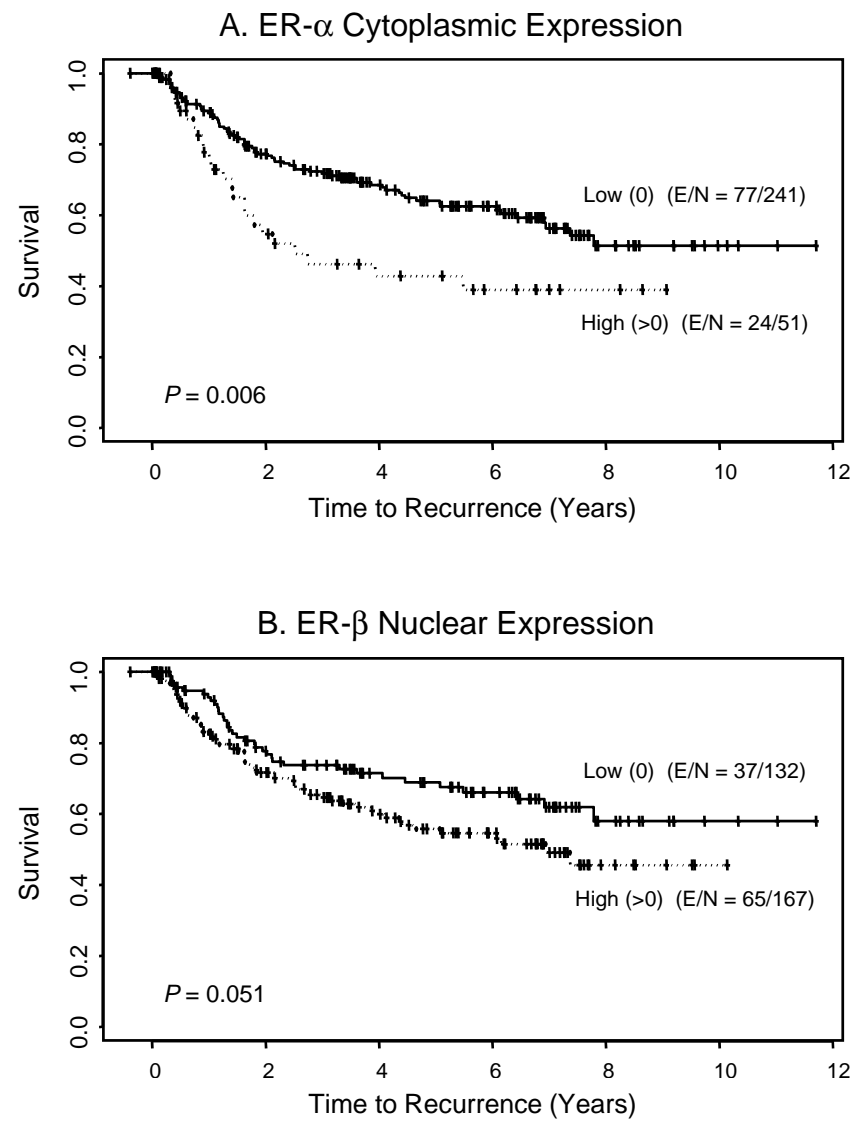
Figure 1

Figure 3

A. ER α Positive

B. ER β Positive

C. ER α and β Negative

Mutant

Mutant

Wild-type

Figure 2

A. ER-α Cytoplasmic Expression

Low (0) (E/N = 77/241)

High (>0) (E/N = 24/51)

P = 0.006

Survival

Time to Recurrence (Years)

B. ER-β Nuclear Expression

Low (0) (E/N = 37/132)

High (>0) (E/N = 65/167)

P = 0.051

Survival

Time to Recurrence (Years)

Genome-wide Hypomethylation in Head and Neck Cancer Is More Pronounced in HPV-negative Tumors and Is Associated with Genomic Instability

Kristy L. Richards[1,4], Baili Zhang[1], Keith A. Baggerly[2,5], Stefano Colella[1], James C. Lang[7], David E. Schuller[7], Ralf Krahe[1,3,5,6]

[1]Departments of Genetics, [2]Bioinformatics and Computational Biology, [3]Thoracic/Head and Neck Medical Oncology, and [4]Division of Cancer Medicine, University of Texas M. D. Anderson Cancer Center, Houston, Texas, United States of America, Graduate Programs in [5]Human and Molecular Genetics and [6]Genes and Development, University of Texas at Houston Graduate School in Biomedical Sciences, Houston, Texas, United States of America, [7]Molecular Biology and Cancer Genetics Programs, Ohio State University, Comprehensive Cancer Center, Columbus, Ohio, United States of America

Current address for K.L. Richards: Division of Hematology/Oncology, Lineberger Comprehensive Cancer Center, University of North Carolina, Chapel Hill, North Carolina, United States of America.
Current address for S. Colella: UMR 203 INRA INSA-Lyon BF2I, Biologie Fonctionnelle Insectes et Interactions, Bât. L. Pasteur, 20 ave. Albert Einstein, F-69621 Villeurbanne Cedex, France.

Corresponding Author: Ralf Krahe, Department of Genetics, Unit 1010, University of Texas M. D. Anderson Cancer Center, 1515 Holcombe Blvd., Houston, Texas, 77030, United States of America; Phone: (713) 834-6345; Fax: (713) 834-6319; E-mail: rkrahe@mdanderson.org.

Abbreviations: HNSCC, head and neck squamous cell carcinoma; HPV, human

papillomavirus; LOH, loss-of-heterozygosity; SNP, single nucleotide polymorphism

Abstract

Loss of genome-wide methylation is a common feature of cancer, and the degree of hypomethylation has been correlated with genomic instability. Global methylation of repetitive elements possibly arose as a defense mechanism against parasitic DNA elements, including retrotransposons and viral pathogens. Given the alterations of global methylation in both viral infection and cancer, we examined genome-wide methylation levels in head and neck squamous cell carcinoma (HNSCC), a cancer causally associated with human papilloma virus (HPV). We assayed global hypomethylation levels in 26 HNSCC samples, compared with their matched normal adjacent tissue, using Pyrosequencing-based methylation assays for LINE repeats. In addition, we examined cell lines derived from a variety of solid tumors for LINE and SINE (*Alu*) repeats. The degree of LINE and *Alu* hypomethylation varied among different cancer cell lines. There was only moderate correlation between LINE and *Alu* methylation levels, with the range of variation in methylation levels being greater for the LINE elements. LINE hypomethylation was more pronounced in HPV-negative than in HPV-positive tumors. Moreover, genomic instability, as measured by genome-wide loss-of-heterozygosity (LOH) SNP analysis, was greater in HNSCC samples with more pronounced LINE hypomethylation. Global hypomethylation was variable in HNSCC. Its correlation with both HPV status and degree of LOH as a surrogate for genomic instability may reflect alternative oncogenic pathways in HPV-positive versus HPV-negative tumors.

Introduction

DNA methylation is an epigenetic DNA modification that occurs via the action of DNA methyltransferases on CpG dinucleotides. Methylated regions of DNA are associated with chromatin remodeling, generally occurring in areas of more condensed chromatin and decreased transcriptional activity [1,2]. Renewed interest in this process arose after it was recognized that two types of aberrant methylation patterns are present in cancer cells [1,3]. The first is gene-specific hyper-methylation, where CpG islands in the promoter regions of genes acquire increased methylation, generally leading to reduced expression of the downstream gene. The second is genome-wide hypo-methylation, a large percentage of which occurs in repetitive DNA elements. In malignancy, global methylation is often aberrantly reduced, whereas gene-specific methylation is often aberrantly increased. While the effects of gene-specific hypermethylation (*e.g.*, reduced expression of a gene that is important for growth control) are easily appreciated, the effects of reduced global methylation are more vague [1,3].

It has been hypothesized that DNA methylation initially evolved as a defense mechanism against viral and other DNA pathogens as a way to silence foreign DNA sequences [4-6]. This is consistent with the observation that LINE and SINE (*Alu*) elements, originating from transposable elements, are heavily methylated in normal cells. Methylation of the HPV viral genome upon integration into the host genome has been reported, and changes in methylation of HPV DNA have been associated with tumorigenesis [7,8].

Global methylation is also clinically relevant, as demonstrated by associations between clinical outcome and global methylation levels in a number of cancer types [9-11]. From a mechanistic standpoint, global methylation appears to be related to cancer progression, since loss of global methylation tends to become more pronounced as precancerous lesions progress [12,13]. Furthermore, in colon cancer cells, loss of LINE methylation is inversely correlated with microsatellite instability and is directly correlated with chromosome instability [14,15].

4

We hypothesized that global methylation levels in cancer, represented by levels of LINE and SINE (*Alu*) methylation, might be correlated with viral infection. We, therefore, examined LINE methylation in relation to HPV status in head and neck cancers. In contrast to cervical cancers, which are nearly all associated with HPV infection, HNSCC is virally mediated in only a subset of cases (25-30%) [16]. To determine the impact of viral infection on global methylation levels in HNSCC, we developed Pyrosequencing-based methylation assays for repetitive DNA elements and compared HPV-positive with HPV-negative cancers. Previous publications have suggested that LINE methylation is variable in HNSCC, but did not find an association between HPV DNA status and LINE methylation levels [21,23]. Here we show that global hypomethylation is variable in HNSCC and correlates with both HPV status and genomic instability.

Results

LINE/SINE (*Alu*) assays are precise and reproducible, but show only moderate correlation between LINE-1 and *Alu* methylation levels

To assay global methylation levels, we adapted our Pyrosequencing-based Methylation Analysis (PMA) assay [17] to assess methylation of repetitive LINE and SINE (*Alu*) elements, similar to genome-wide methylation assays reported previously [18]. To validate the assays, we performed a series of tests: (1) mixing experiments with known amounts of methylated/unmethylated DNA; (2) methylation studies on a variety of cancer cell lines to compare LINE to SINE methylation and to survey global methylation across a broad range of malignancies; and (3) methylation of samples from different ages and genders to eliminate these factors as possible confounders of global methylation measurements.

Stepwise increments of methylated DNA were prepared by mixing universally unmethylated (U2M.L) DNA with universally methylated (UM.L) DNA in various proportions.

5

The mixed samples were then bisulfite treated and subjected to our PMA LINE-1 (LINE) and *Alu* (SINE) assays. Linear regression analysis showed that LINE-1 and *Alu* methylation levels were very closely associated with levels predicted by input fraction of methylated DNA (r = 0.995, p-value <0.0005 for LINE-1, and r = 0.980, p-value<0.0005 for *Alu*; Figure S1). It should be noted that even when input DNA was completely methylated, the maximum global methylation percentage as measured by the PMA assay is just over 50%, not 100%. This is because individual repetitive elements have diverged in sequence over time; and CpG dinucleotides, if mutated to TpG dinucleotides, are indistinguishable from unmethylated CpGs after the bisulfite treatment. This level of background noise is taken into account by normalizing each result to the universally methylated control (*i.e.*, reporting the percent methylated reference, or PMR).

Four pools of normal DNA samples (from peripheral blood leukocytes) were generated to assess the influence of age and gender on LINE-1 and *Alu* methylation levels. Each pool (females ≤40 years old, males ≤40 years old, females >40 years old, males >40 years old) contained DNA from at least five individuals. There were no sex- or age-dependent differences between the pools in LINE-1 or *Alu* methylation levels (data not shown).

Each LINE-1 and *Alu* methylation assay was tested on a panel of 23 cancer cell lines. Different CpG sites were compared by means of three distinct LINE-1 assays and three distinct *Alu* assays, each derived from different regions of the LINE-1 and *Alu* consensus sequences, respectively (Table 1). As a control, we also tested seven normal lymphoblastoid cell lines, which showed normal levels of methylation (all >80% in our LINE-1 assays). In contrast, as expected from previous reports [12-14,19], many of the tumor cell lines showed global hypomethylation, which was most pronounced in the LINE-1 assays (Figure 1). To check the consistency between LINE and SINE methylation levels (represented by our LINE-1 and *Alu* assays, respectively), we compared the degree of correlation between results from the three LINE-1 assays, between results from the three *Alu* assays, and between the various LINE-1 and *Alu* assays. Linear regression analysis showed that the individual LINE-1 assay results were

6

highly correlated with each other, for example $r = 0.93$ for the correlation between the L1-2 and

L1-3 assay results (Figure S2A). The same high degree of correlation was present between

results from the *Alu* assays, for example $r = 0.82$ for the correlation between the Alu-1 and Alu-3

assay results (Figure S2B). However, LINE-1 assay results were only moderately correlated

with *Alu* assay results, for example $r = 0.33$ comparing L1-1 and Alu-1; Figure S2C). A similar

level of moderate correlation between LINE-1 and *Alu* assays was reported previously in

neuroendocrine tumors [20].

LINE-1 hypomethylation of HNSCC patient samples

Matching normal, primary tumor, and where available, lymph node metastases of head

and neck patient samples (Table S1) were tested using our PMA LINE-1 assays (Figure 2).

Because of the greater dynamic range of the LINE-1 assay and limited sample amounts, only

LINE-1 assays were performed for the remainder of this study. In general, HNSCC primary

tumors and metastatic lymph nodes were hypomethylated compared to their matching normal

adjacent tissues. With the LINE1-1 assay, the mean primary tumor PMR was 65.5%, while the

mean normal PMR was 90.0% (p-value = 6.7×10^{-8} using a paired t-test). However, there was

quite a bit of variability in the primary tumors, ranging from 31.2% (severe hypomethylation) to

90.8% (normal). The mean PMR in lymph node metastases (73.8%; range 31.8%-93.8%) was

also highly variable, even with respect to the corresponding primary tumor, sometimes lower

and sometimes higher than the PMR of the primary tumor with which it is associated.

HPV-positive tumors retain more LINE-1 methylation than HPV-negative tumors

Because there was so much variability in the HNSCC tumor PMR, we hypothesized that

the level of global hypomethylation might vary in different subgroups of HNSCC. To explore the

relationship between loss of LINE-1 hypermethylation and HPV status, we compared the mean

LINE-1 methylation level of three groups that differed by their HPV status. The first group (n =

8) was HPV negative (-/-); the second group (n = 8) contained HPV DNA, yet were transcriptionally silent with respect to the E6 viral oncogene, indicating lack of expression of this oncoprotein (+/-). The third group of tumors (n = 8) was positive for HPV DNA and E6 expression (+/+). The mean methylation level of the three groups of tumors is statistically different, with a *p*-value = 0.011 for the trend (Figure 3).

We also compared global methylation levels in matched normal adjacent tissues from the same three groups. In contrast to the results for the primary tumors, there were no differences in global methylation levels in the matching normal tissues and therefore no correlation with HPV status (Figure 3). Based on a previously reported association between LINE-1 methylation and T-N-M stage [21], we looked for such an association in our sample set, but found none (*p*-value = 0.31).

Levels of LINE-1 hypomethylation and LOH in HNSCC tumors are correlated

Colon cancer cell lines with more pronounced LINE hypomethylation were previously reported to have a higher degree of LOH [14,15]. To examine whether this correlation held true in our HNSCC patient samples, we performed a global LOH analysis using 10K SNPChip data. Genotypes were compared between normal adjacent tissue and matched tumor samples; informative loci were those that were heterozygous in the normal tissue. Figure 4 shows a plot of the percentage of informative loci for each primary tumor with LOH versus the degree of LINE-1 methylation in the same specimen. We fit a linear trend to the data, which showed a Pearson correlation of -0.494, with a *p*-value = 0.017. As a check of robustness, we also calculated the Spearman (rank-based) correlation, which was also significant. The Spearman correlation coefficient for this relationship was -0.428 (*p*-value = 0.042), establishing that LOH was indeed significantly correlated with the degree of LINE hypomethylation.

Discussion

      We developed several LINE (LINE-1) and SINE (*Alu*) methylation assays with PCR

primers in conserved regions of these repetitive elements. These assays utilize multiple CpG

sites (3-6) to determine methylation levels and enable the simultaneous amplification of many

individual LINE and SINE elements throughout the human genome as representative genomic

landmarks for global methylation analysis. As expected, results from individual LINE-1 assays

were very well correlated with results from other LINE-1 assays, despite measuring methylation

in different regions of the LINE-1 sequence. The same is true for *Alu* assays, with high

correlation between results from three different assays. However, when LINE-1 and *Alu*

methylation levels were compared with each other, the correlation was more modest, only about

40%. The reasons for this lower correlation may be related simply to differences in assay

sensitivity: LINE-1 assays ranged from 0-50% methylated in mixing studies, while *Alu* assays

had less amplitude, ranging from 0-30% methylated, possibly secondary to higher inter-

individual background noise due to sequence variation between individual *Alu* elements (Figure

S1). Another possibility is that there is a functional or biological difference between the two

types of repetitive DNA in their methylation maintenance. LINE repeats are more frequent in

gene-poor regions of the genome, while *Alu* elements are more common in gene-rich regions

[22]. Since global methylation can be measured by a variety of methods, these inter-assay

differences should be considered when comparing results using different types of assays and

studies.

      Our results show decreases in global methylation in cell lines from a variety of cancer

cell types (Figure 1), similar to previously published results for a variety of tumor types [12-

14,19]. It is worth noting that the cancer cell lines in general had lower levels of methylation

than the HNSCC samples, perhaps reflecting a longer time to accumulate methylation loss or

the clonal nature of these cell lines. However, some cell lines (e.g., RKO) had little if any loss of

methylation. This implies, as for the primary HNSCC tumors, that there is variability in the underlying biology. Further research into what causes this variability could provide important information about pathways of and the role of epigenetic alterations in cancer progression.

Our results demonstrate a positive correlation between maintenance of normal LINE methylation and HPV-positivity. In addition, maintenance of normal LINE methylation was also correlated with less LOH or genome instability. If LOH is viewed as a surrogate for chromosome instability (CIN), this result is consistent with the previously reported result that colon cancers also have an association between CIN and loss of LINE hypermethylation [14,15]. Thus, it is tempting to speculate that LINE methylation and CIN are causally related, perhaps via methylation's known association with more densely chromatin packaging, which may translate into more fidelity during chromosome segregation and therefore less LOH. However, our results and previously reported results are purely correlative; functional studies will be necessary before this causal relationship can be established.

The novel finding in our results is that HPV-positivity is correlated with maintenance of LINE methylation. A recent epidemiologic study identifying risk factors for LINE-1 hypomethylation reported no significant association between HPV DNA status and LINE-1 methylation levels [23]. However, there were methodological differences between that and our study, including the use of both HPV E6 DNA and RNA status in the assignment of HPV status, the use of a different methylation assay, and the use of methylation level as a continuous variable in the analysis. Although Furniss and colleagues did not show a direct association, they showed that outcomes varied by LINE-1 methylation levels for HPV-negative tumors [23]. Further studies are needed to clarify the association between HPV status and LINE methylation. One possible hypothesis is that in an attempt to silence the HPV virus, infected cells induce a more exuberant methylation response, harkening back to the origins of methylation as a viral defense mechanism. Although this will again require mechanistic studies or perhaps studies in additional types of virally mediated cancers (e.g., Hepatitis B and C mediated HCC compared

with non-virally induced HCC, or EBV+ lymphoma vs. EBV- lymphoma) to establish causality, our results along with those of Furniss and colleagues [23] certainly provide more support for the hypothesis that HPV-positive HNSCC and HPV-negative HNSCC represent distinct biologic entities that arise via separate oncogenic pathways.

In summary, we developed several new LINE (LINE-1) and SINE (*Alu*) whole-genome methylation assays, which we applied to determine the methylation status of a variety of cancer cell lines and HNSCC primary tumor samples. We find that cancer cell lines in general have decreased methylation levels of repetitive elements. Even more variability in LINE-1 methylation was noted within HNSCC samples. Importantly, we discovered a correlation between HPV-negativity, increased genome instability, and loss of genome methylation. This correlation reinforces the concept that HPV-positive and HPV-negative cancers are biologically distinct and provides a basis for future studies to further define the biologic mechanism underlying these findings.

Materials and Methods

Patient samples and cell lines

Matched tumor/normal adjacent tissue samples, and when available cervical lymph node metastases from HNSCC patients were collected at Ohio State University as described previously (Table S1) [24]. Genomic DNA was extracted from the DNA-protein phase of TriZol-extracted tissues according to the manufacturer's suggestions (Invitrogen). DNA was extracted using the PureGene kit (Gentra) on cell pellets from four HNSCC cell lines (SCC-4, SCC-9, SCC-15 and SCC-25), five lung cancer cell lines (H1395, H520, H2170, SK-MES-1 and SW-900), one breast cancer cell line (MCF7), one cervical cancer cell line (HeLa), three brain cancer cell lines (U251, SK-N-AS and M059K), one uterine cancer cell line (AN3CA), one sarcoma cell line (HT1080), one kidney cancer cell line (HEK293), and six colon cancer cell

lines (LoVo, SW48, HCT-15, DLD-1, COLO 320DM and RKO) according to the manufacturer's

suggestions. In addition, DNA from the lymphoblastoid cell line BL1395 was used as a

matching control to H1395. All cell lines are available from ATCC (Manassas, VA).

Normal pools and methylated controls

Four pools of normal samples were generated representing different genders and ages.

DNA samples were obtained from anonymous blood donors and were a gift of Dr. Michael J.

Siciliano (University of Texas M. D. Anderson Cancer Center). Three of the pools (females

older than 40 years of age, females age 40 or under, and males age 40 or under) were each

comprised of five individuals per pool. The fourth pool (males older than 40 years of age) was

comprised of six individuals. Commercially prepared universally methylated and universally

unmethylated DNA (UM.C and U2M.C, respectively) were obtained from Chemicon. UM.L

(universally methylated DNA) was generated as a positive control by treating normal peripheral

blood leukocyte (PBL) DNA with the CpG methylase *M.Sss*I (New England Biolabs) [25].

U2M.L (universally unmethylated DNA) was generated as a negative control by amplifying the

same DNA used to generate the positive control DNA using the GenomiPhi kit (GE Healthcare)

as described by the manufacturer.

Primers and PCR conditions

PCR primers and sequencing primers were designed by using PSQ Assay Design

software (Biotage) [26]. Three assays for SINE (*Alu*) elements and three assays for LINE-1

elements were designed (Table 1). PCR was performed in a 25 µl reaction containing Qiagen

HotStart Taq master mix (Qiagen) using 1 µl bisulfite treated DNA (10 ng of DNA equivalents).

To reduce the cost per assay, the amplification protocol was developed using a biotinylated

universal primer approach. Final primer concentrations were 10 nM of the primer tailed with the

universal primer, 100 nM of the untailed primer, and 90 nM of the universal biotinylated primer in

each reaction [17]. The amplification was carried out at the following conditions: denaturation at

95°C for 5 min, followed by 45 cycles at 95°C for 30 sec, 45°C (SINEs) or 53°C (LINEs) for 1

min, 72°C for 45 sec, and a final extension at 72°C for 7 min [17].

PyroMethA (PMA) and methylation assessment

Bisulfite conversion of genomic DNA was done as reported previously [17]. Briefly, 0.5-

1.0 μg of genomic DNA was treated using the CpGenome DNA modification kit (Chemicon),

including DNA sulfonation, deamination, desalting, desulfonation and recovery. Bisulfite-treated

DNA was stored at -20°C until use. PMA is a Pyrosequencing-based technology that can

analyze CpG methylation at multiple sites in a single assay. After a PCR amplification using

bisulfite treated DNA, Pyrosequencing was carried out using the PSQ96HS system (Biotage)

according to the manufacturer's protocol including single strand binding protein (PyroGold

reagents). The results were analyzed using Q-CpG software (Biotage), which calculates the

methylation percentage ($^mC/(^mC+C)$) for each CpG site, allowing quantitative comparisons. The

methylation index (called MI) was calculated as the average value of $^mC/(^mC+C)$ for all

examined CpG sites in the assay. In general, there was very good agreement in methylation

levels among individual CpG sites in the same assay. Bisulfite-treated UM.L was used as the

universally methylated reference. PMA data for these global methylation assays are reported

as a percentage of methylated reference (PMR) value, normalizing the MI of each sample to the

MI of the universally methylated reference (UM.L) DNA [25].

Commercial universally methylated DNA (UM.C) and universally unmethylated DNA

(U2M.C) (Chemicon) were also used to perform this analysis, and the result was linear ($r =$

0.983, *p*-value < 0.0005 for LINE-1; Figure S1). However, commercially available U2M was not

completely unmethylated, since a pure U2M.C sample had residual methylation of

approximately 26%, different from U2M.L prepared in our lab, which had the expected 0%

methylation. We therefore used our own universally unmethylated DNA (U2M.L) for all further studies.

Detection of HPV16 E6 DNA and E6 RNA to determine HPV status

Quantitative real-time PCR was performed to detect either HPV16 E6 DNA or E6 cDNA using the same primer/probe set for both. The primers were designed using the HPV16 serotype, which accounts for ≥90% of all HPV-positive HNSCC cases [27]. To control for possible genomic DNA contamination in the cDNA, amplifications of cDNA from DNAse-treated RNA that had been prepared using the SuperScript First Strand Synthesis System (Invitrogen) both with and without the addition of reverse transcriptase were compared. PCR was performed in a 25 µl reaction containing iQ supermix master mix (Biorad) using 25 ng of genomic DNA or 5 µl of cDNA. Forward primer (5'-CTGCAATGTTTCAGGACCCA-3') and reverse primer (5'-TCATGTATAGTTGTTTGCAGCTCTGT-3') were added to a final concentration of 200 nM each. The Texas Red labeled real-time probe (5'-TR-AGGAGCGACCCAGAAAGTTACCACAGTT-3') was added to a final concentration of 320 nM. Fluorescein was added to each reaction at a final concentration of 10 pM. Each reaction was performed in triplicate. The amplification was carried out at the following conditions: denaturation at 95°C for 8.5 min, followed by 50 cycles at 95°C for 15 sec, 60°C for 1 min and analyzed in real time using an iCycler PCR machine and software (Biorad). Samples that did not amplify were scored as negative, and all samples were grouped into 3 categories based on these results: (+/+), positive for both E6 DNA and E6 RNA; (+/-), positive for E6 DNA, but transcriptionally silent; and (-/-), negative for E6 DNA and RNA. HPV status was successfully determined for 24 of the 26 HNSCC samples, and these were used for subsequent analyses utilizing HPV status.

10K SNPChip LOH analysis

HNSCC genomic DNAs were extracted using the standard TriZol-extraction protocol; they were further purified by ethanol precipitation before and after whole genome amplification using the GenomiPhi kit (GE Healthcare). The Affymetrix 10K *Xba*131 array contains approximately 11,500 SNPs with an average spacing of 210 kb. Standard Affymetrix protocols were followed for these assays. Briefly, about 250 ng genomic DNA was digested with *Xba*I and then ligated to adaptors. Next, one-primer amplification was carried on by using the GeneAmp PCR System 9700 (Applied Biosystems). After purification with Qiagen MinElute 96 UF, a total of about 20 μg of PCR product was fragmented and labeled with biotin. Hybridization was performed in the Affymetrix GeneChip Hybridization Oven at 48°C for 16-18 hours. Arrays were washed and stained with the Affymetrix GeneChip Fludics Station 400 and were scanned with the Affymetrix GeneArray 2500 Scanner. Image processing was performed with GCOS 1.0 software and genotypes were generated with GTYPE 2.0 or higher software.

Statistical analysis

In order to assess the association between levels of methylation and levels of HPV load (a similar analysis was also used to assess the association between levels of methylation and T-N-M stage), we proceeded as follows. All sample methylation values were converted to ranks. One missing value for the LINE1-1 assay, for sample P2, was imputed using the P2 value from the LINE1-3 (correlation between the LINE1-1 and LINE1-3 assays is 0.98). These ranks were then scaled (weighted) by HPV load, with weights of 0, 1 and 2 for -/-, +/-, and +/+, respectively. The final association "score" was the sum of these weighted ranks. The null distribution for this score was assessed by simulations in which we repeatedly allocated samples to HPV groups at random. We ran one million simulations, and defined our *p*-value as two times the proportion of cases in which the simulation score was as large or larger than the one we actually saw. Our simulated *p*-value was 0.011.

Supporting Information

Table S1 Clinical and molecular features of HNSCC samples.

Figure S1 Dynamic range of PMA LINE-1 and Alu Assays.

Figure S2 Correlation analysis of LINE and SINE (*Alu*) global methylation assays.

References

1. Jones PA, Baylin SB (2002) The fundamental role of epigenetic events in cancer. Nat Rev Genet 3: 415-428.

2. Robertson KD (2005) DNA methylation and human disease. Nat Rev Genet 6: 597-610.

3. ones PA, Baylin SB (2007) The epigenomics of cancer. Cell 128: 683-692.

4. Bird AP (1993) Functions for DNA methylation in vertebrates. Cold Spring Harb Symp Quant Biol 58: 281-285.

5. Liu WM, Maraia RJ, Rubin CM, Schmid CW (1994) Alu transcripts: cytoplasmic localisation and regulation by DNA methylation. Nucleic Acids Res 22: 1087-1095.

6. Yoder JA, Walsh CP, Bestor TH (1997) Cytosine methylation and the ecology of intragenomic parasites. Trends Genet 13: 335-340.

7. Rosl F, Arab A, Klevenz B, zur Hausen H (1993) The effect of DNA methylation on gene regulation of human papillomaviruses. J Gen Virol 74 (Pt 5): 791-801.

8. Turan T, Kalantari M, Calleja-Macias IE, Cubie HA, Cuschieri K, et al. (2006) Methylation of the human papillomavirus-18 L1 gene: a biomarker of neoplastic progression? Virology 349: 175-183.

9. Hsiung DT, Marsit CJ, Houseman EA, Eddy K, Furniss CS, et al. (2007) Global DNA methylation level in whole blood as a biomarker in head and neck squamous cell carcinoma. Cancer Epidemiol Biomarkers Prev 16: 108-114.

10. Pattamadilok J, Huapai N, Rattanatanyong P, Vasurattana A, Triratanachat S, et al. (2007) LINE-1 hypomethylation level as a potential prognostic factor for epithelial ovarian cancer. Int J Gynecol Cancer 18: 711-717.

11. Tangkijvanich P, Hourpai N, Rattanatanyong P, Wisedopas N, Mahachai V, et al. (2007) Serum LINE-1 hypomethylation as a potential prognostic marker for hepatocellular carcinoma. Clin Chim Acta 379: 127-133.

12. Chalitchagorn K, Shuangshoti S, Hourpai N, Kongruttanachok N, Tangkijvanich P, et al. (2004) Distinctive pattern of LINE-1 methylation level in normal tissues and the association with carcinogenesis. Oncogene 23: 8841-8846.

13. Hoffmann MJ, Schulz WA (2005) Causes and consequences of DNA hypomethylation in human cancer. Biochem Cell Biol 83: 296-321.

14. Matsuzaki K, Deng G, Tanaka H, Kakar S, Miura S, et al. (2005) The relationship between global methylation level, loss of heterozygosity, and microsatellite instability in sporadic colorectal cancer. Clin Cancer Res 11: 8564-8569.

15. Ogino S, Kawasaki T, Nosho K, Ohnishi M, Suemoto Y, et al. (2008) LINE-1 hypomethylation is inversely associated with microsatellite instability and CpG island methylator phenotype in colorectal cancer. Int J Cancer 122: 2767-2773.

16. Fakhry C, Gillison ML (2006) Clinical implications of human papillomavirus in head and neck cancers. J Clin Oncol 24: 2606-2611.

17. Colella S, Shen L, Baggerly KA, Issa JP, Krahe R (2003) Sensitive and quantitative universal Pyrosequencing methylation analysis of CpG sites. Biotechniques 35: 146-150.

18. Yang AS, Estecio MR, Doshi K, Kondo Y, Tajara EH, et al. (2004) A simple method for estimating global DNA methylation using bisulfite PCR of repetitive DNA elements. Nucleic Acids Res 32: e38.

19. Estecio MR, Gharibyan V, Shen L, Ibrahim AE, Doshi K, et al. (2007) LINE-1 hypomethylation in cancer is highly variable and inversely correlated with microsatellite instability. PLoS ONE 2: e399.

20. Choi IS, Estecio MR, Nagano Y, Kim do H, White JA, et al. (2007) Hypomethylation of LINE-1 and Alu in well-differentiated neuroendocrine tumors (pancreatic endocrine tumors and carcinoid tumors). Mod Pathol 20: 802-810.

21. Smith IM, Mydlarz WK, Mithani SK, Califano JA (2007) DNA global hypomethylation in squamous cell head and neck cancer associated with smoking, alcohol consumption and stage. Int J Cancer 121: 1724-1728.

22. Lander ES, Linton LM, Birren B, Nusbaum C, Zody MC, et al. (2001) Initial sequencing and analysis of the human genome. Nature 409: 860-921.

23. Furniss CS, Marsit CJ, Houseman EA, Eddy K, Kelsey KT (2008) Line region hypomethylation is associated with lifestyle and differs by human papillomavirus status in head and neck squamous cell carcinomas. Cancer Epidemiol Biomarkers Prev 17: 966-971.

24. Colella S, Richards KL, Baggerly KA, Tsavachidis S, Clarke JW, et al. (2008) Molecular signatures of metastasis in head and neck cancer. Head & Neck 30: 1273-1283.

25. Weisenberger DJ, Campan M, Long TI, Kim M, Woods C, et al. (2005) Analysis of repetitive element DNA methylation by MethyLight. Nucleic Acids Res 33: 6823-6836.

26. Price AL, Eskin E, Pevzner PA (2004) Whole-genome analysis of Alu repeat elements reveals complex evolutionary history. Genome Res 14: 2245-2252.

27. Gillison ML, Koch WM, Capone RB, Spafford M, Westra WH, et al. (2000) Evidence for a causal association between human papillomavirus and a subset of head and neck cancers. J Natl Cancer Inst 92: 709-720.

Table 1. LINE-1 and *Alu* PMA Assays.

Assays	GenBank Number [Ref.]	F Primer Seq (5'--3')	R Primer Seq (5'--3')	Sequencing Primer (5'--3')	Amplicon Size (bp)	No. CpG Sites
L1-1	X52235	tttattagggagtgttagatagtggg	GACGGGACACCGCTGATCGTTTA cttcccaaataaaacaatacc	tgggygtaggttagtgggtg (F)	117	6
L1-2	X52235	GACGGGACACCGCTGATCGTTTA ggtattgttttatttgggaag	ccctcctaaccaaatacaaaat	ccaaatacaaaatataatct (R)	196	4
L1-3	M80343	attagggagtgttagatagtggg	GACGGGACACCGCTGATCGTTTA ccccttacrcttcccaaat	gygtaggttagtgtgtgtg (F)	123	5
Alu-1	[26]	GACGGGACACCGCTGATCGTTTA tttttattaaaaatataaaaaattagt	ccaaactaaaatacaataa	aaactaaaatacaataac (R)	170	3
Alu-2	[26]	GACGGGACACCGCTGATCGTTTA tttttattaaaaatataaaaaattagt	tcaacctcccraataactaaaa	aataactaaaattacaaac (R)	96	5
Alu-3	J00085	gagagaattgtttgaatttagga	GACGGGACACCGCTGATCGTTTA cactatcacccaaactaaaataca	tgaatttaggaggtgga (F)	102	4

The sequence for the biotin-labeled universal primer (5'--3') for the 3-primer PCR is underlined, Biotin-GGGACACCGCTGATCGTTTA. F, sequencing primer extends in the forward direction; R, sequencing primer extends in the reverse direction. r, purine (A or G); y, pyrimidine (C or T).

Figure Legends

Figure 1. *Alu* **and LINE-1 methylation in a variety of tumor cell lines.** **A.** *Alu* methylation using the Alu-3 assay. **B.** LINE-1 methylation using the L1-3 assay. Results are reported as the PMR (percent methylated reference) normalized to the universally methylated reference DNA. Universally unmethylated (U2M), universally methylated (UM) controls, and normal control DNA from PBLs are also shown.

Figure 2. LINE-1 methylation in HNSCC tumor samples. Paired tumor and normal samples and, where available, lymph node metastases were assayed for LINE-1 methylation. PMR values are plotted using the normal sample PMR as the x-value and primary tumor (circles) or metastasis (triangle) PMR as the y-value. Horizontal lines represent PMR values for universally methylation (UM) and unmethylated (U2M) controls, normal lymphocytes (green) and for four HNSCC cell lines (yellow). Box plots on the right show the mean and distribution of primary tumors and metastases in the subset of samples where matched metastases and primary tumors were available.

Figure 3. LINE-1 methylation levels are lower in HPV-negative HNSCC. Box plots of methylation levels (PMR) of HNSCC primary tumors (right in each pair) and normal adjacent tissue (left in each pair) are shown according to HPV status. +/+, HPV-positive and expressing E6 viral mRNA; +/-, HPV-positive but transcriptionally silent; and -/-, HPV negative.

Figure 4. LINE-1 hypomethylation is correlated with degree of LOH in HNSCC. LINE-1 methylation is plotted as PMR, and LOH is the fraction of 10K SNP loci that show LOH relative to all informative loci. Pearson correlation coefficient is -0.494 (p-value = 0.01) for the correlation between the two values.
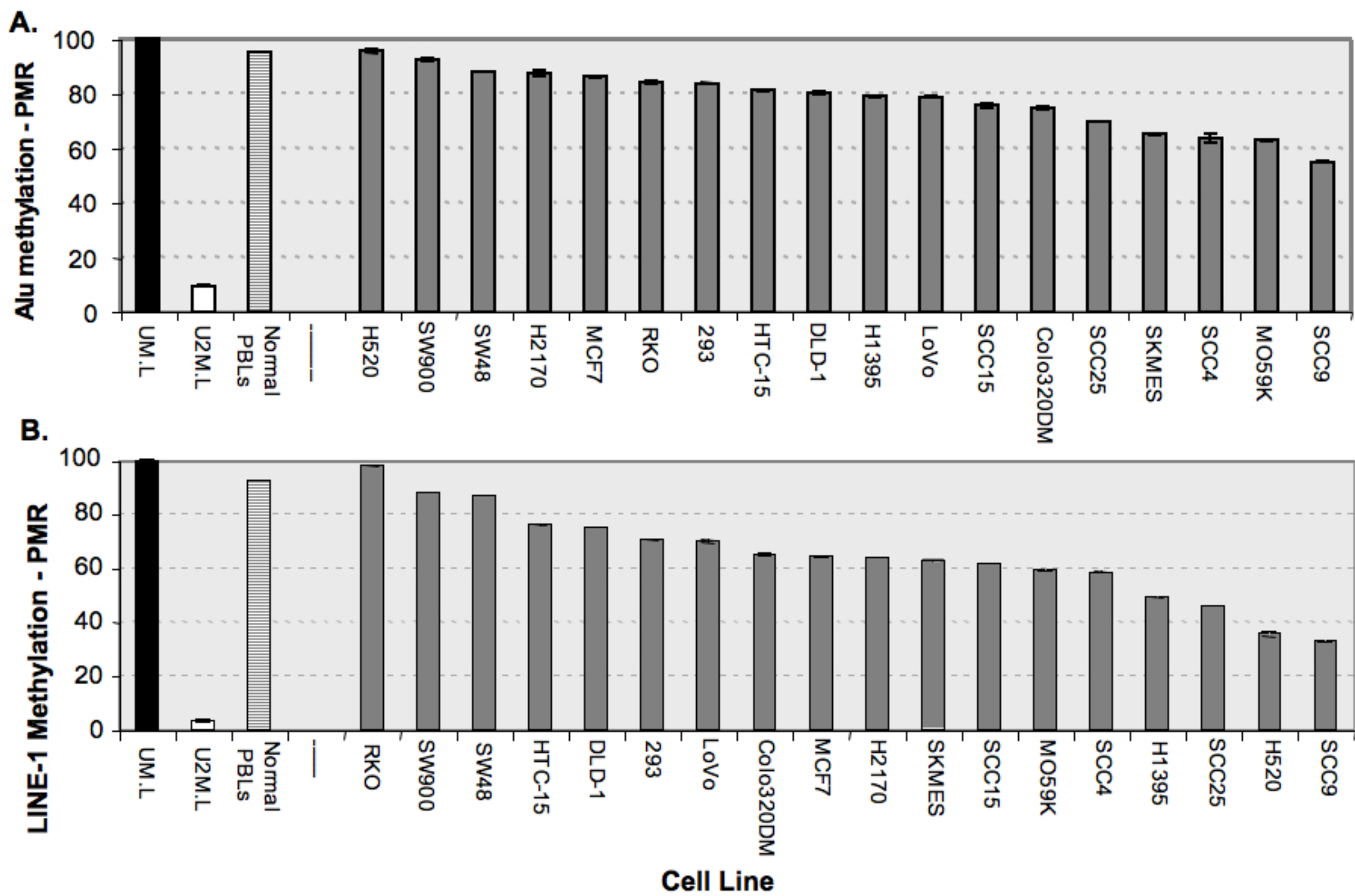
Figure 1
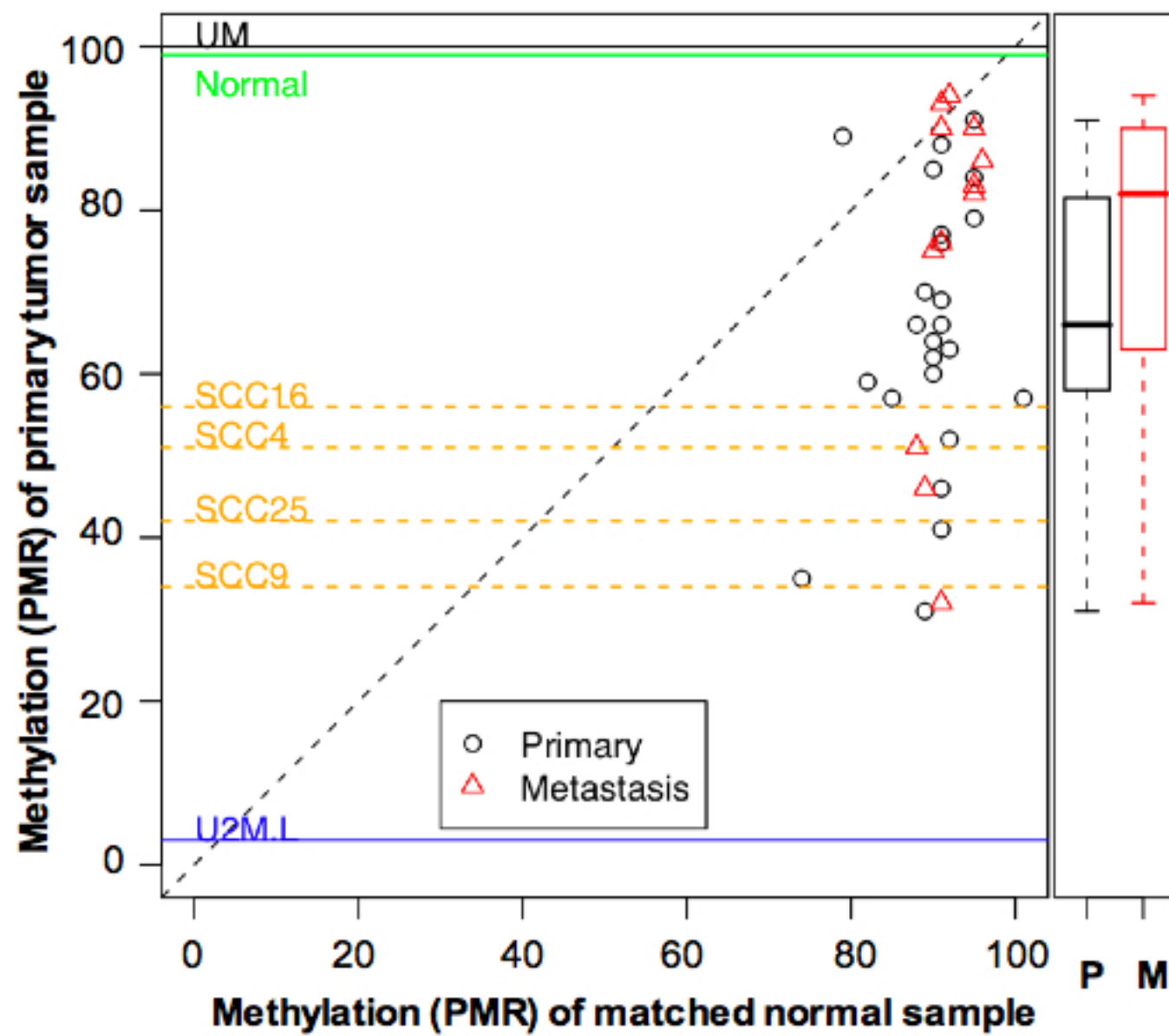
Figure 2
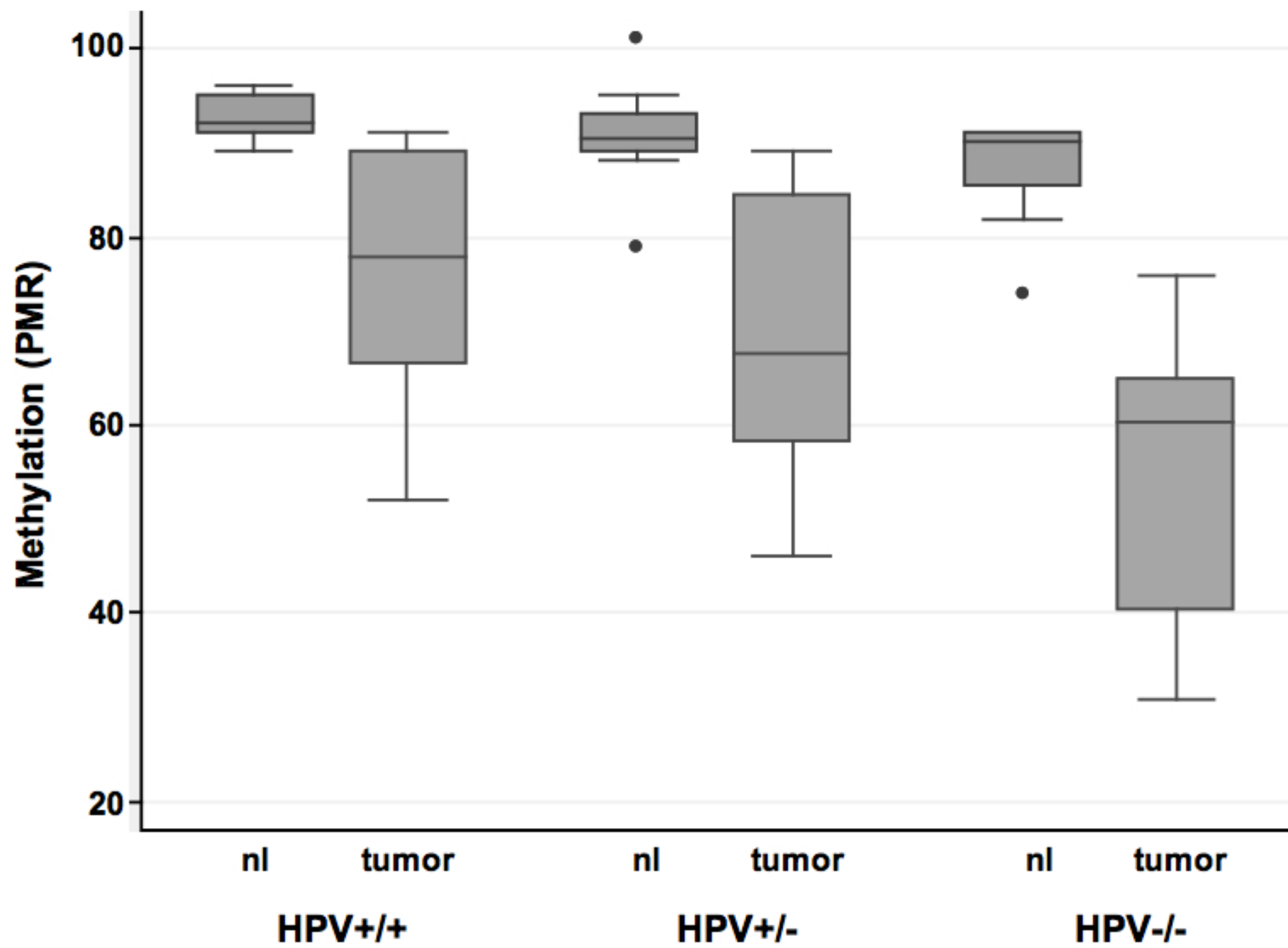
Figure 3
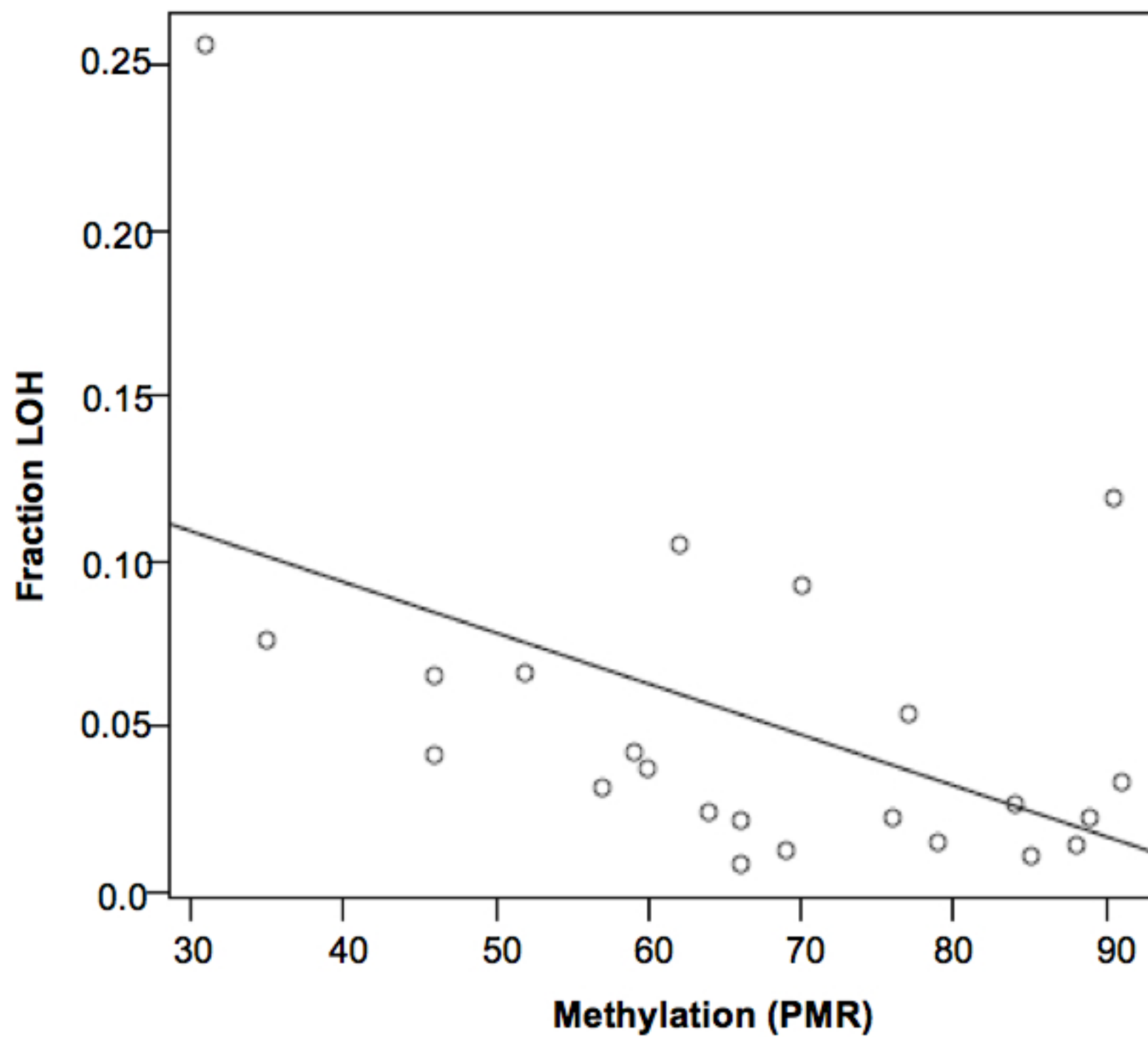
Figure 4

Table S1. Clinical and molecular features of HNSCC samples.

Patient No.	PMR-nl	PMR-prim	PMR-met	HPV Status	#LOH	#AB	#LOH/#AB	Primary Tumor Site	Sex	Age	Tc	Nc	Mc	Stage
2	0.96	0.91	NA	+/+	211	1776	0.119	Oropharynx/tonsil	M	47	4	2	0	IV
5	0.91	0.66	0.93	-/-	21	2532	0.008	Larynx/subglottis	M	76	4	2	0	IV
6	0.91	0.41	0.32	NA	NA	NA	NA	Pharynx	M	50	NA	NA	NA	NA
7	0.89	0.31	0.46	-/-	557	2175	0.256	Larynx/supraglottis	M	48	2	3	0	IV
8	0.95	0.91	0.9	+/+	81	2446	0.033	Oral cavity/tongue	M	65	3	2	0	IV
9	0.95	0.84	0.83	+/-	56	2105	0.027	Oral cavity/tongue	M	45	3	1	0	III
10	0.91	0.88	0.9	+/+	38	2674	0.014	Oropharynx/tonsil	M	54	1	2	0	IV
11	0.92	0.52	0.94	+/+	187	2831	0.066	Larynx/glottis	M	64	4	1	0	IV
12	0.95	0.79	0.82	+/+	39	2582	0.015	Oropharynx/BOT	M	53	3	1	0	III
13	0.92	0.63	NA	+/+	NA	NA	NA	Hypopharynx/pyriform sinus	M	64	3	2	0	IV
14	0.91	0.69	NA	+/-	27	2143	0.013	Oropharynx/BOT	M	49	4	0	0	IV
15	0.88	0.66	0.51	+/-	57	2595	0.022	Larynx/supraglottis	F	54	2	1	0	III
16	0.9	0.64	0.75	-/-	54	2237	0.024	Oral cavity/tongue	F	78	3	2	0	IV
17	0.91	0.77	0.76	+/+	114	2105	0.054	Oropharynx/tonsil	M	47	2	2	0	IV
18	1.01	0.57	NA	+/-	66	2105	0.031	Larynx/supra	M	56	3	0	0	III
19	0.79	0.89	NA	+/-	59	2635	0.022	Larynx/glottis	M	54	4	0	0	IV
20	0.82	0.59	NA	-/-	109	2582	0.042	Larynx/glottis	M	63	3	0	0	III
21	0.85	0.57	NA	NA	NA	NA	NA	Larynx/glottis	M	59	2	0	0	II
22	0.89	0.7	NA	+/+	204	2200	0.093	Hypopharynx/pyriformis	M	56	2	3	0	IV
23	0.91	0.46	NA	+/-	96	2289	0.042	Hypopharynx/pyriformis	M	61	3	2	0	IV
24	0.74	0.35	NA	-/-	161	2109	0.076	Hypopharynx/cricoid	F	62	3	1	0	III
27	0.9	0.85	NA	+/-	27	2418	0.011	Oral cavity/tongue	M	67	2	0	0	II
28	0.9	0.6	NA	+/-	94	2486	0.038	Oropharynx/palate	M	69	1	0	0	I
29	0.91	0.46	NA	-/-	141	2151	0.066	Oropharynx/tonsil	F	70	2	1	0	III
30	0.9	0.62	NA	-/-	244	2315	0.105	Oral cavity/tongue	M	30	3	0	0	III
31	0.91	0.76	NA	-/-	59	2595	0.023	Oropharynx/BOT	M	51	4	0	0	IV

PMR-nl, PMR of normal adjacent tissue; PMR-prim, PMR of primary tumor; PMR-met, PMR of lymph node metastasis. HPV status: +/+, positive at both DNA level and for E6 transcriptional level; +/-, positive at the DNA level but transcriptionally silent for E6; -/-, negative. #LOH, number of 10K SNPs that show loss of heterozygosity; #AB, number of 10K SNPs that are heterozygous in normal adjacent tissue. Tc/Nc/Mc, clinical T-N-M stage.

Supplementary Figure Legends

Figure S1. Dynamic range of PMA LINE-1 and *Alu* Assays. Mixing experiments were performed to determine PMA methylation levels measured with varying proportions of universally methylated and unmethylated DNA. UM.C and U2M.C represent commercially available (Chemicon) universally methylated and unmethylated DNAs, respectively. UM.L and U2M.L were generated from the same DNA by *in vitro* modification in our laboratory.

Figure S2. Correlation analysis of SINE and LINE global methylation assays. A variety of tumor and normal cell line DNAs were assayed with all six of our LINE and SINE assays (three LINE-1 assays and three *Alu* assays). **A.** LINE-1 assays were highly correlated with each other. **B.** *Alu* assays were highly correlated with each other. **C.** However, LINE-1 and *Alu* assays were only moderately correlated. Two representative plots are shown for each series of comparisons.
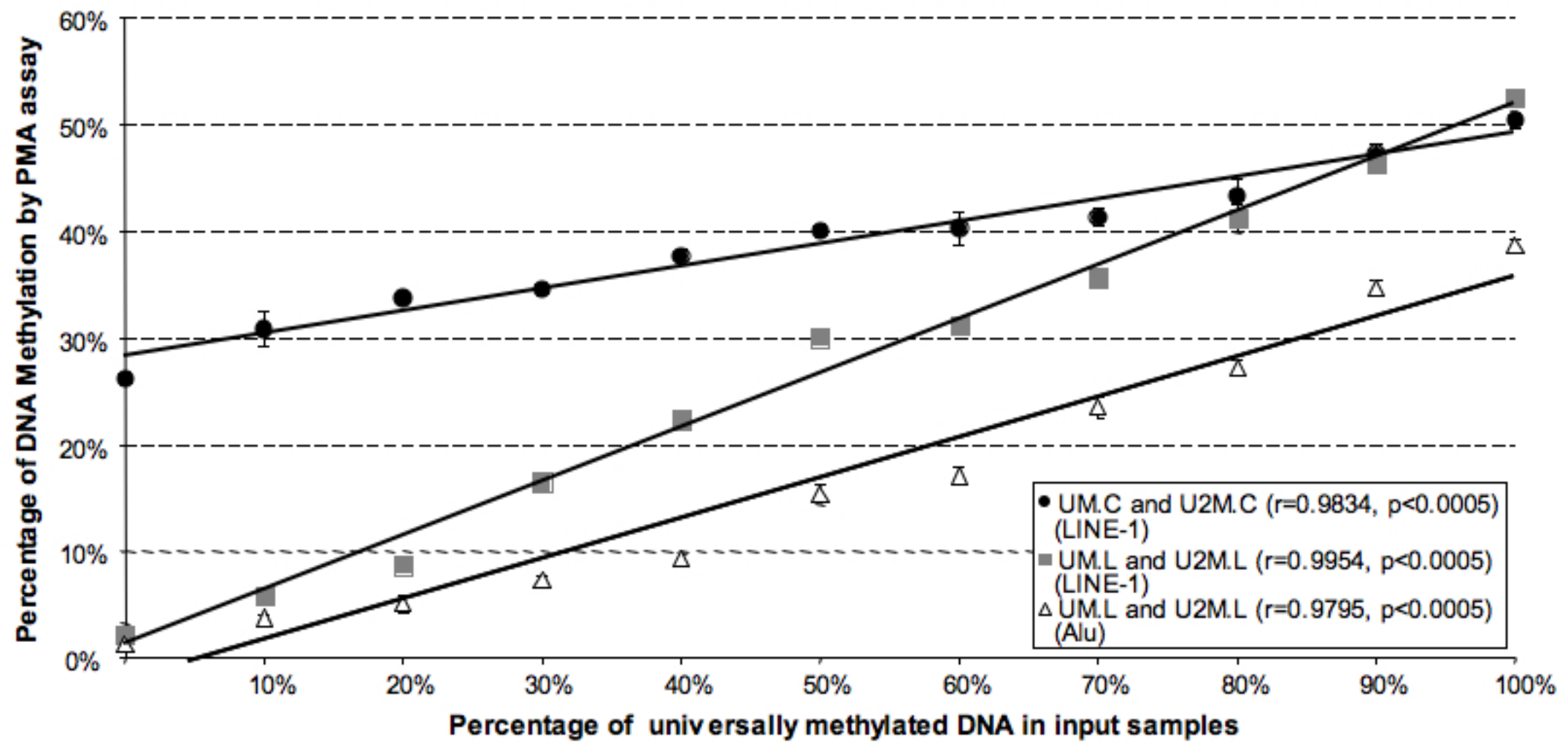
Supplementary Figure 1
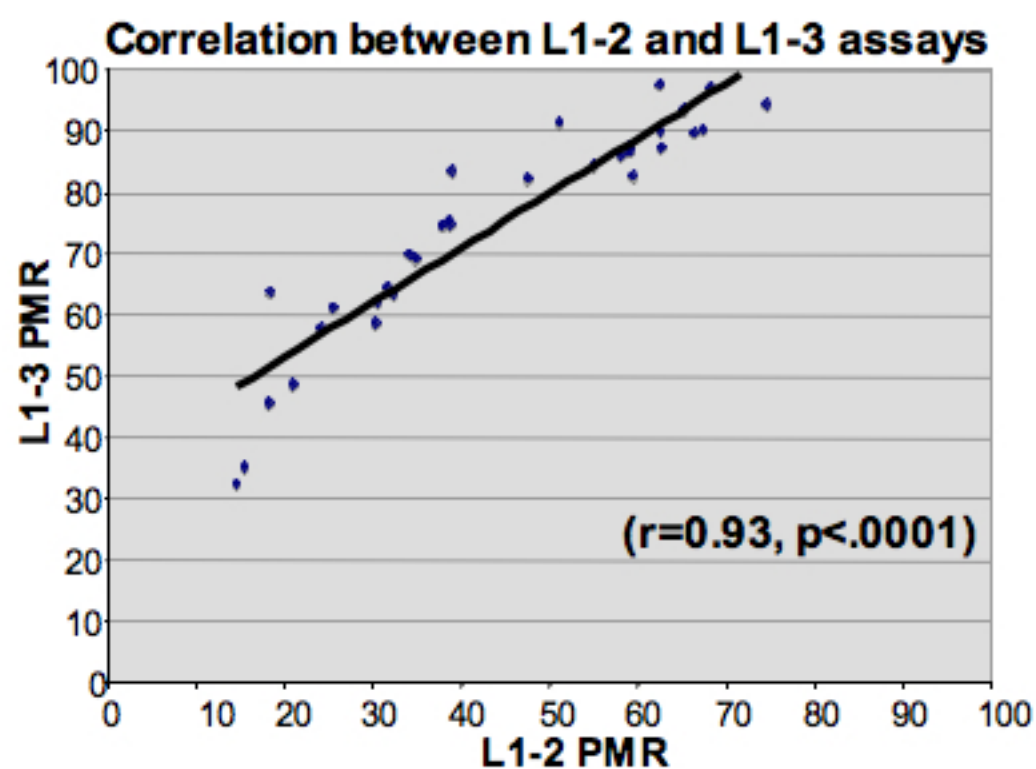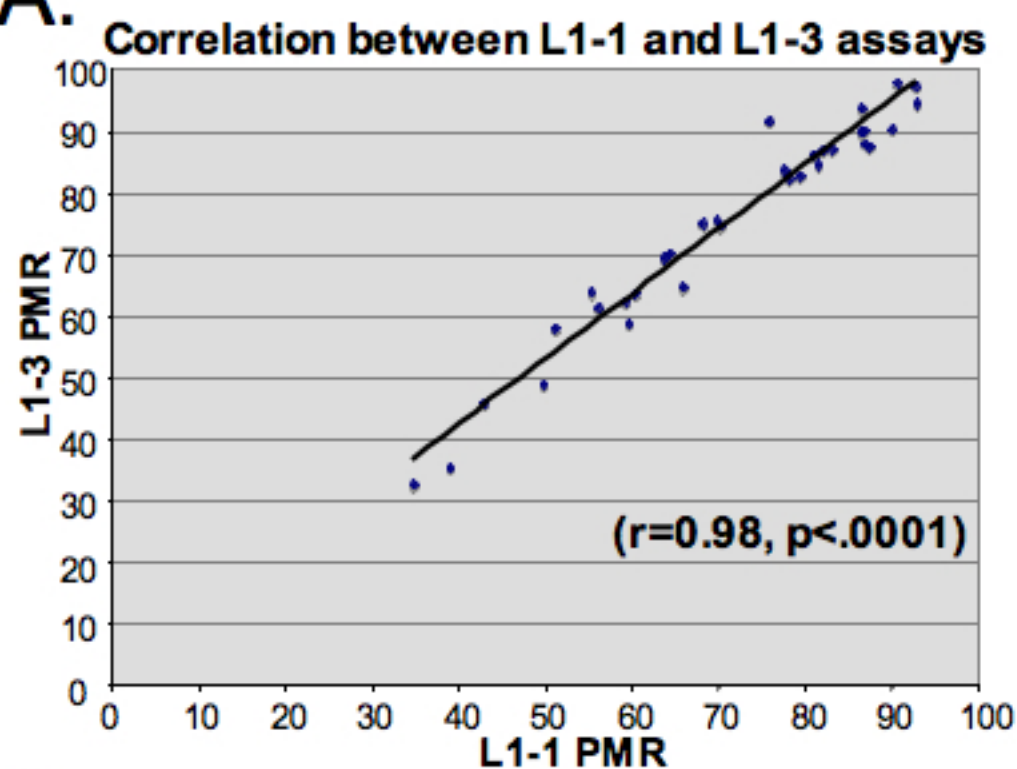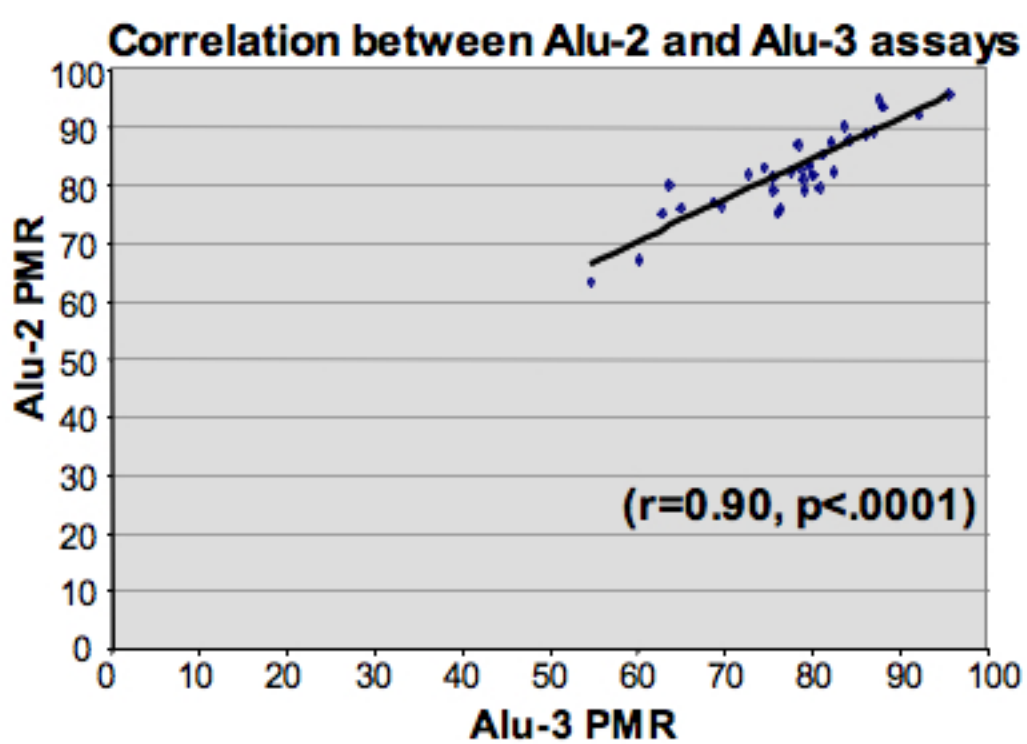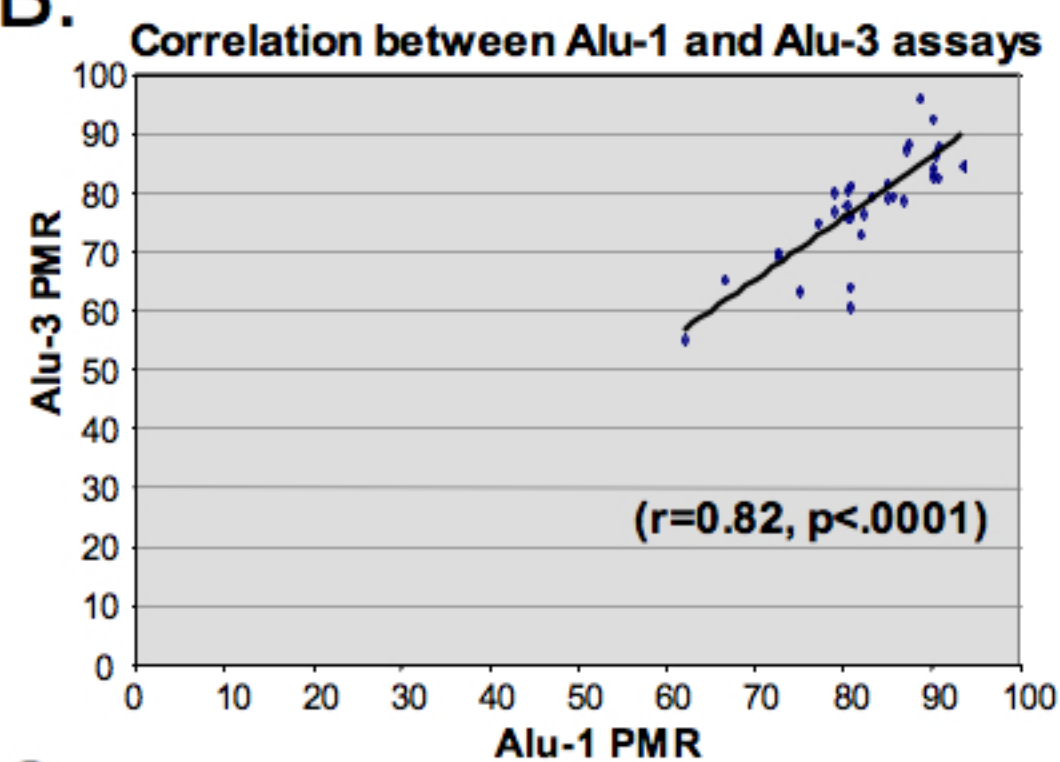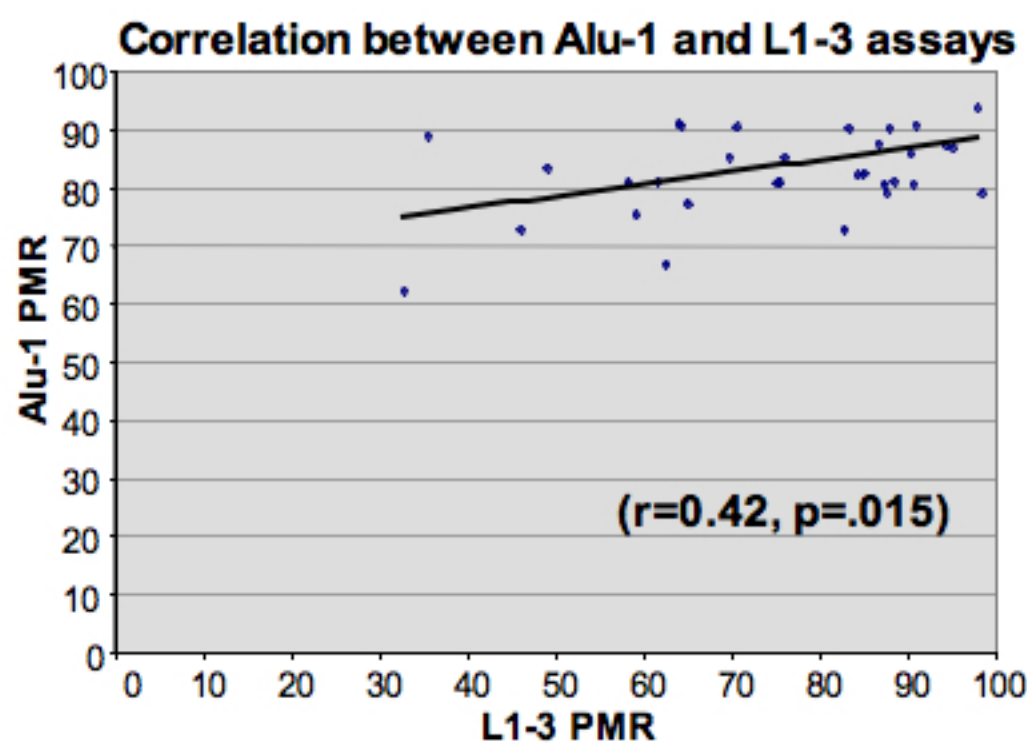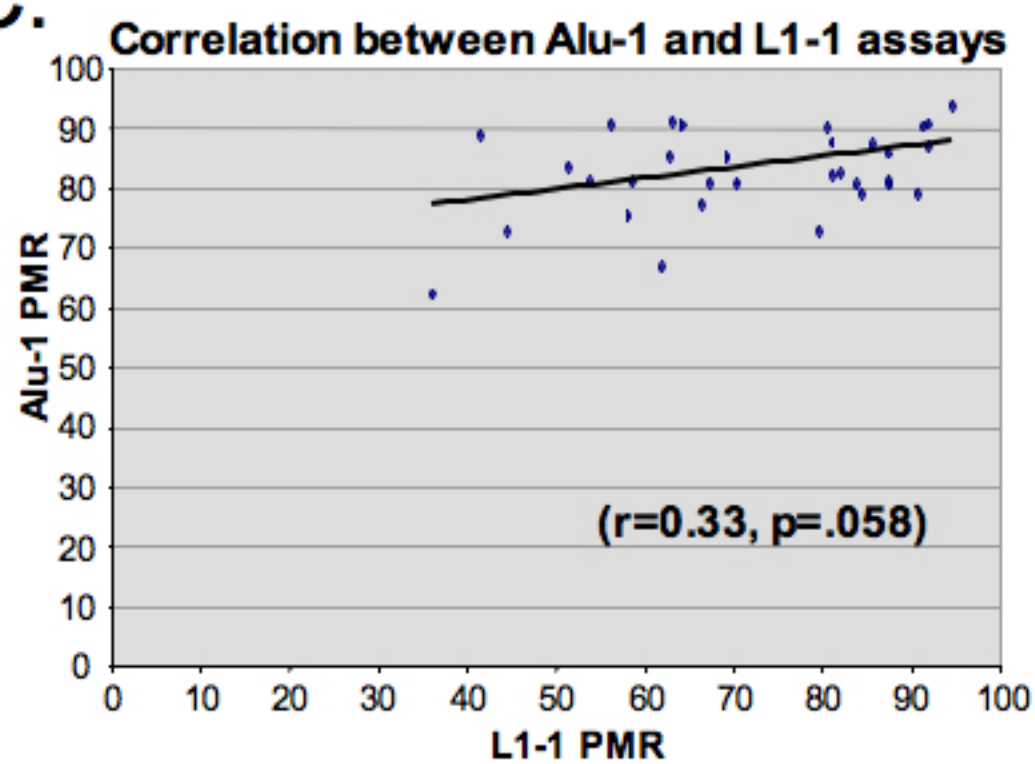
Supplementary Figure 2

HER Family Receptor Abnormalities in Lung Cancer Brain Metastases and Corresponding Primary Tumors

Menghong Sun[1], Carmen Behrens[2], Lei Feng[3], Natalie Ozburn[1], Ximing Tang[2],

Guosheng Yin[3], Ritsuko Komaki[4], Marileila Varella-Garcia[5] , Waun Ki Hong[2], Kenneth

D. Aldape[1], and Ignacio I. Wistuba[1,2].

From the Departments of Pathology[1], Thoracic/Head & Neck Medical Oncology[2],

Biostatistics[3], and Radiation Oncology[4], The University of Texas M. D. Anderson Cancer

Center, Houston, Texas; and Department of Medicine/Medical Oncology and Pathology[5],

University of Colorado Cancer Center, Aurora, Colorado

Running head: HER Abnormalities in Lung Cancer with Brain Metastasis

Correspondence to:
Ignacio I. Wistuba
Department of Pathology, Unit 85
The University of Texas M. D. Anderson Cancer Center
1515 Holcombe Blvd.
Houston TX 77030-4009
Tel: (713) 563-9184
Fax: (713) 792-0309
e-mail: iiwistuba@mdanderson.org

Translational Relevance

Brain metastasis occurs in up to 60% of non-small cell lung carcinomas (NSCLC) and there is little information on the molecular differences between primary tumor and metastases. Our findings indicate that NSCLC brain metastases have some significant differences in HER family receptors-related abnormalities from primary lung tumors. These differences could be related to tumor progression and may cause diverse responses to EGFR-targeted therapy of primary and metastatic tumor sites.

Abstract

Purpose: To compare the characters of HER receptors and their ligands deregulation between primary tumor and corresponding brain metastases of non-small cell lung carcinoma (NSCLC).

Experimental design: Fifty five surgically resected NSCLC primary tumors and corresponding brain metastases tumor specimens were included in tissue microarrays. Immunohistochemical expression of EGFR and phosphorylated (p)–EGFR, their related ligands EGF, transforming growth factor–α (TGF-α), and amphiregulin, and the receptors Her2, Her3, and p-Her3 was investigated. *EGFR* copy number using fluorescent *in situ* hybridization was also performed.

Results. Brain metastases showed significantly higher immunohistochemical expression of p-EGFR (membrane, $P<0.0001$; and cytoplasm, $P=0.14$), EGF (membrane, $P=0.027$; and nucleus, $P=0.008$), amphiregulin (nucleus, $P=0.019$), and p-Her3 (membrane, $P=0.001$) than primary tumors did. Primary tumors showed significantly higher expression of cytoplasmic ($P=0.01$) TGF–α. In adenocarcinomas, an identical high frequency of *EGFR* copy number gain (high polysomy and amplification) was detected in primary and brain metastasis (65%) sites. However, adenocarcinoma metastases (30%) showed higher frequency of *EGFR* amplification than corresponding primary tumors (13%). Patients whose primary tumors showed *EGFR* amplification tended to develop brain metastases at an earlier time points.

Conclusions. Our findings indicate that NSCLC brain metastases have some significant differences in HER family receptors-related abnormalities from primary lung tumors.

These differences could be related to tumor progression and may cause the diverse responses to EGFR-targeted therapy of primary and metastatic tumor sites.

Introduction

Lung cancer is the leading cause of cancer-related deaths in the United States (1). Lung cancer includes several histological types, the most frequently occurring of which (~80%) are two types of non–small cell lung carcinoma (NSCLC), adenocarcinoma and squamous cell carcinoma (2). The brain is one of the main sites of metastasis in patients with lung cancer: brain metastasis has an incidence of up to 60% in patients with lung adenocarcinoma (3-6). The median survival for lung cancer patients with brain metastasis is usually 3–6 months (6,7). The use of systemic chemotherapy and cranial irradiation has been shown to be unsuccessful in the treatment of NSCLC brain metastasis (3,8), and this in turn has motivated the search for new therapeutic strategies for this disease.

During the past few years, significant advances have been made in the development of new molecularly targeted agents for lung cancer (9). One example of such targets is the epidermal growth factor receptor (EGFR) that belongs to the HER family tyrosine kinase (TK) receptors composed of four homologous cell membrane receptors, including Her2 and Her3 (10). These receptors are activated by seven known ligands, including, EGF, transforming growth factor alpha (TGF-α), and amphiregulin (11). Deregulation of HER receptors, especially EGFR, appears to play an important role in the pathogenesis and progression of NSCLC (12). In lung cancer cells, the constitutive activation of EGFR is achieved by several mechanisms, including increased production of ligands, increased levels of the receptor, and mutation of *EGFR* (12-14).

Small-molecule inhibitors that target the TK domain of the *EGFR* produce tumor responses in approximately 10% of patients with advanced NSCLC that has progressed despite prior chemotherapy (12,15). However, the brain is still a frequent site of disease

recurrence in NSCLC patients after an initial response to treatment with EGFR TK inhibitors (TKIs), regardless of disease control in the lungs (4). Activating mutations in the EGFR TK domain, an increased *EGFR* copy number, and increased EGFR protein expression have been associated with a favorable response to treatment with EGFR TKIs (12,15). Previous reports demonstrated that metastatic NSCLC brain tumors respond to EGFR TKIs (16,17). However, it is still unclear whether *EGFR* and its related receptors' abnormalities differ in metastases compared with primary NSCLC tumors.

We investigated the immunohistochemical expression of EGFR and related ligands and receptors in 55 paired primary and brain metastasis NSCLCs. In addition, we compared *EGFR* copy number abnormalities using fluorescent in situ hybridization (FISH) analysis. The study was performed in tissue microarrays (TMAs) prepared from surgically resected NSCLC specimens.

Material and Methods

NSCLC tissue specimens. We obtained archived formalin-fixed paraffin-embedded (FFPE) material from surgically resected specimens from 55 NSCLC patients with primary lung cancers and corresponding brain metastases containing tumor tissues. These cases were selected based on the availability of enough archival tissue for the immunohistochemistry and FISH analyses. All specimens were from the Lung Cancer tissue bank at The University of Texas M. D. Anderson Cancer Center (Houston, TX) and had been collected between 1988 and 2002. The study was approved by the M. D. Anderson institutional review board. After histologic examination, TMAs were constructed using three 1-mm-diameter cores per tumor.

Detailed clinical and pathological information—including demographic, pathologic TNM staging, overall survival, and time of brain metastasis occurrence—was obtained for all patients (Table 1). Pathologic TNM stage had been determined for lung cancers according to the revised International System for Staging Lung Cancer (18) at time of primary tumor surgery with curative intent. In all cases the NSCLC brain metastases were solitary, and 11 patients also developed metastases at other brain sites (median, 13 months; range, <1–94 months) over a median period of 12 months (range, <1–27 months). Forty-four (80%) of 55 patients developed clinically detectable brain metastases after primary lung cancer surgical resection (median, 13 months; range, <1–94 months); in 11 (20%) patients the brain metastases were detected at the same time as the lung tumors, and they were surgically removed before (median, less <1 month; range, <1–11 months) the primary lung cancer surgery.

Immunohistochemical staining and evaluation. For our analysis, antibodies against the following molecules were purchased and used: EGF (EMD Biosciences; San Diego, CA; dilution 1:50), amphiregulin (Lab Vision, Freemont, CA; dilution 1:150), TGF-α (EMD Biosciences; dilution 1:150), EGFR (Zymed, Carlsbad, CA; clone 31G7; dilution 1:100), phosphorylated (p)–EGFR Tyr 1086 (Invitrogen, Carlsbad, CA, dilution 1:100), Her2 (Dako, San Diego, CA; dilution 1:100), Her3 (GenTex; San Antonio, TX; dilution 1:50), and p-Her3 (Cell Signaling, Danvers, MA; dilution 1:100). Immunohistochemical staining was performed using 5-µg-thick TMA histologic sections as previously described (19,22). The immunohistochemical protein expression was quantified, using white light microscopy with x20 magnification, by two experienced thoracic pathologists (M.S. and I.W.) blinded to clinical and other molecular variables. All markers were examined for membrane, cytoplasm, and nucleus localization in tumor cells. As previously described (20-22), immunohistochemical expression was quantified using a three-value intensity score (0, 1+, 2+, and 3+) for all markers, except for membrane EGFR and p-EGFR, for which a four-value intensity score (0, 1+, 2+, 3+, and 4+), and the percentage (0% to 100%) of the extent of reactivity were used. Next, expression scores were obtained by multiplying the intensity and reactivity extension values (range, 0–300 for all markers, except for membrane EGFR and p-EGFR with a range of 0–400).

***EGFR* FISH analysis.** We analyzed the gene copy number per cell using the LSI *EGFR* SpectrumOrange/CEP 7 SpectrumGreen Probe (Abbott Molecular, Des Plaines, IL), as previously described (23,24). Tumor specimens were classified into six FISH strata according to the frequency of cells with each *EGFR* gene copy number and referred to

the chromosome 7 centromere, as follows: (1) disomy (three or four copies in <10% of cells); (2) low trisomy (three copies in 10% to <40% of cells and four copies in <10% of cells); (3) high trisomy (three copies in ≥40% of cells and four copies in <10% of cells); (4) low polysomy (four copies in 10% to <40% of cells); (5) high polysomy (four or more copies in ≥40% of cells); and (6) gene amplification (presence of loose or tight *EGFR* gene clusters with ≥4 copies, *EGFR* gene to CEP 7 ratio ≥ 2, or 15 copies of *EGFR* per cell in ≥10% of cells). The high polysomy and gene amplification categories were considered to indicate high *EGFR* copy number (*EGFR* FISH positive), and the other categories were considered to indicate no significant increase in the *EGFR* copy number (*EGFR* FISH negative), as previously described (23,24).

Statistical analysis. Data were summarized using standard descriptive statistics and frequency tabulations. Associations between the marker expression and patients' clinical demographical variables, including age, sex, histology type, and pathologic stage, were assessed using appropriate methods, including the chi-squared test or Fisher's exact test for categorical variables and the Wilcoxon rank sum test or the Kruskal-Wallis test for continuous variables. The Wilcoxon signed rank test was used to test the differences in biomarker expression between primary lung tumors and brain metastases. Cox proportional hazard models were used for univariate analysis of time to metastasis according to biomarker expression. Hazard ratios with 95% confidence intervals and P values are reported. All tests were two-sided. P values smaller than 0.05 were considered to indicate statistical significance.

Results

Immunohistochemical expression of HER receptors and ligands in NSCLC primary tumors and corresponding brain metastases. All eight markers, including the ligands EGF, amphiregulin and TGF-α, and the receptors EGFR, p-EGFR, Her2, Her3, and p-Her3 showed protein expression in tumor cells from primary and metastasis sites at the membrane and cytoplasm levels (Figure 1). Of those, amphiregulin, EGF, p-EGFR, and p-Her3 showed also nuclear expression in malignant cells (Figure 1). Although showing overlapping, brain metastases had significantly higher immunohistochemical expression scores of EGF (membrane and nucleus), amphiregulin (nucleus), p-EGFR (membrane and cytoplasm), and p-Her3 (membrane) than did corresponding primary tumors (Figure 2 and Supplementary Table 1). Only the protein expression score of TGF-α at the cytoplasmic level was significantly higher in malignant cells from primary tumors than in brain metastasis cells (Figure 2 and Supplementary Table 1).

EGFR **copy number analysis by FISH in NSCLC primary tumors and corresponding brain metastases.** Overall, the presence of high frequency of gain in *EGFR* copy number (FISH positive: high polysomy and amplification; Figure 3) was similar in NSCLC primary (34/55 [62%]) and brain metastasis (36/55 [65%]) sites (Table 2). Although a relatively lower frequency of high polysomy was detected in metastases than in primary tumors (38 % versus 45%), brain metastases showed a nonsignificant higher frequency of *EGFR* amplification than corresponding primary tumors did (31 versus 16%, P = 0.53). In adenocarcinomas (n=40 cases), an identical frequency (65%) of gain in *EGFR* copy number was detected in primary tumors and corresponding

metastases. However, brain metastases of lung adenocarcinoma showed a nonsignificant higher frequency of *EGFR* amplification than primary lung tumors (30% versus 13%, P = 0.53). Although a higher frequency gain in *EGFR* copy number gain was detected in brain metastases among squamous cell carcinomas, the data were difficult to interpret because of the small number of cases available for analysis.

A relatively high level of concordance (45/55 [82%]) for gain in *EGFR* copy number gain was found between primary tumors and metastases (Supplementary Table 2). Fifteen (27%) paired primary/metastasis cases were *EGFR* FISH negative in both sites, whereas 30 (55%) paired cases showed gain in *EGFR* copy number at both tumor sites. Discordance in *EGFR* copy number status was detected in 10 cases (18%); in 7 of these, brain metastasis sites had a gain in copy number while primary tumors were FISH negative. The levels of concordance for high polysomy (14/31 [45%]) and amplification (6/19 [32%]) were low when primary tumors and corresponding brain metastases were compared.

Two consecutive brain metastasis samples were available for analysis from each of five adenocarcinoma cases. In all comparisons, paired consecutive brain metastasis specimens showed identical *EGFR* copy number status. One pair was FISH negative and the other four were FISH positive. FISH-positive specimens included two pairs showing *EGFR* high polysomy and two showing gene amplification.

We correlated *EGFR* copy number status with markers' immunohistochemical expression at both tumor sites. The only associations detected were that *EGFR* FISH-positive primary tumors and brain metastases demonstrated significantly higher protein

expression scores of p-EGFR (P=0.018) and Her2 (P=0.015), respectively, than FISH negative tumors.

Correlation between immunohistochemical expression of markers and *EGFR* copy number and time to brain metastasis. We investigated the correlation between the immunohistochemical expression of the markers examined and *EGFR* copy number abnormalities in primary lung tumors and the time to brain metastasis development. In this analysis, we included only the 44 patients whose brain metastases were diagnosed after surgical resection of the primary tumor. Overall, the median time to brain metastasis for all 44 patients was 1.23 years (95% Confidence Interval [CI], 0.89–1.62 years). The median time to brain metastasis development for patients with adenocarcinoma was 1.43 years (95% CI, 0.96–2.04 years), and that for patients with squamous cell carcinoma was 0.89 years (95% CI, 0.63 to not available) Using the Cox proportional hazard regression models, we identified that adenocarcinoma, compared with squamous cell carcinoma, was significantly correlated with a longer time to brain metastasis occurrence (P=0.009; HR, 0.347; 95% CI, 0.157–0.769), whereas EGFR protein expression scores (P=0.025; HR, 1.003; 95% CI, 1.000–1.006) and *EGFR* amplification (vs. no-amplification) were significantly correlated (P=0.0039; HR, 3.492; 95% CI, 1.494–8.162) with a shorter time to brain metastasis development. None of these markers were demonstrated in the multivariate analysis to be statistically significant predictors of metastasis development.

Discussion

In NSCLC, overexpression and activation of EGFR, Her2, and Her3 are well known phenomena (10,12). However, to the best of our knowledge, the overexpression of those TK receptors has not been previously reported in NSCLC brain metastasis. In this study, we have described for the first time higher levels of immunohistochemical expression of EGFR, p-EGFR, Her2, Her3, and p-Her3 in a series of NSCLC brain metastases. Interestingly, we found that the expression of phosphorylated forms of EGFR and Her3 proteins at the cytoplasmic and membrane level of malignant cells was significantly increased in brain metastasis compared with expression in corresponding primary lung tumors. These findings are consistent with the notion that activation of the EGFR and Her3 pathways is important in the progression and metastasis of lung cancer (12,15). Similarly to brain metastasis, we recently showed that in *EGFR* mutant lung adenocarcinomas, p-EGFR immunohistochemical expression was significantly increased in nine lymph node metastases compared with expression in corresponding primary tumors (19).

It is known that the receptors of the HER family are activated after binding to ligands or peptide growth factors, which include EGF, amphiregulin, and TGF- α (11). Of these, TGF- α (25,26) and amphiregulin (27) have been shown to be frequently expressed in primary NSCLC tumors, and EGF has been shown to expressed in NSCLC cell lines (28). We found that, compared with the corresponding primary tumors, NSCLC brain metastases had significantly higher immunohistochemical expression of membrane and nuclear EGF and of nuclear amphiregulin—ligands associated with activation of EGFR dimmers (11). These findings are consistent with the concomitant high level of

overexpression of p-EGFR in the NSCLC brain metastasis that we studied and indicate the presence of an autocrine secretion mechanism of these ligands. In contrast to EGF and amphiregulin, the cytoplasmic expression of TGF- α, another EGFR ligand (11), was significantly higher in malignant cells from primary tumors than in cells from brain metastases. Overexpression of TGF-α has been associated with the metastatic potential of NSCLC (28) and colon cancer (29) cell lines in favoring modifications of the tumor microenvironment conducive to metastasis, such as increasing angiogenesis.

In our study, we have identified that two of ligands, amphiregulin and EGF, and two receptors, p-EGFR and p-Her3, had nuclear expression in malignant NSCLC cells. There is evidence that TK receptors, as well as their ligands, translocate into the nucleus via receptor-mediated endocytosis for degradation or to be recycled back to the cell surface (30-34). However, it now seems clear that these complexes reach into the cell nucleus where participate directly in the control of cell proliferation, cell differentiation, and cell survival (34).

The current concept of metastasis development states that metastases are the result of tumor cells interacting with a specific organ microenvironment, also called the "seed and soil" hypothesis (35). Thus, the microenvironments of different organs, including the brain, are biologically unique and can explain the expression of HER receptors and ligands in the brain metastasis tissue specimens differing from expression in the corresponding primary lung tumors. In addition, these observations have important implications for the development of molecularly targeted therapy in lung cancer patients. The fact that potential therapeutic targets (amphiregulin, EGF, TGF-α, EGFR, and Her3) are expressed differently in metastases from corresponding primary tumors suggests that

different molecular properties among tumor sites may influence differing responses to treatment and affect the levels of biomarkers that may be predictive of the response to treatment. Although immunohistochemical testing of EGFR has been shown not to be an optimal method for identifying patients who may respond to treatment with anti-EGFR drugs (15), there are preliminary data suggesting that the expression in tumor tissue of Her3 (14) amphiregulin, and TGF- α (27) correlates with sensitivity and resistance to EGFR TKI therapy. The immunohistochemical overexpression of Her3 in NSCLC tissue specimens has been correlated with EGFR TKI sensitivity (14). In contrast, increased expression of amphiregulin and TGF- α has been correlated with resistance to such therapy (27).

An increase in *EGFR* gene copy number, including high polysomy and gene amplification (as shown by FISH), has been detected in 22% of patients with surgically resected (stages I–IIIA) NSCLC (20). Higher frequencies (40%–50%) of *EGFR* high copy number have been reported in patients with more-advanced metastatic NSCLC (stage IV) (36-40) In the present study, we have identified even a higher frequency (62%) of gain in *EGFR* copy number in surgically resected primary NSCLC specimens from patients who developed brain metastases. Recently, we reported that a gain in *EGFR* gene copy number was detected in 74% of primary NSCLC tumors from patients who developed brain metastasis (24). Altogether, these data suggest a stepwise increase in the frequency of gain in *EGFR* copy number in primary tumors with increasing tumor stage and, more important, with the development of brain metastasis. Interestingly, in our cases the presence of *EGFR* amplification, along with membrane EGFR protein overexpression, was significantly correlated with shorter time to brain metastasis

development in the univariate analysis, further suggesting the important role of this genetic abnormality in the progression and metastasis of NSCLC.

Recently, we (19) and others (41) have shown that *EGFR* copy number gain, and specifically gene amplification, is a late phenomenon in the development of lung adenocarcinoma, appearing at invasive tumor stages and progressing in lymph node metastases, and that it is preceded by gene mutation. In the present study, we have expanded some of these observations to NSCLC brain metastasis. Although it was not statistically significant, we found that brain metastases of lung adenocarcinomas had a higher frequency of *EGFR* amplification than the corresponding primary tumors (30% versus 13%). Although a relatively high level (82%) of concordance for gain in *EGFR* copy number (when high polysomy and amplification were analyzed together) was detected when primary tumors and metastases were compared, there were 10 discordant cases (18%), including 7 brain metastases that had increased copy numbers while primary tumors did not. In contrast, we found that *EGFR* gene amplification had a low level of concordance (32%) when primary and metastatic tumors were compared, indicating a high level of heterogeneity for this phenomenon. The distinct rate of *EGFR* gene amplification between primary tumors and corresponding brain metastases may support the influence of this phenomenon on differing responses to treatment and may impact the assessment of this specific biomarker for anti-EGFR therapy.

In summary, our findings indicate that NSCLC brain metastases exhibit important differences in abnormalities related to the HER family receptors from primary lung tumors. These differences may cause different responses to EGFR-targeted therapy of primary and metastatic tumor sites. Although our series of cases is relatively small and

restricted to one metastatic site per patient, the data strongly suggest that the analysis of both primary and metastasis tumor sites may be critical for the identification of novel therapeutic targets and corresponding predictive biomarkers in lung cancer.

References

1. Jemal A, Siegel R, Ward E, et al. Cancer statistics, 2008. CA Cancer J Clin 2008; 58:71-96.

2. Travis WD, Brambilla E, Muller-Hermelink HK, Harris CC. Tumours of the Lung, Pleura, Thymus and Heart. World Health Orgnaziation Classification of Tumours. Pathology & Genetics. Lyon, International Agency for Research on Cancer (IARC), 2004, pp 9-124.

3. Stuschke M, Eberhardt W, Pottgen C, et al. Prophylactic cranial irradiation in locally advanced non-small-cell lung cancer after multimodality treatment: long-term follow-up and investigations of late neuropsychologic effects. J Clin Oncol 1999; 17:2700-9.

4. Omuro AM, Kris MG, Miller VA, et al. High incidence of disease recurrence in the brain and leptomeninges in patients with nonsmall cell lung carcinoma after response to gefitinib. Cancer 2005; 103:2344-8.

5. Mamon HJ, Yeap BY, Janne PA, et al. High risk of brain metastases in surgically staged IIIA non-small-cell lung cancer patients treated with surgery, chemotherapy, and radiation. J Clin Oncol 2005; 23:1530-7.

6. Chen AM, Jahan TM, Jablons DM, Garcia, J., Larson DA. . Risk of cerebral metastases and neurological death after pathological complete response to neoadjuvant therapy for locally advanced nonsmall-cell lung cancer: clinical implications for the subsequent management of the brain. Cancer 2007; 109:1668-75.

7. Zabel A, Debus J. Treatment of brain metastases from non-small-cell lung cancer (NSCLC): radiotherapy. Lung Cancer 2004; 45 Suppl 2:S247-52.

8. Lester JF, MacBeth FR, Coles B. Prophylactic cranial irradiation for preventing brain metastases in patients undergoing radical treatment for non-small-cell lung cancer: a Cochrane Review. Int J Radiat Oncol Biol Phys 2005; 63:690-4.

9. Lynch TJ, Bonomi PD, Butts C, et al. Novel agents in the treatment of lung cancer: Fourth Cambridge Conference. Clin Cancer Res 2007; 13:s4583-8.

10. Herbst RS. Review of epidermal growth factor receptor biology. Int J Radiat Oncol Biol Phys 2004; 59:21-6

11. De Luca A, Carotenuto A, Rachiglio A, et al. The role of the EGFR signaling in tumor microenvironment. J Cell Physiol 2008; 214:559-67.

12. Sequist LV, Lynch TJ. EGFR tyrosine kinase inhibitors in lung cancer: an evolving story. Annu Rev Med 2008; 59:429-42.

13. Herbst RS, Bunn PA, Jr.. Targeting the epidermal growth factor receptor in non-small cell lung cancer. Clin Cancer Res 2003; 9:5813-24.

14. Fujimoto N, Wislez M, Zhang J, et al. High expression of ErbB family members and their ligands in lung adenocarcinomas that are sensitive to inhibition of epidermal growth factor receptor. Cancer Res 2005; 65:11478-85.

15. Ciardiello F, Tortora G. EGFR antagonists in cancer treatment. N Engl J Med 2008; 358:1160-74.

16. Cappuzzo F, Ardizzoni A, Soto-Parra H, et al. Epidermal growth factor receptor targeted therapy by ZD 1839 (Iressa) in patients with brain metastases from non-small cell lung cancer (NSCLC). Lung Cancer 2003; 41:227-31.

17. Namba Y, Kijima T, Yokota S, et al. Gefitinib in patients with brain metastases from non-small-cell lung cancer: review of 15 clinical cases. Clin Lung Cancer 2004; 6:123-8.

18. Mountain CF. Revisions in the International System for Staging Lung Cancer. Chest 1997 ; 111:1710-7.

19. Tang X, Varella-Garcia M, Xavier AC, et al. EGFR abnormalities in the pathogenesis and progression of lung adenocarcinomas. Cancer Prev Res 2008; 1:192-200.

20. Hirsch FR, Varella-Garcia M, Bunn PA, Jr., et al. Epidermal growth factor receptor in non-small-cell lung carcinomas: correlation between gene copy number and protein expression and impact on prognosis. J Clin Oncol 2003; 21:3798-807.

21. Merrick DT, Kittelson J, Winterhalder R, et al. Analysis of c-ErbB1/epidermal growth factor receptor and c-ErbB2/HER-2 expression in bronchial dysplasia: evaluation of potential targets for chemoprevention of lung cancer. Clin Cancer Res 2006; 12:2281-8.

22. Tsao AS, Tang XM, Sabloff B, et al. Clinicopathologic characteristics of the *EGFR* gene mutation in non-small cell lung cancer. J Thorac Oncol 2006; 1:231-9.

23. Varella-Garcia M. Stratification of non-small cell lung cancer patients for therapy with epidermal growth factor receptor inhibitors: the *EGFR* fluorescence in situ hybridization assay. Diagn Pathol 2006; 1:19.

24. Massarelli E, Varella-Garcia M, Tang X, et al. KRAS mutation is an important predictor of resistance to therapy with epidermal growth factor receptor tyrosine kinase inhibitors in non-small-cell lung cancer. Clin Cancer Res 2007; 13:2890-6.

25. Rusch V, Klimstra D, Venkatraman E, Pisters PW, Langenfeld J, Dmitrovsky E. Overexpression of the epidermal growth factor receptor and its ligand transforming growth factor alpha is frequent in resectable non-small cell lung cancer but does not predict tumor progression. Clin Cancer Res 1997; 3:515-22.

26. Volante M, Saviozzi S, Rapa I, et al. Epidermal growth factor ligand/receptor loop and downstream signaling activation pattern in completely resected nonsmall cell lung cancer. Cancer 2007; 110:1321-8.

27. Kakiuchi S, Daigo Y, Ishikawa N, et al. Prediction of sensitivity of advanced non-small cell lung cancers to gefitinib (Iressa, ZD1839). Hum Mol Genet 2004; 13:3029-43.

28. Wu W, O'Reilly MS, Langley RR, et al. Expression of epidermal growth factor (EGF)/transforming growth factor-alpha by human lung cancer cells determines their response to EGF receptor tyrosine kinase inhibition in the lungs of mice. Mol Cancer Ther 2007 ; 6:2652-63.

29. Sasaki T, Nakamura T, Rebhun RB, et al. Modification of the primary tumor microenvironment by transforming growth factor alpha-epidermal growth factor receptor signaling promotes metastasis in an orthotopic colon cancer model. Am J Pathol 2008; 173:205-16.

30. Carpenter G: Nuclear localization and possible functions of receptor tyrosine kinases. Curr Opin Cell Biol 2003; 15:143-8.

31. Johnson HM, Subramaniam PS, Olsnes S, Olsnes S. Trafficking and signaling pathways of nuclear localizing protein ligands and their receptors. Bioessays 2004; 26:993-1004.

32. Krolewski JJ. Cytokine and growth factor receptors in the nucleus: what's up with that? J Cell Biochem 2005; 95:478-87.

33. Massie C, Mills IG. The developing role of receptors and adaptors. Nat Rev Cancer 2006; 6:403-9.

34. Schlessinger J, Lemmon MA. Nuclear signaling by receptor tyrosine kinases: the first robin of spring. Cell 2006; 127:45-8.

35. Fidler IJ. The pathogenesis of cancer metastasis: the 'seed and soil' hypothesis revisited. Nat Rev Cancer 2003; 3:453-8.

36. Cappuzzo F, Hirsch FR, Rossi E, et al. Epidermal growth factor receptor gene and protein and gefitinib sensitivity in non-small-cell lung cancer. J Natl Cancer Inst 2005; 97:643-55.

37. Tsao MS, Sakurada A, Cutz JC, et al. Erlotinib in lung cancer - molecular and clinical predictors of outcome. N Engl J Med 2005; 353:133-44.

38. Hirsch FR, Varella-Garcia M, McCoy J, et al. Increased Epidermal Growth Factor Receptor Gene Copy Number Detected by Fluorescence In Situ Hybridization Associates With Increased Sensitivity to Gefitinib in Patients With Bronchioloalveolar Carcinoma Subtypes: A Southwest Oncology Group Study. J Clin Oncol, 2005 ; 23 :3186-97.

39. Jackman DM, Holmes AJ, Lindeman N, et al. Response and resistance in a non-small-cell lung cancer patient with an epidermal growth factor receptor mutation and leptomeningeal metastases treated with high-dose gefitinib. J Clin Oncol 2006; 24:4517-20.

40. Bunn PA, Jr., Dziadziuszko R, Varella-Garcia M, et al. Biological markers for non-small cell lung cancer patient selection for epidermal growth factor receptor tyrosine kinase inhibitor therapy. Clin Cancer Res 2006; 12:3652-6.

41. Yatabe Y, Takahashi T, Mitsudomi T. Epidermal growth factor receptor gene amplification is acquired in association with tumor progression of *EGFR*-mutated lung cancer. Cancer Res 2008; 68:2106-11.

Figure Legends

Figure 1. Representative microphotographs of immunohistochemical expression of HER receptors (EGFR, p-EGFR, Her2, Her3, and p-Her3) and ligands (EGF, TFG-α, and amphiregulin) in primary tumors and corresponding brain metastases (magnification, x400). All markers showed protein expression (brown staining) in tumor cells from primary and/or metastasis sites at the membrane and cytoplasm levels. In this microphotographs, amphiregulin and EGF showed also nuclear expression in malignant cells.

Figure 2. Box plots showing scores of immunohistochemical expression of multiple markers comparing primary tumors with corresponding brain metastases. Panel *a* and *b*, EGF membrane and nuclear scores. Panel *c*, amphiregulin nuclear score. Panel *d*, TGF-α cytoplasmic score. Panel *e*, p-EGFR membrane and cytoplasmic scores. Panel *f*, p-Her3 membrane score. *P* values comparing normal epithelial and tumor histologic types are shown for all comparisons.

Figure 3. Representative microphotographs of FISH showing *EGFR* copy number in primary tumors (PT) and corresponding brain metastases (BM) (magnification, x1000). Red signals (red arrows) represent *EGFR* gene copies and green signals (white arrows) represent the chromosome 7 centromere probe. Cell nuclei stained blue with DAPI. High polysomy is defined by ≥4 copies in ≥40% of cells, and gene amplification by the presence of loose or tight *EGFR* gene clusters and a ratio of *EGFR* gene to chromosome of 2 or 15 copies of *EGFR* per cell in 10% of the analyzed cells.

Table 1. Summary of clinicopathologic features of 55 NSCLC patients with primary tumors and corresponding brain metastases.

Characteristic	Number	%
Tumor Histology		
Ademocarcinoma	40	73
Squamous cell carcinoma	13	23
Large cell carcinoma	1	2
Adenosquamous carcinoma	1	2
Age		
≤60 years	30	55
>60 years	25	45
Gender		
Female	19	35
Male	36	65
Pathological Stage[1]		
I	13	23
II	10	18
III	17	31
IV[2]	13	23

[1] The staging was performed at time of surgical resection of the primary lung tumor.
[2] In 11 cases the brain metastases were surgically removed before the primary tumor.

Table 2. *EGFR* copy number by FISH in 55 NSCLC primary and corresponding brain metastases by tumor histology.

Copy Number Categories	Adenocarcinoma (*n*=40)		Squamous Cell Ca (*n*=13)		Total (*n*=55)[1]	
	Primary	Metastasis	Primary	Metastasis	Primary	Metastasis
	n (%)	*n* (%)	*n* (%)	*n* (%)	*n* (%)	*n* (%)
FISH Negative	14 (35)	14 (35)	7 (54)	5 (38)	21 (38)	19 (35)
Disomy	1 (3)	2 (5)	0 (0)	0 (0)	1 (2)	2 (4)
Trisomy	2 (5)	2 (5)	1 (7)	0 (0)	3 (5)	2 (4)
Low Polysomy	11 (28)	10 (25)	6 (46)	5 (38)	17 (31)	15 (27)
FISH Positive	26 (65)	26 (65)	6 (46)	8 (62)	34 (62)	36 (65)
High Polysomy	21 (53)	14 (35)	2 (14)	5 (38)	25 (45)	21 (38)
Amplification	5 (13)	12 (30)	4 (31)	3 (23)	9 (16)	17 (31)

[1] One adenosquamous carcinoma and one large cell carcinoma showed *EGFR* high polysomy in the primary tumors and amplification in the brain metastasis specimen.

Figure 1

Figure 2

Figure 3

Adenocarcinoma

Adenocarcinoma

Squamous Cell Carcinoma

Adenocarcinoma
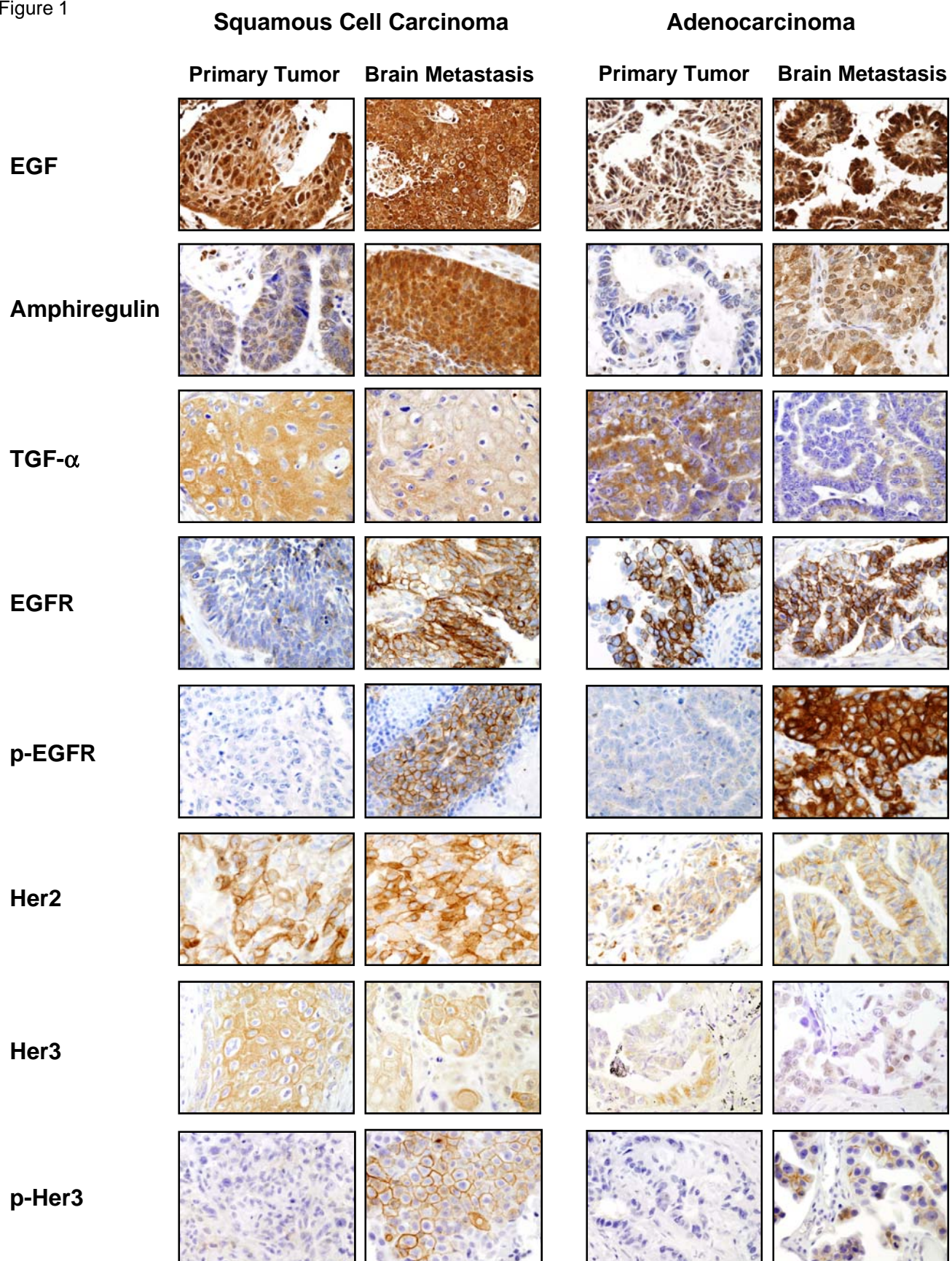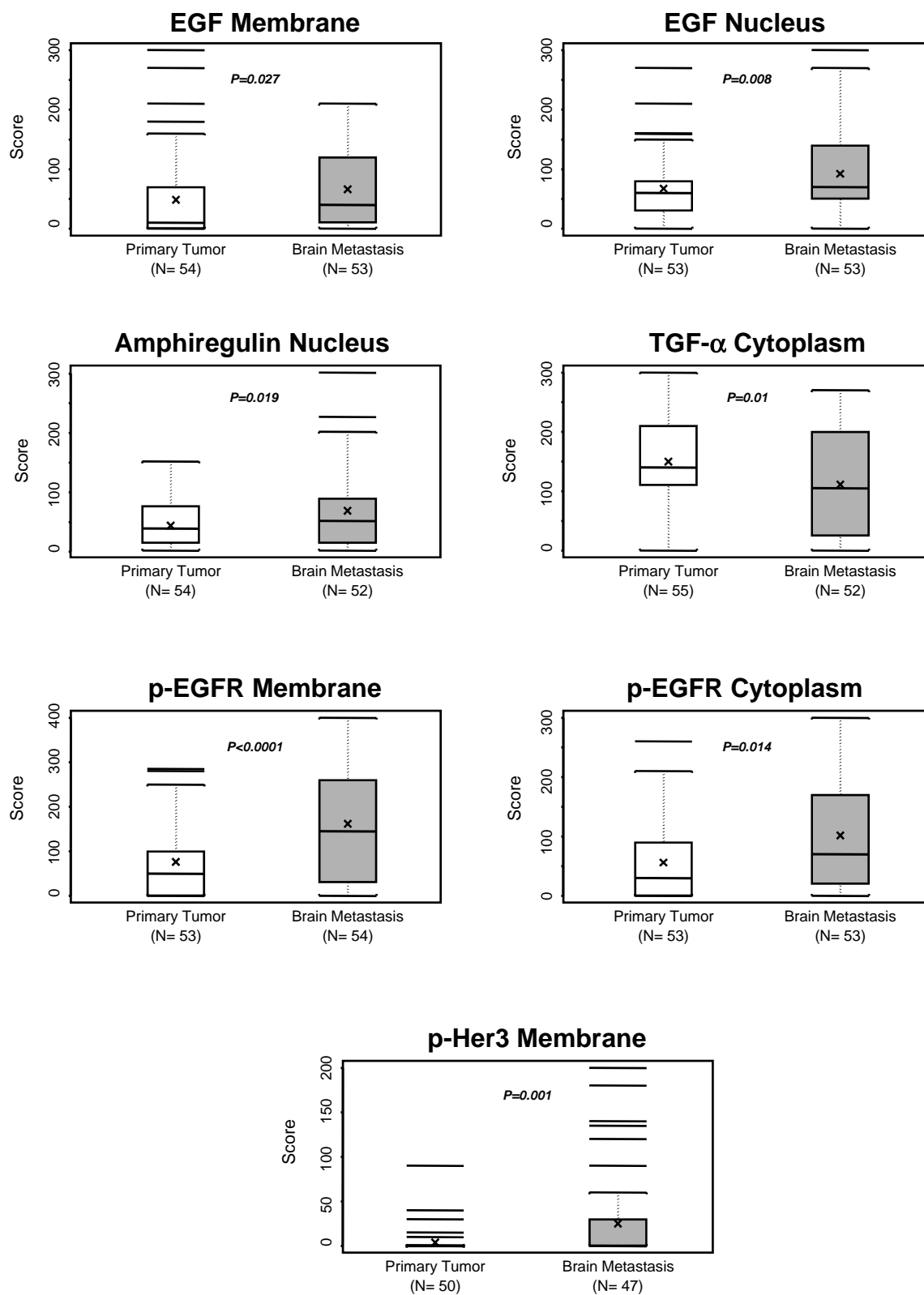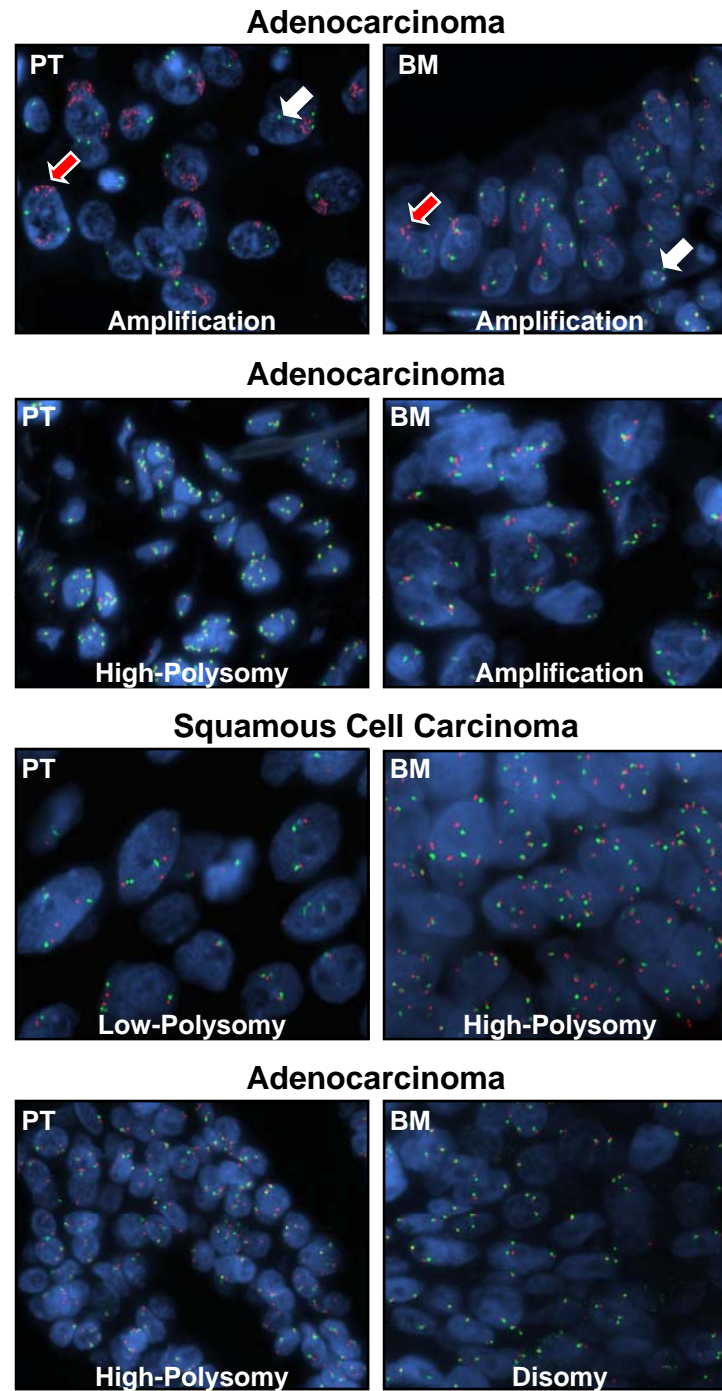
Bayesian Adaptive Randomization using Predictive Probability

Guosheng Yin, Jack J. Lee and Diane D. Liu

Department of Biostatistics

The University of Texas M. D. Anderson Cancer Center

Houston, Texas 77030, U.S.A.

SUMMARY.   We propose a new Bayesian adaptive randomization scheme based on the predictive probability in phase II trials. We illustrate the proposed method using a phase II melanoma clinical trial, and conduct extensive simulation studies to examine the operating characteristics of the design.

KEY WORDS: Adaptive design; Bayesian inference; Phase II trial.

1   Introduction

Assume that we compare K treatments in a K-arm phase II trial. Let p_k be the response rate of drug k, and we assign p_k a prior distribution of $\text{Beta}(\alpha_k, \beta_k)$, for $k = 1, \ldots, K$. Given the observed data y_k responses out of n_k subjects, $Y_k \sim \text{Binomial}(n_k, p_k)$, the posterior distribution of p_k is

$$p_k | Y_k = y_k \sim \text{Beta}(\alpha_k + y_k, \beta_k + n_k - y_k).$$

If the maximum sample size is N_k, then the number of responses in the future $N_k - n_k$ patients, X_k, follows a beta-binomial distribution $\text{Beta-Binomial}(N_k - n_k, \alpha_k + y_k, \beta_k + n_k - y_k)$. When $X_k = x_k$, the posterior probability of the response rate,

$$p_k | (Y_k = y_k, X_k = x_k) \sim \text{Beta}(\alpha_k + y_k + x_k, \beta_k + N_k - y_k - x_k).$$

Considering only two treatments, $K = 2$, we compute the predictive probability

$$\text{PP}_2 = \sum_{x_1=0}^{N_1-n_1} \sum_{x_2=0}^{N_2-n_2} P(X_1 = x_1 | Y_1 = y_1) P(X_2 = x_2 | Y_2 = y_2)$$

$$\times I\{P(p_2 > p_1 | Y_1 = y_1, X_1 = x_1, Y_2 = y_2, X_2 = x_2) \geq \theta\},$$

and $\text{PP}_1 = 1 - \text{PP}_2$. Note N_k is unknown due to adaptive randomization, while n_k is known based on the observed data. Let the number of total remaining subjects be $m = N_1 + N_2 - n_1 - n_2$, which is known. Then we approximate N_k by $m \times P(p_2 > p_1 | Y_1 = y_1, Y_2 = y_2)$, for $k = 1, 2$, where $P(p_2 > p_1 | Y_1 = y_1, Y_2 = y_2)$ is the posterior probability. We assign a new subject to treatment 2 with probability PP_2.

We can also use a Bayesian hierarchical model for efficacy, which allows us to borrow information across multiple treatment arms. Let $(p_1, \ldots, p_K)$ denote the response rates corresponding to the K treatments, and assume that among n_k patients treated in arm k, y_k subjects have experienced efficacy. We model efficacy using the Bayesian hierarchical model:

$$
\begin{aligned}
y_k &\sim \text{Binomial}(n_k, p_k) \\
p_k &\sim \text{Beta}(\zeta, \xi) \\
\zeta &\sim \text{Gamma}(0.01, 0.01) \\
\xi &\sim \text{Gamma}(0.01, 0.01)
\end{aligned}
\tag{1}
$$

where $Bi(n_k, p_k)$ denotes a binomial distribution, and $Be(\zeta, \xi)$ denotes a beta distribution with a shape parameter ζ and a scale parameter ξ. We take vague gamma prior distributions $Ga(0.01, 0.01)$ with mean one, for ζ and ξ to ensure that the data will dominate the posterior distribution. The full conditional distribution of p_k follows $Be(\zeta + y_k, \xi + n_k - y_k)$, but those of ζ and ξ do not have closed forms. We sample from their conditional distributions using the adaptive rejection Metropolis method (Gilks, Best and Tan, 1995). We continuously update the posterior estimates of the p_k's under the model (1) based on accumulated data, and adaptively randomize new patients to efficacious arms.

2

Once the adaptive randomization is in effect, the maximum numbers of subjects in arm 1 and arm 2 are random. Let the remaining subjects in the trial be m which is fixed, and let Z be the number of subjects that would be assigned to arm 2. If we denote the posterior probability

$$\pi = P(p_2 > p_1|D) = P(p_2 > p_1|Y_1 = y_1, Y_2 = y_2),$$

then $Z \sim Bi(m, \pi)$, i.e.,

$$P_Z(z|D) = \binom{m}{z}\pi^z(1 - \pi)^{m-z}.$$

We would claim arm 2 as a superior treatment arm if

$$\pi = P(p_2 > p_1|D) \geq \theta,$$

where θ can be calibrated by simulation studies.

We can average over Z, and then conditional on $Z = z$ average over X_1 and X_2. Therefore, we compute the predictive probability

$$
\begin{aligned}
\mathrm{PP}_2 &= \sum_{z=0}^{m}\sum_{x_1=0}^{m-z}\sum_{x_2=0}^{z} P_Z(z|D)P(X_1 = x_1|Y_1 = y_1, m - Z = m - z) \\
&\quad \times P(X_2 = x_2|Y_2 = y_2, Z = z)I\{P(p_2 > p_1|Y_1 = y_1, X_1 = x_1, Y_2 = y_2, X_2 = x_2) \geq \theta\}, \\
&= \sum_{z=0}^{m}\sum_{x_1=0}^{m-z}\sum_{x_2=0}^{z} \binom{m}{z}\pi^z(1 - \pi)^{m-z}P(X_1 = x_1|Y_1 = y_1, m - Z = m - z) \\
&\quad \times P(X_2 = x_2|Y_2 = y_2, Z = z)I\{P(p_2 > p_1|Y_1 = y_1, X_1 = x_1, Y_2 = y_2, X_2 = x_2) \geq \theta\}, \\
&= \sum_{z=0}^{m}\sum_{x_1=0}^{m-z}\sum_{x_2=0}^{z} \binom{m}{z}\{P(p_2 > p_1|Y_1 = y_1, Y_2 = y_2)\}^z\{1 - P(p_2 > p_1|Y_1 = y_1, Y_2 = y_2)\}^{m-z} \\
&\quad \times P(X_1 = x_1|Y_1 = y_1, m - Z = m - z)P(X_2 = x_2|Y_2 = y_2, Z = z) \\
&\quad \times I\{P(p_2 > p_1|Y_1 = y_1, X_1 = x_1, Y_2 = y_2, X_2 = x_2) \geq \theta\},
\end{aligned}
$$

which can be computationally intensive.

Erlotinib enhances RAD001's anticancer activity *in vivo* involving abrogation of mTOR inhibition-induced eIF4E phosphorylation. Songqing Fan, Xuerong Wang, Ping Yue, John Kauh, Suresh S. Ramalingam, Fadlo R. Khuri, Shi-Yong Sun. *Department of Hematology and Medical Oncology, Winship Cancer Institute, Emory University School of Medicine, Atlanta, GA 30322.*

The synergistic anticancer activity between an mTOR inhibitor (e.g. RAD001) and an EGFR inhibitor (e.g., erlotinib) has been documented in several studies including ours. However, the underlying mechanisms remain unknown. It is well known that mTOR activates cap-dependent translation initiation by preventing 4E-BP1 from binding to eIF4E by phosphorylating 4E-BP1. Paradoxically, mTOR inhibitors increase eIF4E phosphorylation while inhibiting mTOR signaling (Sun et al. Cancer Res, 2005). As a result, mTOR inhibitors' effects on suppression of cap-dependent translation as well as of cancer cell growth may be compromised (Wang et al, Mol Cell Biol, 2007). In the current study, we further show that lung cancer xenografts treated with RAD001 for 14 days exhibited significantly higher levels of p-eIF4E than vehicle-treated controls although the growth of these xenografts was indeed partially inhibited, thus confirming our *in vitro* finding on mTOR inhibition-mediated eIF4E phosphorylation *in vivo*. In xenografts treated with the combination of RAD001 and erlotinib, eIF4E phosphorylation was not increased compared with RAD001-treated tumors. Accordingly, the combination of RAD001 and erlotinib was more potent than each agent alone in inhibiting the growth of lung cancer xenografts. Moreover, we noted that the expression of Mcl-1, which is regulated by cap-dependent translation mechanism and important for eIF4E-mediated oncogenesis, was slightly increased in RAD001-treated tumors, but significantly inhibited in lung tumors treated with the combination of RAD001 and erlotinib. Collectively, we suggest that erlotinib enhances RAD001's anticancer activity *in vivo* involving abrogation of mTOR inhibition-induced eIF4E phosphorylation. Accordingly, modulation of eIF4E phosphorylation may serve as a predictive biomarker for RAD001/erlotinib-based cancer therapy.

USING AN EDUCATIONAL VIDEOGAME TO TACKLE TOBACCO USE AMONG YOUTH

A.V. Prokhorov, E.R. Gritz, S. Marani

Research Design: An interactive, tailored educational videogame was developed for smoking prevention and cessation among youth. A preliminary study was conducted using a pretest-posttest cohort design with assessments at baseline, 7 days and 6 months post-intervention. Feasibility and impact of the videogame on some tobacco-related measures at 6-month follow-up are reported.

Baseline Demographic Profile: A total of 239 high-risk alternative-school students were recruited. Mean age of the participants was 16.2 years (SD=1.0), 79% were male. Thirty-six percent of the participants were Hispanic and 49% were African American. Twenty-five percent were smokers.

Six-Month Feasibility Analysis: To date the 6-month survey has been completed by 144 participants. All participants played the videogame at least once and 40% played twice or more times. Over 85% of participants reported ease of use of this educational tool and the majority of participants enjoyed the experience. After playing the videogame, 94% reported increased knowledge about the tobacco effects, 82% were inspired never to start or to quit and 82% planned to share the videogame with family or friends.

Mediating Variables of Smoking at 6-month Follow-up: The primary outcomes of interest in this study were the mediating determinants of smoking initiation and cessation including the pros and cons of tobacco use, decisional balance and temptations to smoke. These outcomes were analyzed using mixed model regression with time and baseline smoking status and their interaction as fixed effects. There was as a significant interaction effect for cons of smoking ($F = 5.3$; $p<.05$), decisional balance ($F = 8.0$; $p<.01$), and temptations to smoke ($F = 7.6$; $p<.01$). For baseline smokers 6-month temptations to smoke were significantly lower than baseline, and 6-month cons of smoking were significantly higher than baseline. For nonsmokers these variables did not change significantly.

The educational videogame showed considerable promise in terms of increasing tobacco knowledge and changing attitudes among high-risk youth.

AACR Meeting Abstracts Online

Cancer Research	Clinical Cancer Research
Cancer Epidemiology Biomarkers & Prevention	Molecular Cancer Therapeutics
Molecular Cancer Research	Cancer Prevention Research
Cancer Prevention Journals Portal	Cancer Reviews Online
Annual Meeting Education Book	Meeting Abstracts Online

Institution: MD ANDERSON HOSPITAL | Sign In via User Name/Password

QUICK SEARCH: [advanced]
Author: behrens   Keyword(s): NOTCH   Go

99th AACR Annual Meeting-- Apr 12-16, 2008; San Diego, CA

This Article

Services
- Similar articles in this journal
- Download to citation manager

Google Scholar
- Articles by Prudkin Silva, M.
- Articles by Wistuba, I.

PubMed
- Articles by Prudkin Silva, M.
- Articles by Wistuba, I.

Molecular Correlates 1: Poster Presentations - Proffered Abstracts

Abstract #2168

NOTCH3/JAGGED1 pathway is involved in non-small cell lung cancer pathogenesis and interacts with EGFR pathway

Maria Prudkin Silva, Diane Liu, Joelle Tchinda, Denise Woods, Carmen Behrens, B Bekele, Cesar Moran, Charles Lee, Jon Aster, Bin-Bing Zhou and Ignacio Wistuba

UT MD Anderson Cancer Ctr., Houston, TX, Brigham and Women's Hospital, Boston, MA, Tanox Inc, Houston, TX

Notch3 (N3) is a member of the family of Notch transmembrane receptors, which are activated by ligands such as Jagged1 (JAG1). In addition to roles in normal cellular differentiation and cell-fate determination, the Notch pathway is involved in tumorigenesis. N3 is differentially expressed in lung cancer and sensitizes tumors to EGFR inhibition. However, the relationship of N3 and JAG1 protein expression with EGFR has not been studied in lung cancer. We used immunohistochemical analysis in tissue microarrays to evaluate N3, JAG1, EGFR and pEGFR protein expression in 318 non-small cell lung carcinomas (NSCLCs), including 200 adenocarcinomas (ADC) and 118 squamous cell carcinomas (SCC). We correlated these findings with the pathologic features of the tumors and the clinical characteristics of the patients. We also investigated possible *N3* rearrangement and amplification using FISH, and determined the mutational status of *EGFR* in a subset of cases (181 ADCs). Cytoplasmic staining of tumor cells for N3 and JAG1 was detected in 60% (SCC 56%; ADC 62%) and 95% (SCC 99%; ADC 93%) of NSCLCs, respectively. Staining of reactive fibroblasts for N3 was noted in 78% of tumors, and was particularly frequent in SCCs (SCC 85% vs. ADC 74%, $p=0.03$). Staining of reactive endothelial cells for JAG1 was observed in 60% of tumors, and was also significantly higher in SCCs (SCC 74% vs. ADC 52%; $p=0.0002$). *N3* amplification was detected in 20 (8%) of NSCLCs being significantly ($p=0.02$) higher in SCCs, but did not correlate with N3 protein staining within tumor cells. Tumor cell staining for N3 was associated with female gender ($p=0.04$), and *N3* amplification and staining in stromal cells were significantly higher in ever smokers compared to never smokers ($p=0.0$ and 0.02, respectively). In NSCLCs, pEGFR nuclear staining was associated with JAG1 cytoplasmic staining ($p=0.02$), whereas in ADCs, *EGFR* mutations were strongly associated with higher levels of staining for N3

(p=0.0001). Our findings indicate that N3-JAG1 proteins are frequently expressed NSCLC. *N3* amplification is associated with smoking history and squamous cell differentiation, while N3 protein levels in ADCs are correlated with the presence of *EGFR* mutations. These findings suggest that NSCLC is commonly associated with aberrations in the N3-JAG1 pathway (Supported by Grant DoD-W81XWH-05-2-0027 and NCI-SPORE-P50CA70907).

This Article

Services

- **Similar articles in this journal**
- **Download to citation manager**

Google Scholar

- **Articles by Prudkin Silva, M.**
- **Articles by Wistuba, I.**

PubMed

- **Articles by Prudkin Silva, M.**
- **Articles by Wistuba, I.**

99th AACR Annual Meeting-- Apr 12-16, 2008; San Diego, CA

Molecular Correlates 1: Poster Presentations - Proffered Abstracts

Abstract #2165

Immunohistochemical expression of estrogen and progesterone receptors identifies a subset of non-small cell lung cancers and correlates with *EGFR* Mutations

Maria Raso, Carmen Behrens, Suyu Liu, Ludmila Prudkin, Denisse Woods, Natalie Ozburn, Cesar Moran , J Jack Lee and Ignacio Wistuba

MD ANDERSON CANCER CENTER, Houston, TX

Estrogen (ER) α and β and progesterone (PR) receptors are transcription factors that regulate the expression of multiple genes and have been involved in the pathogenesis of non-small cell lung cancer (NSCLC). There are conflictive results reported on the immunohistochemical (IHC) expression of ER receptors in NSCLC tissue specimens using different commercially available antibodies (Abs). Correlation between ER expression and *EGFR* mutation status has been reported in lung cancer cell lines. Our aims were to compare the IHC expression pattern in tumor tissues of six commercially available ER antibodies (four α and two β) in a large set (N=317) of NSCLCs tissue microarrays containing 201 adenocarcinomas and 116 squamous cell carcinomas, and correlate the expression of ER and PR with patients' clinical-pathologic characteristics, and in adenocarcinomas with *EGFR* mutation status. The Abs used were: a) ERα: clone 6F11(2 abs), clone HC-20 and clone 1D5N; b) ERβ: clone H-150 and 14C8; and, c) PR: polyclonal. ER α and β expression were detected in the cytoplasm (ERα clone HC-20 and clone 1D5N)18%-42%; ERβ 20-98%) and the nucleus (ERα 5%-36%; ERβ 42-56%) of malignant cells, however the frequency of expression in tumors varied between Abs. PR expressed only at nuclear level in 63% of tumors. Higher nuclear expression of most ERα Abs significantly correlated with adenocarcinoma tumor histology, female gender and never smoking history. The Ab raised against the ERα N-terminus protein (clone 1D5N, Lab Vision Co, Fremont, CA) significantly correlated with all those variables when stained in the nucleus and with worse recurrence free survival (HR 1.77, 95% CI 1.12, 2.82; *P*=0.015) when stained in the cytoplasm. Higher nuclear and cytoplasmic expressions of ERα Abs clones HC-20 and 1D5N, and higher nuclear expression an ERβ Ab clone H150 correlated with the presence of *EGFR* mutation in adenocarcinomas (*P*=0.0029 to <0.00001). We conclude that both ERs

and PR express in NSCLC, and we identified Abs against ERs that distinguish a subset on NSCLC having defined clinical-pathologic features, including *EGFR* mutation in lung adenocarcinoma histology. Then, we studied the expression of ER and PR in the early pathogenesis of lung cancer, and for ER we selected one Ab for each type of receptor (α clone 1D5N; β clone H150). We found that cytoplasmic ERβ and nuclear PR were frequently expressed in the normal bronchial and bronchiolar epithelium (n=194) adjacent to lung adenocarcinomas as a field effect phenomenon. Of interest, normal and hyperplastic alveolar cells did not express those receptors, suggesting a cell type-based specific field abnormality. Our findings suggest that hormonal receptor antagonist therapy could be considered in the development of novel therapeutic and chemopreventive strategies in NSCLC (Supported by Grant DoD-W81XWH-04-1-0142 and W81XWH-05-2-0027).

99th AACR Annual Meeting-- Apr 12-16, 2008; San Diego, CA

Molecular Correlates 1: Poster Presentations - Proffered Abstracts

Abstract #2163

EGFR increased copy number is frequent in non-small cell lung cancer with brain metastasis

Menghong Sun, Erminia Massarelli, Natalie Ozburn, Ximing Tang, Ludmila Prudkin, Ritsuko Komaki , Waun Ki Hong, Cesar Moran, Kenneth Aldape, Marileila Varella-Garcia and Ignacio Wistuba

UT MD Anderson Cancer Ctr., Houston, TX, University of Colorado Health Sciences Center, Aurora, CO

The brain is one of the main metastatic sites for lung cancer, occurring in ~50% of patients with non-small cell lung carcinoma (NSCLC). Despite recent advances in lung cancer targeted therapy, there is limited information on the molecular characteristics of lung cancer brain metastasis. In NSCLC, *EGFR* gene increased copy number has been involved in tumor development and it has been detected in ~23% of surgically resected tumors. In advanced tumors, it has been associated to prediction of response of EGFR tyrosine kinase inhibitors. To better characterize NSCLC brain metastasis, we investigated the *EGFR* copy number by fluorescence *in situ* hybridization (FISH) in 58 paired NSCLC primary tumors (42 adenocarcinomas, 14 squamous cell carcinomas, and 2 others) and corresponding brain metastasis using tissue microarrays. We correlated these findings with the immunohistochemical expression of HER family ligands and receptors in the same tumor specimens, including EGF, amphiregulin, TGFα, EGFR, p-EGFR, Her2, Her3, and p-Her3. *EGFR* FISH (+) or increased copy number was defined as high-polysomy and/or gene amplification. Higher frequency of *EGFR* FISH+ was seen in brain metastasis (68%), especially gene amplification (29%), compared to corresponding primary tumors (FISH+ 59%; gene amplification 17%). Correlation of FISH status between primary tumor and corresponding metastasis was 78%. In primary tumors and brain metastases the frequency of FISH+ was higher in adenocarcinomas (64% and 71%, respectively) compared to squamous cell carcinomas (43% and 57%, respectively). In primary tumors, similar high level of *EGFR* FISH+ was found comparing stages I/II (60%) and III/IV (62%). *EGFR* FISH+ correlated with higher expression of amphiregulin (P=0.011) and Her2 (P=0.006) in primary tumors, and with pEGFR (P=0.024) in brain metastases. Primary tumors with *EGFR* gene amplification demonstrated the shortest time for brain metastasis development after surgical resection with curative intent. Our findings indicate that NSCLC brain metastasis and their corresponding primary tumors

demonstrate a high frequency of *EGFR* increased copy number by FISH, especially gene amplification, suggesting that this molecular abnormality may be involved in tumor progression phenomenon (Supported by Grant W81XWH-05-2-0027).

This Article

Services

▶ **Similar articles in this journal**
▶ **Download to citation manager**

Google Scholar

▶ **Articles by Sun, M.**
▶ **Articles by Wistuba, I.**

PubMed

▶ **Articles by Sun, M.**
▶ **Articles by Wistuba, I.**

TITF-1 and EGFR gene copy variations are associated with prognosis for the patients with non-small cell lung cancer

Ximing Tan, Diane Liu, Carmen Behrens, Dandan He, Menghong Sun, David Rice, J. Jack Lee, Waun K. Hong, and Ignacio I. Wistuba

UT MD Anderson Cancer Center, Houston, TX 77030

Thyroid transcription factor -1 (TITF-1, a lineage-specific transcription factor), and the epidermal growth factor receptor (EGFR, a tyrosine kinase membrane receptor) have shown frequent gene amplification in non-small cell lung carcinomas (NSCLC). We investigated the clinico-pathologic characteristics of NSCLCs having *TITF-1* andor *EGFR* gene copy number abnormalities by examining gene copy number status using quantitative polymerase chain reaction (qPCR) and DNA extracted from microdissected formalin-fixed and paraffin-embedded tissue from 53 adenocarcinomas and 29 squamous cell carcinomas. ß-actin gene was used as reference. In tumors, gene copy ratio referred to *ß-actin* ranged from 0.22 to 74.93 (median=1.52) for *TITF-1*, and 0.05 to 6.28 (median=1.51) for *EGFR*. Ratios 1 to 2 were defined as normal gene copy number (NGC). Ratios <1 and >2 were defined as low gene copy (LGC) and high gene copy (HGC) number, respectively. Both, LGC and HGC categories were defined as abnormal gene copy. Similar frequencies of *TITF-1* and *EGFR* copy number categories were detected comparing adenocarcinoma (*TITF-1*: LGC 15, 28%; NGC 20, 38%; HGC 18, 34%; *EGFR*: LGC 9, 17%; NGC 27, 51%; HGC, 17, 32%) with squamous cell carcinoma (*TITF-1*: LGC 8, 28%; NGC 14, 48%; HGC 7, 24%; *EGFR* : LGC 5, 17%; NGC 18, 62%; HGC 6, 21%). We found a statistically significant correlation between *TITF-1* and *EGFR* copy numbers (Spearman correlation coefficient=0.36, *P*=0.0008). In both tumor histologies, neither *TITF-1* nor *EGFR* gene copy increase (ratio >2) correlated with disease prognosis**.** However, in adenocarcinomas, Kaplan-Meier and log rank tests revealed that the median time to death was longer in patients with normal copy number compared with those with abnormal copies for *TITF-1* (median 4.76 years, 95% CI 2.95~NA, *P* = 0.04) and *EGFR* (4.76 years, 95% CI 3.13~ NA, *P*=0.04). Moreover, adenocarcinoma patients with combined *TITF-1* and *EGFR* abnormal copy showed worse overall survival (3.56 years, 95% CI 3.13~ NA) compared with patients with normal copy

status (median not reached, *P*=0.003). In these patients, multicovariate Cox modeling indicated that combined copy abnormality of both genes is an independent factor for worse overall survival (HR 4.566, *P*=0.0057). Our findings suggest that loss and gain of *TITF1* and *EGFR* are frequent abnormalities in both adenocarcinomas and squamous cell carcinomas of the lung, and in adenocarcinoma patients correlate with disease outcome. (Supported by Grant DoD-W81XWH-04-1-0142 and W81XWH-05-2-0027).

(***TITF-1*** **and** ***EGFR*** **gene copies in lung cancer**)

AACR Meeting Abstracts Online

Cancer Research	Clinical Cancer Research
Cancer Epidemiology Biomarkers & Prevention	Molecular Cancer Therapeutics
Molecular Cancer Research	Cancer Prevention Research
Cancer Prevention Journals Portal	Cancer Reviews Online
Annual Meeting Education Book	Meeting Abstracts Online

Institution: MD ANDERSON HOSPITAL | Sign In via User Name/Password

QUICK SEARCH: [advanced]

Author: prudkin   Keyword(s):   [Go]

99th AACR Annual Meeting-- Apr 12-16, 2008; San Diego, CA

This Article

Services
- Similar articles in this journal
- Download to citation manager

Google Scholar
- Articles by Tang, X.
- Articles by Wistuba, I.

PubMed
- Articles by Tang, X.
- Articles by Wistuba, I.

Molecular Markers for Cancer Diagnosis and Determination of Patient Outcomes: Oral Presentations - Proffered Abstracts

Abstract #4952

TITF-1 gene amplification and protein expression pattern identify adenocarcinoma of lung with worse prognosis

Ximing Tang, Menghong Sun, Carmen Behrens, Ludmina Prudkin, Natalie Ozburn, Adi Gazdar, Cesar Moran , Marileila Varella-Garcia and Ignacio Wistuba

UT M.D. Anderson Cancer Center, Houston, TX, UT Southwestern Medical Center, Dallas, TX, University of Colorado, Aurora, CO

Thyroid transcription factor -1 (TITF-1), a lineage-specific transcription factor frequently overexpressed in lung adenocarcinoma, has been recently reported to show gene amplification in a subset of these tumors. To better characterize *TITF-1* copy number in non-small cell lung carcinomas (NSCLC) and correlate it with protein expression, we studied both gene copy number and protein expression using fluorescent *in situ* hybridization (FISH) and immunohistochesmistry stain (IHC) assays in a large series (N=324) of surgical resected NSCLCs placed in tissue microarrays, including 205 adenocarcinomas and 119 squamous cell carcinomas. We correlated our findings with patients' clinico-pathologic characteristics, and in a subset of adenocarcinomas with *EGFR* (exons 19-21) and *KRAS* (exons 1 and 2) mutation status. *TITF-1* amplification (FISH+, clustered gene signals) was detected in 19% (51 out of 269) of tumors, without differences by histology (18% of squamous cell carcinoma and 19% of adenocarcinoma). TITF-1 protein high level expression (IHC+, semiquantitative score $\geq$200, range 0-300) was detected exclusively in adenocarcinomas (48% of cases), and in this tumor type correlated with gene amplification (P=0.005). No correlation between TITF1 abnormalities and patients' age, gender, smoking status and TNM stages was detected. In adenocarcinomas, IHC+, but not FISH+, correlated with *EGFR* and *KRAS* mutations: IHC+ was more frequently found in *EGFR* (16/21, 76% vs. 59/172, 34%, P<0.001) and *KRAS* (8/11, 72% vs. 26/75, 34%, P=0.016) mutant compared with wild-types tumors. Survival analysis showed that for adenocarcinoma *TITF-1* FISH+ correlated with worse recurrence-free survival (P=0.001), while IHC+ correlated with better recurrence-free survival (P=0.036). Our findings indicate that *TITF-1* amplification occurs in a subset of NSCLCs, including both major tumor histologies: adenocarcinoma and squamous cell carcinoma. The association of TITF1 expression with *EGFR* and *KRAS*

mutation in lung adenocarcinomas may correlate with the peripheral airway origin of these tumors. Both *TITF-1* gene amplification and protein expression correlate with NSCLC patients' prognosis. (Supported by Grant DoD-W81XWH-04-1-0142 and W81XWH-05-2-0027).

This Article

Services

- **Similar articles in this journal**
- **Download to citation manager**

Google Scholar

- **Articles by Tang, X.**
- **Articles by Wistuba, I.**

PubMed

- **Articles by Tang, X.**
- **Articles by Wistuba, I.**

Title: Pharmacokinetics, Biodistribution, Metabolism, and Radiation Dosimetry of [18F]F-PEG6-IPQA in Non-Human Primates: A pre-IND Study.

Author Block: Mei Tian[1], Kazuma Ogawa[1], Hsin Hsien Yeh[1], Julius Balatoni[1], Uday Mykhopadhyay[1], Asutosh Pal[1], James Jackson[1], Osama Mawlawi[1], Richard Wendt[1], Rajesh Uthamanthil[1], Agatha Borne[1], David Brammer[1], Carlos Gonzales Lepera[2], Mian Alauddin[1], Juri G. Gelovani[1], [1]MD Anderson Cancer Center, Houston, TX, USA; [2]Cyclotope, Houston, TX, USA. Contact e-mail: mei.tian@di.mdacc.tmc.edu

Presentation Number: 0120

Category: Advances in PET/SPECT Probes

Introduction: Recently, a novel radiotracer [18F]F-PEG6-IPQA was developed by us for PET imaging of active-mutant EGFR expression lung carcinomas. For preparation of an IND for a clinical Phase I trial, the pharmacokinetics (PK), biodistribution, metabolism, and radiation dosimetry of [18F]F-PEG6-IPQA was studied in non-human primates.

Methods: The [18F]F-PEG6-IPQA was synthesized in several steps. The intermediate, 2-[2-(2-{2-[2-(2-[4-(3-Iodophenylamino)-6-nitro-quinazoline-7-yloxy]-ethoxy]-ethoxy}-ethoxy)-ethoxy]-ethoxy}-ethanol was mesylated and radiofluorinated with [18F]KF/Kryptofix$_{222}$ in DMSO (120°C, 30 min). Thereafter, the 6-nitro group was reduced to amine and converted to an acrylamide. The final purification of [18F]F-PEG6-IPQA was accomplished with HPLC (>99% pure). Three rhesus macaques (6-10 kg) were injected intravenously with [18F]F-PEG6-IPQA (5 mCi/animal). Dynamic imaging was performed using Discovery ST8 PET/CT (GE Healthcare) for the first 30 min covering the thoraco-abdominal area, followed by whole body static images at 60, 90, 120, and 180 min. Blood was sampled at 1-1.5-2-3-5-8-16-32-60-90-120-180 min, urine - at the end of imaging and extracted with 3-fold volume of acetonitrile. Radiolabeled metabolites were analyzed by HPLC. The PK and radiation dosimetry estimates were obtained from blood sampling and region of interest analysis (ROI) data measured on PET/CT images.

Results: [18F]F-PEG6-IPQA exhibited rapid redistribution upon i.v. injection and a bi-exponential blood clearance with fast and slow phase half-times of ~2 and ~22 min, respectively, via both hepatobiliary and renal pathways. The degradation of [18F]F-PEG6-IPQA to [18F]F-PEG6 was slow (T1/2~4min). The radiation dose-limiting organs were liver, upper intestine and kidneys. Lung tissue exhibited low uptake of [18F]F-PEG6-IPQA. Diagnostic doses up to 20 mCi of [18F]F-PEG6-IPQA can be safely administered to human patients.

Conclusion: The pharmacokinetic and radiation dosimetry characteristics of [18F]F-PEG6-IPQA should be
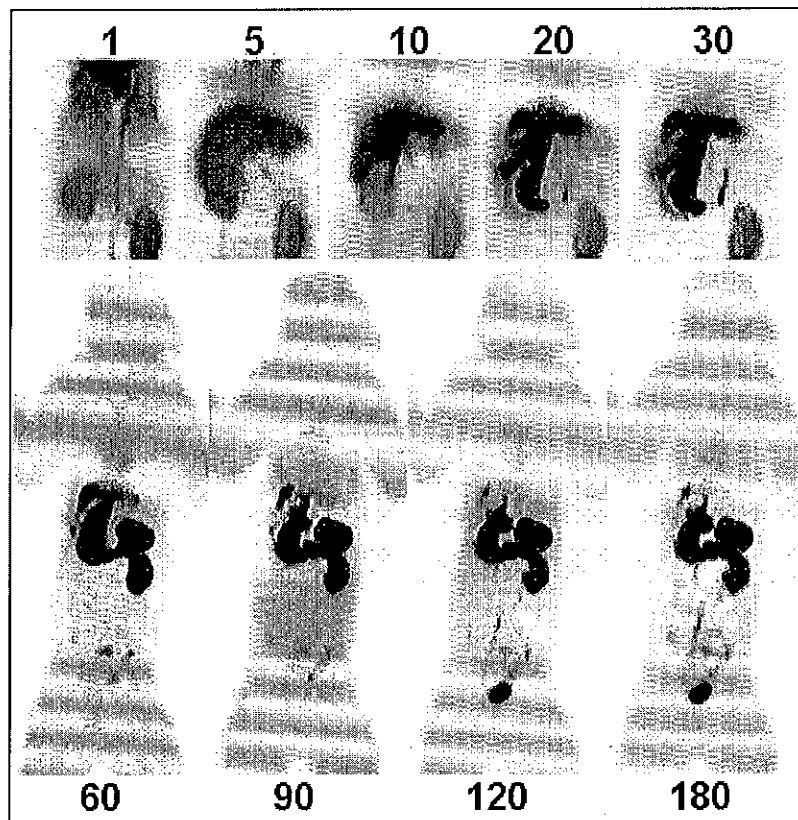
suitable for PET imaging in humans.

The epithelial-to-mesenchymal transition (EMT) governs the radiation sensitivity of non-small cell lung cancer (NSCLC) cells. Yuhui Yuan, Jenny Liu, Anupama Munshi, Kathleen A. Jensen, Ashley Roberts, and Raymond E. Meyn. *Department of Experimental Radiation Oncology, The University of Texas M. D. Anderson Cancer Center, Houston, TX.*

EMT has important roles during embryonic development where it controls tissue remodeling. EMT is also known to be important in cancer where mesenchymal-like tumor cells that have undergone EMT have lost cell-cell junctions and acquired traits characteristic of malignancy, including the ability to invade and migrate. This loss of cell adhesion is due to a down-regulation of E-cadherin expression at the level of gene transcription. Thus, loss of E-cadherin expression is a hallmark of EMT. It has been reported recently that the EMT status of NSCLC cells correlates with their sensitivity to inhibitors of the epidermal growth factor receptor (EGFR). Since there is considerable interest in combining such inhibitors with radiotherapy for the treatment of cancer, we tested whether EMT status also governs radiosensitivity of NSCLC cells. A total of 8 NSCLC cell lines were selected based on their status of E-cadherin expression, and tested for radiosensitivity using clonogenic survival analysis. Four lines expressing E-cadherin—H322, H358, H292 and Calu 3—had surviving fraction at 2 Gy (SF_2) values ranging from 0.20 to 0.44. Four lines negative for E-cadherin expression—H1299, A549, H460 and H520—had SF_2 values ranging from 0.51 to 0.74. Thus, there was a general correlation between EMT based on loss of E-cadherin expression and radioresistance. To further test this relationship, we restored E-cadherin expression in H1299 and A549 cells using an E-cadherin expression vector. Stable clones of H1299 and A549 cells expressing E-cadherin were isolated and clonogenic survival analysis on these indicated that they were radiosensitive compared to similarly isolated clones expressing a control vector. Based on these results, we conclude that EMT may govern the radiosensitivity of NSCLC cells. Strategies that are designed to restore E-cadherin expression in NSCLC that have undergone EMT may be useful when combined with radiotherapy for the treatment of this disease.

Title: Imaging Expression-Activity and Mutational Status of EGFR in Intracerebral Glioma Xenografts in Mice with [^{124}I]I-PEG6-IPQA and PET.

Author Block: **Hsin Hsien Yeh,** Asutosh Pal, Julius Balatoni, Kazuma Ogawa, Leo Flores, Andrei Volgin, Daniel Yang, Juri G. Gelovani, MD Anderson Cancer Center, Houston, TX, USA. Contact e-mail: hsinhsien.yeh@di.mdacc.tmc.edu

Presentation Number: 1151

Category: Cancer Detection Imaging

Introduction: In gliomas, epidermal growth factor receptor (EGFR) amplification and activating mutations (i.e., EGFRvIII) are critical for oncogenesis, maintenance and progression. Positron emission tomography (PET) with active EGFR kinase-specific radiolabeled tracers could provide the means for noninvasive imaging of the magnitude and spatial heterogeneity of EGFR expression in gliomas in individual patients, that is critical for selection and monitoring of therapy with EGFR inhibitors and for prognosis. In this study, the efficacy of [^{124}I]I-PEG6-IPQA PET was assessed for imaging EGFRvIII expression in intracerebral glioblastoma xenografts in mice.

Methods: Nude mice (N=12) were implanted intracerebrally with human U87/GFP-Luc cells expressing wild-type EGFR or retrovirally transduced with EGFRvIII (U87GFP-Luc/EGFRvIII) 10^6 cell/animal. Tumor growth was monitored by BLI. Ten days later, the mice were injected with [^{124}I]I-PEG6-IPQA 150 μCi, 100μl, i.v.) and dynamic PET imaging was preformed for 2h, followed by static imaging at 3h. Thereafter, the animals were sacrificed, brains removed, frozen, and cryosectioned at 20μm. Adjacent cryosections were used for quantitative autoradiography (QAR) and immunohistochemical (IHC) staining for EGFR and EGFRvIII. Treatment group (N=6) received EGFR kinase inhibitor Iressa (100 mg/kg, i.p. in DMSO, 1h prior to [^{124}I]I-PEG6-IPQA administration).

Results: Dynamic PET imaging demonstrated a more rapid dynamics of [^{124}I]I-PEG6-IPQA accumulation in U87GFP-Luc/EGFRvIII, as compared to U87/GFP-Luc xenografts. Iressa treatment reduced 2h accumulation levels of [^{124}I]I-PEG6-IPQA in U87/EGFRvIII xenografts two-fold from 1.2±0.1 to 0.63±0.04 %ID/g, as compared to non-treated animals. Smaller changes were observed in U87/GFP-Luc xenografts - 0.42±0.05 to 0.36±0.03 %ID/g, respectively. Comparison of QAR and IHC, demonstrated good spatial correspondence between the radioactivity distribution and EGFRvIII expression.**Conclusions:** PET imaging with [^{124}I]I-PEG6-IPQA demonstrated efficacy for non-invasive visualization and quantitation of of wild-type EGFR and active-mutant EGFRvIII expression in intracerebral human glioma xenografts in mice and could be applicable for prediction of responsiveness to therapy with EGFR kinase inhibitors.

Title: PET with [124I]I-PEG6-IPQA for Imaging Expression-Activity and Mutational Status of EGFR in Four Different Non Small Cell Carcinoma Xenografts in Mice.

Author Block: Hsin Hsien Yeh[1], Ryuichi Nishii[2], Julius Balatoni[1], Asutosh Pal[1], Suren Soghomonyan[1], Leo Flores[1], Andrei Volgin[1], Daniel Yang[1], Juri G. Gelovani[1], [1]MD Anderson Cancer Center, Houston, TX, USA; [2]Shiga Medical Center, Moriyama, Japan. Contact e-mail: hsinhsien.yeh@di.mdacc.tmc.edu

Disclosure Block: H. Yeh, None; **R. Nishii**, None; **J. Balatoni**, None; **A. Pal**, None; **S. Soghomonyan**, None; **L. Flores**, None; **A. Volgin**, None; **D. Yang**, None; **J.G. Gelovani**, NIH, DOE, DOD, Merck, Astra-Zeneca, GE, Siemens, Company/Organization, 1. Grant/research support; IBA, Comecer, Company/Organization, 2. Consultant; GE, Company/Organization, 3. Speakers bureau.

Presentation Number: 1152

Category: Cancer Detection Imaging

Introduction: Response to EGFR kinase inhibitor therapy in NSCLCs is associated with overexpression and activating mutations in the *EGFR* kinase domain, observed only in 8% of caucasian and 54% east-asian patients. Non-invasive imaging of EGFR expression-activity in NSCLCs would provide the means for prediction of responses to therapy with EGFR kinase inhibitors. Therefore, we assessed the efficacy of [124I]I-PEG6-IPQA for PET imaging of active-mutant EGFR expression in NSCLCs.

Methods: Subcutaneous tumor xenografts were established in immunecompromised mice using four non-small cell lung carcinoma (NSCLC) cell lines (N=6 per line) with different levels of wild-type and active-mutant epidermal growth factor receptors (EGFRs) and different responsiveness to EGFR kinase inhibitors: a) H441 (wild-type EGFR; resistant); b) PC14 (wild-type EGFR; resistant); c) H3255 (active-mutant L858R EGFR; sensitive); d) H1975 (double-mutant L858R and T790M EGFR; resistant). Control and Iressa-treated groups (prior to 1h imaging, 100 mg/kg of 100 μl in DMSO i.p.) were injected with [124I]I-PEG6-IPQA 150 μCi, 100μl, i.v.) and dynamic PET imaging was preformed for 2h, followed by a static scan at 3h. Thereafter, the animals were sacrificed, tumors removed, frozen, and cryosectioned at 20µm. Adjacent cryosections were used for QAR and immunohistochemical (IHC) staining for EGFR and phoshoEGFR.

Result: *In vivo* PET and QAR images obtained at 3 hours post [124I]I-PEG6-IPQA injection demonstrated preferential accumulation of radioactivity in H3255 carcinomas expressing the active-mutant EGFR (1.4±0.1=2 %ID/g) and in H441 carcinomas over-expressing the wild-type EGFR (1.2±0.1 %ID/g). Pre-treatment with Iressa inhibited [124I]I-PEG6-IPQA accumulation in H3255 and H441 carcinomas (0.64±0.04 0.75±0.06 %ID/g, respectively). [124I]I-PEG6-IPQA accumulation levels in all studied tumor types correlated positively with wild-type pEGFR or active-mutant EGFR expression in corresponding regions. **Conclusion:** [124I]I-PEG6-IPQA demonstrated efficacy for PET imaging of overexpression of wild-type and active-mutant EGFR in NSCLC in tumors and for prediction of responsiveness to therapy with EGFR kinase inhibitors.